

A Stochastic Heat Engine Based on Prandtl-Tomlinson Model

Dongyang Zhao^{a,1}

^aDepartment of Mechanical Engineering, Tsinghua University, 100084 Beijing, China

Stick-slip is an ubiquitous phenomenon in many scientific fields, such as earthquake and glacier dynamics, acoustics, cell biology, interface science and tribology. As a fundamental mechanism of energy dissipation in nanofriction, it can be interpreted by the Prandtl-Tomlinson (PT) model. In this paper we will show that aided by a specifically designed temperature field, stick-slip can be used to extract energy from the environment, i.e. forming a stochastic heat engine based on PT model (PTSHE). Utilizing Langevin dynamics simulation and the framework of stochastic thermodynamics, two mechanisms of work output, i.e. the potential mechanism and the thermolubricity mechanism, are distinguished. An approximate work output limit based on the former one is derived, reminiscent of Carnot's limit. The latter one can make the work output limit larger than that predicted by the former one while the excess of it can also lead to work output reduction. The mean cycle work curves with respect to the driving velocity is characteristic of PT model in both the PTSHE and nanofriction. The nonlinear bifurcation in zero temperature and the stochastic resonance in finite temperature of the PT model are analyzed preliminarily. With the corrugation number of the PT model increasing, the mean cycle work output first increases and then decreases. Besides stick-slip nanofriction and the PTSHE, the PT model is a promising system for studying nonlinear double- or multiple-well dynamics and is valuable to be explored further both theoretically and experimentally.

Stochastic heat engine | Prandtl-Tomlinson Model | Stick-slip | Nonlinear Bifurcation | Stochastic Resonance

Fric tion converts mechanical work into heat dissipation irreversibly and cause the efficiency of heat engines to reduce below the Carnot limit. Due to the development of Friction Force Microscope (FFM), study of friction has advanced to the nanoscale regime (1, 2). The tip of the FFM driven by a uniformly moving support goes through the potential landscape of an atomically plain surface. At low temperature, due to the ups and downs of the surface potential, the tip sticks and slips, causing great energy dissipation, which can be modelled by the Plandtl-Tomlinson (PT) model (3, 4) (Figure 1 and SI Appendix Sec. 3). A trapped ion friction simulator has been theoretically proposed (5–8) and then experimentally implemented (9) and utilized to study the velocity dependence of the friction force of a single ion driven through an optical lattice by a Paul trap (10), emulating the PT model. At high temperature or low velocity, thermal fluctuations of the ion (or the tip of FFM) make it jump over the middle energy barrier easily with a vanishing amount of energy loss, which is known as thermolubricity (11).

Thermal fluctuation also plays an important role in a lot of microscale (12, 13) and nanoscale (14–17) heat engines. Using a single micrometer-sized colloidal particle as the working agent and a breathing laser trap, i.e. a parabola potential $V_h' = \frac{1}{2}\kappa(t)x(t)^2$ with controllable stiffness $\kappa(t)$ coupled with heat baths of relevant temperature protocols, a stochastic heat

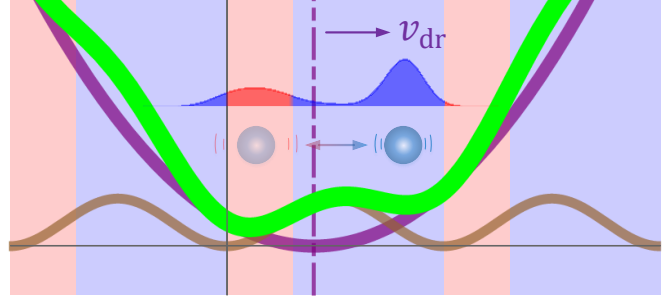


Fig. 1. Diagram of the stochastic heat engine based on PT model (PTSHE). The one-dimension PT model consists of three elements: the particle m with time-varying position $x(t)$, the purple harmonic potential $V_h = \frac{1}{2}\kappa[x(t) - X(t)]^2$ with uniformly moving center $X(t) = v_{dr}t$, and the brown lattice potential $V_l = \frac{V_0}{2}[1 - \cos(\frac{2\pi}{a}x(t))]$ with lattice period a . As the harmonic potential center moves forward, the shape of the green resultant potential $V = V_h + V_l$ changes and can cause stick-slip at zero temperature (SI Appendix Sec. 3). In the PTSHE, the geometry of the resultant potential curve couples with the duty ratio of the periodic temperature field, which modulates the thermal fluctuation of the particle. The particle oscillates around one of, or jumps back and forth between, the two local minimum points of V , with probability $p(x(t), t)$. We can see that although the left local minimum of V is lower than the right one at the selected instant here, the particle distributes on the right more likely due to the specially designed temperature field, as is indicated by the distribution curve and the transparency of the particle.

engine has been analyzed using stochastic thermodynamics (18) and realized experimentally (12). In the microscopic Stirling engine cycle in (12), the harmonic potential expands [$\kappa(t)$ increases] in the high temperature stage and heat is absorbed while it shrinks [$\kappa(t)$ decreases] in the low temperature stage and work is outputted.

Significance Statement

In nanofriction, energy can be dissipated through a phenomenon called stick-slip, where work is done on the system in 'stick' and then dissipated to the environment as heat in 'slip'. On the contrary, heat engine can extract heat from the environment to the system and convert it into work output. To transform stick-slip into an energy-extracted process, we design a stochastic heat engine based on the Prandtl-Tomlinson (PT) model, which is fundamental in atomic stick-slip friction. Two mechanisms of work output are distinguished. One leads to a Carnot-like approximate efficiency and the other can increase the work output and also reduce it if excessive. Exotic nonlinear bifurcation as well as stochastic resonance of the PT model are analyzed preliminarily too.

D.Y.Z. designed and performed research, analyzed data and wrote the paper.

The authors declare no competing interest.

¹To whom correspondence should be addressed. E-mail: dy-zhao14@mails.tsinghua.edu.cn

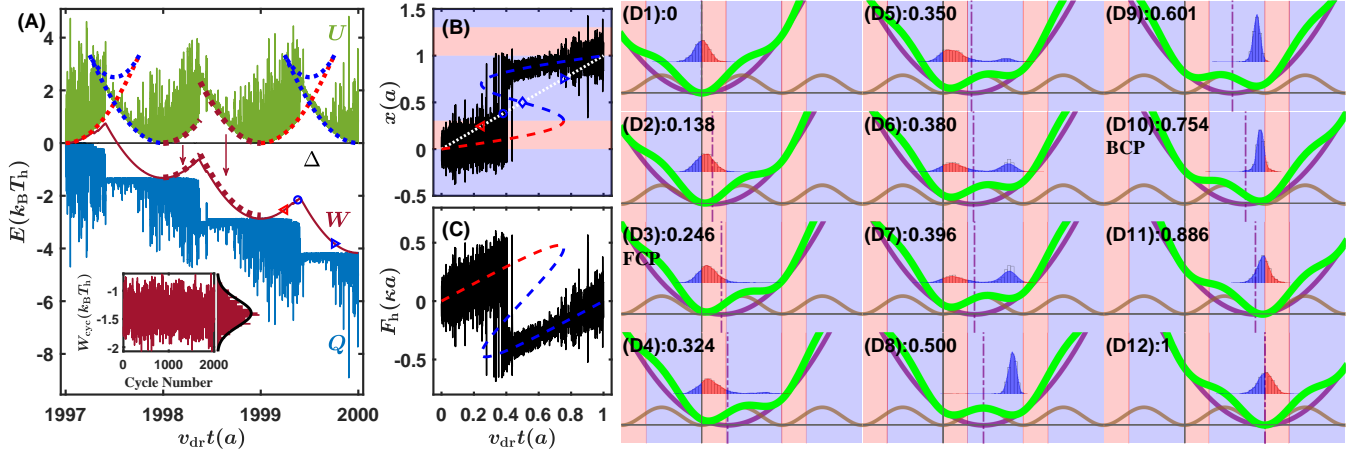


Fig. 2. Simulation results of the PTSHE. (A) The internal energy U , work input W , heat to the heat bath Q and the difference between them $\Delta = \Delta U + Q - W$ in the last three consecutive engine cycles among 2000 in total at $v_{dr} = 10^{-5} \text{ m/s}$. The work decreases to $-\infty$, i.e. work is outputted. The dotted red and blue curves are the resultant potential at the balanced points (SI Appendix Sec. 2) with the red ones in the hot zone and the blue ones in cold. The inset of (A) represents the cycle work of 2000 consecutive simulation cycles and its distribution. The x -coordinate $v_{dr}t(a)$ is the nondimensional position of the driver center, which is proportional to time t . The dimension of the energy is $k_B T_h$ with k_B the Boltzmann's constant and T_h the high temperature. The dotted dark red curves indicate the shape similarity between the work curve and the lower bound of the internal energy. $\Delta \equiv 0$ indicates the first law of thermodynamics (SI Appendix Sec. 5). (B) The displacement of the particle in the typical 2000th cycle with respect to the driver center's position, relative to the starting point of this cycle. The dotted white line represents the driver center's position with respect to itself. The dashed red and blue curves are the loci of the balanced points (SI Appendix Figure S3) in the hot and cold zones respectively. (C) Variation of the harmonic force in the 2000th engine cycle. The x -coordinate matches to that of (B). Time ratio of negative harmonic force in one cycle is larger than that of positive one, consistent with the work output. The dashed red and blue curves are the balanced harmonic force at the balanced point in hot and cold zones respectively (SI Appendix Figure S3). (D1)-(D12) Diagrams of the shapes of the resultant potential and the corresponding displacement distributions of the particle at different instants of the engine cycle. The displacement distribution at a certain instant relative to the latest cycle starting point (D1) is obtained from the total 2000 simulation cycles. The decimal following the id of each frame is the nondimensional position of the driver center (or the nondimensional instant) relative to the cycle starting point (D1). The purple curve represents the moving harmonic potential and the brown one represents the lattice potential. The red and blue zones represent high and low temperatures respectively. In one engine cycle, the particle starts at the point when the harmonic potential local minimum overlaps with one of the lattice potential local minimum (D1). As the driver center goes forward, the shape of the resultant potential curve changes. After the appearance of the FCP (D3), there occurs a new local minimum on the right. In (D7), the particle distributes in the right well more likely, although the right local minimum is still higher than the left one. At the middle of the cycle (D8), the particle almost completely distributes in the right well and stays there until the end of one cycle (D12). Parameters: $\eta = 3.0$, $\mu = 4 \times 10^4 \text{ s}^{-1}$, $\Theta_{h,c} = 0.4, 0.04$ and others are in SI Appendix Sec. 8.H.

In analogy, in the PT model, the resultant potential superposed by the harmonic and the sinusoidal lattice potential has a local minimum which rises and uplifts the particle's potential energy in the stick stage when the harmonic potential moves forward [$X(t)$ increases], cf. SI Appendix Sec. 3. If the particle is immersed in high temperature during this stage and in low temperature in the rest of one period, i.e. coupling the resultant potential with a specific temperature field, energy may be extracted from the heat bath. In this paper, we will design such a heat engine, which will transform the energy-dissipated stick-slip process into an energy-extracted process.

We will first describe the design of the stochastic heat engine based on PT model (PTSHE) and then analyze it in detail through Langevin dynamics simulation and the framework of stochastic thermodynamics in the Results section, the contents of which are indicated by the subheadings. In the Discussion section, we will go deep into the results further, including comparing the PTSHE with the analogous Büttiker-Landauer heat engine as a complement to this introduction.

Results

Engine Cycle and Temperature Protocol. The diagram of our PTSHE is given in Figure 1. As the center of the harmonic potential (driver center) goes forward to the right with uniform velocity v_{dr} , the resultant potential,

$$V(x(t), t) = \frac{1}{2} \kappa [x(t) - v_{dr}t]^2 + \frac{V_0}{2} [1 - \cos(\frac{2\pi}{a} x(t))], \quad [1]$$

changes periodically, as can be seen in Figure 2(D1)-(D12), where we plot the resultant potential (the green curves) at different instants of one engine cycle. The nondimensional corrugation number $\eta = \frac{2\pi^2 V_0}{\kappa a^2}$ determines the shape of the resultant potential. As η ranges between 1 and 4.6, the resultant potential has at most two local minima (9, 19, 20), cf. SI Appendix Sec. 4.

In one engine cycle, the driver center travels from one lattice potential local minimum to the next one, with the temporal period $\frac{a}{v_{dr}}$. The particle starts around the global minimum point of the resultant potential [Figure 2(D1)] and is driven through high (red) and low (blue) temperature zones in succession. The resultant potential first has one global minimum [Figure 2(D1)-(D3)], then two local minima separated by one local maximum [(D4)-(D9)], and then one global minimum again [(D10)-(D12)]. The local or global minimum points are stable balanced points where the harmonic force and the lattice force are equal while the local maximum point is unstable balanced point.

The spatially varying temperature of the heat bath couples with the resultant potential. In one spatial lattice period, the high temperature zone (red one) ranges from one lattice potential local minimum to the point where the resultant potential left local minimum and middle local maximum merge [backward critical point (BCP) in Figure 2(D10)], i.e. as the left global or local minimum rises, it won't get out of the hot zone until it disappears. The low temperature zone (blue one) ranges from the BCP to the next lattice potential local

minimum point. The procedure to calculate the BCP as the boundary of high and low temperature zone is given in SI Appendix Sec. 2.

Four Stages of the Engine Cycle and the Potential Mechanism of Work Output. We use Langevin dynamics simulation and the framework of stochastic thermodynamics (Methods and SI Appendix Sec. 5, 7 and 8) to analyze the PTSHE. The solid dark red curve in Figure 2(A) represents the work input by the driver at a low driving velocity $v_{dr} = 10^{-5} \text{ m/s}$ (i.e. the particle is at quasi-equilibrium state, see the next subsection). In each cycle, the work curve first increases and then decreases. The variation of work in the decreasing stage is greater than that in the increasing stage, i.e. outputted work is more than inputted work and in an entire cycle, work is outputted. The cycle work W_{cyc} is a stochastic variable and distributes approximately normally [inset of Figure 2(A)] with the mean value negative. Therefore, the PTSHE can indeed output work stably. As a comparison, we also simulate the cases of the homogeneous temperature heat bath with high and low temperature in SI Appendix Sec. 6.A and 6.B, where the mean cycle work is positive and on average work has to be inputted. The dimension of the work is $k_B T_h$, indicating that the PTSHE works in micro- or nanoscale where thermal fluctuations are significant (12, 21).

Diagrams of the resultant potential energy curve and the particle's displacement distribution at 12 selected instants in one engine cycle are given in Figure 2(D1)-(D12). The entire engine cycle can be divided into four stages.

First stage. From the beginning (D1) to the appearance of the FCP [forward critical point, (D3)]. On the work curve of the 2000th cycle in Figure 2(A), this stage ranges from the beginning to the red left triangle. In this stage, the resultant potential energy has only one global minimum moving forward and upward. The particle fluctuates around the minimum point [Figure 2(B)] and the particle's displacement relative to the cycle starting point at a specific instant of the cycle has an approximate normal distribution centered at the minimum point [(D1)-(D3)]. On average the particle falls behind the driver center gradually and is pulled. Hence work is done on the particle so that the work curve goes up. In this stage, the harmonic force fluctuates around and rises along the balanced harmonic force curve [Figure 2(C)], leading to the slope of the work curve increasing. As work is done on the particle, the resultant potential energy of the particle increases (explained below) and as the driver moves forward the particle fluctuates more in the hot zone so that its kinetic energy also increases. As a whole, the internal energy U of the particle increases in this stage [Figure 2(A)].

Second stage. From the appearance of the FCP to the cusp instant of the work curve. After the FCP appears, the resultant potential energy has two local minima and becomes double-well [(D4)-(D9)]. Because of the violent thermal fluctuation of the particle in the high temperature zone, the particle will sometimes cross over the middle energy barrier from the left well to the right one and the jumping back and forth event occurs more frequently as the driver moves forward [Figure 2(B)]. In the right well, the particle is on average ahead of the driver center, i.e. $x > v_{dr}t$, so the harmonic force $F_h = \kappa[v_{dr}t - x(t)] < 0$ [Figure 2(C)] and the driver is

driven by the particle and work is done by the particle to the driver. At the beginning of this stage, the backward energy barrier is low and it's easy for the particle to jump back to the left well and the particle's position still mainly distributes nearby the left balanced point [(D4)-(D5)]. Thereby, the net work input is still positive on average and the work curve continues to rise. As the driver goes forward, the forward barrier gets lower and the backward barrier gets higher, so the particle jumps forward over the barrier more easily and the right peak of its displacement distribution gets higher. In (D6), the two peaks have equal height approximately and afterwards the right peak is higher than the left one, although the left local minimum is still lower than the right one (D7). At some point the particle lanches over the barrier to the right and never jumps back. Before the jumping point, the harmonic force is on average positive while after that, the harmonic force is on average negative [Figure 2(C)]. So the slope of the work curve is positive before and negative after the jumping point, causing the cusp. The blue circle in Figure 2(A) and (B) represents the instant of (D6), around which the particle stays in the two wells equally likely. Before or after this instant, the jumping point (i.e. the instant of the cusp) of one cycle occurs stochastically, causing the cycle work a stochastic variable, which will be discussed in detail below. And therefore the time durations of this and next stage are stochastic.

Third stage. From the cusp instant of the work curve to the appearance of the BCP [(D10) and the blue right triangle on the work curve in Figure 2(A)]. Because of the low temperature, the particle calms down in the right well. In (D8), while the forward and backward energy barriers are equal, the distribution of the particle's displacement is almost completely on the right cold zone. Pushed by the lattice force, the particle is ahead of the driver center [Figure 2(B)] and the harmonic force is negative [Figure 2(C)] so that work is done by the particle on the driver and is outputted. As the driver moves forward, the distance between it and the particle gets smaller [Figure 2(B)] and the absolute harmonic force reduces along the balanced force curve [Figure 2(C)]. Therefore the work curve descends with decreasing absolute slope. In the cold zone, as the potential well gets deeper and narrower, the distribution gets thinner [(D9)-(D10)] and the amplitude of the particle's thermal fluctuation gets smaller [Figure 2(B)]. The fluctuations of the internal energy U and the heat to the environment Q are also inhibited [Figure 2(A)].

Fourth stage. From the disappearance of the BCP to the end of one cycle (D12). In this stage, there is again only one global minimum, which is now ahead of the driver center. Work is still outputted and the work curve continues to descend. The absolute slope of the work curve decreases as the driver center catches up with the particle gradually [Figure 2(B)] and the absolute value of the average harmonic force reduces [Figure 2(C)]. As the driver goes close to the end of the cycle, the particle frequently fluctuates to the hot zone of next cycle so that the amplitude of its thermal fluctuation increases gradually [Figure 2(B)] and its displacement distribution diverges, although the potential well continues to get deeper and narrower. The fluctuation of the internal energy U and the released heat Q increases too [Figure 2(A)].

In Figure 2(A), the dotted red and blue curves represent the

resultant potential energy at the local extremum points (i.e. balanced points) with respect to the driver center's position [SI Appendix Figure S1(B)]. The left minimum branch (dotted red) and the right minimum branch (dotted blue) cross in the middle three-extremum zone. According to our design, the rising left minimum branch is immersed in high temperature, while the middle maximum branch and the settling right minimum branch is immersed in low temperature. The internal energy U fluctuates, with the two local minimum branches as its lower bound, indicating that the particle's kinetic energy frequently relaxes to near zero and then regains, mainly resulting from the stochastic forces.

At the cusp instant of the work curve, the internal energy U lanches from the left minimum branch to the right one like climbing a cliff, while the heat Q falls off a cliff, indicating that heat is absorbed by the particle and transformed into its internal energy abruptly and won't be released back. On the left of the energy barrier heat is absorbed from the high temperature heat bath and the kinetic energy of the particle increases, leading to its high fluctuating amplitude and its jumping over the barrier to the right, where the potential energy is high and the kinetic energy is low. After the particle calms down on the right, unlike the kinetic energy, the potential energy can't transform back to heat and will gradually transform into work output, in analogy to a falling body. The shape of the ascent and descent stages of the internal energy on the left and right minimum branches are similar to the respective ascent and descent segments of the work curve as indicated by the dotted dark red curves in Figure 2(A), i.e. approximately the work input transforms into the potential energy of the particle on the ascent branch and the potential energy on the descent branch transforms into work output. A derivation to explain the similarity is given in SI Appendix Sec. 6.C. The net work output in one cycle is the difference between the work output in the descent segment and the work input in the ascent segment. Because of the symmetry of the left minimum branch and the right one, if the cusp is before the middle instant of the engine cycle (the blue diamond), the descent segment is larger than the ascent segment in height and work is outputted as a whole, cf. Figure 3(A3).

On the other hand, if the cusp is after the middle instant of the cycle as in the homogeneous low temperature case (SI Appendix Sec. 6.A), the descent segment of the work curve is smaller than the ascent segment in height and work should be inputted. This is the stick-slip process, where the ascent segment is in the 'stick' stage and the descent segment is in the 'slip' stage. In the cliff, potential energy transforms into kinetic energy and then the kinetic energy is dissipated into heat because of damping. In our PTSHE, this process is reversed: heat is first absorbed and transforms into kinetic energy, and then kinetic energy transforms into potential energy.

At homogeneous high temperature (SI Appendix Sec. 6.B), due to such large stochastic forces, the particle almost cannot feel the middle energy barrier and jumps between the two wells frequently after the right local minimum appears and before the left local minimum disappears so that the positive and negative harmonic forces (and also the work input and output) cancel out a lot in an entire cycle. This phenomenon is thermolubricity (11) and will be revisited below.

At this point we can summarize that the mechanism for the

PTSHE to output work has two features: (1) the cusp point of the work curve is before the middle instant of one cycle; (2) the shape of the two segments of the work curve is similar to that of the two local minimum branches of the balanced resultant potential energy curve, cf. Figure 3(A3). The two features are realized by the special geometry of the balanced resultant potential energy and the spatially alternative high and low temperature field coupled with it. This mechanism will be referred to as potential mechanism. And there is still a second mechanism for work output related to the thermolubricity effect to be elucidated deeply below.

Mean Cycle Work with Respect to Driving Velocity at Different Parameters. The mean cycle work

$$\langle W_{\text{cyc}} \rangle = - \left\langle \int_{t_0}^{t_0 + \frac{a}{v_{\text{dr}}}} \kappa [x(t) - v_{\text{dr}} t] v_{\text{dr}} dt \right\rangle \quad [2]$$

with respect to the driving velocity v_{dr} is plotted in Figure 3 at different parameters.

In Figure 3(A), we change the damping coefficient μ from 0 to $4 \times 10^7 \text{ s}^{-1}$. When μ is as high as $4 \times 10^6 \text{ s}^{-1}$, the $\langle W_{\text{cyc}} \rangle - v_{\text{dr}}$ curve is nearly exponential, indicating it's in the overdamped regime, and there is stable work output at low driving velocity v_{dr} . In the underdamped regime where $\mu \lesssim 4 \times 10^5 \text{ s}^{-1}$, there is stable work output at low v_{dr} too and the work output in both the overdamped and underdamped regimes seems approximately identical, cf. SI Appendix Sec. N.3.

In Figure 3(B), we can see that at low v_{dr} , the mean cycle work has a limit which gets lower with η increasing from 1 to 4.6, i.e. we can get more work output by increasing V_0 with constant κ (SI Appendix, Sec. 8.H). This is the significance of the lattice potential in the PTSHE, cf. SI Appendix Sec. F.3.

In both Figure 3(A) and (B), we can see that work output occurs at low driving velocity. Therefore low driving velocity, i.e. quasi-equilibrium, is also a condition for stable work output. We can derive an approximation of the equilibrium limit of the mean cycle work based on the potential mechanism. Assume that the boundary of the high and low temperature zone is at the barrier peak point exactly [Figure 3(A2)]. At the mean cusp instant, the probability of the particle jumping forward over the middle energy barrier from the hot zone is equal to the probability of it jumping backward from the cold zone. Therefore at equilibrium the jumping forward and backward barriers $\Delta V_{\text{h,c}}$ and the high and low temperatures $T_{\text{h,c}}$ should satisfy $\exp(-\frac{\Delta V_{\text{h}}}{k_{\text{B}} T_{\text{h}}}) = \exp(-\frac{\Delta V_{\text{c}}}{k_{\text{B}} T_{\text{c}}})$ (SI Appendix Sec. 6.E), leading to

$$\frac{\Delta V_{\text{h}}}{\Delta V_{\text{c}}} = \frac{T_{\text{h}}}{T_{\text{c}}}, \quad [3]$$

which is reminiscent of Carnot's formula if ΔV_{h} and ΔV_{c} are replaced by the absorbed and released heat Q_{h} and Q_{c} in the hot and cold heat bath respectively. In line with the stochastic thermodynamics, the cycle heat absorbed from the hot heat bath should be calculated by $Q_{\text{h}} = \int_{\text{hot zone}} dQ = \int_{\text{hot zone}} [m\dot{x}(t) - \xi(t)] dx$ [(22) and SI Appendix Sec. 5], which is a little tough to calculate in that the particle fluctuates violently and traverses through different temperature zones all the time and the integral intervals are divided into many random non-overlapping subintervals. The same case occurs to the heat released to the cold heat bath Q_{c} . To circumvent this difficulty, here we can approximate $Q_{\text{h,c}}$ by $\Delta V_{\text{h,c}}$ and

then the Carnot-like limit efficiency for the PTSHE can be defined as $\Lambda = 1 - T_c/T_h$, which is an approximation (23).

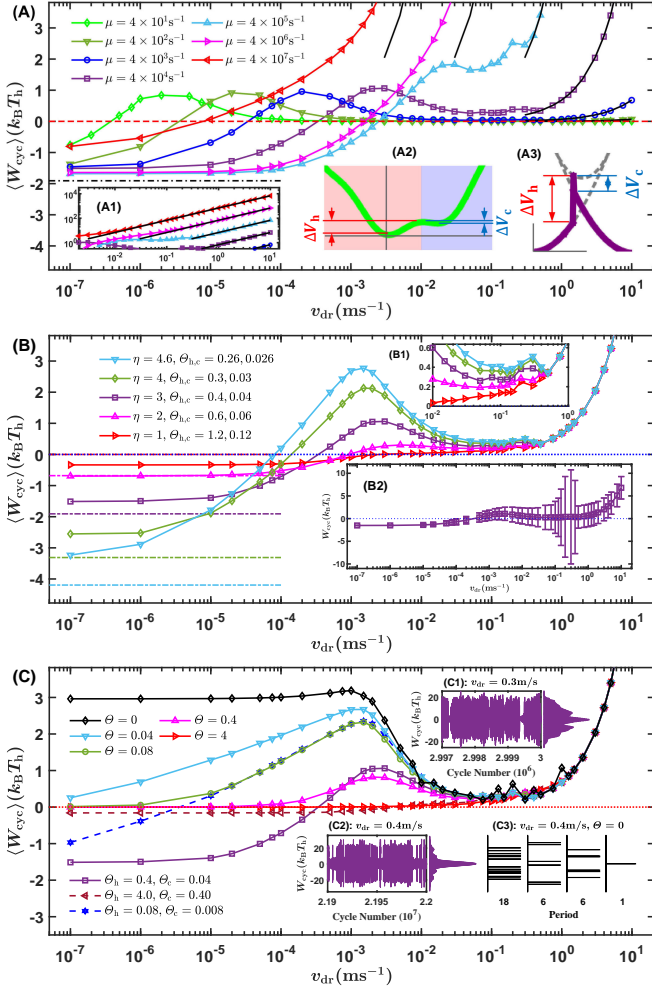


Fig. 3. The mean cycle work with respect to the driving velocity at different parameters. (A) The damping coefficient μ varies with $\eta = 3.0$, $\theta_{h,c} = 0.4, 0.04$. The solid black curves on the right are the high velocity limit of $\langle W_{\text{cyc}} \rangle$ (SI Appendix Sec. 6.D). The high-velocity parts of the curves outside the figure are plotted with log-log coordinate in the inset (A1). The dot-dashed line on the left is the equilibrium limit of the mean cycle work approximated based on the potential mechanism: $W_{\text{cyc,e.p.}}$. The green curve in the inset (A2) represents the resultant potential curve at the mean cusp instant when the probability of the particle jumping forward over the middle energy barrier and that of it jumping backward are equal. The inset (A3) is the schematic describing how to calculate $W_{\text{cyc,e.p.}}$. (B) η varies with $\mu = 4 \times 10^4 \text{ s}^{-1}$. The absolute temperatures $T_{h,c}$ of the heat bath are the same, while the nondimensional temperatures $\theta_{h,c} = T_{h,c}/V_0$ are different for different η because of the different V_0 at different η with κ keeping constant (SI Appendix Sec. 8.H). The dot-dashed lines on the left represent $W_{\text{cyc,e.p.}}$ at different η with the same color as the corresponding $\langle W_{\text{cyc}} \rangle - v_{\text{dr}}$ curve. The inset (B1) shows the detail of the curves at $v_{\text{dr}} \in [10^{-2}, 10^0] \text{ m/s}$. The inset (B2) gives the standard deviations of W_{cyc} for the case of $\eta = 3.0$, $\theta_{h,c} = 0.4, 0.04$. (C) The temperature field of the heat bath varies with $\eta = 3.0$, $\mu = 4 \times 10^4 \text{ s}^{-1}$. The insets (C1) and (C2) plot the cycle work near the end of the simulation time range and its count distribution at $v_{\text{dr}} = 0.3 \text{ m/s}$ and 0.4 m/s respectively for the case of $\theta_{h,c} = 0.4, 0.04$ (SI Appendix Figure S40 in Sec. 6.I), and the inset (C3) represents the cycle work count distribution of the four solutions at $v_{\text{dr}} = 0.4 \text{ m/s}$ and $\theta = 0$ with different periods, cf. SI Appendix Figure S42 in Sec. 6.J. The six subfigures in (C2) and (C3) share the same W_{cyc} axis on the left. The dimension of all the $\langle W_{\text{cyc}} \rangle$ is $k_B T_h$, with T_h the high absolute temperature of the case of $\eta = 3.0$, $\mu = 4 \times 10^4 \text{ s}^{-1}$ and $\theta_{h,c} = 0.4, 0.04$ [the purple curve with squares in (A), (B) and (C)].

potential curve, the approximate cusp instant can be calculated. And considering the similarity of the shape of the work curve and that of the lower bound of the internal energy, the equilibrium limit of the mean cycle work output can be approximated by $W_{\text{cyc,e.p.}} = \Delta V_h - \Delta V_c$, cf. Figure 3(A3). The subscript e. of $W_{\text{cyc,e.p.}}$ represents equilibrium and p. represents potential indicating that $W_{\text{cyc,e.p.}}$ is approximated based on the potential mechanism. A nonlinear equation system should be solved to calculate $W_{\text{cyc,e.p.}}$ (SI Appendix Sec. 6.E) and the obtained value of $-W_{\text{cyc,e.p.}}$ is represented by the dot-dashed lines on the left of Figure 3(A) and (B). As $W_{\text{cyc,e.p.}}$ is determined by T_h/T_c and η and independent on μ , there is only one $W_{\text{cyc,e.p.}}$ in Figure 3(A) and five different $W_{\text{cyc,e.p.}}$'s in Figure 3(B). For $\eta \gtrsim 3.0$, $W_{\text{cyc,e.p.}}$ is an upper bound, partly because the boundary of high and low temperature is designate on the left of the barrier peak, resulting in the particle frequently fluctuating to the low temperature zone and can't lanch to the right until the energy barrier is lower. If we set the boundary at the barrier peak point once it appears, the results will be closer to $W_{\text{cyc,e.p.}}$. For $\eta \lesssim 2.0$, the simulating results is larger than $W_{\text{cyc,e.p.}}$, especially at $\eta = 1.0$ where the approximate $W_{\text{cyc,e.p.}}$ should be 0. The reason is that the other mechanism of work output takes effect and we will analyze it in the next subsection. At homogeneous finite temperature $W_{\text{cyc,e.p.}}$ is equal to zero, which is accurate as shown in Figure 3(C).

The Second Mechanism of Work Output and the Consequence of Its Excess.

In Figure 3(B2), the standard deviations of W_{cyc} of the case of $\eta = 3.0$, $\mu = 4 \times 10^4 \text{ s}^{-1}$, $\theta_{h,c} = 0.4, 0.04$ are plotted. We can see that at low v_{dr} , the standard deviations of W_{cyc} are small, indicating that each cycle work is nearly the same. The reason is that at very low driving velocity the particle has enough time to relax to equilibrium state at each instant, so that the time integral of each cycle W_{cyc} (time average) is equal to the ensemble average over all the cycles $\langle W_{\text{cyc}} \rangle$, and thus the standard deviation of W_{cyc} is zero. Therefore the nonzero standard deviations of W_{cyc} at higher velocities indicate nonequilibrium. So instead of a nonequilibrium ensemble of engine cycles [Figure 2(D)], in terms of the equilibrium limit of the mean cycle work, we can analyze one cycle at a low driving velocity at which the standard deviation of W_{cyc} is small enough, whose weakness, nonetheless, is that it's not easy to obtain the displacement distribution at certain instant due to the large number of simulation time steps in one single engine cycle.

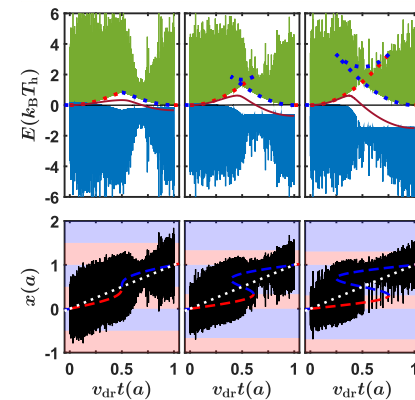


Fig. 4. Energy and displacement of the particle at $v_{\text{dr}} = 10^{-7} \text{ m/s}$. From left to right $\eta = 1, 2$ and 3 respectively. Other parameters are the same as those in Figure 3(B). Types and colors of the curves are the same as those in Figure 2(A) and (B). $k_B T_h$ is equal to that in Figure 3. At low η , the low energy barrier leads to the particle's kinetic energy partly converted into its potential energy, so the work input is reduced before the cusp of the work curve.

With Eq. 3 and the geometry of the balanced resultant

In Figure 4, we plot the energy and displacement curves

of the particle at $v_{dr} = 10^{-7}$ m/s for the cases of $\eta = 1, 2$ and 3 corresponding to those in Figure 3(B). For the middle $\eta = 2$ case, we can see that the work curve before the cusp point is lower than the dotted red curve, different from that of the right $\eta = 3$ case, so that the ascent segment of the work curve is shortened in height, resulting in the net cycle work output increasing. From SI Appendix Sec. 6.C we know that if the average position of the particle is on the balanced point exactly, the work curve will overlap with the dotted balanced resultant potential curves. However, from the bottom displacement curve, we can see that the average position of particle approaches the driver center (the white dotted curve) before the cusp instant. Although at the same absolute temperature T_h as the $\eta = 3$ case, the nondimensional temperature Θ_h of the $\eta = 2$ case relative to the lattice potential amplitude V_0 is higher (0.6 v.s. 0.4), resulting in the particle's easily crossing over the energy barrier, its tending to neglect the lattice potential and its distribution center approaching to the driver center (SI Appendix Sec. 6.F.1). Therefore the harmonic force and thus the slope of the work curve both reduce so that the work curve gets lower.

For the left $\eta = 1$ case, although there is no energy barrier and only one global minimum first immersed in the hot and then in the cold zone, represented by the dotted red and blue curves (SI Appendix Sec. 6.F.2), the particle still fluctuates around the minimum point and the work curve is still similar to the dotted curves especially in the second half of the cycle. In the first half, the work curve is gradually lower than the dotted red curve in that at $\eta = 1$ there is no energy barrier and the particle almost cannot feel the lattice potential so the particle again approaches to the driver center like in the $\eta = 2$ case and the harmonic force from the driver to the particle gets smaller and the inputted work is reduced.

In the left top subfigure of Figure 4, we can see that the upper bound of the dark blue heat curve of the $\eta = 1$ case decreases before and then increases a little after the middle of the cycle. In the hot zone heat is absorbed and transformed into kinetic energy, leading to the particle fluctuating violently approaching to the driver center where the resultant potential is high. So the kinetic energy is transformed into potential energy and the work input needed to increase the resultant potential energy is reduced. After the middle instant, the minimum point of the resultant potential is ahead of the driver center and there is still a short period when the particle frequently traverses the hot zone and approaches to the driver center from ahead. Therefore the high kinetic energy becomes resistance and the work output tends to stay unchanged in a short period and both the potential and the kinetic energy reduce and transform into heat (SI Appendix Sec. 6.F.2). So after the middle of the cycle the upper bound of the heat curve rises a little, which is smaller than the decreased value before the middle instant. In an entire cycle heat absorbed is larger than heat released and the net heat absorbed is converted into the net work output.

So we can see that although there is no energy barrier in the $\eta = 1$ case so that the equilibrium limit of the cycle work output $W_{cyc,e.p.}$ approximated by the potential mechanism is zero, due to the reduction of the ascent segment of the work curve caused by the high temperature and with the descent segment changed a little, there is still a small quantity of work output.

In the $\eta = 2$ and 3 cases in Figure 4, we can also see that before the middle of the engine cycle, heat is absorbed and gradually transformed into the particle's potential energy, leading to the work input reduced. It's more distinct for the $\eta = 2$ case because the high nondimensional temperature and low energy barrier lead to the particle crossing over the energy barrier easily and its fluctuating center is near the driver center. For the $\eta = 3$ case, the nondimensional temperature is low and the energy barrier is high so it's harder for the particle to cross over the barrier. Because at such a low driving velocity the particle has enough time to traverse the middle states between the two local minimum so that the particle is nearly at equilibrium at each instant and the upper bound of the heat curve decreases gradually rather than suddenly like that in Figure 2(B). Nonetheless, the particle still stays most of the time on the right after and left before the cusp instant and there is still a cusp on the work curve, although a little dull. And the work input reduction is not that significant.

In all the three cases in Figure 4, after the cusp instant, the particle is mainly in the cold zone and on average fluctuates around the right local minimum point so the work curve is nearly parallel to the dotted blue curve and work is done by the particle to the driver and is outputted.

So we can conclude the second mechanism for work output is that the particle's position distribution center approaches to the driver center, so that the harmonic force and thus the work input reduces. This mechanism is realized by the low energy barrier or equivalently the particle's high kinetic energy, resulting in the particle's tending to neglect the lattice potential energy. In this mechanism heat is absorbed and first transformed into kinetic energy, and then the kinetic energy transforms into the potential energy so that the work input needed to increase the potential energy is reduced. This effect is similar to thermolubricity (11) and will be referred to as thermolubricity mechanism.

The equilibrium limit of the mean cycle work output $W_{cyc,e.p.}$ we derived in the previous subsection only considers the potential mechanism and it gives us a skeleton with an ascent segment and a descent segment [Figure 3(A3)]. The thermolubricity mechanism, on the other hand, reduces the ascent segment. If we keep the low temperature Θ_c constant and increase the high temperature Θ_h , the cycle work output from the potential mechanism will increase because of the cusp instant moving to the left [Figure 3(A3)], and due to the thermolubricity mechanism the work input will be reduced further. However, we cannot increase Θ_h without limit. In Figure 5(A), the circles represent the simulation mean cycle work at $v_{dr} = 10^{-7}$ m/s varying with Θ_h . The absolute low temperature T_c of the four cases of $\eta = 1, 2, 3$ and 4 is the same. We can see that as Θ_h increases, the mean cycle work at $v_{dr} = 10^{-7}$ m/s first decreases and then increases for all the four cases. The dot-dashed curves represent the equilibrium mean cycle work limit $-W_{cyc,e.p.}$ approximated by the potential mechanism, which decreases to a lower limit with Θ_h increasing (SI Appendix, Eq. 41). As we have explained, the offset of the descending stage of each set of circles from the corresponding dot-dashed curves of the same η and Θ_c results from the thermolubricity mechanism.

We next explain that the ascending stage of each set of circles roots in the same mechanism. In Figure 5(B), the work curves in one cycle corresponding to the purple circles of $\eta = 3$

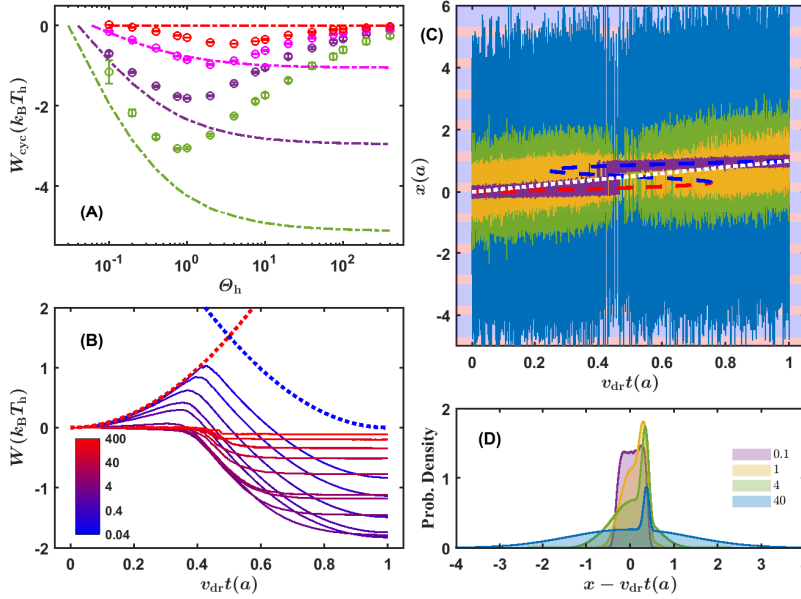


Fig. 5. The mean cycle work varies with the high temperature. (A) The cycle work W_{cyc} at $v_{dr} = 10^{-7}$ m/s with respect to the nondimensional high temperature Θ_h at different η . The circles with their errorbars represent the mean values and standard deviations averaged from 18 simulation cycles. The dot-dashed curves represent the approximated equilibrium cycle work limit $-W_{cyc,e.p.}$. From bottom to top, the curves and circles with the same color represent the cases of $\eta = 4.0$, $\Theta_c = 0.03$; $\eta = 3.0$, $\Theta_c = 0.04$; $\eta = 2.0$, $\Theta_c = 0.06$ and $\eta = 1.0$, $\Theta_c = 0.12$ respectively with $\mu = 4 \times 10^4 s^{-1}$. The absolute low temperature T_c is the same for all the four cases [cf. Figure 3(B)]. (B) The work curves in one cycle corresponding to the purple circles of $\eta = 3$, $\Theta_c = 0.04$ in (A), with the high temperature Θ_h denoted by the gradually varying color of the curves. The dotted red and blue curves represent the resultant potential at the balanced points [cf. Figure 2(A)]. In (A) and (B), $k_B T_h$ is equal to that in Figure 3. (C) The displacement of the particle in one cycle for the case of $\eta = 3$, $\Theta_c = 0.04$ in (A) at four typical high temperatures: $\Theta_h = 0.1$ (purple), 1 (dark yellow), 4 (dark green) and 40 (dark blue). The dotted white line denotes the position of the driver center. The dashed red and blue curves represent the position of the balanced points of the resultant potential [cf. Figure 2(B)]. (D) The probability density distributions of the particle's relative displacement to the driver center $x - v_{dr} t$ in one cycle at four typical Θ_h for the case of $\eta = 3$, $\Theta_c = 0.04$ in (A).

in Figure 5(A) are plotted. We can see that from $\Theta_h = 0.1$ to 1.0, the cusps of the work curves move to the left because the ratio Θ_h/Θ_c increases, cf. Figure 3(A3). At the same time the ascent segments of the work curve before the cusps gradually get lower and lower because of the thermolubricity mechanism. In this range of Θ_h , the descent segments of the work curves keep parallel to each other and also to the dotted blue curve. As a whole the cycle work output increases in this range of Θ_h . However, as $\Theta_h \geq 2$ the ascent segments of the work curves become nearly flat and the cusps almost disappear, in that the temperature is so high that the thermolubricity effect touches ground. Moreover, the descent segments are no longer parallel to the dotted blue curve and get flatter and flatter with Θ_h increasing, leading to that the right ends of the work curves rise so that the cycle work output decreases. In Figure 5(C), we plot four typical displacement curves of $\Theta_h = 0.1, 1, 4$ and 40 corresponding to the four respective purple circles at $\eta = 3$ in Figure 5(A). We can see that when Θ_h is high, the particle fluctuates violently with amplitude as high as several lattice periods as it is close to the end of the engine cycle because it frequently traverses through the high temperature zone in the next lattice period. So the particle's mean position almost overlaps with the driver center rather than the right local or global minimum point. The harmonic force then is reduced to near zero so that the absolute slope of the work curve decreases to near zero and it becomes flat at its right end. As Θ_h goes higher, the range of the particle's no feeling of the lattice potential extends so that the residual descent segment of the work curve shrinks and the cycle work output decreases further.

The quantity $x - v_{dr} t$, which is the integrand of W_{cyc} in Eq. 2 neglecting a constant, can be regarded as the particle's displacement relative to the driver center. In Figure 5(D), we plot the probability density distributions of the $(x - v_{dr} t)/a$ value in an engine cycle at $v_{dr} = 10^{-7}$ m/s at four Θ_h . The average value of the distribution is proportional to the cycle work W_{cyc} . At $\Theta_h = 0.1$, there is a little pingo on the right because the nonhomogeneous temperature causes the particle jumps forward to the right local minimum a little earlier so

that in an entire cycle the particle tends to distribute a little more on the right of the driver center. From $\Theta_h = 0.1$ to $\Theta_h = 1$, the left plateau declines while the right hill rises so that the particle distributes more on the right of the driver center and the cycle work increases. When $\Theta_h > 1$, however, both sides of the distribution curve expand so that the right hill gets thin and short in that Θ_h is so high that the work output part is diluted.

In Figure 5(A), all the standard deviations of the mean cycle work are small except the point at $\Theta_h = 0.1$ of the case of $\eta = 4$, $\Theta_c = 0.03$ because the temperature is so low that the velocity $v_{dr} = 10^{-7}$ m/s is not low enough for the particle to relax to equilibrium with such a high middle energy barrier. As we have stated above, the small standard deviations at low driving velocity indicate equilibrium.

In SI Appendix, Sec. 6.G, we give the results corresponding to those in Figure 5(B), (C) and (D) for the cases of $\eta = 1, 2$ and 4 for reference.

The Stall Regime of the PTSHE: Connection with Nanofriction.

As the driving velocity increases exceeding the zero points of the $\langle W_{cyc} \rangle - v_{dr}$ curves, the PTSHE stalls (12, 18), i.e. work has to be inputted to the particle by the driver. When the damping coefficient μ is small (underdamped), at the stall regime, the $\langle W_{cyc} \rangle - v_{dr}$ curve first increases to a plateau and then decreases to a valley and finally increases to $+\infty$ [Figure 3(A)]. The position of the plateau moves to the left being approximately proportional to the decreasing μ and the range of the valley expands both to the left and right. The plateau also rises and moves to the left as η increases at the same absolute temperature [Figure 3(B)]. When μ is large enough (overdamped) the plateau and the valley both vanish. At very high driving velocity the mean cycle work increases linearly [Figure 3(A1)] because the damping force dominates and thus an analytical expression can be derived (SI Appendix Sec. 6.D) represented by the solid black curves in Figure 3(A). It is independent on η and $\Theta_{h,c}$ indicated by the coincident part of the $\langle W_{cyc} \rangle - v_{dr}$ curves in Figure 3(B) and (C).

In homogeneous (not very high) temperature, the $\langle W_{cyc} \rangle -$

v_{dr} curves in Figure 3(C) are characteristic in nanofriction (24–26). The mean cycle work $\langle W_{cyc} \rangle$ is equal to the mean harmonic (minus friction) force $\langle \bar{F}_h \rangle$ times the lattice period a . The $\langle W_{cyc} \rangle - v_{dr}$ curve goes to zero at low driving velocity in homogeneous finite temperature [Figure 3(C)] corresponding to the thermal drift regime of nanofriction (1). As the temperature reduces, the thermal drift regime shrinks to the left and disappears at zero temperature. Except for the negative mean cycle work, the $\langle W_{cyc} \rangle - v_{dr}$ curves of the PTSHE in Figure 3(A) and (B) are similar to those of homogeneous finite temperature heat baths in Figure 3(C). At the ascent stage after the zero point and before the plateau peak, stick-slip occurs so that work has to be inputted to compensate the energy dissipation. After the plateau peak, stick-slip is weakened because of the interference of the not completely attenuated oscillation from the last cycle (10, 27). We analyze the transition of the energy, displacement and harmonic force in one cycle with the driving velocity in SI Appendix, Sec. 6.H.

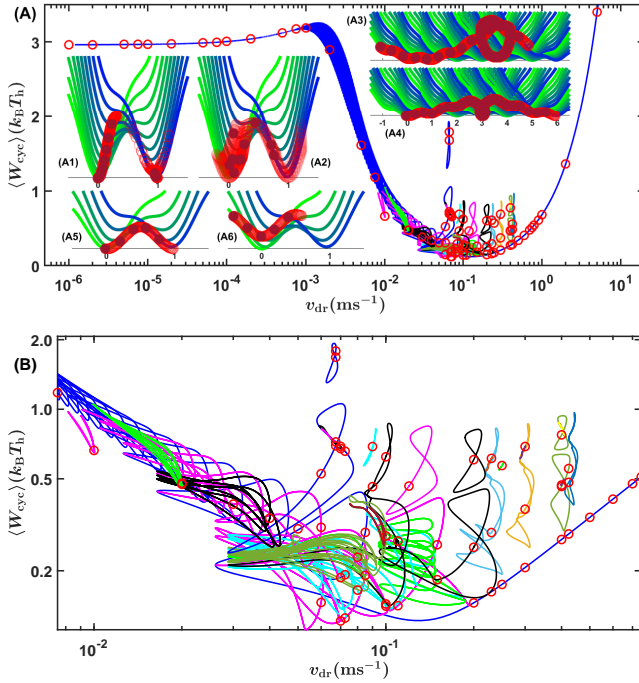


Fig. 6. The bifurcation diagram of $\langle W_{cyc} \rangle$ with v_{dr} as parameter at zero temperature. In (A), the red circles are simulation results and the solid curves are results of continuation. Curves with different color have different cycle number period $P_{c.n.} = T v_{dr} / a$. (B) is a zoomin of (A). The dimension $k_B T_h$ of $\langle W_{cyc} \rangle$ is the same as that in Figure 3. More details of the upper one are given in SI Appendix Sec. 6.K.2. Here $\eta = 3.0$, $\mu = 4 \times 10^{-1} s^{-1}$ and other parameters are given in SI Appendix Sec 8.H. The six insets in (A) are schematics of the particle's position (dark red balls) projected on the resultant potential curves (with color gradually varying from green to blue during one engine cycle) varying with time. (A1), (A2) and (A6) correspond to $v_{dr} = 10^{-5} m/s$ ($P_{c.n.} = 1$, stick-slip), $0.003 m/s$ (no period, velocity weakening) and $10 m/s$ ($P_{c.n.} = 1$) respectively in one engine cycle, cf. SI Appendix Figure S25. (A3), (A4) and (A5) correspond to three solutions at $v_{dr} = 0.4 m/s$, with $P_{c.n.} = 6, 6$ and 1 respectively in Figure 3(C3), cf. SI Appendix Sec. 6.J.

Bifurcation of Mean Cycle Work with Driving Velocity as Parameter at Zero Temperature. In Figure 3(B1) and (C) we find that the $\langle W_{cyc} \rangle - v_{dr}$ curves are not smooth in the velocity range $(7.5 \times 10^{-3}, 3) m/s$ where there are some small peaks especially on the zero temperature curve. What's more, in

this velocity regime, the standard deviations are large [Figure 3(B2)] and the count distributions of W_{cyc} have some peculiar peaks [Figure 3(C1) and (C2), and SI Appendix Sec. 6.I]. We then simulated more results for the zero temperature case (the differential equation of which is ordinary), and found that in this regime, the mean cycle work $\langle W_{cyc} \rangle$ has multiple solutions with different limit cycles dependent on the initial conditions, as shown by more than one $\langle W_{cyc} \rangle$ value (the red circles) at some v_{dr} in Figure 6, cf. SI Appendix Sec. 6.J. Different solution may have different period and solutions with the same period may lead to different $\langle W_{cyc} \rangle$, e.g. the four solutions at $v_{dr} = 0.4 m/s$ shown in Figure 3(C3) and three of them in Figure 6(A3), (A4) and (A5). That's a kind of nonlinear bifurcation resulting from the sinusoidal lattice potential of the PT model. Through continuation with MatCont (28), we can obtain the bifurcation diagram of $\langle W_{cyc} \rangle$ with v_{dr} as the parameter in Figure 6 (SI Appendix Sec. 6.K).

We can see that at zero temperature, the $\langle W_{cyc} \rangle - v_{dr}$ curve shows strong nonlinearity. At low and high driving velocity ends there is only one solution with period $T = a/v_{dr}$ for each v_{dr} [Figure 6(A1) and (A6)]. While v_{dr} is in $(8 \times 10^{-4}, 0.2) m/s$, the blue backbone curve with period $T = a/v_{dr}$ twines up from right to left, on which there are a lot of period doubling branches (29), among which we plot only a small part (more detail is given in SI Appendix Figure S44). In the velocity range $(0.02, 0.5) m/s$, there're a lot of isolated loops with different cycle number period $P_{c.n.} = T v_{dr} / a$ indicated by different color. And almost on all the isolated loops, there are period doublings, only several of which are plotted. From Figure 6(B), we can see that it's nearly chaotic when v_{dr} is in the interval $(0.025, 0.09) m/s$.

When the frequency of the driver center's moving over the lattice periods, i.e. v_{dr}/a , equals from the frequency of the harmonic potential $\frac{\omega_0}{2\pi}$ to the maximum frequency of the resultant potential $\frac{\omega_0}{2\pi} \sqrt{1+\eta}$, the driving velocity v_{dr} ranges from 0.0673 to $0.1347 m/s$. This range is contained in the strong nonlinear bifurcation regime characterized by many isolated loops. So the strong nonlinear bifurcation is related to resonance. In Figure 6, we can actually see at $v_{dr} = 0.0673$ two red circles much higher than others and a clear resonance peak nearby. Moreover, in Figure 3(B2), we can see that in this regime the standard deviation of W_{cyc} has a peak at nearby $v_{dr} = 0.3 m/s$, indicating that stochastic resonance occurs (30). Compared with the example of the double-well potential superposed with a periodic driving in (30), in the PT model the particle has more than two states to switch among. Here the different states correspond to different steady-state periodic solutions of the zero temperature Langevin equation, which can be represented by the bifurcation diagram Figure 6, rather than the local minima of the potential like that in (30). In Figure 6(B) we can see that when there is no noise ($\theta = 0$) at $v_{dr} = 0.4 m/s$ there are more than two states, four of which are plotted in Figure 3(C3) represented by the steady-state count distribution of W_{cyc} and three of which are plotted in Figure 6(A3), (A4) and (A5) represented by the particle's position projected on the resultant potential curve varying with time at steady state. At finite temperature (e.g. $\theta_{h,c} = 0.4, 0.04$), the particle can switch induced by noise among these states so that W_{cyc} has a peculiar distribution in Figure 3(C2). At different v_{dr} the states are different, so the distributions of W_{cyc} at different v_{dr} 's are different (SI

Appendix Sec. 6.I). When stochastic resonance occurs, the particle's hopping among these states synchronizes with the driver center's moving over the lattice periods, leading to the standard deviation of W_{cyc} maximizes (SI Appendix Sec. 6.I).

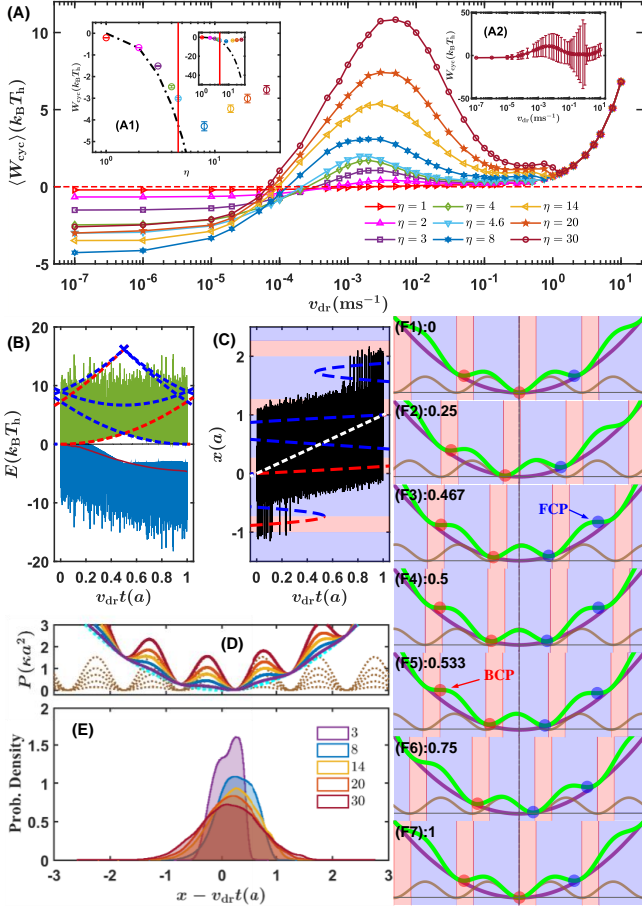


Fig. 7. Simulation results of the cases of $\eta > 4.6$. (A) Mean cycle work at $\Theta_{h,c} = 0.4, 0.04$, $\mu = 4 \times 10^4 \text{ s}^{-1}$ from $\eta = 1$ to $\eta = 30$. The circles with their errorbars in the inset (A1) are the mean values and standard deviations of W_{cyc} averaged from 18 simulation cycles at $v_{\text{dr}} = 10^{-7} \text{ m/s}$ with respect to η , and the colors of the circles are the same as the corresponding $\langle W_{\text{cyc}} \rangle - v_{\text{dr}}$ curves. As η increases, the low velocity limit of $\langle W_{\text{cyc}} \rangle$ first decreases and then increases. The black dot-dashed curve is the equilibrium cycle work approximated by the potential mechanism $-W_{\text{cyc,e.p.}}$, which decreases to $-\infty$ with η increasing [see the inset of (A1)]. The red vertical line represents the critical value $\eta = 4.6033388487517$ (SI Appendix Sec. 4). The inset (A2) gives the standard deviations of W_{cyc} at $\eta = 30$. (B) and (C) Energy and displacement curves at $\eta = 8$, $\Theta_{h,c} = 0.4, 0.04$ and $\mu = 4 \times 10^4 \text{ s}^{-1}$, curve colors and types are the same as those in Figure 2(A) and (B). (D) The solid curves are the resultant potential curves at different η denoted by different colors corresponding to those in (E). The cyan dotted curve represents the harmonic potential which is kept constant. The brown dotted curves represent the sinusoidal lattice potential leading to different η . (E) The probability density distribution of the particle's relative displacement to the driver center $x - v_{\text{dr}} t$ at $v_{\text{dr}} = 10^{-7} \text{ m/s}$ and different η . Each distribution curve is obtained from three consecutive steady state engine cycles. (F1)-(F7) Diagrams of the resultant potential curves at different instants in one engine cycle of the $\eta = 8$ case. Here we keep the harmonic potential stationary and move the lattice potential and the temperature field to the left uniformly, which is equivalent to keeping the latter two stationary and moving the former to the right uniformly like that in Figure 2(D). The red balls denote the local minima in the hot zones and the blue ones denote those in the cold zones. The decimals following the id's are the relative instant to the starting of the cycle (F1).

Mean Cycle Work at $\eta > 4.6$. In the above we only considered the cases of $\eta \leq 4.6$, in which the resultant potential curves

have at most two local minima. In this subsection, we will preliminarily consider the cases of $\eta > 4.6$ with the resultant potential curves having more than two local minima (SI Appendix Sec. 4). In Figure 7(A), we plot the $\langle W_{\text{cyc}} \rangle - v_{\text{dr}}$ curves at different η and $\Theta_{h,c} = 0.4, 0.04$. We can see that while the $\langle W_{\text{cyc}} \rangle - v_{\text{dr}}$ curves have similar shapes at different η , the low velocity limits of $\langle W_{\text{cyc}} \rangle$ are very different. In the inset (A1), the mean values and standard deviations of W_{cyc} at $v_{\text{dr}} = 10^{-7} \text{ m/s}$ are plotted with respect to η , from which we can see that the absolute value of the low velocity limit of $\langle W_{\text{cyc}} \rangle$ first increases and then decreases with η increasing. On the other hand, the approximate equilibrium cycle work $W_{\text{cyc,e.p.}}$ represented by the dot-dashed black curve, however, decreases to $-\infty$ [cf. SI Appendix Figure S55(d)]. We can also see that when η is large the standard deviations are also large especially at $\eta > 4.6$, indicating that equilibrium needs to be achieved at lower driving velocity than $v_{\text{dr}} = 10^{-7} \text{ m/s}$. Next we will give a preliminary explanation to these phenomena.

In Figure 7(F1)-(F7), the resultant potential curves at $\eta = 8$ are plotted at different instants in one engine cycle. Here instead of moving the harmonic potential uniformly to the right, we keep it stationary and move the temperature field and the sinusoidal potential to the left with the same magnitude of velocity, which will lead to the same results. It looks like a rack moving to the left and driving a gear. We can see that there are at most four local minima between the instant of the FCP (F3) and the instant of the BCP (F5), and three in the rest of one cycle. The red and blue balls denote the local minima in the hot and cold zones respectively. From the starting point of one cycle (F1) to the instant of the BCP (F5), the leftmost red ball, i.e. the leftmost local minimum, goes leftward and upward in the same hot zone and then disappears at the instant of the BCP. The middle red ball, i.e. the middle global minimum in (F1) goes leftward and upward in its right neighbor hot zone and becomes the leftmost red ball at the end of one cycle. So it takes more than one cycle for the middle red ball starting at the global minimum point to go through the hot zone to the BCP and then out of the hot zone, rather than within one cycle as $\eta \in (1, 4.6]$.

Besides, the particle now can stay in one of these wells or hop among them. For example, in (F2) or (F6), besides to the middle well, the particle can jump out of the leftmost well to the rightmost one. This phenomenon is similar to multislip (19) of nanofriction in homogeneous temperature and in Figure 7(C) we can see that at the beginning and end of one cycle when the forward and backward energy barrier from the middle well are low enough [(F1) and (F7)], the displacement of the particle covers all the three local minima, so that the particle will with high probability jump from the leftmost well to the rightmost one or vice versa.

In Figure 7(B), we can see that the dotted curves of the resultant potential at the balanced points are more complex than those of the $\eta \leq 4.6$ cases (Figure 4). An unbroken version of these curves is given in SI Appendix Figure S51. In the $\eta = 8$ case, the potential mechanism still plays a leading role and we can see that both the right energy barrier and the right local minimum (blue ball) neighbor to the middle global minimum (red ball) in (F1) have already occurred before the beginning of the engine cycle, and the work curve in its middle stage is approximately parallel to the bottommost dotted blue curve, which is the mark of the potential mechanism similar

to the $\eta \leq 4.6$ cases in Figure 4. However, because at the beginning and end of one cycle the particle can hop among the wells due to the low energy barriers and tends to neglect the lattice potential, the beginning and end stage of the work curve descend slower than the bottommost dotted blue branch.

Therefore, we can conclude that for the $\eta = 8$ case, the potential mechanism results in its high mean cycle work output, which is declined a little by the particle's covering more wells at the beginning and end of one engine cycle. However, when η increases further, the left and right wells neighbor to the middle one become relatively more reachable for the particle (cf. SI Appendix Sec. L), resulting in that the particle spends a longer period remaining in the neighbor wells both ahead of and behind the global one, i.e. covering more wells. In Figure 7(E), we can see that when η increases from 8 to 30, the probability density distribution of the particle's displacement relative to the driver center gets fat both to the left and right and the average value of the distribution, which is approximately proportional to the mean cycle work, gets diluted and approaches to zero. So at $\eta > 8$ the particle's covering more wells leads to the work output declined more, cf. SI Appendix Sec. L.

In the above analysis, we have kept the nondimensional temperatures $\Theta_{h,c}$ constant with η varying. When η is higher, the absolute temperatures $T_{h,c}$ are also higher due to the higher V_0 . In terms of the particle's position distribution center approaching to the driver center and its tending to neglect the lattice potential, the high absolute temperatures, or rather thermolubricity, play an important role in the reduction of the equilibrium cycle work output at high η . To have a complete understanding about the effect of the increasing number of teeth of the resultant potential with increasing η on the equilibrium limit of $\langle W_{cyc} \rangle$, we can keep the absolute temperatures $T_{h,c}$ constant to see how $\langle W_{cyc} \rangle$ varies with η or keep η constant at a high value to see how $\langle W_{cyc} \rangle$ varies with $\Theta_{h,c}$, at low driving velocity. However, because of the large number of time steps at high η , it's not easy by Langevin dynamics simulation to achieve a low enough driving velocity necessary for the particle to relax to quasiequilibrium in low $\Theta_{h,c}$, see the next subsection. The circles' large standard deviations at $\eta \geq 8$ in Figure 7(A1) indicate $v_{dr} = 10^{-7}$ m/s is not low enough. A qualitative analysis is given in SI Appendix, Sec. 6.L. Methods based on the Fokker-Planck or Kramers equation (31) are promising to be used to investigate this problem further, with which other features such as the increasing plateau peak value with the increasing η may also be elucidated.

Discussion

More on the Temperature. In the following discussion, we return to the $\eta \leq 4.6$ cases, unless otherwise specified. In the above we have focused mainly on the effect of the high temperature Θ_h . Nevertheless, attention should also be paid to the low temperature Θ_c , whose value we have chosen is kind of mediate. When the low temperature is high, such as the $\Theta_{h,c} = 4.0, 0.4$ case in Figure 3(C), the mean cycle work output is much smaller than the $\Theta_{h,c} = 0.4, 0.04$ case. That's because it's easy for the particle to cross over the barrier from both the high and low temperature zone at such high temperatures and the particle's fluctuation center is close to the driver center whether behind or ahead of it, i.e. the negative thermolubricity mechanism. Nevertheless, due to the potential mechanism,

there is still a bit of net work output. Because in the PTSHE $\Theta_h > \Theta_c$, when Θ_c gets extremely high, the result is similar to the homogeneous very high temperature case (SI Appendix Sec. 6.B) and the mean cycle work output will go to zero.

In Figure 3(C), the result of the $\Theta_{h,c} = 0.08, 0.008$ case is also given. We can see that it's more difficult for this low temperature case to achieve equilibrium, in that the probabilities of jumping over the barrier, $\exp(-\frac{\Delta V_{h,c}}{k_B T_{h,c}})$, are small in both the forward and the backward direction and the driving velocity should be small enough for the crossover event to occur considerable times in one cycle. It's not easy to use Langevin dynamics simulation to explore the cases at such low temperature and we may turn to the Fokker-Planck or Kramers equation method (31).

So to achieve distinct mean cycle work output, the low temperature should be lower than the lattice potential energy barrier V_0 enough to avoid the negative thermolubricity effect: $\Theta_c = \frac{k_B T_c}{V_0} \ll 1$. And to avoid the driving velocity being too small, it should not be too low. $\Theta_c \approx 0.01$ is a good choice for the parameter ranges considered for the $\eta \leq 4.6$ cases above. As for the high temperature, as we have elucidated, it should not be too high or too low either and $\Theta_h \approx 1$ is a good choice for the parameter ranges considered for the $\eta \leq 4.6$ cases above.

Some more remarks are given in SI Appendix Sec. 6.M.

Practical Implementation of the PTSHE. There are three systems promising for the practical realization of the PTSHE from atomic- to microscale: the trapped ion system like the trapped ion friction simulator (9, 10, 19, 32), the optical levitated nanosphere system in cavity (33) and the colloidal microparticle system in liquid medium (12). We give a preliminary discussion about some topics on the practical implementation of the PTSHE in SI Appendix Sec. 6.N.

Comparison with the Büttiker-Landauer Heat Engine. The PTSHE is reminiscent of the Brownian motor or ratchet (34–37) in which thermal fluctuations (or diffusion) play an important role and the heat bath is usually of constant temperature. It could be traced back to Feynman's ratchet and pawl (38). In (39), Büttiker calculated the flux of an overdamped particle transmitting through a periodic potential with a spatially varying diffusion coefficient at the same period, which can be realized by a spatially varying temperature field. He showed that when the diffusion coefficient is not in phase with the potential, the particle can achieve directional movement. This mechanism is known as the Büttiker-Landauer ratchet (22, 40–42). With a load applied on the particle, the ratchet becomes a heat engine (43). Usually the load force is predetermined and constant (23, 43–48). Or it can also vary with time as in (49, 50), although the temperature is constant in the two works. In our PTSHE, besides the periodic sinusoidal lattice potential and the alternative high and low temperature field, an uniformly moving harmonic potential is added, resulting in that the load, i.e. the harmonic force, is stochastically varying. This property is characteristic of the PT model. And we have shown that with the addition of such kind of an external load, the limit extractable work increases with the corrugation number η when η is not very large. Besides, with a uniform driving velocity v_{dr} , we can define the engine cycle conveniently by identifying it as the process for the driver center moving over one lattice period, so that we can discuss

the cycle work W_{cyc} . On the other hand, the driving velocity v_{dr} of the harmonic potential should be uniform, so feedback control may be needed in practical implementation. Instead of moving the harmonic potential, we can try to move uniformly the sinusoidal potential and the temperature field, i.e. making two standing waves into two travelling waves, cf. Figure 7(F1)-(F7). Nonuniform driving velocity of the harmonic potential, predetermined or stochastic, should be okay and may lead to better performance.

Based on the principles of stable work output, there is potential to design other stochastic heat engines of this type with a resultant potential energy curve of other shape and an appropriate temperature field. An asymmetric lattice potential composed of two or more harmonics superposed with a harmonic potential may be okay, and we can consider the optimum shape of the asymmetric lattice potential. Optimization of the driving velocity, damping coefficient, temperature profile, the shape of the resultant potential energy and other parameters of the PTSHE is an interesting topic.

The Nonlinearity of the PT Model. We have seen that the nonlinearity of the PT model plays an essential role both in the design of the PTSHE and in the occurrence of stick-slip. The nonlinearity of stick-slip friction has been discussed in (51–54). In this paper we have given a preliminary analysis of the bifurcation of the mean cycle work of the PT model with the driving velocity as parameter at zero temperature. At finite temperature, the nonlinear bifurcation can be reflected by the stochastic resonance represented by the standard deviations of W_{cyc} as in Figure 3(B2), Figure 7(A2) and SI Appendix Figure S18. In homogeneous temperature (SI Appendix Figure S18), this variation can be experimentally validated through levitating a nanosphere by a sinusoidal optical lattice superposed by a harmonic Paul trap as in (33) or through the trapped ion system (9, 10, 19, 32) which we have actually adopted as the model system in this paper (SI Appendix Sec. 8.H).

The stochastic resonance peak's position is not as easy to calculate and should be treated in the future. And the stochastic resonance of the PT model system should be investigated further to explore its potential to apply on noise-induced amplification schemes (55, 56) for weak signal detection. The stability of the bifurcation diagram in Figure 6 hasn't been considered. The nonlinearity of the ordinary differential equation based on PT model is peculiar and there are still a lot of its features to be explored (SI Appendix Sec. 6.K.3).

Conclusion and Outlook. To conclude, we designed a stochastic heat engine based on the Prandtl-Tomlinson model. With the Langevin dynamics simulation and the framework of stochastic thermodynamics we obtained the particle's phase trajectories and the thermodynamic quantities, from which we analyzed two mechanisms of work output of the PTSHE. Based on the potential mechanism, we obtained an approximation of the equilibrium cycle work output and an approximate Carnot-like efficiency of the PTSHE. The thermolubricity mechanism makes the equilibrium cycle work output greater than the approximation based on the potential mechanism and can also lead to the work output reduction if the temperature is excessively high. Mean cycle work is analyzed over a wide range of velocity, giving us a complete picture of the work output regime of the PTSHE as well as the work input regime when it stalls. The latter is similar to that in the nanofriction

and we have compared the PTSHE with the homogeneous temperature cases in nanofriction. In the middle velocity regime of the mean cycle work, the strong and peculiar nonlinear bifurcation at zero temperature and the stochastic resonance at finite temperature of the mean cycle work with respect to the driving velocity are analyzed preliminarily, both of which are still needed to be explored further. When $\eta > 4.6$, the PTSHE has some different features from the $\eta \leq 4.6$ cases and we found that the work output first increases and then decreases with η at the same $\Theta_{h,c}$ and a preliminary analysis is given which still needs to be investigated further.

Combining the stick-slip process and the heat engine, the PTSHE can serve as a thermolubricity strategy and is a candidate system to study the thermodynamics in nanofriction (57–59). The double-well potential is common in many laser trap experiments such as that in verification of the Landauer's limit by a single colloidal particle trapped in a modulated double-well potential (60) and that in the direct measurement of Kramers turnover with a optically levitated nanoparticle (61). Implementation of the PT model at nanoscale through trapped ion system or optically levitated nanoparticle system or at microscale through laser trapped colloidal particle system gives a candidate scheme for studies relevant to the bistable dynamics (55) or multistable dynamics (when $\eta > 4.6$). In the micro- or nanoscale, the thermodynamics quantities are stochastic variables due to the nonneglected thermal fluctuations and the framework of stochastic thermodynamics (62–64) is an important tool to analyze the experimental results (12, 13, 60, 65). The PTSHE can be analyzed further by the Fokker-Planck or Kramers equation method (31), with which the accurate efficiency, the very low temperature case and the high η cases may be treated relatively easily and other issues such as the entropy product, the fluctuation theorems (62) and the power of the PTSHE can also be investigated. The alternative high and low temperature field not only has promising application but also draws forth many interesting physics and is worth being studied. In this paper we consider the PTSHE as a classical system and the effect of quantum tunneling through the barriers should be considered when implemented with, for instance, the trapped ion system at very low temperature.

Methods

The dynamics of the particle in the harmonic and sinusoidal lattice potential and the alternative high and low temperature field can be described by the Langevin equation (1, 2, 66–68)

$$m\ddot{x}(t) = -m\mu\dot{x}(t) - \frac{\partial V(x(t), X(t))}{\partial x} + \xi(t), \quad [4]$$

where the left hand side (LHS) is the inertial force. The first term on the right hand side (RHS) is the damping force term which is proportional to the particle's velocity $\dot{x}(t)$ with μ the damping coefficient; the second term on the RHS is the conservative force exerting by the potential field of the PT model, $\frac{\partial V(x(t), X(t))}{\partial x} = F_h + F_l = \kappa[x(t) - v_{\text{dr}}t] + \frac{\pi}{a}V_0 \sin(\frac{2\pi}{a}x(t))$; the third term on the RHS is the fluctuating force $\xi(t) = \Gamma\zeta(t)$ satisfying the fluctuation-dissipation theorem $\Gamma = \sqrt{2m\mu k_B T(x)}$ with a zero mean Gaussian white noise whose covariance $\langle \zeta(t)\zeta'(t') \rangle = \delta(t - t')$, where $\delta(t)$ is the Dirac delta function. We integrate the Langevin equation with the 4th order stochastic Runge-Kutta method and the detail is given in SI Appendix, Sec. 8, where the numerical method is evaluated carefully to guarantee that it's reasonable and practical.

After integration of the Langevin equation, we obtain the phase trajectories of the particle $(x(t), \dot{x}(t))$. And we use the framework

of stochastic thermodynamics (62–64) to extract the change of the particle's internal energy ΔU , the heat from the particle to the heat bath Q and the work done on the particle W by

$$\begin{aligned}\Delta U &= U(t) - U(t_0), \\ Q &= - \int_{t_0}^t \left\{ \kappa [x(t) - v_{\text{dr}} t] + \frac{\pi}{a} V_0 \sin\left[\frac{2\pi}{a} x(t)\right] \right\} dx \\ &\quad - \left[\frac{1}{2} m \dot{x}(t)^2 - \frac{1}{2} m \dot{x}(t_0)^2 \right], \\ W &= - \int_{t_0}^t \kappa [x(t) - v_{\text{dr}} t] v_{\text{dr}} dt.\end{aligned}\tag{5}$$

The details of the derivation are given in SI Appendix, Sec. 5.

ACKNOWLEDGMENTS. I'm deeply indebted to Dr. Dorian Gangloff (Cambridge University, UK) and Prof. Vladan Vuletić (Massachusetts Institute of Technology, USA) for their answering my so many questions about (9, 10) and their kind offer of the original experimental data and codes of Figure 2 in (10). I thank Prof. Tian Yu for helpful discussion. I also acknowledge Prof. Kim Kihwan for his comments about the experimental realization and Prof. Ou-Yang Zhong-Can and Prof. Tu Zhan-Chun for their kind feedback of our manuscript. I thank Prof. Guo Fei for his reading and advice on this manuscript and his and Prof. Liu Xiangfeng's support of this research. This work is partially supported by the National Natural Science Foundation of China (Grant No.U1937602).

1. SY Krylov, JWM Frenken, The physics of atomic-scale friction: Basic considerations and open questions. *physica status solidi (b)* **251**, 711–736 (2014).
2. A Vanossi, N Manini, M Urbakh, S Zapperi, E Tosatti, Colloquium: Modeling friction: From nanoscale to mesoscale. *Rev. Mod. Phys.* **85**, 529–552 (2013).
3. L Prandtl, Ein Gedankenmodell zur kinetischen Theorie der festen Körper. *ZAMM - J. Appl. Math. Mech. / Zeitschrift für Angewandte Math. und Mech.* **8**, 85–106 (1928).
4. GA Tomlinson, CVI, A molecular theory of friction. *The London, Edinburgh, Dublin Philos. Mag. J. Sci.* **7**, 905–939 (1929).
5. A Benassi, A Vanossi, E Tosatti, Nanofriction in cold ion traps. *Nat Commun* **2**, 236 (2011).
6. D Mandelli, A Vanossi, E Tosatti, Stick-slip nanofriction in trapped cold ion chains. *Phys. Rev. B* **87** (2013).
7. I Garcia-Mata, OV Zhirov, DL Shepelyansky, Frenkel-Kontorova model with cold trapped ions. *The Eur. Phys. J. D* **41**, 325–330 (2006).
8. T Pruttivarasin, M Ramm, I Talukdar, A Kreuter, H Häfner, Trapped ions in optical lattices for probing oscillator chain models. *New J. Phys.* **13** (2011).
9. A Bylinskii, D Gangloff, V Vuletić, Tuning friction atom-by-atom in an ion-crystal simulator. *Science* **348**, 1115–1118 (2015).
10. D Gangloff, A Bylinskii, I Counts, W Jhe, V Vuletić, Velocity tuning of friction with two trapped atoms. *Nat. Phys.* **11**, 915–919 (2015).
11. KB Jinesh, SY Krylov, H Valk, M Dienwiebel, JWM Frenken, Thermolubricity in atomic-scale friction. *Phys. Rev. B* **78**, 155440 (2008).
12. V Blickle, C Bechinger, Realization of a micrometre-sized stochastic heat engine. *Nat. Phys.* **8**, 143–146 (2011).
13. IA Martinez, et al., Brownian Carnot engine. *Nat Phys* **12**, 67–70 (2016).
14. A Dechant, N Kiesel, E Lutz, All-optical nanomechanical heat engine. *Phys Rev Lett* **114**, 183602 (2015).
15. J Roßnagel, et al., A single-atom heat engine. *Science* **352**, 325–329 (2016).
16. O Abah, et al., Single-ion heat engine at maximum power. *Phys Rev Lett* **109**, 203006 (2012).
17. J Rosnagel, O Abah, F Schmidt-Kaler, K Singer, E Lutz, Nanoscale heat engine beyond the Carnot limit. *Phys Rev Lett* **112**, 030602 (2014).
18. T Schmiedl, U Seifert, Efficiency at maximum power: An analytically solvable model for stochastic heat engines. *EPL (Europhysics Lett.)* **81**, 20003 (2007).
19. I Counts, et al., Multislip Friction with a Single Ion. *Phys Rev Lett* **119**, 043601 (2017).
20. SN Medyanik, WK Liu, IH Sung, RW Carpick, Predictions and observations of multiple slip modes in atomic-scale friction. *Phys Rev Lett* **97**, 136106 (2006).
21. C Bustamante, J Liphardt, F Ritort, The Nonequilibrium Thermodynamics of Small Systems. *Phys. Today* **58**, 43–48 (2005).
22. G Benenti, G Casati, K Saito, RS Whitney, Fundamental aspects of steady-state conversion of heat to work at the nanoscale. *Phys. Reports* **694**, 1–124 (2017).
23. I Derényi, RD Astumian, Efficiency of Brownian heat engines. *Phys. Rev. E* **59**, R6219–R6222 (1999).
24. E Granato, SC Ying, Non-Monotonic Velocity Dependence of Atomic Friction. *Tribol. Lett.* **39**, 229–233 (2010).
25. E Djiha Tchaptchet, G Dujidje Kenmoe, Velocity and forced excitation effects on atomic friction force with deformable substrate. *Nonlinear Dyn.* **82**, 961–969 (2015).
26. DW Lee, X Banquy, JN Israelachvili, Stick-slip friction and wear of articular joints. *Proc. Natl. Acad. Sci.* **110**, E567–E574 (2013).
27. EA Jagla, Velocity weakening and possibility of aftershocks in nanoscale friction experiments. *Phys. Rev. B* **86** (2012).
28. A Dhooge, W Govaerts, YA Kuznetsov, HGE Meijer, B Sautois, New features of the software MatCont for bifurcation analysis of dynamical systems. *Math. Comput. Model. Dyn. Syst.* **14**, 147–175 (2008).
29. R Seydel, Stability of Periodic Solutions in *Practical Bifurcation and Stability Analysis*. (Springer New York, New York, NY), pp. 303–356 (2010).
30. L Gammaitoni, P Hänggi, P Jung, F Marchesoni, Stochastic resonance. *Rev. Mod. Phys.* **70**, 223–287 (1998).
31. H Risken, Solutions of the Kramers Equation in *The Fokker-Planck Equation: Methods of Solution and Applications*. (Springer Berlin Heidelberg, Berlin, Heidelberg), pp. 229–275 (1996).
32. L Karpa, A Bylinskii, D Gangloff, M Cetina, V Vuletić, Suppression of ion transport due to long-lived subwavelength localization by an optical lattice. *Phys Rev Lett* **111**, 163002 (2013).
33. J Millen, PZG Fonseca, T Mavrogordatos, TS Monteiro, PF Barker, Cavity Cooling a Single Charged Levitated Nanosphere. *Phys. Rev. Lett.* **114**, 123602 (2015).
34. P Hänggi, F Marchesoni, Artificial Brownian motors: Controlling transport on the nanoscale. *Rev. Mod. Phys.* **81**, 387–442 (2009).
35. P Reimann, Brownian motors: noisy transport far from equilibrium. *Phys. Reports* **361**, 57–265 (2002).
36. RD Astumian, P Hänggi, Brownian Motors. *Phys. Today* **55**, 33–39 (2002).
37. PS Burada, P Hänggi, F Marchesoni, G Schmid, P Talkner, Diffusion in confined geometries. *Chemphyschem* **10**, 45–54 (2009).
38. RP Feynman, RB Leighton, M Sands, Chapter 46. Ratchet and pawl in *The Feynman lectures on physics*, Lectures on physics. (New York : Basic Books, New York), Vol. 1, New millennium edition, pp. 46–1–46–14 (2010).
39. M Büttiker, Transport as a consequence of state-dependent diffusion. *Zeitschrift für Physik B Condens. Matter* **68**, 161–167 (1987).
40. R Landauer, Motion out of noisy states. *J. Stat. Phys.* **53**, 233–248 (1988).
41. NGv Kampen, Relative stability in nonuniform temperature. *IBM J. Res. Dev.* **32**, 107–111 (1988).
42. IA Martinez, E Roldan, L Dinis, RA Rica, Colloidal heat engines: a review. *Soft Matter* **13**, 22–36 (2016).
43. F Berger, T Schmiedl, U Seifert, Optimal potentials for temperature ratchets. *Phys Rev E Stat Nonlin Soft Matter Phys* **79**, 031118 (2009).
44. R Benjamin, R Kawai, Inertial effects in Büttiker-Landauer motor and refrigerator at the over-damped limit. *Phys Rev E Stat Nonlin Soft Matter Phys* **77**, 051132 (2008).
45. M Matsuo, Si Sasa, Stochastic energetics of non-uniform temperature systems. *Phys. A: Stat. Mech. its Appl.* **276**, 188–200 (2000).
46. M Aslaw, M Bekele, Current, maximum power and optimized efficiency of a Brownian heat engine. *The Eur. Phys. J. B - Condens. Matter Complex Syst.* **38**, 457–461 (2004).
47. M Aslaw, Modeling an efficient Brownian heat engine. *The Eur. Phys. J. B* **65**, 109–116 (2008).
48. A Gomez-Marín, JM Sancho, Tight coupling in thermal Brownian motors. *Phys. Rev. E* **74**, 062102 (2006).
49. MB Tarlie, RD Astumian, Optimal modulation of a Brownian ratchet and enhanced sensitivity to a weak external force. *J. Proc. Natl. Acad. Sci.* **95**, 2039–2043 (1998).
50. S Saikia, Ratchet effect in an underdamped periodic potential and its characterisation. *Phys. A: Stat. Mech. its Appl.* **468**, 219–227 (2017).
51. M Urbakh, J Klafter, D Gourdon, J Israelachvili, The nonlinear nature of friction. *Nature* **430**, 525–528 (2004).
52. N Manini, OM Braun, E Tosatti, R Guerra, A Vanossi, Friction and nonlinear dynamics. *J. Physics: Condens. Matter* **28**, 293001 (2016).
53. MG Rozman, M Urbakh, J Klafter, Stick-Slip Motion and Force Fluctuations in a Driven Two-Wave Potential. *Phys. Rev. Lett.* **77**, 683–686 (1996).
54. MG Rozman, M Urbakh, J Klafter, Origin of stick-slip motion in a driven two-wave potential. *Phys. Rev. E* **54**, 6485–6494 (1996).
55. F Ricci, et al., Optically levitated nanoparticle as a model system for stochastic bistable dynamics. *Nat. Commun.* **8**, 15141 (2017).
56. WJ Venstra, HJR Westra, HSJ van der Zant, Stochastic switching of cantilever motion. *Nat. Commun.* **4**, 2624 (2013).
57. F Pellegrini, E Panizon, GE Santoro, E Tosatti, Thermally assisted lubricity and negative work tails in sliding friction. *Phys. Rev. B* **99** (2019).
58. PC Torche, T Polcar, O Hovorka, Thermodynamic aspects of nanoscale friction. *Phys. Rev. B* **100** (2019).
59. PC Torche, P Nicolini, T Polcar, O Hovorka, Stochastic thermodynamics of nanoscale friction. *Phys. Rev. E* **103**, 052104 (2021).
60. A Berut, et al., Experimental verification of Landauer's principle linking information and thermodynamics. *Nature* **483**, 187–9 (2012).
61. L Rondin, et al., Direct measurement of Kramers turnover with a levitated nanoparticle. *Nat. Nanotechnol.* **12**, 1130–1133 (2017).
62. U Seifert, Stochastic thermodynamics, fluctuation theorems and molecular machines. *Rep Prog Phys* **75**, 126001 (2012).
63. K Sekimoto, Kinetic Characterization of Heat Bath and the Energetics of Thermal Ratchet Models. *J. Phys. Soc. Jpn.* **66**, 1234–1237 (1997).
64. K Sekimoto, Langevin Equation and Thermodynamics. *Prog. Theor. Phys. Suppl.* **130**, 17–27 (1998).
65. V Blickle, T Speck, L Helden, U Seifert, C Bechinger, Thermodynamics of a colloidal particle in a time-dependent nonharmonic potential. *Phys Rev Lett* **96**, 070603 (2006).
66. Y Dong, A Vadakkepat, A Martini, Analytical Models for Atomic Friction. *Tribol. Lett.* **44**, 367–386 (2011).
67. MH Müser, Velocity dependence of kinetic friction in the Prandtl-Tomlinson model. *Phys. Rev. B* **84** (2011).
68. ZJ Wang, TB Ma, YZ Hu, L Xu, H Wang, Energy dissipation of atomic-scale friction based on one-dimensional Prandtl-Tomlinson model. *Friction* **3**, 170–182 (2015).

Supplementary Information for

A Stochastic Heat Engine Based on Prandtl-Tomlinson Model

Dongyang Zhao

Dongyang Zhao.

E-mail: dy-zhao14@mails.tsinghua.edu.cn

This PDF file includes:

Supplementary text
Figs. S1 to S67
Tables S1 to S6
SI References

Supporting Information Text

This supporting information appendix is a little long for the purpose of describing the mathematical models in detail and pedagogically. Although we have tried our best to make this paper self-consistent, there are still aspects we cannot include. If there are anywhere unclear or any mistakes, the authors are grateful for the readers to contact them freely.

Many derivations and results in this supporting information appendix are not original and must have been derived or obtained before, although we have tried our best to cite the relevant works. If we didn't cite what should be cited, the originality should be credited to the original authors.

This SI Appendix has 8 sections. In Sec. 1 we give some references for the Abstract of the main text for the readers to have a knowledge of the ubiquity of the stick-slip phenomenon in many scientific fields.

In Sec. 2, we show how to determine the boundaries of the hot and the cold zones of the PTSHE.

In Sec. 3, we introduce the geometric root of the stick-slip phenomenon based on the PT model with different quantities. Curves of these quantities at the balanced points with respect to the driver center's position are plotted and are used to analyze the mechanisms of stable work output of the PTSHE in the main text.

In Sec. 4, we give a brief derivation of the critical values of η . In the main text, we mainly focus on the range $[1, 4.6]$ and the higher order behavior of the PTSHE when $\eta > 4.6$ is also discussed preliminarily.

In Sec. 5, the first law of thermodynamics is derived from the Langevin equation utilizing the framework of stochastic thermodynamics. The formula of calculating the internal energy, released heat and inputted work are derived, which are mentioned in the Methods section of the main text.

In Sec. 6, we gather all the appendices for the Results and Discussion section of the main text.

In Sec. 7, we give a brief derivation of a form of fluctuation-dissipation theorem based on the linear Langevin equation for the harmonic oscillator, which is equivalent to the equipartition theorem. And we have assumed that it is also satisfied by our nonlinear Langevin Eq. 4 in the main text. We didn't find a detailed derivation in the textbooks accessible to us so we derive it ourselves here for self-consistency of the paper. It is also used for evaluation of the SRK4 method in the next section.

In Sec. 8, we introduce the Langevin dynamics simulation in detail. Because Langevin simulation is the main methods of this paper, we describe as elaborately as we could. We evaluate the SRK4 method carefully to make sure that it satisfies the equipartition theorem with enough accuracy for the case of the linear Langevin equation, that it performs as well as another nonlinear method with the appropriately chosen time stepsize, that it satisfies the first law of thermodynamics with low accumulative error and that it can duplicate the experimental results without fitting parameters.

The last two sections are a little long so we arrange them at the end of this SI Appendix. They can also be placed above Sec. 6.

For the use of this SI Appendix, we suggest the readers first read the main text subsection by subsection and glance over the corresponding cited parts of this SI Appendix without thorough reading to have a first impression. After finishing reading at least one subsection of the main text, the readers can read through the corresponding SI Appendix parts if necessary. As for a specific subsection in this SI Appendix, we suggest the readers first read through the entire subsection including all the figures without caring too much about the incomprehensions encountered, which may be figured out after finishing reading the whole subsection.

Contents

1	References for the abstract of the main text	3
2	Determination of the boundaries of different temperature zones	3
3	The geometric explanation of the stick-slip phenomenon based on PT model	5
4	The derivation of the critical values of η	7
5	The first law of thermodynamics derived from the Langevin equation	8
6	Appendices for the Results and the Discussion section of the main text	8
A	The homogeneous low temperature heat bath: stick-slip	8
B	The homogeneous high temperature heat bath: thermolubricity	10
C	The similarity of the shape of the work curve and that of the lower bound of the internal energy	11
D	The high velocity limit of the mean cycle work	12
E	The equilibrium limit of the mean cycle work approximated by the potential mechanism	12
F	The reason for the higher work output at $\eta = 2$ and $\eta = 1$ than the potential mechanism approximation	14
F.1	The case of $\eta = 2$	14
F.2	The case of $\eta = 1$	14
F.3	The simulation results at $\eta < 1$	16
G	The simulation results with the high temperature Θ_h varying for the $\eta = 1, 2, 4$ cases	16
H	Transition of the energy, displacement and harmonic force during one cycle with the driving velocity	18

I	The count distribution of W_{cyc} and its standard deviation	37
J	The multiple solutions of the zero temperature Langevin equation	38
K	The nonlinear bifurcation of $\langle W_{\text{cyc}} \rangle$ with respect to v_{dr}	39
K.1	Continuation of the zero temperature $\langle W_{\text{cyc}} \rangle - v_{\text{dr}}$ curve	39
K.2	Details of the $\langle W_{\text{cyc}} \rangle - v_{\text{dr}}$ bifurcation diagram	40
K.3	Some of the peculiar nonlinear features of the ordinary differential equation based on the PT model	42
L	More on the $\eta > 4.6$ cases	50
M	More remarks on the temperature	55
N	Topics about the practical implementation of the PTSHE	55
N.1	Parameter choice constrained by the obtainable values of and the mutual relations between temperature and other quantities	55
N.2	Implementation of the spatially alternative high and low temperature field	55
N.3	On the damping coefficient	56
7	Fluctuation-dissipation theorem	57
8	Langevin dynamics simulation	59
A	Nondimensionalization of the Langevin equation	59
B	Equivalent form of the Stratonovich and the Ito stochastic differential equation	59
C	The mid-point rule of discretizing the Stratonovich stochastic integral	60
D	The continuous temperature function	62
E	Stochastic Runge-Kutta method to integrate the Langevin equation	62
F	Choice of the time stepsize	63
G	Evaluation of the SRK4 method	63
H	Parameters used in the simulation	70
I	Further check of the simulation method: the first law of thermodynamics	72
J	Further check of the simulation method: comparison with the experimental results	73
	Reference	80

1. References for the abstract of the main text

In the abstract we mention that stick-slip is an ubiquitous phenomenon in many scientific fields and here are some references: earthquake and glacier dynamics (1–10), acoustics (11, 12), cell biology (13, 14), interface science (15–20) and tribology (21–23).

2. Determination of the boundaries of different temperature zones

We first nondimensionalize the resultant potential

$$V(x(t), X(t)) = \frac{1}{2} \kappa [x(t) - X(t)]^2 + \frac{V_0}{2} [1 - \cos(\frac{2\pi}{a} x(t))] \quad [1]$$

to

$$\tilde{V}(z(\tau), \tilde{X}(\tau)) = \frac{V(x(t))}{\kappa a^2 / (4\pi^2)} = \frac{1}{2} [z(\tau) - \tilde{X}(\tau)]^2 + \eta [1 - \cos(z(\tau))], \quad [2]$$

where $z(\tau) = \frac{2\pi}{a} x(t)$, $\tau = \frac{\omega_0}{2\pi} t$, $\tilde{X}(\tau) = \frac{2\pi}{a} X(t)$, $\eta = \frac{2\pi^2 V_0}{\kappa a^2}$ and $X(t) = v_{\text{dr}} t$. Here $\omega_0 = \sqrt{\kappa/a}$ is the intrinsic frequency of the parabola potential V_h .

At a specific driver center position $\tilde{X}(\tau)$, set the first partial derivative of $\tilde{V}(z(\tau), \tilde{X}(\tau))$ with respect to z to be zero,

$$\frac{\partial \tilde{V}(z(\tau), \tilde{X}(\tau))}{\partial z} = [z(\tau) - \tilde{X}(\tau)] + \eta \sin(z(\tau)) = 0, \quad [3]$$

yielding

$$\tilde{X}(\tau) = z(\tau) + \eta \sin(z(\tau)), \quad [4]$$

solving which we can obtain the local minima and maxima, i.e. the stable and unstable balanced points, of $\tilde{V}(z(\tau), \tilde{X}(\tau))$: $z(\tau)^*$, satisfying

$$\tilde{X}(z(\tau)^*) = z(\tau)^* + \eta \sin(z(\tau)^*). \quad [5]$$

Substitute Eq. 5 into Eq. 2, we will get

$$\tilde{V}(z(\tau)^*) = \frac{1}{2} \eta^2 \sin^2(z(\tau)^*) + \eta [1 - \cos(z(\tau)^*)]. \quad [6]$$

The meaning of $\tilde{V}(z(\tau)^*)$ is that at $z(\tau)^*$, the nondimensional resultant potential $\tilde{V}(z(\tau), \tilde{X}(z(\tau)^*))$ achieves its extremum $\tilde{V}(z(\tau)^*)$ and the driver center is at $\tilde{X}(z(\tau)^*)$, cf. Figure S1(A), in which we plot $\tilde{V}(z(\tau)^*)$, $\tilde{X}(z(\tau)^*)$ and $z(\tau)^*$ with respect

to $z(\tau)^*$ in one period $[0, 2\pi)$. There are three zones separated by the two maximum points of $\tilde{V}(z(\tau)^*)$. Let the second partial derivative of $\tilde{V}(z(\tau), X(\tau))$ with respect to z at $z(\tau)^*$ equal zero,

$$\frac{\partial^2 \tilde{V}(z(\tau)^*, \tilde{X}(z(\tau)^*))}{\partial z^2} = 1 + \eta \cos(z(\tau)^*) = 0, \quad [7]$$

we get the critical maximum points separating the zones,

$$z_1^{**} = 2n\pi + \arccos(-\frac{1}{\eta}), z_2^{**} = 2n\pi - \arccos(-\frac{1}{\eta}), n \in \mathbb{Z}. \quad [8]$$

In the period $[0, 2\pi)$, the two critical points are $z_1^{**} = \arccos(-\frac{1}{\eta})$ and $z_2^{**} = 2\pi - \arccos(-\frac{1}{\eta})$. We will refer to z_1^{**} and z_2^{**} as the backward critical point (BCP) and the forward critical point (FCP) respectively.

In Figure S1(C1)-(C9), we plot the potential curves at 9 selected instants during one temporal period during which the driver center goes over a lattice period. The FCP and the BCP are both inflection and stationary points of the resultant potential curve $\tilde{V}(z(\tau), X(\tau))$. From the starting instant of one temporal period [Figure S1(C1)] to the appearance of FCP [Figure S1(C3)], the resultant potential energy curve has only one global minimum in the left zone. There are no other extrema in the other two zones of one spatial lattice period. From the disappearance of the FCP to the appearance of the BCP [Figure S1(C7)], there are two local minima and one local maxima in the left, the right and the middle zone of one spatial lattice period, respectively. After the disappearance of the BCP [Figure S1(C7)] till the end of one temporal period [Figure S1(C9)], there is only one global minimum again in the right zone. So in one temporal period, the left zone covers the left local or global minimum of $\tilde{V}(z(\tau), X(\tau))$, the middle zone covers the local maximum of $\tilde{V}(z(\tau), X(\tau))$, and the right zone covers the right local or global minimum of $\tilde{V}(z(\tau), X(\tau))$. The FCP appears and divides into the right local minimum and the local maximum and from then on there are three extrema, until the left local minimum and the local maximum merges into the BCP that then disappears.

From the starting instant [Figure S1(C1)] to the BCP [Figure S1(C7)], the global or left local minimum rises from zero to its highest value before it merges into the BCP and disappears, and during this process it stays in the left zone $[0, z_1^{**})$ in the temporal interval $[0, z_2^{**}/\tilde{v}_{dr})$. We set the spacial intervals $[2n\pi, z_1^{**} + 2n\pi), n \in \mathbb{Z}$ in the high temperature T_h and the rest of the spatial lattice periods $[z_1^{**} + 2n\pi, 2\pi), n \in \mathbb{Z}$ in the low temperature T_c .

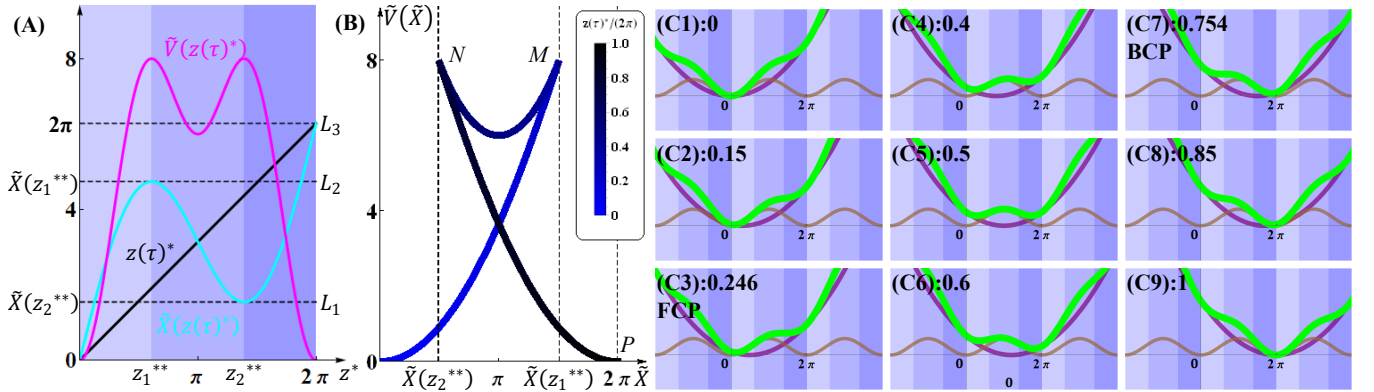


Fig. S1. Determination of the boundaries of different temperature zones. (A) The resultant potential $\tilde{V}(z(\tau)^*)$ at the balanced point $z(\tau)^*$ and the corresponding change of the driver center $\tilde{X}(z(\tau)^*)$ in one period with respect to $z(\tau)^*$. Two critical points z_1^{**} (BCP) and z_2^{**} (FCP) separate one spatial lattice period into three zones. Two lines $L_1 : \tilde{X}(z(\tau)^*) = \tilde{X}(z_2^{**})$ and $L_2 : \tilde{X}(z(\tau)^*) = \tilde{X}(z_1^{**})$ separate one temporal period, in which the driver center $\tilde{X}(z(\tau)^*)$ goes over one lattice period, into three parts. Between the x -axis and L_1 , there is one solution for a horizontal line intersecting the $\tilde{X}(z(\tau)^*) - z(\tau)^*$ curve, corresponding to the only one global minimum in (C1)-(C2). Between L_1 and L_2 , there are three solutions for a horizontal line intersecting the $\tilde{X}(z(\tau)^*) - z(\tau)^*$ curve, corresponding to the two local minima, and one local maximum in between in (C4)-(C6). Between L_2 and $L_3 : \tilde{X}(z(\tau)^*) = 2\pi$, there is one solution again for a horizontal line intersecting the $\tilde{X}(z(\tau)^*) - z(\tau)^*$ curve, corresponding to the only one global minimum in (C8)-(C9). (B) The $\tilde{V}(z(\tau)^*, \tilde{X}(z(\tau)^*)) - \tilde{X}(z(\tau)^*)$ curve with $z(\tau)^*$ as parameter. \widehat{OM} represents the left (first global and then local) minimum's resultant potential rising with \tilde{X} from the starting instant of one temporal period (C1) to the appearance of the BCP (C7). \widehat{NM} represents the middle maximum's resultant potential changing with \tilde{X} from the disappearance of the FCP to the appearance of the BCP [(C3) to (C7)], with N corresponding to the instant of the FCP (C3) and M the instant of the BCP (C7). \widehat{NP} represents the right (first local and then global) minimum's resultant potential setting with \tilde{X} from the disappearance of the FCP (C3) to the end of the same temporal period (C9). In the interval $(\tilde{X}(z_2^{**}), \tilde{X}(z_1^{**}))$, the three extrema coexist, which is more clear in (C4) to (C6). It is crucial to note that on \widehat{OM} , the left global or local minimum is always behind the driver center while on \widehat{NP} , the right local or global minimum is always ahead of the driver center. In our PTSHE, the particle will stay around the minimum points (stable balanced points) of the resultant potential, and if it is around the left one, the driver pulls the particle and work is inputted to the particle, while if it is around the right one, the particle pulls the driver and work is outputted from the particle to the driver. (C1)-(C9) The key frames of the potential curves at 9 selected instants during one temporal period. The purple, brown and green curves represent the moving harmonic potential, the lattice potential and the resultant potential respectively. The decimal following each label represents the relative position of the driver center $X(t)/a = v_{dr}t/a$ to its starting point in (C1), which is proportional to the time t .

In Figure S1(A), we also plot $\tilde{X}(z(\tau)^*)$ with respect to $z(\tau)^*$, which has one local minimum and one local maximum. The extremum points can be obtained by setting the partial derivative of Eq. 5 to be zero,

$$\frac{\partial \tilde{X}(z(\tau)^*)}{\partial z^*} = 1 + \eta \cos(z(\tau)^*) = 0, \quad [9]$$

leading to the same values as Eq. 8. The $\tilde{X}(z(\tau)^*)$ is plotted with respect to the stationary point $z(\tau)^*$ at which the resultant potential achieves its extremum. In the left zone, at each point $z(\tau)^*$, the resultant potential can only have the global or the left local minimum. In the middle zone, at each point $z(\tau)^*$, the resultant potential can only have the local maximum. While in the right zone, at each point $z(\tau)^*$, the resultant potential can only have the global or the right local minimum. In the middle zone $\tilde{X}(z(\tau)^*)$ goes down as $z(\tau)^*$ increases because in this zone the resultant potential energy has only one local maximum moving backwards to the left as the driver goes forward [Figure S1(C3)-(C7)]. The two extremum points of $\tilde{X}(z(\tau)^*)$ divide one temporal period into three parts too. When $\tilde{X}(z(\tau)^*) \in [0, \tilde{X}(z_2^{**})]$, i.e. between the x -axis and L_1 , there is only one global minimum [Figure S1(C1)-(C2)]. When $\tilde{X}(z(\tau)^*) \in (\tilde{X}(z_2^{**}), \tilde{X}(z_1^{**}))$, i.e. between the L_1 and L_2 , there are three extrema, i.e. the left local minimum, the middle local maximum and the right local minimum [Figure S1(C4)-(C6)]. It's clear that there are three intersection points of the $\tilde{X}(z(\tau)^*) - z(\tau)^*$ curve with a horizontal line in this interval, distributed in the three zones separated by the FCP (z_2^{**}) and BCP (z_1^{**}). When $\tilde{X}(z(\tau)^*) \in (\tilde{X}(z_1^{**}), 2\pi)$, i.e. between L_2 and L_3 , there is only one global minimum again [Figure S1(C8)-(C9)].

From Eq. 6 and Eq. 5, we can treat $\tilde{V}(z(\tau)^*)$ as a function of $\tilde{X}(z(\tau)^*)$ with $z(\tau)^*$ as parametar,

$$\begin{cases} \tilde{X}(z(\tau)^*) = z(\tau)^* + \eta \sin(z(\tau)^*), \\ \tilde{V}(z(\tau)^*) = \frac{1}{2}\eta^2 \sin^2(z(\tau)^*) + \eta[1 - \cos(z(\tau)^*)], \end{cases} \quad [10]$$

whose curve is plotted in Figure S1(B). In Figure S1(B), it's clearer that as the driver moves from left to right in one period, there is one global minimum in the interval $[0, \tilde{X}(z_2^{**})]$, then three local extrema in $(\tilde{X}(z_2^{**}), \tilde{X}(z_1^{**}))$ and then one global minimum again in $(\tilde{X}(z_1^{**}), 2\pi)$. In Figure S1(B), the singular points $M(\tilde{X}(z_1^{**}), \tilde{V}(z_1^{**}))$ and $N(\tilde{X}(z_2^{**}), \tilde{V}(z_2^{**}))$ correspond to the instants when (and also the position of the driver center where) the BCP and the FCP appear respectively. The curve \widehat{OM} represents the rising of the left minimum with respect to $\tilde{X}(z(\tau)^*)$, which corresponds to Figure S1(C1)-(C7). At M , the left local minimum merges with the middle local maximum and both of them then disappear. In the main text, we refer to the curve \widehat{OM} as the left minimum branch and is colored in red because this branch is immersed in the hot zone. The right minimum branch \widehat{NP} and the middle maximum branch \widehat{MN} are immersed in the cold zone and are colored in blue.

3. The geometric explanation of the stick-slip phenomenon based on PT model

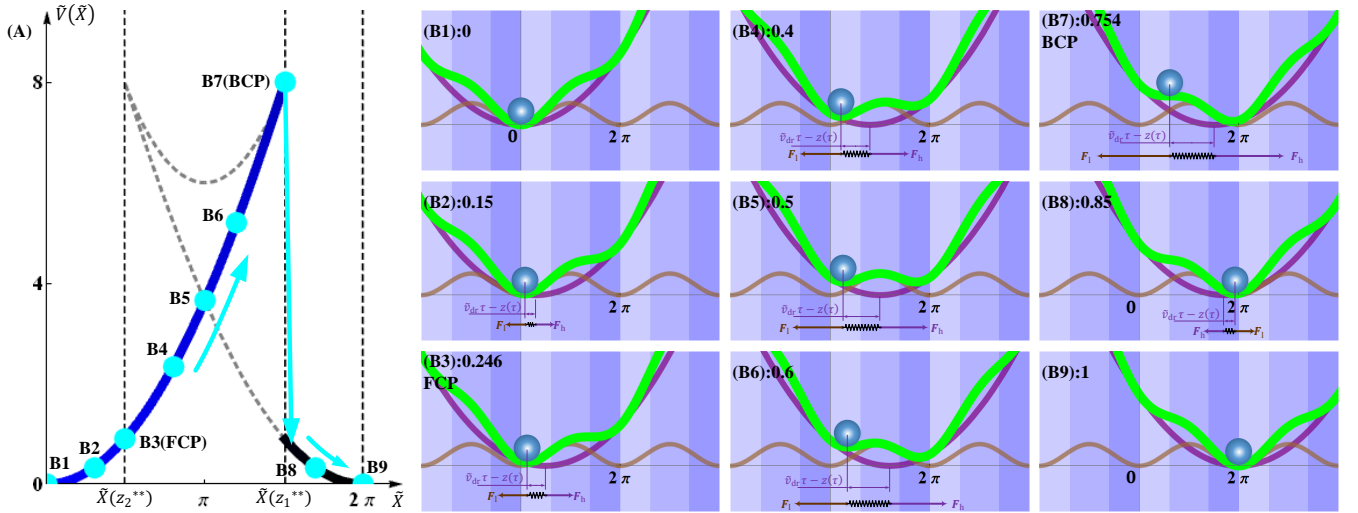


Fig. S2. The stick-slip process interpreted by the PT model. The resultant potential energy change of the particle in the stick-slip process is represented by the solid curves in (A) with the blue balls B1-B9 corresponding to the frames in (B1)-(B9). The dashed gray backbone curve is inherited from Figure S1(B). As the particle is driven to the right by the driver, the potential energy of it rises from minimum (B1) to maximum at the BCP (B7), which is the stick process. After the BCP disappears, the particle is exerted by a resultant force pointing to the right and accelerates (slips) to the right minimum which is now global. And then the particle is pushed by the lattice force and drives the driver to the right until the end of one period (B9), where the driver center and the particle overlap. Work is done on the particle from the driver before the instant of the BCP, while work is outputted from the particle to the driver after the particle has slipped to the right global minimum. Here the particle is assumed to be acted on by an infinitely large damping force besides the harmonic force and the lattice force at zero temperature so that it tends to stay at the local minimum (stable balanced) point all the time and slips exactly at the instant of the BCP.

In Figure S2(B1)-(B9) there is a particle driven by the driver starting at the global minimum of the resultant potential when the harmonic potential minimum overlaps with one of the lattice potential minima [Figure S2(B1)]. The resultant potential energy of the particle is represented by the solid curves in Figure S2(A) with the blue balls B1-B9 corresponding to the frames in (B1)-(B9). Assuming the particle is exerted by an infinitely large damping force besides the harmonic force F_h from the driver and the lattice force F_l at zero temperature so that there is no relaxing process and it tends to stay in balance all the time, i.e. this is a quasistatic model. Then the particle will stay on the left (at first global and then local) minimum following

the driver. The potential energy of the particle rises along the curve \widehat{OM} to the maximum value $\tilde{V}(z_1^{**})$ at the BCP $z(\tau) = z_1^{**}$ in Figure S2(A) and this is the stick process. At the BCP the left local minimum merges with the middle local maximum and then both of them disappear and the harmonic force F_h and the lattice force F_l can't continue to balance with each other because $\frac{\partial V}{\partial x} = F_h + F_l$ can't any longer equal 0. The particle will then be exerted by the resultant force $\frac{\partial V}{\partial x} = F_h + F_l > 0$ pointing to the right and accelerate (slip) until $\frac{\partial V}{\partial x} = F_h + F_l = 0$ again at the right minimum which is now the only global minimum. Then the particle remains at this global minimum point until the end of the period when the harmonic potential minimum overlaps with the next lattice potential minimum. This is the geometric explanation of the stick-slip process (24–28).

Note that after the particle slips and stays in the right global minimum, the particle is on the right of (ahead of) the driver center and $F_l > 0$, i.e. pointing to the right, and $F_h < 0$, i.e. pointing to the left, so that the particle is pushed by the lattice force F_l and the particle drives the driver forward, i.e. work is done by the particle on the driver. That's the key point for the work output of our PTSHE.

In Figure S3, we plot three more quantities with respect to the driver center's position, which we will use in the main text and below. The upper left one is the nondimensional balanced point position $z(\tau)^*$, i.e. the position of the resultant potential extrema. It can be expressed by the parametric equation

$$\begin{cases} \tilde{X}(z(\tau)^*) = z(\tau)^* + \eta \sin(z(\tau)^*), \\ z(\tau)^* = z(\tau)^*, \end{cases} \quad [11]$$

with $z(\tau)^*$ as the parameter. This curve is the same as the cyan curve in Figure S1(A) except for the exchange of the x - and y -coordinates.

The upper middle one is the nondimensional lattice potential $\tilde{V}_l(z(\tau)^*)$ at the balanced point $z(\tau)^*$. It can be expressed by the parametric equation

$$\begin{cases} \tilde{X}(z(\tau)^*) = z(\tau)^* + \eta \sin(z(\tau)^*), \\ \tilde{V}_l(z(\tau)^*) = \eta[1 - \cos(z(\tau)^*)], \end{cases} \quad [12]$$

with $z(\tau)^*$ as the parameter.

The upper right one is the nondimensional harmonic force

$$\tilde{F}_h(z(\tau)^*) = \frac{F_h(x(t))}{\kappa a/(2\pi)} = \frac{\kappa[X(t) - x(t)]}{\kappa a/(2\pi)} \quad [13]$$

at the balanced point $z(\tau)^*$. The parametric equation for it is

$$\begin{cases} \tilde{X}(z(\tau)^*) = z(\tau)^* + \eta \sin(z(\tau)^*), \\ \tilde{F}_h(z(\tau)^*) = \tilde{X}(z(\tau)^*) - z(\tau)^* = \eta \sin(z(\tau)^*), \end{cases} \quad [14]$$

with $z(\tau)^*$ as the parameter.

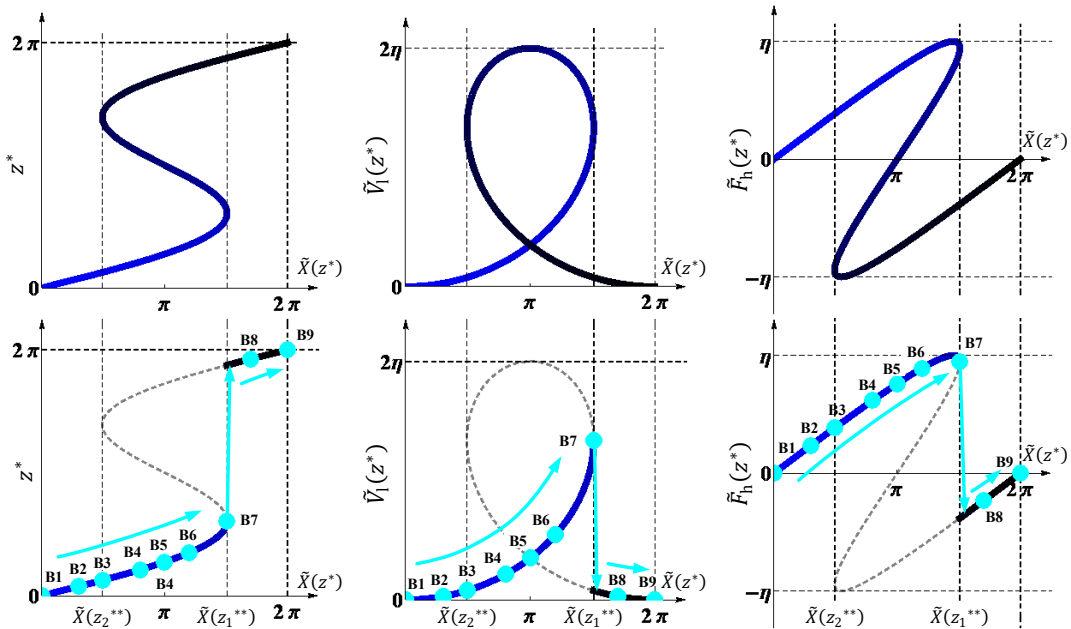


Fig. S3. Quantities at the balanced points of the PT model and the stick-slip process represented by them. The upper three subfigures are the balanced point position z^* , the lattice potential $\tilde{V}_l(z^*)$ at the balanced point and the harmonic force $\tilde{F}_h(z^*)$ at the balanced point with respect to the position of the driver center $\tilde{X}(z^*)$ at the balanced point from the left to the right respectively. The bottom three subfigures are the stick-slip process represented by the upper three quantities respectively at infinitely large damping force and zero temperature as in Figure S2(A). The blue balls B1-B9 in the bottom three subfigures correspond to the 9 frames in Figure S2(B1)-(B9).

The lower three schematics are the stick-slip process represented by the upper three quantities. We can see that all of the four quantities $[z^*, \tilde{V}_1(z^*), \tilde{F}_h(z^*)$ in Figure S3 and $\tilde{V}(z^*)$ in Figure S2] slips at the same driver center position $\tilde{X}(z_1^{**})$.

4. The derivation of the critical values of η

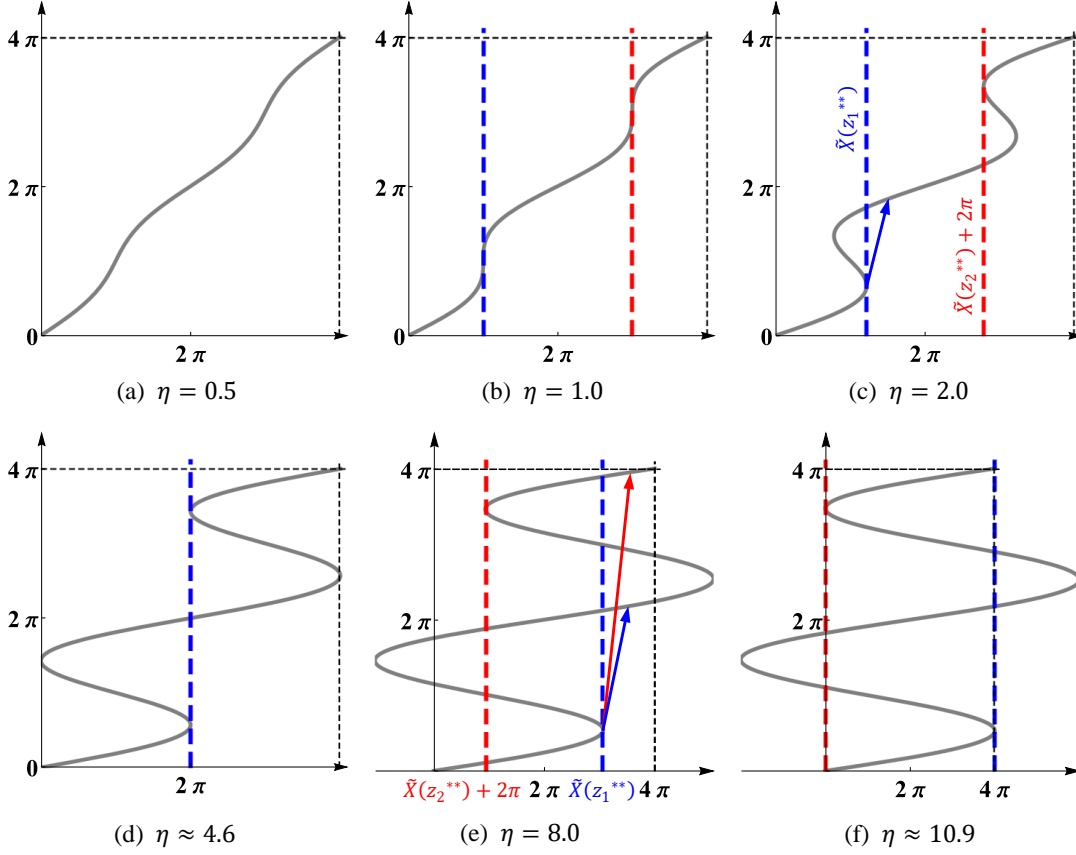


Fig. S4. Schematic of calculating the critical value of η . All the x-coordinates are $\tilde{X}(z^*)$ and all the y-coordinates are z^* . The blue dashed line corresponds to the driver center position at the BCP of the first cycle $\tilde{X}(z_1^{**})$ and the red one corresponds to that at the FCP of the second cycle $\tilde{X}(z_2^{**}) + 2\pi$. At the first critical value $\eta = 1.0$ (b), the two dashed lines occur. At the second critical value $\eta \approx 4.6$ (d), the two dashed lines overlap at 2π . At the third critical value $\eta \approx 10.9$ (f), $\tilde{X}(z_1^{**}) = 4\pi$ and $\tilde{X}(z_2^{**}) + 2\pi = 0$. The arrows in (c) and (e) represent the slip event and when $\eta = 8$, there are two possible landing points for the particle at the slip instant.

In the main text, we mention that our attention is mainly paid to η in the range of $[1, 4.6]$, where the resultant potential energy has at most two maxima. The critical value of η can be obtained by the method used in (29). Here we give a geometric derivation. We take the $z^* - \tilde{X}(z^*)$ curve as an example. In Figure S4, we can see that when $\eta = 0.5$, the $z^* - \tilde{X}(z^*)$ curve is monotonous while when $\eta = 2.0$, it becomes nonmonotonous and there is a fold in one cycle with two points, i.e. the FCP ($\tilde{X}(z_2^{**}), z_2^{**}$) and the BCP ($\tilde{X}(z_1^{**}), z_1^{**}$), having infinite slope, both of which are symmetric about the middle of the cycle. Therefore there is a critical value of η between 0.5 and 2, at which a point with infinite slope occurs, i.e. at this point

$$\frac{d\tilde{X}(z^*)}{dz^*} = 1 + \eta_1 \cos(z^*) = 0. \quad [15]$$

From symmetry we know that this point is $z^* = \pi$, so that $\eta_1 = 1$.

At $\eta = 2.0$, $\tilde{X}(z_1^{**}) < 2\pi$, the stick-slip event has only one landing point at the instant of the BCP as indicated by the blue arrow in Figure S4(c). While at $\eta = 8.0$, $\tilde{X}(z_1^{**}) > 2\pi$, the stick-slip event can have two landing points at the instant of the BCP as indicated by the blue and red arrows in Figure S4(e). Therefore, at the second critical value of η ,

$$\tilde{X}(z_1^{**}) = 2\pi = z_1^{**} + \eta_2 \sin(z_1^{**}) = \arccos(-\frac{1}{\eta_2}) + \eta_2 \sin(\arccos(-\frac{1}{\eta_2})), \quad [16]$$

where Eq. 8 is utilized. Solve this equation with a nonlinear solver, we can obtain the second critical value $\eta_2 = 4.6033388487517$. By the same reasoning we can obtain the other critical values of η by solving the nonlinear equations

$$\tilde{X}(z_1^{**}) = z_1^{**} + \eta_{n+1} \sin(z_1^{**}) = \arccos(-\frac{1}{\eta_{n+1}}) + \eta_{n+1} \sin(\arccos(-\frac{1}{\eta_{n+1}})) = 2\pi n, \quad n = 2, 3, 4, \dots \quad [17]$$

The third critical value $\eta_3 = 10.949879869826264$, and the fourth critical value $\eta_4 = 17.24976556755863$.

When we set $n = 0.5$ in this equation, i.e. $\tilde{X}(z_1^{**}) = \pi$, we will obtain the same result as Eq. 15.

We can also obtain the same results utilizing the FCP (the red dashed lines) by solving the equations

$$\tilde{X}(z_2^{**}) + 2\pi = z_2^{**} + \eta_{n+1} \sin(z_2^{**}) = 2\pi - \arccos(-\frac{1}{\eta_{n+1}}) + \eta_{n+1} \sin(2\pi - \arccos(-\frac{1}{\eta_{n+1}})) = 2\pi - 2\pi(n-1), \quad n = 0.5, 1, 2, \dots \quad [18]$$

5. The first law of thermodynamics derived from the Langevin equation

We use the framework of stochastic thermodynamics (30–34) to calculate the thermodynamic quantities of the particle from its displacement and velocity obtained from the Langevin dynamics simulation. Mutiplying both sides of Eq. 4 in the main text with dx and then adding $\frac{\partial V(x(t), X(t))}{\partial X} dX$ to both sides yield

$$m\ddot{x}(t)dx + \frac{\partial V(x(t), X(t))}{\partial x} dx + \frac{\partial V(x(t), X(t))}{\partial X} dX = [-m\mu\dot{x}(t) + \xi(t)]dx + \frac{\partial V(x(t), X(t))}{\partial X} dX,$$

which can be reorganized into

$$d[\frac{1}{2}m\dot{x}(t)^2 + V(x(t), X(t))] + [m\mu\dot{x}(t) - \xi(t)]dx = \frac{\partial V(x(t), X(t))}{\partial X} dX.$$

In accordance with the first law of thermodynamics, the first term on the LHS can be identified as the differential internal energy of the particle dU , with $U(t) = \frac{1}{2}m\dot{x}(t)^2 + V(x(t), X(t))$ and the kinetic energy of the particle $K(t) = \frac{1}{2}m\dot{x}(t)^2$. $V(x(t), X(t))$ is still the particle's resultant potential energy. The second term on the LHS can be identified as the differential heat transferred to the heat bath from the particle $dQ = [m\mu\dot{x}(t) - \xi(t)]dx$. And the RHS term can be identified as the differential work done by the driver to the particle $dW = \frac{\partial V(x(t), X(t))}{\partial X} dX = -\kappa[x(t) - X(t)]dX$. Then we can obtain the change of the internal energy ΔU , the heat to the heat baths Q and the work input W by integration:

$$\Delta U = \int_{U(t_0)}^{U(t)} dU = U(t) - U(t_0), \quad [19]$$

$$\begin{aligned} Q &= \int_{x(t_0)}^{x(t)} dQ = \int_{x(t_0)}^{x(t)} [m\mu\dot{x}(t) - \xi(t)] dx \\ &= \int_{x(t_0)}^{x(t)} \left[-\frac{\partial V(x(t), X(t))}{\partial x} - m\ddot{x}(t) \right] dx \\ &= -\int_{t_0}^t \left\{ \kappa[x(t) - v_{dr}t] + \frac{\pi}{a} V_0 \sin\left[\frac{2\pi}{a}x(t)\right] \right\} dx - \int_{t_0}^t d\left[\frac{1}{2}m\dot{x}(t)^2\right], \\ &= -\int_{t_0}^t \left\{ \kappa[x(t) - v_{dr}t] + \frac{\pi}{a} V_0 \sin\left[\frac{2\pi}{a}x(t)\right] \right\} dx - \left[\frac{1}{2}m\dot{x}(t)^2 - \frac{1}{2}m\dot{x}(t_0)^2 \right], \end{aligned} \quad [20]$$

$$\begin{aligned} W &= \int_{x(t_0)}^{x(t)} dW = \int_{X(t_0)}^{X(t)} -\kappa[x(t) - X(t)] dX \\ &= -\int_{t_0}^t \kappa[x(t) - v_{dr}t] v_{dr} dt. \end{aligned} \quad [21]$$

The third equality of Eq. 20 results from Langevin Eq. 4 in the main text. The mid-point rule, i.e. the Stratonovich rule, should be used to discretize the integral in Eq. 20 (30, 34). A brief derivation is given in Sec. 8.C.

6. Appendices for the Results and the Discussion section of the main text

A. The homogeneous low temperature heat bath: stick-slip. When the temperature is low ($\Theta = 0.04$), the fluctuation of the particle is small. In Figure S5, we plot the simulation results for the particle immersed in the homogeneous low temperature $\Theta = 0.04$ at $v_{dr} = 10^{-5}$ m/s. We can also divide one low temperature isothermal cycle into four stages as we have done for the PTSHE in the main text.

The first stage ranges from the beginning of one cycle (D1) to the instant of the FCP [(D3) and the left blue triangle in (A) and (B)]. In this stage there is only one global minimum on the resultant potential curve gradually falling behind the driver center and work is inputted.

The second stage ranges from the instant of the FCP to the cusp instant of the work curve. In this stage there coexist two local minima and an energy barrier between them. The particle is still behind the driver center and work is still inputted.

The third stage ranges from the cusp instant to the instant of the BCP [(D10) and the right blue triangle in (A) and (B)]. In this stage there are still two local minima and the particle has jumped over the barrier and fluctuates around the right local minimum point. The particle is ahead of the driver center so that work is outputted.

The fourth stage ranges from the instant of the BCP to the end of one cycle (D12). In this stage, there is again only one global minimum and the particle is ahead of the driver center so that work is again outputted.

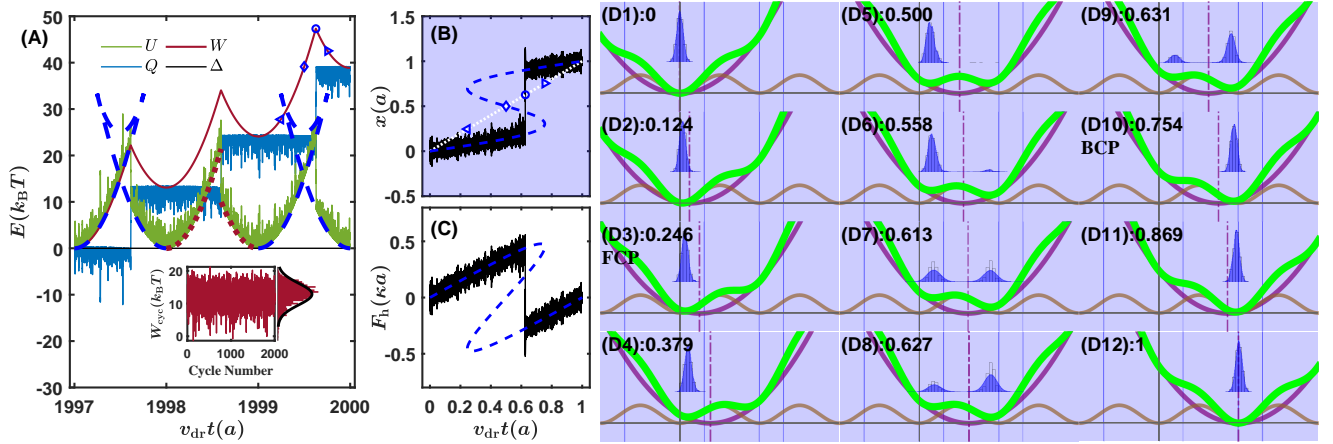


Fig. S5. Simulation results for the particle immersed in the homogeneous low temperature $\Theta = 0.04$. (A) The internal energy U , work input W , heat to the heat bath Q and the difference between them $\Delta = \Delta U + Q - W$ in the last three consecutive low temperature isothermal cycles among 2000 in total at $v_{\text{dr}} = 10^{-5} \text{ m/s}$. The work increases to $+\infty$, i.e. work is inputted. The dashed blue curves are the resultant potential at the balanced points (Sec. 2). The inset of (A) represents the cycle work in 2000 consecutive cycles and its distribution. The x -coordinate $v_{\text{dr}} t(a)$ is the nondimensional position of the driver center, which is proportional to time t . The dimension of the energy is $k_B T$ with k_B the Boltzmann's constant and $T (= \Theta V_0)$ the absolute temperature. The dotted dark red curves indicate the lower bound of the internal energy. $\Delta \equiv 0$ indicates the first law of thermodynamics (Sec. 5). (B) The displacement of the particle in the typical 2000th homogeneous low temperature isothermal cycle with respect to the driver center's position, relative to the starting point of the cycle. The dotted white line represents the driver center's position with respect to itself. The dashed blue curve is the loci of the balanced point (Figure S3). The blue background represents the homogeneous low temperature. (C) The variation of harmonic force in the 2000th cycle. The x -coordinate matches that of (B). Time ratio of minus harmonic force in one cycle is smaller than that of plus one, consistent with the work input. The dashed blue curve is the balanced harmonic force at the balanced point (Figure S3). (D1)-(D12) Diagrams of the shapes of the resultant potential and the corresponding displacement distributions of the particle at different instants of the homogeneous low temperature isothermal cycle. The displacement distribution at a certain instant relative to the latest cycle starting point is obtained from the total 2000 simulation cycles. The decimal following the id of each frame is the nondimensional position of the driver center (or the nondimensional instant) relative to the cycle starting point (D1). The purple curve represents the moving harmonic potential and the brown one represents the lattice potential. The blue background represents the homogeneous low temperature. In (D6)-(D9), although the particle's displacement distribution obtained from the total 2000 simulation cycles disperses around both of the two local minimum points, in terms of a specific cycle, the particle only stays around one of the two local minimum points, which can be seen in (B) where the jumping-back-and-forth events between the two local minimum points are rare. This is an indicator of nonequilibrium in such a low temperature at such a relatively high velocity (see the text). Such a low temperature leads to the low fluctuation of the particle so that it hardly jumps over the energy barrier until the forward barrier is low enough. Therefore, in (D4) and (D5), although there are two resultant potential local minima, the particle's position nearly all distributes nearby the left local minimum point. And in (D6), even though the right local minimum is lower than the left one, the particle still tends to distribute around the left one. The relatively high driving velocity leads to the particle unable to arrive at equilibrium state. For instance, in (D7) even though the right local minimum is lower than the left one, the particle distributes around the left and right local minimum points approximately equally likely rather than distributing more around the right one. After (D7), the forward energy barrier is low enough for the particle to cross over at this temperature so the particle has a higher probability to stay around the right local minimum point until the appearance of the BCP (D10), where the left local minimum disappears. Parameters: $v_{\text{dr}} = 10^{-5} \text{ m/s}$, $\eta = 3.0$, $\mu = 4 \times 10^4 \text{ s}^{-1}$, $\Theta = 0.04$ and others are in Sec. 8.H.

When the driving velocity is very low so that at each instant the system is at equilibrium state, there will be enough time for the event of jumping back and forth over the middle energy barrier to occur and the displacement distribution of the particle will be proportional to $\exp(-\frac{V}{k_B T})$. Then the cusp will be in the middle of one cycle exactly and no longer that sharp and the cycle work will be zero. In Figure 3(C) in the main text, we can actually see that the $\Theta = 0.04$ curve goes to zero as $v_{\text{dr}} \rightarrow 0$. Nonetheless, we can see from this curve that at $v_{\text{dr}} = 10^{-5} \text{ m/s}$, the cycle work input is much greater than zero, indicating that the particle cannot achieve equilibrium state at such a relatively high driving velocity in such a low temperature. In other words, due to the small fluctuation in the low temperature and the relatively high driving velocity, the particle won't be able to go over the high forward energy barrier until it is low enough and it rarely jumps back and forth between the two wells. The latter can be seen in Figure S5(B) where the lanching from the left minimum point to the right one nearby the blue circle ($v_{\text{dr}} t/a = 0.613a$) is sharp and there is nearly no jumping back and forth, while the former can be concluded from that in all the 2000 simulation cycles the particle almost never crosses over the energy barrier before the middle of one cycle, cf. Figure S5(D5), and not until $v_{\text{dr}} t/a = 0.613$ [Figure S5(D7)] will the particle distribute approximately equally likely around either (not both) of the two local minima. As in the PTSHE, the jumping instant is stochastic and ranges approximately from the middle of one cycle [Figure S5(D5)] to before the BCP [Figure S5(D10)].

At the instant of the cusp, when the particle slips, the internal energy U falls off a cliff while the released heat Q lanches over a cliff, so that the high potential energy around the left local minimum transforms into the low potential energy around the right local minimum and kinetic energy. Then most of the kinetic energy dissipates into heat quickly because of damping.

We can see that a main difference between the PTSHE and the homogeneous low temperature heat bath case is whether the instant of the cusp is before or after the middle of one cycle.

As in such low temperature and at such a relatively high velocity the jumping-back-and-forth events are rare and the particle's distribution nearly always centered at one of the local (or at the global) minimum point(s), the shape of the work curves is nearly the same as that of the resultant potential energy local minimum branches, cf. Sec. 6.C.

B. The homogeneous high temperature heat bath: thermolubricity. When the temperature is homogeneous and high ($\Theta = 0.4$) and the driving velocity is low ($v_{dr} = 10^{-5}$ m/s), the particle tends to be at thermal equilibrium state at each instant, because in such a high temperature the particle's acute fluctuation leads to its easily crossing over the energy barrier to achieve equilibrium quickly, which is quicker than the driver's moving forward at such a relatively low driving velocity. So in the homogeneous high temperature $\Theta = 0.4$ case, $v_{dr} = 10^{-5}$ m/s is a relatively low driving velocity rather than a high one compared with the homogeneous low temperature $\Theta = 0.04$ case in the last subsection. As we have mentioned in the last subsection, at equilibrium the particle's displacement obeys the Boltzmann distribution and is proportional to $\exp(-\frac{V}{k_B T})$ which can be verified in Figure S6(D1)-(D12). As $v_{dr} \rightarrow 0$, the particle is at equilibrium at each instant so that the isothermal cycle is reversible and the work input in the forward direction is the same as the work output in the reversed direction. And because of the symmetry of the forward and the reversed cycle, the work curve in one cycle is symmetric about the middle so that the low velocity limit of the mean cycle work is zero as can be verified in Figure 3(C) in the main text.

In fact $v_{dr} = 10^{-5}$ m/s is still not low enough so that the standard deviations of W_{cyc} is not very small as can be seen in the inset of Figure S6(A) and Figure S41. When the temperature is high, the mean cycle work and thus the mean friction force can achieve near-zero at a relatively low driving velocity. This effect is thermolubricity (35).

When the driving velocity goes to zero, the isothermal cycle is reversible and the work input is zero. On the other hand, when the driving velocity is finite, the isothermal cycle is irreversible so that the work input is nonzero. So the second law of thermodynamics is obeyed.

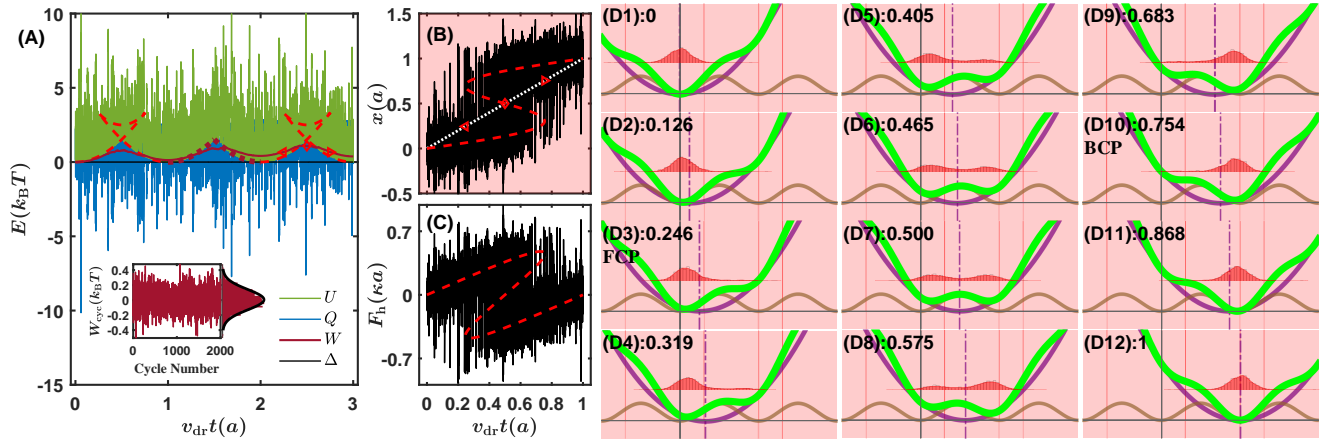


Fig. S6. Simulation results for the particle immersed in the homogeneous high temperature $\Theta = 0.4$. (A) The internal energy U , work input W , heat to the heat bath Q and the difference between them $\Delta = \Delta U + Q - W$ in the last three consecutive high temperature isothermal cycles among 2000 in total at $v_{dr} = 10^{-5}$ m/s. The dashed red curves are the resultant potential at the balanced points (Sec. 2). The inset of (A) represents the cycle work in 2000 consecutive cycles and its distribution. The mean cycle work is approximately zero. The x -coordinate $v_{dr}t(a)$ is the nondimensional position of the driver center, which is proportional to time t . The dimension of the energy is $k_B T$ with k_B the Boltzmann's constant and $T(= \Theta V_0)$ the absolute temperature. The dotted dark red curves indicate the lower bound of the internal energy. $\Delta \equiv 0$ indicates the first law of thermodynamics (Sec. 5). (B) The displacement of the particle in the typical 2000th homogeneous high temperature isothermal cycle with respect to the driver center's position, relative to the starting point of the same cycle. The dotted white line represents driver center's position with respect to itself. The dashed red curve is the loci of the balanced point (Figure S3). The red background represents the homogeneous high temperature. Because of the violent fluctuation of the particle in such a high temperature, once getting through the FCP (the left triangle) the particle's shuttling between the two resultant potential local minimum points begins and then becomes even intense because of the forward energy barrier getting lower with the driver center moving forward. Nearby the middle instant of one cycle, the shuttling reaches its peak and then it recedes because of the rising again of the backward energy barrier until the instant of the BCP (the right triangle). (C) The variation of harmonic force in the 2000th cycle. The x -coordinate matches that of (B). Ratio of time of minus harmonic force in one cycle is approximately equal to that of the plus one, consistent with the near-zero mean cycle work. The dashed red curve is the balanced harmonic force at the balanced point (Figure S3). The amplitude of the oscillation of the harmonic force is larger than that of the PTSHE and that of the homogeneous low temperature case. And it is even doubled around the middle instant of one cycle because of the violent shuttling of the particle between the two local minimum points. (D1)-(D12) Diagrams of the shapes of the resultant potential and the corresponding displacement distributions of the particle at different instants of the homogeneous high temperature isothermal cycle. The displacement distribution at a certain instant relative to the latest cycle starting point is obtained from the total 2000 simulation cycles. The decimal following the id of each frame is the nondimensional position of the driver center (or the nondimensional instant) relative to the starting point of the cycle (D1). The purple curve represents the moving harmonic potential and the brown one represents the lattice potential. The red background represents the homogeneous high temperature. In the homogeneous high temperature isothermal cycle case the shuttling process begins almost immediately the right potential local minimum appears at the instant of the FCP and won't end until the left potential local minimum disappears at the instant of the BCP. When the particle fluctuates around the left local minimum point, it is on average behind the driver center and the driver pulls it and does work on it, while when it oscillates around the right local minimum point, it is on average ahead of the driver center so that it pulls the driver and outputs work. Shortly after the appearance of the right local minimum, the particle is in high probability on the left local minimum and there is work input to the particle as a whole. Whereas, as the driver is moving forward to the right, the left local minimum is going up and the right local minimum is going down. So the particle is more and more likely to stay around the right local minimum point and less and less likely to stay around the left local minimum point [(D4)-(D6)]. As a result, the work consumed by the particle gradually gets less and that outputted by it gradually gets more, which leads to descending slope of the work curve in (A). When the work input and output of the particle are balanced, the slope of the work curve will be zero, which won't happen until the driver moves close to the middle of one cycle ($v_{dr}t = \frac{1}{2}a$) when the two potential local minima are equal (D7). As the driver continues to move forward and the local minimum on the left goes up while the right one goes down, the particle oscillates around the right local minimum point with higher probability and is more likely to pull the driver. Thus the work done by the particle to the driver is more than that done by the driver to the particle and the particle outputs work in total. The work output of the particle increases and the input decreases due to the lowering of the right resultant potential local minimum and the highening of the left one, leading to the absolute slope of the work curve increasing until around the instant of the BCP. Parameters: $v_{dr} = 10^{-5}$ m/s, $\eta = 3.0$, $\mu = 4 \times 10^4$ s $^{-1}$, $\Theta = 0.4$ and others are given in Sec. 8.H.

At low enough driving velocity so that the particle is nearly at equilibrium at each instant, the homogeneous high temperature

isothermal cycle can also be divided into four stages.

The first stage ranges from the starting point of one cycle [Figure S6(D1)] to the instant of the FCP [Figure S6(D3) and the left red triangle in Figure S6(A) and (B)]. In this stage there is only one global minimum on the resultant potential curve and on average the driver center is ahead of the particle so that work is done by the driver to the particle. The mean value point of the particle's displacement distribution, which is approximately Boltzmann's distribution and proportional to $\exp(-\frac{V}{k_B T})$, gradually gets nearer to the driver center and farther away from the global minimum point so that the work curve gradually gets lower than the dashed red balanced resultant potential curve, cf. Sec. 6.C.

The second stage ranges from the instant of the FCP to the maximum instant of the work curve of one cycle, which approximately coincides with the middle instant of one cycle [Figure S6(D7) and the red diamond in Figure S6(A) and (B)]. In this stage there are two local minima and an energy barrier between them. The particle's displacement distribution has two peaks and the left one is higher than the right one so that the mean displacement is between the left local minimum point and the driver center and gradually approaches the driver center as the left local minimum gets higher and the right one gets lower, with the driver moving forward. At the middle instant the two local minima are equal in height so that the two peaks of the displacement distribution are of the same height and the mean displacement are around the driver center. Afterwards the mean displacement is ahead of the driver center. Therefore, before the middle of one cycle, work is inputted and after the middle of one cycle, work is outputted so that there is a maximum on the work curve nearby the middle instant. When the driving velocity goes to zero, the maximum point will be at the middle instant of the cycle exactly.

The third stage ranges from the maximum instant of the work curve of one cycle to the instant of the BCP [Figure S6(D10)]. In this stage, there are still two local minima and one energy barrier between them. The displacement distribution has two peaks, the left of which gradually gets lower than the right one until it vanishes at the BCP instant. The mean displacement is ahead of and gradually gets farther away from the driver center so that the work curve goes down and its absolute slope gets larger.

The fourth stage ranges from the instant of the BCP to the end of one cycle [Figure S6(D12)]. In this stage, there is again one global minimum and one displacement distribution peak. The mean displacement is between the driver center and the global minimum point so that work is still outputted. As the driver center gradually catches up with the global minimum point and also the mean displacement point (at the end of one cycle the driver center, the global minimum point and the mean displacement point are coincident), the absolute slope of the work output curve decreases to zero.

We have to note that the analysis above and in Figure S6 is qualitative and not very rigorous. It's an interesting problem to find whether the inflection points of the work curve are at the FCP and the BCP instant and the equilibrium mean displacement value at each instant could also be figured out.

C. The similarity of the shape of the work curve and that of the lower bound of the internal energy. The lower bound of the internal energy is on the resultant potential energy minimum branches indicating that the particle frequently relaxes to one of the stable balanced points due to the damping force and because of the stochastic force, the particle can regain kinetic energy and the internal energy will again exceed the local minimum resultant potential energy.

At low velocity, the particle fluctuates around a stable balanced point which is approximately the average position of the particle. At the balanced point $z(\tau)^*$ the driver center's position $\tilde{X}(z(\tau)^*)$ satisfies Eq. 5. Therefore at low velocity the inputted work can be approximated by

$$\begin{aligned}
W(\tau) &\approx \int_{t_0}^t \kappa [X(x(t)^*) - x(t)^*] dX(x(t)^*) \\
&= \int_{\tau_0}^{\tau} \kappa a^2 [\tilde{X}(z(\tau)^*) - z(\tau)^*] d\tilde{X}(z(\tau)^*) \\
&= \int_{\tau_0}^{\tau} \kappa a^2 \eta \sin(z(\tau)^*) d[z(\tau)^* + \eta \sin(z(\tau)^*)] \\
&= \kappa a^2 \eta [-\cos(z(\tau)^*) + \cos(z(\tau_0)^*)] + \kappa a^2 \eta^2 \frac{1}{2} [\sin^2(z(\tau)^*) - \sin^2(z(\tau_0)^*)] \\
&= \kappa a^2 \eta [-\cos(z(\tau)^*) + \cos(z(\tau_0)^*)] + \kappa a^2 \eta^2 \frac{1}{2} \left\{ \left[\frac{1}{\eta} (\tilde{X}(z(\tau)^*) - z(\tau)^*) \right]^2 - \sin^2(z(\tau_0)^*) \right\} \\
&= \frac{1}{2} \kappa a^2 [\tilde{X}(z(\tau)^*) - z(\tau)^*]^2 + \kappa a^2 \eta [1 - \cos(z(\tau)^*)] + \kappa a^2 \eta [-1 + \cos(z(\tau_0)^*)] - \frac{1}{2} \kappa a^2 \eta^2 \sin^2(z(\tau_0)^*) \\
&= \kappa a^2 \tilde{V}(z(\tau)^*, \tilde{X}(z(\tau)^*)) + \kappa a^2 \eta [-1 + \cos(z(\tau_0)^*)] - \frac{1}{2} \kappa a^2 \eta^2 \sin^2(z(\tau_0)^*) \\
&= C_1 \tilde{V}(z(\tau)^*, \tilde{X}(z(\tau)^*)) + C_2,
\end{aligned} \tag{22}$$

where C_1 and C_2 are constants. Therefore the shape of the work curve and that of the resultant potential energy local minimum branch are similar.

Intuitively, when the driver center moves forward ahead of the particle, the particle fluctuates around the left local minimum point of the resultant potential energy which goes forward and upward, so the work done on the particle is transformed into its potential energy. On the other hand, when the driver center moves forward behind the particle, the particle fluctuates around

the right local minimum point of the resultant potential energy which goes forward and downward so the potential energy is transformed into work output. The latter is analogous to the free falling body transforming its gravity potential energy into kinetic energy which can be utilized to do work, and of course here the particle is not free.

D. The high velocity limit of the mean cycle work. Here we give a derivation of the high velocity limit of the mean cycle work. The nonlinear Langevin equation 4 in the main text can be reformulated into

$$m\ddot{x}(t) + m\mu\dot{x}(t) + \kappa[x(t) - v_{\text{dr}}t] + \frac{\pi}{a}V_0 \sin\left(\frac{2\pi}{a}x(t)\right) - \xi(t) = 0. \quad [23]$$

At very high driving velocity v_{dr} , the damping force $m\mu\dot{x}(t)$ dominates on the LHS, so that we can omit the inertia force $m\ddot{x}(t)$, the lattice force $\frac{\pi}{a}V_0 \sin\left(\frac{2\pi}{a}x(t)\right)$ and the fluctuation force $\xi(t)$. Then, Eq. 23 can be approximated by

$$m\mu\dot{x}(t) + \kappa[x(t) - v_{\text{dr}}t] = 0, \quad [24]$$

i.e.

$$-\kappa[x(t) - v_{\text{dr}}t] = m\mu\dot{x}(t). \quad [25]$$

Then we can calculate the work through

$$W = - \int_{t_0}^t \kappa[x(t) - v_{\text{dr}}t] v_{\text{dr}} dt = \int_{t_0}^t m\mu\dot{x}(t) v_{\text{dr}} dt = m\mu v_{\text{dr}} \int_{t_0}^t dx(t) = m\mu v_{\text{dr}} [x(t) - x(t_0)]. \quad [26]$$

And the mean cycle work at high velocity can be calculated by

$$\langle W_{\text{cyc, hvlim}} \rangle = m\mu v_{\text{dr}} [\langle x(t_0 + \frac{a}{v_{\text{dr}}}) \rangle - x(t_0)] = m\mu v_{\text{dr}} a, \quad [27]$$

which is linear with v_{dr} .

Note that at the high driving velocity limit, the time range of one engine cycle is small so that we can neglect the fluctuation force $\xi(t)$, which has a low probability to achieve very high value in such a short period. However, at the low driving velocity limit, the time range of one engine cycle is large and the fluctuation force $\xi(t)$ has a high probability to achieve very high value. Then we cannot omit $\xi(t)$. When the damping coefficient μ is large, we can still omit the inertia force $m\ddot{x}(t)$ and obtain the overdamped Langevin equation

$$m\mu\dot{x}(t) + \kappa[x(t) - v_{\text{dr}}t] + \frac{\pi}{a}V_0 \sin\left(\frac{2\pi}{a}x(t)\right) - \xi(t) = 0. \quad [28]$$

E. The equilibrium limit of the mean cycle work approximated by the potential mechanism. At equilibrium in the classical limit, we assume the probability distribution of the particle's energy E relative to its resultant potential energy local minimum has a Boltzmann distribution (36)

$$p_E = \frac{1}{k_B T} \exp\left(-\frac{E}{k_B T}\right). \quad [29]$$

We also assume that on the left of the energy barrier peak point [Figure 3(A2) in the main text and Figure S7], the heat bath is of high temperature and on the right of the energy barrier peak point, the heat bath is of low temperature, which is different from the periodic alternative high and low temperature heat bath of the PTSHE. In the hot zone, the probability of the particle jumping forward over the energy barrier can be approximated (36) by

$$\begin{aligned} P_h(E > \Delta V_h) &= \int_{\Delta V_h}^{+\infty} p_E dE \\ &= \int_{\Delta V_h}^{+\infty} \frac{1}{k_B T_h} \exp\left(-\frac{E}{k_B T_h}\right) dE \\ &= \exp\left(-\frac{\Delta V_h}{k_B T_h}\right), \end{aligned} \quad [30]$$

and that of the particle jumping backward over the energy barrier from the cold zone to the hot one can be approximated by

$$\begin{aligned} P_c(E > \Delta V_c) &= \int_{\Delta V_c}^{+\infty} p_E dE \\ &= \int_{\Delta V_c}^{+\infty} \frac{1}{k_B T_c} \exp\left(-\frac{E}{k_B T_c}\right) dE \\ &= \exp\left(-\frac{\Delta V_c}{k_B T_c}\right). \end{aligned} \quad [31]$$

At the average cusp instant of the work curve, the probabilities of the particle jumping forward and backward over the energy barrier satisfy

$$P_h(E > \Delta V_h) = P_c(E > \Delta V_c), \quad [32]$$

i.e.

$$\exp\left(-\frac{\Delta V_h}{k_B T_h}\right) = \exp\left(-\frac{\Delta V_c}{k_B T_c}\right), \quad [33]$$

leading to Eq. 3 in the main text. The equilibrium limit of the mean cycle work

$$W_{\text{cyc,e.p.}} = \Delta V_h - \Delta V_c. \quad [34]$$

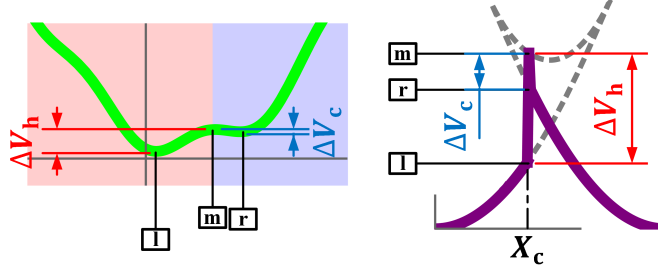


Fig. S7. The schematic of calculating the equilibrium limit of the mean cycle work $W_{\text{cyc,e.p.}}$. In the left subfigure, the green curve represents the resultant potential at the cusp instant when the driver center is at X_c . l, m, r represents the left local minimum, the middle local maximum and the right local minimum respectively. The red and blue backgrounds represent the high and low temperature heat baths respectively. In the right subfigure, the dashed gray curve represents the resultant potential at its local extremum points. The solid purple curve represents the resultant potential energy at the local minimum points passed through by the particle, with the vertical line at X_c representing the particle jumping from the hot zone to the cold one.

It is shown in the inset of Figure 3(A2) and (A3) in the main text and Figure S7 that at the average cusp instant when the driver center is at \tilde{X}_c the two local minima points z_l , z_r and the local maximum point z_m satisfy

$$\begin{aligned} \frac{\partial \tilde{V}}{\partial z}(z_l) &= z_l - \tilde{X}_c + \eta \sin(z_l) = 0, \\ \frac{\partial \tilde{V}}{\partial z}(z_m) &= z_m - \tilde{X}_c + \eta \sin(z_m) = 0, \\ \frac{\partial \tilde{V}}{\partial z}(z_r) &= z_r - \tilde{X}_c + \eta \sin(z_r) = 0, \end{aligned} \quad [35]$$

(c.f. Eq. 2) and the nondimensional $\Delta \tilde{V}_h$ and $\Delta \tilde{V}_c$ can be calculated by

$$\begin{aligned} \Delta \tilde{V}_h &= \tilde{V}(z_m) - \tilde{V}(z_l), \\ \Delta \tilde{V}_c &= \tilde{V}(z_m) - \tilde{V}(z_r). \end{aligned} \quad [36]$$

Considering Eq. 3 in the main text (or Eq. 34), we obtain the equation system

$$\begin{cases} \tilde{V}(z_m) - \tilde{V}(z_l) = \frac{\Theta_h}{\Theta_c} [\tilde{V}(z_m) - \tilde{V}(z_r)], \\ z_l - \tilde{X}_c + \eta \sin(z_l) = 0, \\ z_m - \tilde{X}_c + \eta \sin(z_m) = 0, \\ z_r - \tilde{X}_c + \eta \sin(z_r) = 0, \end{cases} \quad [37]$$

which can be solved by a nonlinear solver with the ranges of z_l , z_m and z_r being

$$\begin{cases} z_l & \in (0, \arccos(-1/\eta)), \\ z_m & \in (\arccos(-1/\eta), 2\pi - \arccos(-1/\eta)), \\ z_r & \in (2\pi - \arccos(-1/\eta), 2\pi), \end{cases} \quad [38]$$

c.f. Sec. 2.

Therefore we can get z_l , z_r and z_m and then $\Delta \tilde{V}_h$ and $\Delta \tilde{V}_c$. So the equilibrium limit of the mean cycle work approximated by the potential mechanism

$$W_{\text{cyc,e.p.}} = \frac{m\omega_0^2 a^2}{4\pi^2} (\Delta \tilde{V}_h - \Delta \tilde{V}_c). \quad [39]$$

As the ratio $\frac{T_h}{T_c} = \frac{\Theta_h}{\Theta_c} \rightarrow +\infty$ so that $\frac{\Delta V_h}{\Delta V_c} \rightarrow +\infty$ (the main text Eq. 3), we can see from Figure S7 that the jumping point $X_c \rightarrow \tilde{X}(z_2^{**})$, cf. Figure S1(B). Then both z_r and z_m go to $z_2^{**} = 2\pi - \arccos(-\frac{1}{\eta})$ (Eq. 8) and in the limit z_l satisfies

$$z_l - \tilde{X}(z_2^{**}) + \eta \sin(z_l) = 0, \quad [40]$$

with $\tilde{X}(z_2^{**}) = z_2^{**} + \eta \sin(z_2^{**})$ and $z_l \in (0, \arccos(-1/\eta))$. Solve this equation with a nonlinear solver we can get the limit of z_l , and then we can obtain the limit of $W_{\text{cyc,e.p.}}$ as $\frac{\Theta_h}{\Theta_c} \rightarrow +\infty$ by Eq. 39. This limit is an upper bound of $W_{\text{cyc,e.p.}}$.

At $\eta = 2, 3$ and 4 , as $\frac{\Theta_h}{\Theta_c} \rightarrow +\infty$,

$$-W_{\text{cyc,e.p.}} \rightarrow -1.05k_B T_h, -2.96k_B T_h \text{ and } -5.15k_B T_h, \quad [41]$$

respectively with $k_B T_h = 0.4 \frac{3m\omega_0^2 a^2}{2\pi^2}$ the same as that of the main text Figure 5(A) and the three limits are what the three corresponding dot-dashed curves in the main text Figure 5(A) go to as $\Theta_h \rightarrow +\infty$. At $\eta = 1$, $-W_{\text{cyc,e.p.}} \equiv 0$.

F. The reason for the higher work output at $\eta = 2$ and $\eta = 1$ than the potential mechanism approximation.

F.1. The case of $\eta = 2$. In Figure 4 of the main text, we plot the energy and displacement curves of the particle at $v_{\text{dr}} = 10^{-7} \text{ m/s}$ for the case of $\eta = 2$. Comparing with the results at $v_{\text{dr}} = 10^{-7} \text{ m/s}$, we can see that the nonequilibrium features are evident at $v_{\text{dr}} = 10^{-5} \text{ m/s}$ in Figure S8. The cusp of the work curve is sharper and there is a short cliff on the heat curve [Figure S8(A)] and also on the internal energy [Figure S8(A)], the displacement [Figure S8(B)] and the harmonic force [Figure S8(C)] curves. The standard deviation is finite (although not very large) as can be seen in the inset of Figure S8(A).

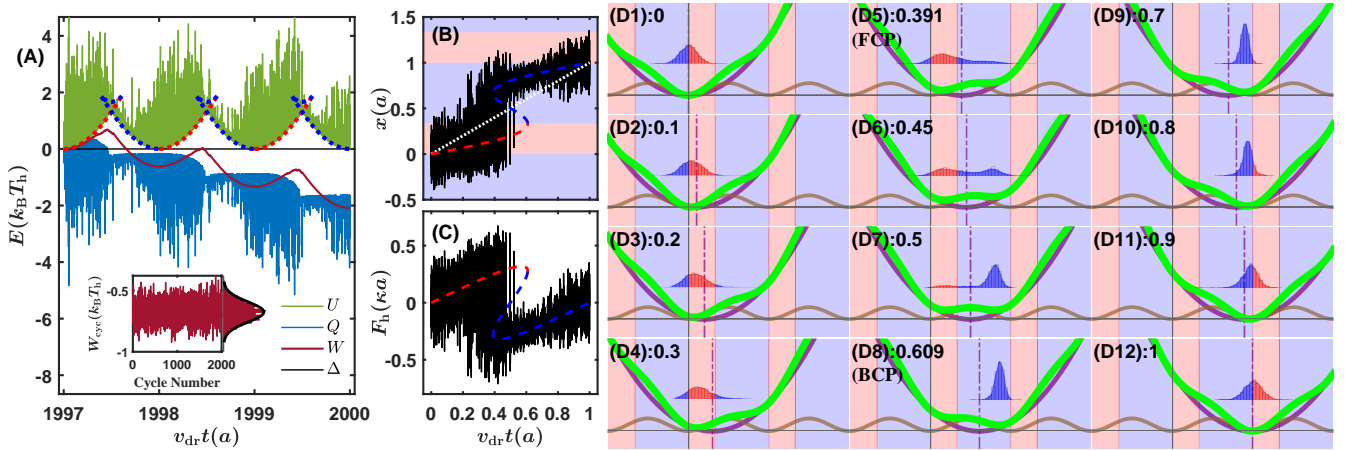


Fig. S8. The simulation results of the case of $\eta = 2$, $\mu = 4 \times 10^4 \text{ s}^{-1}$, $\Theta_{h,c} = 0.6, 0.06$ at $v_{\text{dr}} = 10^{-5} \text{ m/s}$. The layout of this figure is similar to that of the main text Figure 2. The colors and types of the curves are the same as those in the main text Figure 2. The temperature T_h in the dimension $k_B T_h$ is the same as that in the main text Figure 3. In the typical 2000th engine cycle, the heat Q absorbed before the cliff instant is of a large amount and larger than that absorbed at the cliff instant, cf. (A). Because of the relatively flat resultant potential resulting from the relatively flat lattice potential, the particle oscillates in a large spatial range even before the FCP occurs and frequently goes ahead of the driver center [(B) and (D3)-(D5)]. So besides the amount of work output transformed from the potential energy, which is mainly converted from the heat absorbed at the cliff instant, a large amount of kinetic energy, which is converted from the heat absorbed in the hot zone before the cliff instant, is transformed into the particle's potential energy, resulting in the work input being reduced, cf. the main text. And this amount of reduced work input is relatively more significant than that of the high η cases at the same absolute temperature, where the particle's crossing over the middle energy barrier happens less frequently because of the higher energy barrier. Other parameters are given in Sec. 8.H.

As we have mentioned in the main text, the advantage of the nonequilibrium (or quasi-equilibrium) results at $v_{\text{dr}} = 10^{-5} \text{ m/s}$ is that we can get the displacement distribution of the particle benefited from the less simulation time steps in one cycle. The displacement distribution at $v_{\text{dr}} = 10^{-5} \text{ m/s}$ in Figure S8(D1)-(D12) can be treated as an approximation of the equilibrium displacement distribution. We can see that before the mean cusp instant [(D1)-(D6)] the particle's displacement distribution is divergent and a large part is ahead of the driver center, resulting in that the average position of the particle is farther away from the left global or local minimum point and nearer to the driver center so that the work curve gets lower than dotted red curve in (A), cf. Sec. C. On the other hand, after the cusp instant, the particle's displacement distribution is convergent and the average displacement is close to the right local or global minimum point [(D8)-(D10)]. So the work curve is similar to the dotted blue curve in (A).

F.2. The case of $\eta = 1$. In Figure S9(D1)-(D12), we can see the resultant potential at $\eta = 1$ has only one global minimum and no energy barrier. At the starting point of one cycle (D1), the resultant potential is symmetric and then becomes asymmetric. Before the middle of one cycle (D7), the resultant potential is steeper on the left and flatter on the right of the global minimum and as the driver goes forward, the bottom of the resultant potential curve gets flatter and flatter. Therefore in the hot zone during the first half of one cycle, the particle distributes more and more dispersedly. After $v_{\text{dr}} t/a = 0.5$, the distribution of the particle's position shrinks quickly and at $v_{\text{dr}} t/a = 0.6$ (D8) it distributes around the global minimum in the cold zone and is almost all ahead of the driver center. When approaching to the end of one cycle, the particle's displacement distribution expands again because of its frequently traversing to the hot zone in the next lattice period.

In Figure S9(B), we can see that after the middle of one cycle, the fluctuation amplitude of the particle reduces due to the damping force and also the small stochastic force in the cold zone, which can only maintain a small fluctuation amplitude of

the particle. From (D7) to (D8), we can also see that after the middle instant the particle's displacement distribution shrinks. Small fluctuation and convergent displacement distribution indicate small kinetic energy and the amount of declined kinetic energy is dissipated into heat. So the upper bound of the heat curve ascends. On the other hand, shortly after the middle instant, the particle's high kinetic energy resulting from its frequently traversing backwards through the hot zone leads to its average displacement point nearly overlapping with the driver center so that the work curve stays almost unchanged. In this period, the potential energy of the particle decreases. As the work output is nearly zero, the reduced potential energy is transformed into kinetic energy and the kinetic energy is transformed into heat, which also contributes to the ascent of the upper bound of the heat curve. As the driver continues to move forward, the particle goes deep into the cold zone and its displacement distribution shrinks with the average value point catches up with the global minimum point (D8). So the work curve gradually decreases and its slope increases and becomes similar to that of the dotted blue balanced resultant potential curve. Afterwards, the upper bound of the heat curve stays constant and the kinetic energy and the heat transforms into each other interactively. The work curve is parallel to the balanced resultant potential curve so the potential energy gradually transforms into work output.

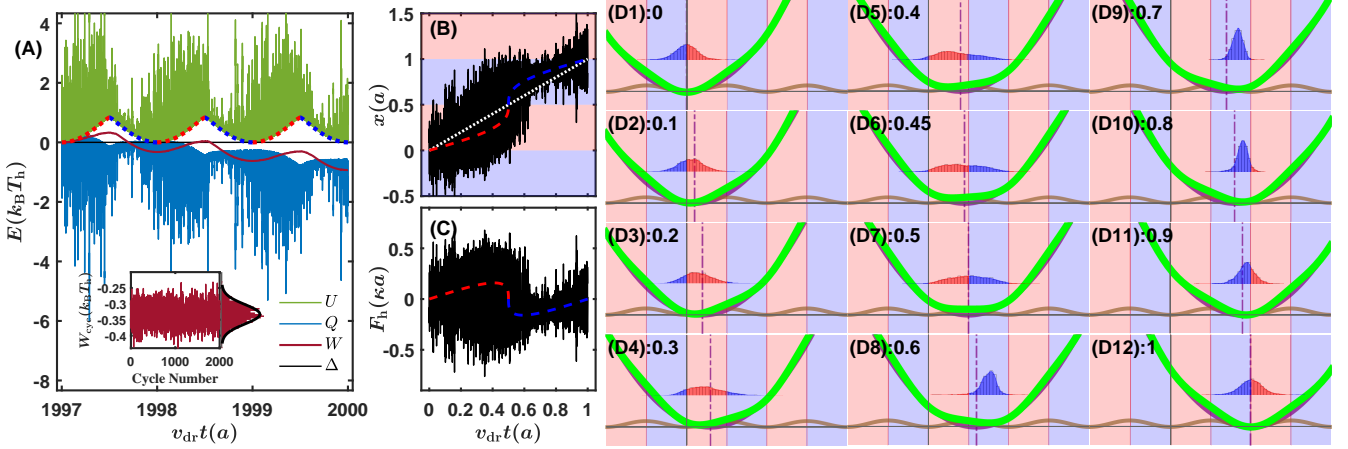


Fig. S9. The simulation results of the case of $\eta = 1$, $\mu = 4 \times 10^4 \text{ s}^{-1}$, $\Theta_{h,c} = 1.2, 0.12$ at $v_{dr} = 10^{-5} \text{ m/s}$. The layout of this figure is similar to that of the main text Figure 2. The colors and types of the curves are the same as those in the main text Figure 2. The temperature T_h in the dimension $k_B T_h$ is the same as that in the main text Figure 3. Other parameters are given in Sec. 8.H.

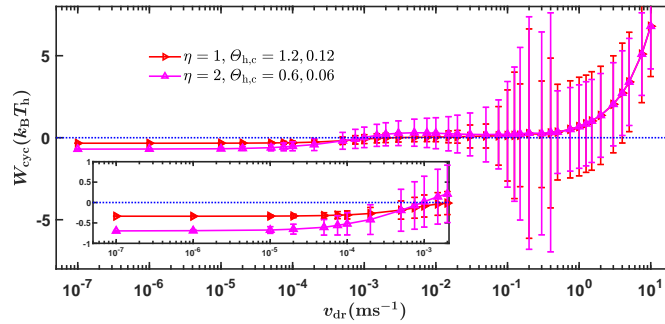


Fig. S10. The standard deviations of W_{cyc} of the cases of $\eta = 1$ and $\eta = 2$ in Figure 3(B) in the main text. Because of the higher $\Theta_{h,c}$ in the $\eta = 1$ case and there being no energy barrier resulting in that the particle relaxing to equilibrium more quickly, the standard deviations on the low velocity end are smaller than those of the $\eta = 2$ case. On the high driving velocity end, however, the higher $\Theta_{h,c}$ and no energy barrier make the particle fluctuates in a larger range so that the standard deviations of W_{cyc} are larger in the $\eta = 1$ case. Another special characteristic of the standard deviations at such low η is that the standard deviation has more than one peaks varying with the driving velocity. We can see that there are at least 3 peaks in the $\eta = 1$ case and 2 peaks in the $\eta = 2$ case.

In such high relative temperatures $\Theta_{h,c} = 1.2, 0.12$ and because there is no energy barrier in the $\eta = 1$ case, the nonequilibrium feature at $v_{dr} = 10^{-5} \text{ m/s}$ is not as distinct as the case of $\eta = 2$. The standard deviation is small as can be seen in the insets of Figure S9(A) and Figure S10. Nevertheless we can still see the difference between the results at $v_{dr} = 10^{-7} \text{ m/s}$ (Figure 4 in the main text) and that at $v_{dr} = 10^{-5} \text{ m/s}$ (Figure S9), especially for the displacement curve. Because of the low driving velocity, the particle has enough time to traverse more states and seems to distribute widely and centered at the dotted white line particularly at the beginning and end of the cycle in the bottom left subfigure of the main text Figure 4. Nonetheless, from the work curve we know that the mean displacement point actually deviates from the driver center. Otherwise the slope of the work curve will be zero. When the driving velocity goes to zero, we can imagine that the displacement of the particle should cover the full range of the interval $(-\infty, +\infty)$. So it's necessary to obtain the displacement distribution through e.g.

the Fokker-Planck or Kramers equation method (37) which may avoid the excessive computing resource and time cost of the Langevin dynamics simulation.

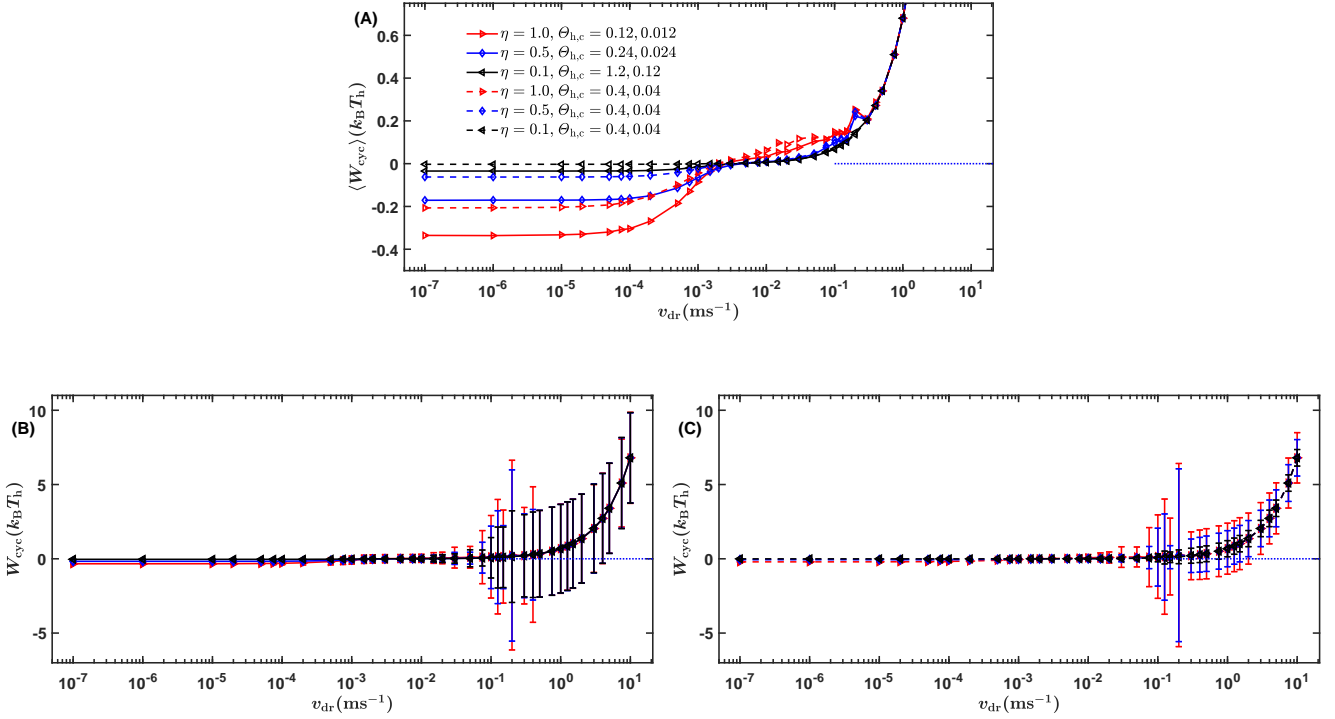


Fig. S11. Simulation results at $\eta \leq 1$. Here $\mu = 4 \times 10^4 \text{ s}^{-1}$ and three of the six cases are of the same absolute high and low temperature $T_{h,c}$ and the other three are of the same nondimensional high and low temperature $\Theta_{h,c}$. The boundaries of the high and low temperature zones are at the local minimum and maximum points of the lattice potential, i.e. the driver center crosses the boundaries at the beginning, end and middle instants of one engine cycle like that in the case of $\eta = 1$ in Figure S9. The $\langle W_{\text{cyc}} \rangle - v_{\text{dr}}$ curves are plotted in (A) and the standard deviations of W_{cyc} are given in (B) and (C). We can see that with η decreasing, the equilibrium work output decreases too, indicating the necessity of the sinusoidal lattice potential for the PTSHE to output work. In (B) and (C), we can speculate that for the cases of $\eta \leq 1$ at the high driving velocity end, the standard deviation of W_{cyc} is determined by the absolute temperature rather than the nondimensional one, which is not true for the $\eta > 1$ cases, cf. Figure S10 where the absolute temperature for the $\eta = 1$ and $\eta = 2$ cases is the same while the standard deviations at the high driving velocity end are different. We can also see that the standard deviation has more than one peaks in the resonance regime at $\eta < 1$ similar to the cases of $\eta = 1$ and 2 in Figure S10. Other parameters are given in Sec. 8.H.

F.3. The simulation results at $\eta < 1$. In Figure S11, we plot the simulation results at $\eta \leq 1$. Three of them are of the same absolute high and low temperatures while the other three are of the same nondimensional high and low temperatures. For all of these cases, the high and low temperature boundaries are at the local maximum and minimum points of the lattice potential, i.e. the driver center crosses the boundaries at the beginning, end and middle instants of one engine cycle, like that in the case of $\eta = 1$ in Figure S9(D1)-(D12). We can see that as η decreases, the mean cycle work output at the low driving velocity limit decreases too. Because we keep ω_0 constant, the intensity of the lattice potential V_0 decreases proportionally with η . With V_0 decreasing, the resultant potential approaches to the parabola harmonic potential, which is symmetric about its center (i.e. the driver center) during the entire engine cycle. In a symmetric parabola resultant potential, the particle will oscillate around the driver center and distribute ahead of and behind the driver center symmetrically about the middle instant of its going through each high or low temperature zone, from entering to exiting it, so that the particle will neither output nor input work in total at equilibrium in each homogeneous temperature zone. Therefore the cycle work output at equilibrium approaches to zero as η goes to zero. And this conclusion can be generalized to an alternative high and low temperature field with the high and low temperature zones of different length and with an arbitrary phase shift. Therefore it's necessary to have a finite lattice potential for the PTSHE to output work at low driving velocity.

G. The simulation results with the high temperature Θ_h varying for the $\eta = 1, 2, 4$ cases. In Figure S12, we plot the work curves in one cycle corresponding to the $\eta = 1, 2, 4$ cases in the main text Figure 5(A). For the three cases, the shape of the work curve has a varying trend with respect to Θ_h similar to that of the $\eta = 3$ case in the main text Figure 5(B).

For the $\eta = 1$ case, because there is no energy barrier so that the potential mechanism has no effect, the cusp (if there is one) is at the middle instant of the engine cycle exactly. And after the middle instant, the work curve tends to keep nearly unchanged for a short period due to the thermolubricity effect, cf. Sec. 6.F.2. The upmost curve represents the case of $\Theta_h = 0.04 < \Theta_c = 0.12$, from which we can see that in this case the cycle work is positive, i.e. work should be inputted.

For the $\eta = 2$ case, due to the low energy barrier, the cusp (if there is one) shifts to the left more mildly than the $\eta = 3$ case.

For the $\eta = 4$ case, the energy barrier is high and the cusp (if there is one) shifts to the left more violently than the $\eta = 3$

case and the work curve is less smooth. When Θ_h is small, the cusp is sharp because of nonequilibrium, cf. Figure S13(c) and the work curve nearly overlaps with the dotted red curve before the cusp instant, e.g. the upmost $\Theta_h = 0.04$ curve.

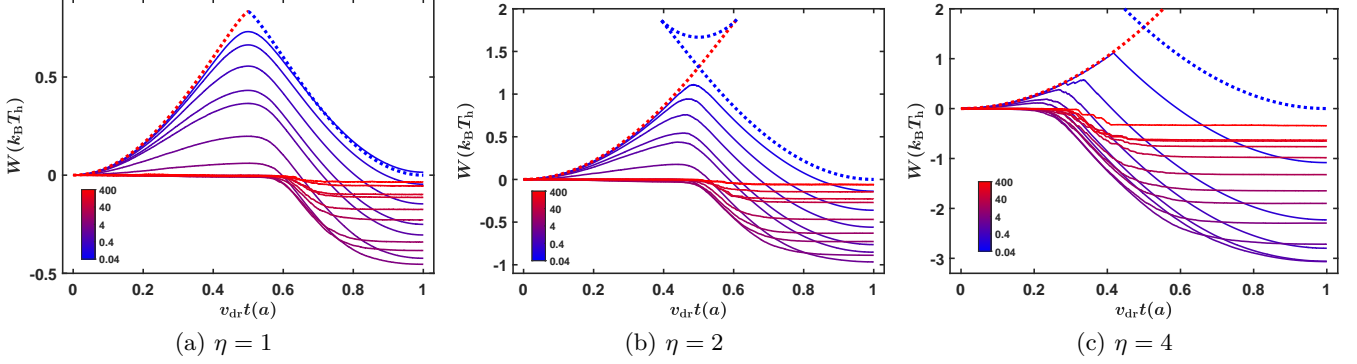


Fig. S12. The work curves in one cycle corresponding to the circles of the $\eta = 1, 2$ and 4 cases in the main text Figure 5(A), with the high temperature Θ_h denoted by the gradually varying color of the curves. The dot-dashed curves represent the resultant potential at the balanced points. Here $k_B T_h$ is equal to that of the $\eta = 3$ case in the main text Figure 5.

In Figure S13, we plot the displacement of the particle in one cycle for the cases of $\eta = 1, 2$ and 4 in the main text Figure 5(A) at four typical Θ_h 's. Because of the higher V_0 value at higher η , the absolute temperature corresponding to $\Theta_h = 40$ is higher at $\eta = 4$ than that at $\eta = 2$ and $\eta = 1$, so that the dark blue curve's range expands when η increases from 1 to 4.

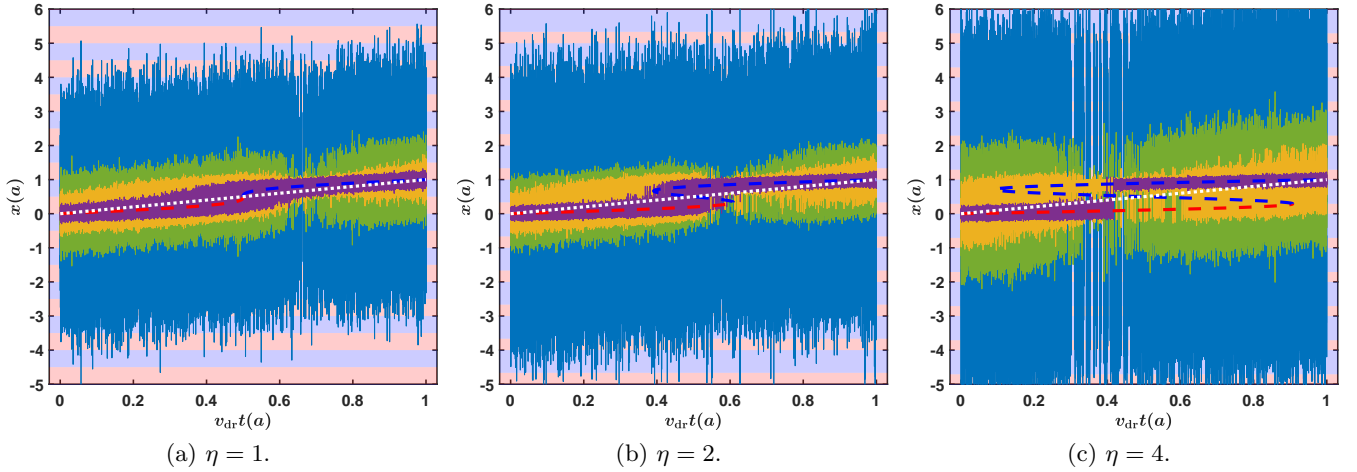


Fig. S13. The displacement of the particle in one cycle for the cases of $\eta = 1, 2$ and 4 in the main text Figure 5(A) at four typical Θ_h 's. The dark blue, dark green, dark yellow and purple curves represent the cases of $\Theta_h = 40, 4, 1, 0.2$ respectively in (a); $40, 2, 0.75, 0.1$ respectively in (b) and $40, 4, 0.75, 0.1$ respectively in (c). The dotted white line denotes the position of the driver center. The dashed red and blue curves represent the position of the balanced point of the resultant potential.

In Figure S14, we plot the probability density distributions of the particle's relative displacement to the driver center $x - v_{dr}t$ in one cycle at four typical Θ_h 's for the cases of $\eta = 1, 2$ and 4 in the main text Figure 5(A). For all the four cases including the $\eta = 3$ case in the main text, as the high temperature Θ_h increases a peak extrudes on the right and with η increasing, the peak's position shifts to the right so that the average value of the distribution and thus the cycle work increases.

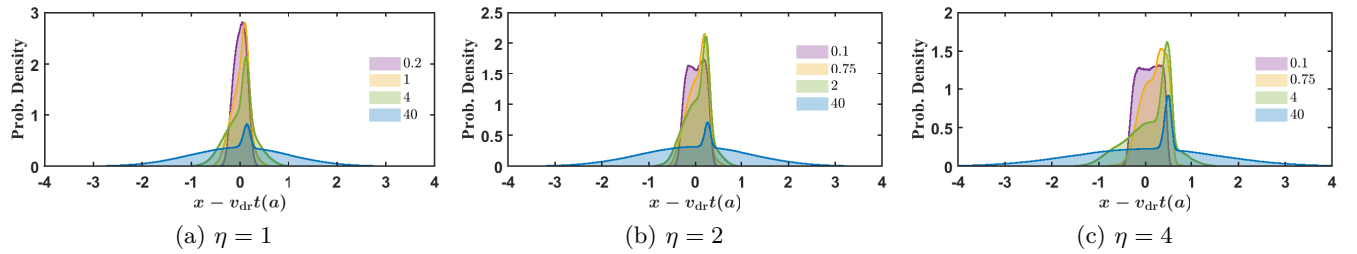


Fig. S14. The probability density distributions of the particle's relative displacement to the driver center $x - v_{dr}t$ in one cycle at four typical Θ_h 's for the cases of $\eta = 1, 2$, and 4 in the main text Figure 5(A).

H. Transition of the energy, displacement and harmonic force during one cycle with the driving velocity. We can map the energy curves' transition with the driving velocity to the change of the $\langle W_{\text{cyc}} \rangle - v_{\text{dr}}$ curve, which is shown in Figure S15. We can see that on the left end of the $\langle W_{\text{cyc}} \rangle - v_{\text{dr}}$ curve where work is outputted, the cusp of the mean work curve (here the mean internal energy curve also has a cusp) during one engine cycle is before the middle instant of the cycle. After the engine stalls the cusp of the mean internal energy curve surpasses the cycle middle instant to the right and the mean cycle work input $\langle W_{\text{cyc}} \rangle$ increases until an extremum, and this is the stick-slip regime.

The insets of Figure S15 are chosen from Figure S16, in which the mean internal energy, mean heat and mean work curves at all the driving velocities of the data points on the $\langle W_{\text{cyc}} \rangle - v_{\text{dr}}$ curve (Table S3) are plotted. The detail of how to calculate the mean values are given in the caption of this figure. For comparison, in Figure S17, we plot the one single cycle internal energy, heat and work curves at all the simulation driving velocities correspondingly. And we also plot the mean displacement curves (Figure S18), the one single cycle displacement curves (Figure S19), the mean harmonic force curves (Figure S20) and the one single cycle harmonic force curves (Figure S21) at all the corresponding simulation driving velocities. These 6 figures are of the case of $\eta = 3.0$, $\mu = 4 \times 10^4 \text{s}^{-1}$ and $\Theta_{h,c} = 0.4, 0.04$ corresponding to the purple $\langle W_{\text{cyc}} \rangle - v_{\text{dr}}$ curve in the main text Figure 3(B). We also give the similar $3 \times 6 = 18$ figures for the 3 homogeneous temperature cases: $\eta = 3.0$, $\mu = 4 \times 10^4 \text{s}^{-1}$ and $\Theta = 0$ [Figure S22, S23, S24, S25 (38), S26 and S27] corresponding to the black curve in the main text Figure 3(C); $\eta = 3.0$, $\mu = 4 \times 10^4 \text{s}^{-1}$ and $\Theta = 0.4$ (Figure S28, S29, S30, S31, S32 and S33) corresponding to the pink curve in the main text Figure 3(C); $\eta = 3.0$, $\mu = 4 \times 10^4 \text{s}^{-1}$ and $\Theta = 0.04$ (Figure S34, S35, S36, S37, S38 and S39) corresponding to the cyan curve in the main text Figure 3(C). From these figures, we can have an overall perspective about the transition of the energy, displacement and harmonic force during one cycle with the driving velocity and make it more clear about the reason for the ups and downs, i.e. different regimes such as the stick-slip regime mentioned above and the velocity weakening and resonance regimes explained below, of the $\langle W_{\text{cyc}} \rangle - v_{\text{dr}}$ curves. A lot of information can be obtained from these figures, and we will mention some in the following paragraphs and some others in the captions of these figures.

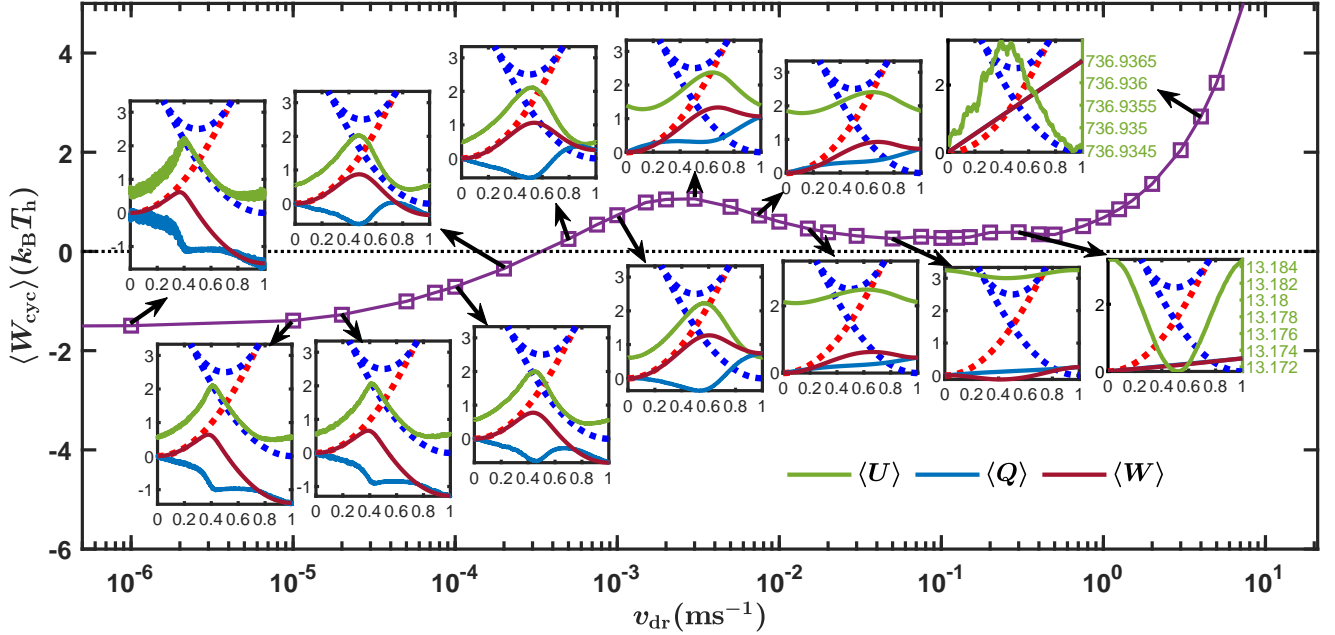


Fig. S15. The transition of the energy curves with the driving velocity. The backbone purple $\langle W_{\text{cyc}} \rangle - v_{\text{dr}}$ curve is the same as the purple one in Figure 3(B) in the main text. The insets give the mean internal energy $\langle U \rangle$, the mean heat to the heat bath $\langle Q \rangle$ and the mean work input to the particle $\langle W \rangle$ during one cycle at the corresponding driving velocities marked by the arrows. These insets are chosen from Figure S16.

It's not easy to recognize the oscillating relaxation process after slipping from the one single cycle displacement or harmonic force curves in Figure S19 and S21 because of the stochastic feature of the single trajectories during one cycle resulting from the finite temperature. We can see that the oscillating relaxation processes at finite temperature is modulated by the stochastic force in Figure S19, S21; Figure S31, S33 and Figure S37, S39. The oscillating relaxation process is more distinct in the homogeneous zero temperature case ($\Theta = 0$, Figure S25 and S27).

From the one single cycle displacement curve of the $\Theta = 0$ case in Figure S25, we can see that as the driving velocity increases before $v_{\text{dr}} = 10^{-3} \text{m/s}$, i.e. the black $\langle W_{\text{cyc}} \rangle - v_{\text{dr}}$ curve's plateau peak point in the main text Figure 3(C), the particle's oscillating relaxation process after slipping gets longer *relative to the driver center* and gradually extends to next cycle. And at $v_{\text{dr}} = 10^{-3} \text{m/s}$ the relative oscillating relaxation process is long enough to arrive at the slip instant of the next cycle and with v_{dr} increasing further the slip instant advances to the left. (We want to emphasize that the x -coordinate is the driver center's nondimensional position $v_{\text{dr}} t / a$, so the displacement curves are relative to the driver center and with the driving

velocity v_{dr} increasing, the oscillating relaxation process gets longer relative to the driver center's position.) The residual kinetic energy from the last cycle is equivalent to a finite temperature heat bath and as the driving velocity increases, the increasing residual kinetic energy from the last cycle increases the effective temperature in the stick process so the particle tends to cross over the middle energy barrier earlier, i.e. slip earlier, resulting in the work input reduced, which is similar to the potential mechanism except that the slip instant is after the middle instant of the cycle. At the same time, the higher effective temperature also leads to the work input reduced further because of the thermolubricity mechanism. On the other hand, the kinetic energy from slipping also results in the increasing effective temperature immediately after slipping so that the work output after the slip instant is also reduced a little due to the negative thermolubricity mechanism, causing the net cycle work input to recover a little from the reduction before the slip instant. Nonetheless, as a whole $\langle W_{cyc} \rangle$ reduces, and after the plateau peak point of the $\langle W_{cyc} \rangle - v_{dr}$ curve, the mean cycle work curve decreases with the driving velocity increasing. This velocity range is the so called velocity weakening regime (39, 40).

As the driving velocity continues to increase so that v_{dr}/a is comparative to the frequency of the particle oscillating around the resultant potential local or global minimum points, the energy, displacement and harmonic force curves are odd (cf. Figure S16-S38) due to the nonlinearity of the PT model, cf. the main text subsection “Bifurcation of Mean Cycle Work with Driving Velocity as Parameter at Zero Temperature”. In this regime resonance occurs and we will refer to it as the resonance regime. After the resonance regime the mean cycle work curve increases linearly due to the so large damping force, cf. the main text Figure 3(A) and Sec. 6.D.

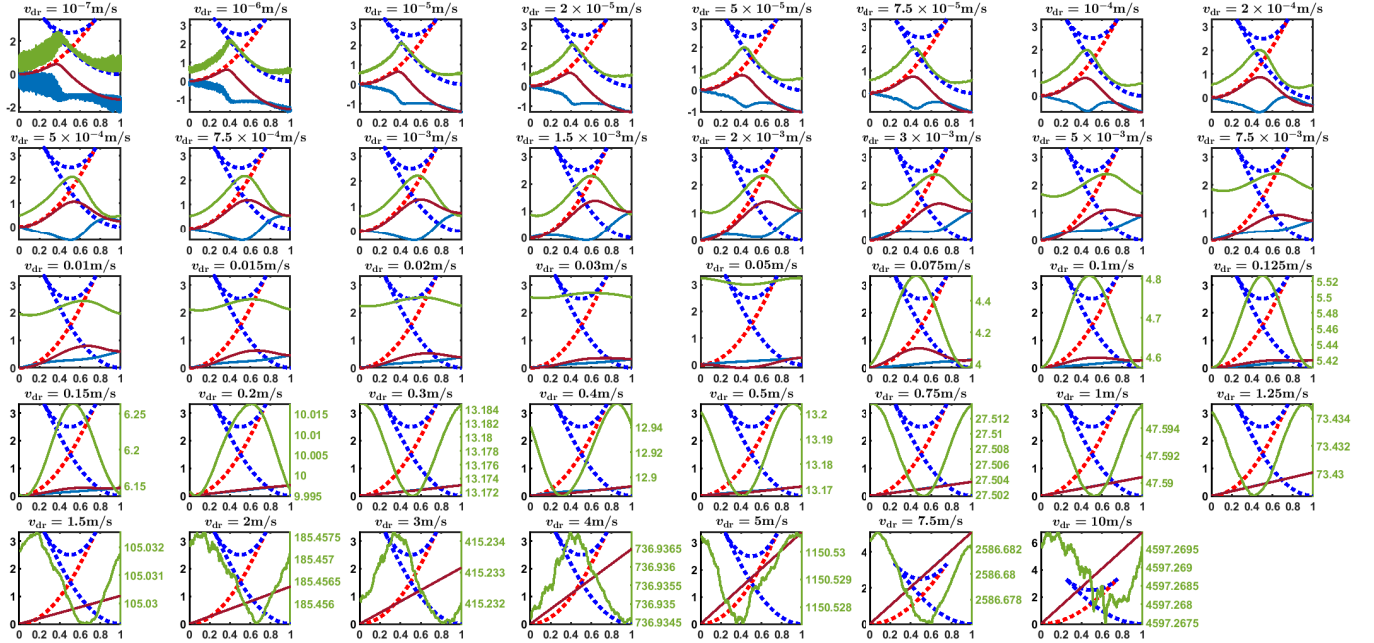


Fig. S16. The mean internal energy $\langle U \rangle$ (dark green), the mean heat to the heat bath $\langle Q \rangle$ (dark blue) and the mean work input to the system $\langle W \rangle$ (dark red) during one cycle at different driving velocities of the case of $\eta = 3$, $\mu = 4 \times 10^4 \text{s}^{-1}$ and $\Theta_{h,c} = 0.4, 0.04$. All the x-coordinates are the driver center's nondimensional position $v_{dr}t/a$ relative to the latest cycle starting point, i.e. the same as those in the main text Figure 2(B) and (C). All the y-coordinates and the dotted red and blue curves are the same as those in the main text Figure 2(A). Other parameters are given in Sec. 8.H. The numbers of simulation cycles used to calculate the three mean quantity curves at each driving velocity are given in Table S3. At each driving velocity, all of the simulation cycles are computed sequentially with the initial values of the first simulation cycle inherited from the end values of the last simulation cycle used to calculate the corresponding point at the same v_{dr} on the purple $\langle W_{cyc} \rangle - v_{dr}$ curve of the $\eta = 3$, $\Theta_{h,c} = 0.4, 0.04$ case in the main text Figure 3(B), so that we can make sure that the steady state has already been achieved and we don't need to exclude a certain number of cycles at the beginning transient process as we have done when calculating the mean values and standard deviations of W_{cyc} and obtaining the count distributions of W_{cyc} in Figure S40, cf. Sec. 8.H.

From $v_{dr} = 10^{-7} \text{m/s}$ to $7.5 \times 10^{-5} \text{m/s}$, we can see that the mean internal energy curve before its cusp is higher than the dotted red balanced resultant potential curve because of the particle's high kinetic energy in the high temperature zone and so is the part of this curve near the end of the engine cycle because of the particle's frequently traversing to the hot zone in the next lattice period, compared with the segment on the right of the cusp where it is close to the dotted blue curve. At and after $v_{dr} = 10^{-4} \text{m/s}$ the mean internal energy curve on the right of the cusp is uplifted from left to right gradually due to the kinetic energy from the oscillating relaxation process after the slipping event, which gets longer relative to the driver center's position with v_{dr} increases. And at around $v_{dr} = 10^{-3} \text{m/s}$ the mean internal energy curve at the beginning of the cycle begins to be uplifted from the left end because of the residual kinetic energy from the last cycle's slipping event. At the end of one cycle this curve is also uplifted because of the periodicity so the entire mean internal energy curve begins to be uplifted. At and after $v_{dr} = 0.075 \text{m/s}$, the mean internal energy curve is higher than the entire dotted balanced resultant potential curve, so we put its y-axis to the right separately, and we can see that its shape varies and it continues to be entirely uplifted gradually with the driving velocity increasing. When the driving velocity v_{dr} is very high, the mean internal energy curve stays nearly constant and the mean work and heat curves are nearly linear whose slopes increase with the increasing v_{dr} .

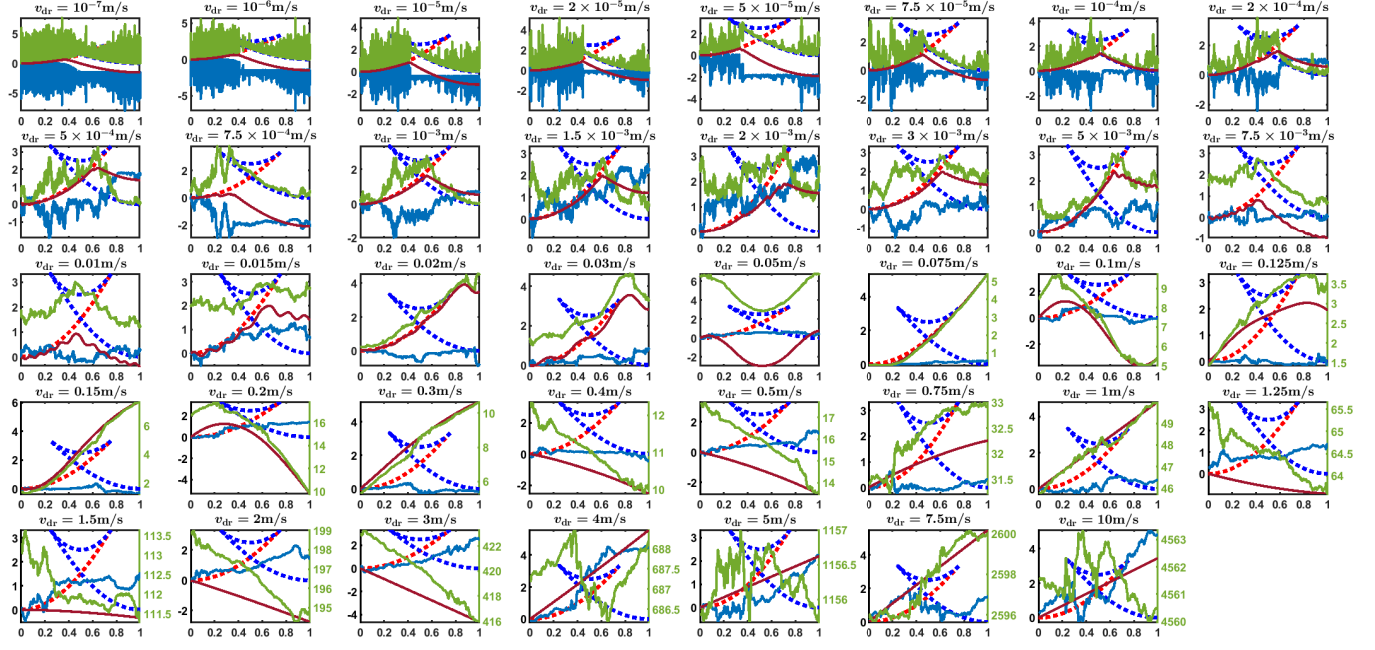


Fig. S17. The internal energy U (dark green), the heat to the heat bath Q (dark blue) and the work input to the system W (dark red) during one single cycle at different driving velocities of the case of $\eta = 3$, $\mu = 4 \times 10^4 \text{s}^{-1}$ and $\Theta_{h,c} = 0.4, 0.04$. All the x -coordinates are the driver center's nondimensional position $v_{dr}t/a$ relative to the latest cycle starting point, i.e. the same as those in the main text Figure 2(B) and (C). All the y -coordinates and the dotted red and blue curves are the same as those in the main text Figure 2(A). Other parameters are given in Sec. 8.H. At each driving velocity, the simulation cycle is computed with the initial values inherited from the end values of the last simulation cycle used to calculate the corresponding point at the same v_{dr} on the purple $\langle W_{cyc} \rangle - v_{dr}$ curve of the $\eta = 3$, $\Theta_{h,c} = 0.4, 0.04$ case in the main text Figure 3(B), so that we can make sure that the steady state has already been achieved.

We can see that even without average, the work curve is smooth at all the driving velocities. From $v_{dr} = 10^{-7} \text{m/s}$ to $2 \times 10^{-4} \text{m/s}$, the work curves all have a cusp, while after average the cusp vanishes, cf. Figure S16. The stochastic feature of the one single cycle trajectories is clear compared with the mean curves in Figure S16.

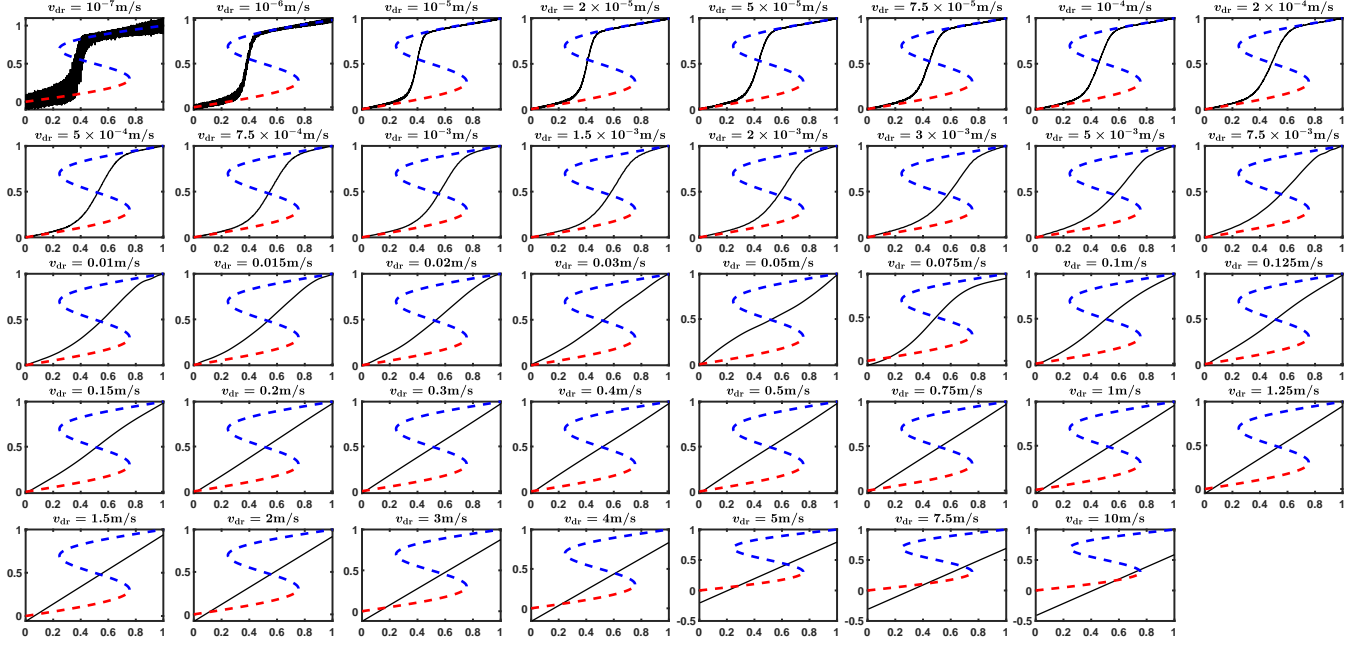


Fig. S18. The mean displacement of the particle $\langle x \rangle$ during one cycle at different driving velocities of the case of $\eta = 3$, $\mu = 4 \times 10^4 \text{s}^{-1}$ and $\Theta_{h,c} = 0.4, 0.04$. All the x -coordinates are the driver center's nondimensional position $v_{dr}t/a$ relative to the latest cycle starting point, i.e. the same as that in the main text Figure 2(B). All the y -coordinates and the dashed red and blue curves are the same as those in the main text Figure 2(B). Other parameters are given in Sec. 8.H. The number of simulation cycles at each driving velocity is given in Table S3. At each driving velocity, all of the simulation cycles are computed sequentially with the initial values of the first simulation cycle inherited from the end values of the last simulation cycle used to calculate the corresponding point at the same v_{dr} on the purple $\langle W_{cyc} \rangle - v_{dr}$ curve of the $\eta = 3$, $\Theta_{h,c} = 0.4, 0.04$ case in the main text Figure 3(B), so that we can make sure that the steady state has already been achieved and we don't need to exclude a certain number of cycles at the beginning transient process as we have done when calculating the mean values and standard deviations of W_{cyc} and obtaining the count distributions of W_{cyc} in Figure S40, cf. Sec. 8.H.

We can see that average leads to the jumping cliff of the one single cycle displacement curve in Figure S19 smoothened. When the driving velocity is very high, the mean displacement curve falls behind the dashed red and blue curves (so that the particle falls behind the driver center) a lot. On the other hand, at not very high driving velocities, the starting and end points of the mean displacement curves during one cycle overlap with the starting and end positions of the driver center in one cycle.

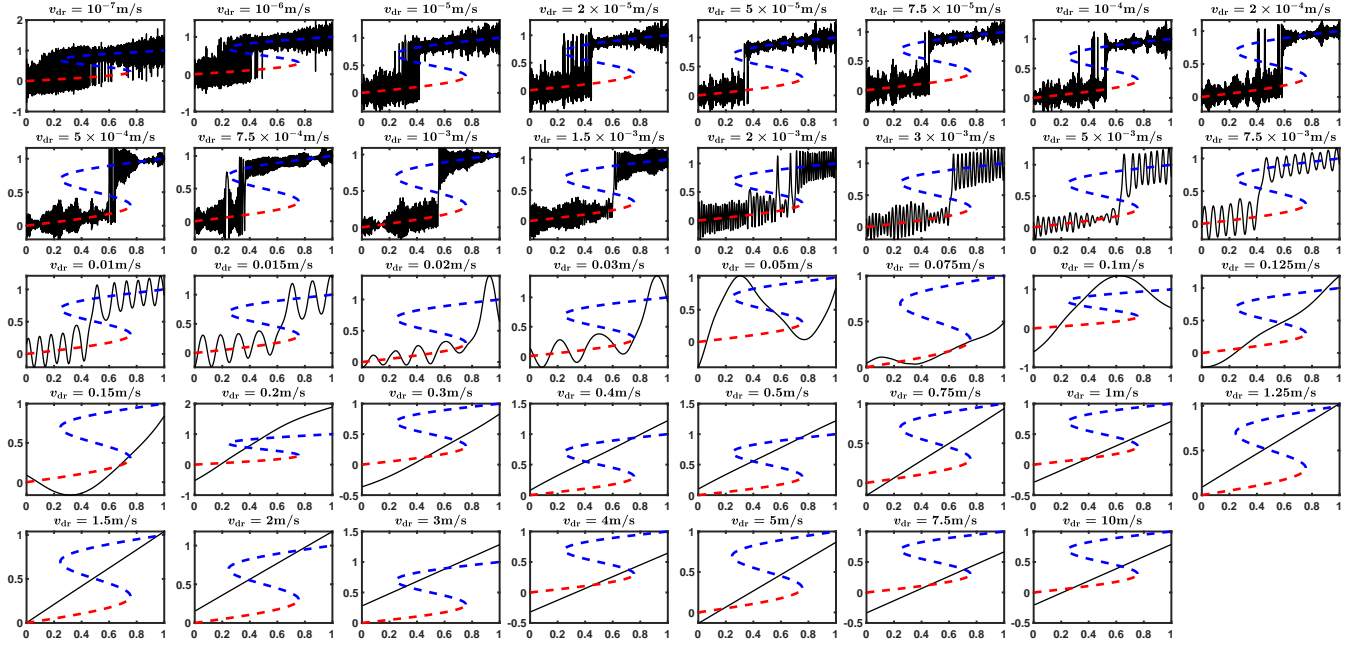


Fig. S19. The displacement of the particle x during one single cycle at different driving velocities of the case of $\eta = 3$, $\mu = 4 \times 10^4 \text{s}^{-1}$ and $\Theta_{h,c} = 0.4, 0.04$. All the x -coordinates are the driver center's nondimensional position $v_{dr} t / a$ relative to the latest cycle starting point, i.e. the same as that in the main text Figure 2(B). All the y -coordinates and the dashed red and blue curves are the same as those in the main text Figure 2(B). Other parameters are given in Sec. 8.H. At each driving velocity, the simulation cycle is computed with the initial values inherited from the end values of the last simulation cycle used to calculate the corresponding point at the same v_{dr} on the purple $\langle W_{cyc} \rangle - v_{dr}$ curve of the $\eta = 3$, $\Theta_{h,c} = 0.4, 0.04$ case in the main text Figure 3(B), so that we can make sure that the steady state has already been achieved. As the driving velocity increases, the number of oscillations of the particle during one cycle are reduced. So the waveform of the displacement curve is gradually clearer with the increasing driving velocity v_{dr} . The waves are modulated by the stochastic force so that their amplitudes are stochastically changing. In the resonance regime the particle's oscillation period is approximately equal to the cycle period so that there is approximately one wave in one cycle, which is affected by the stochastic force and irregular. At even higher driving velocity, the particle is far behind the driver center and the displacement curve is close to linear, cf. Figure S25. Due to the stochastic force, the particle's one single cycle displacement curve is random and doesn't overlap with the corresponding mean displacement curve in Figure S18, even at the high driving velocity end.

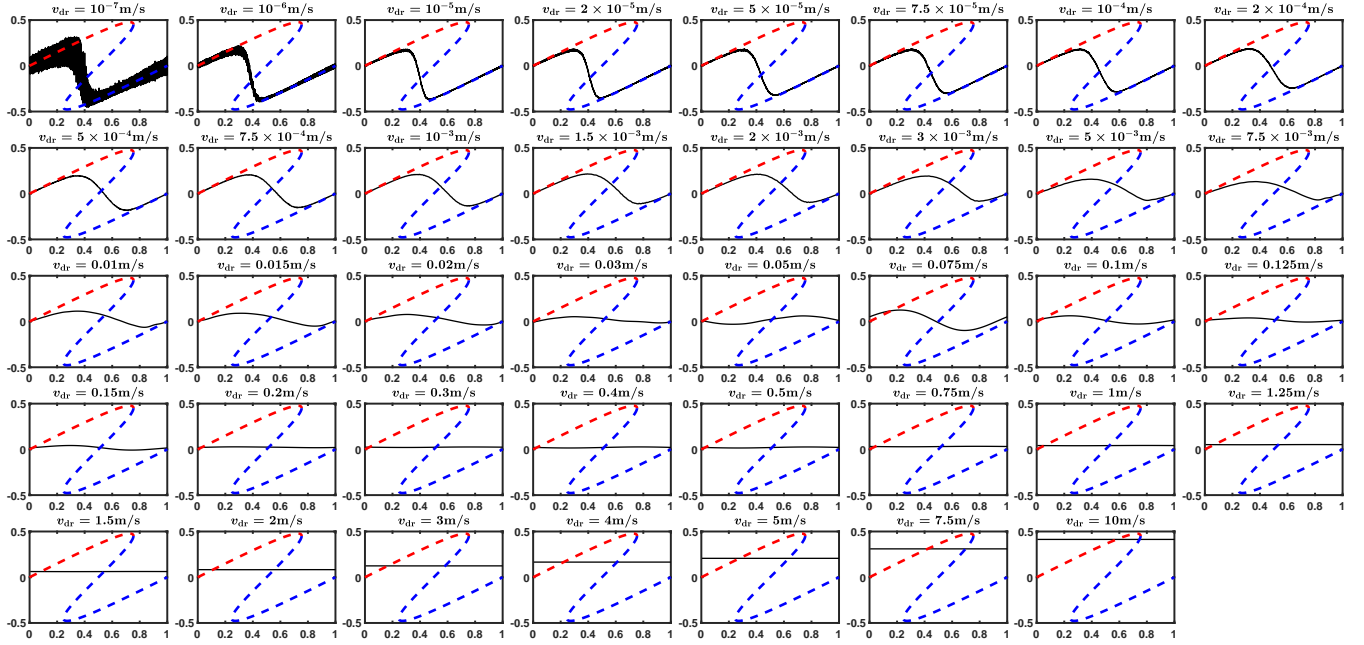


Fig. S20. The mean harmonic force $\langle F_h \rangle$ during one cycle at different driving velocities of the case of $\eta = 3$, $\mu = 4 \times 10^4 \text{s}^{-1}$ and $\Theta_{h,c} = 0.4, 0.04$. All the x -coordinates are the driver center's nondimensional position $v_{dr}t/a$ relative to the latest cycle starting point, i.e. the same as that in the main text Figure 2(C). All the y -coordinates and the dashed red and blue curves are the same as those in the main text Figure 2(C). Other parameters are given in Sec. 8.H. The number of simulation cycles at each driving velocity is given in Table S3. At each driving velocity, all of the simulation cycles are computed sequentially with the initial values of the first simulation cycle inherited from the end values of the last simulation cycle used to calculate the corresponding point at the same v_{dr} on the purple $\langle W_{cyc} \rangle - v_{dr}$ curve of the $\eta = 3$, $\Theta_{h,c} = 0.4, 0.04$ case in the main text Figure 3(B), so that we can make sure that the steady state has already been achieved and we don't need to exclude a certain number of cycles at the beginning transient process as we have done when calculating the mean values and standard deviations of W_{cyc} and obtaining the count distributions of W_{cyc} in Figure S40, cf. Sec. 8.H.

Like the mean displacement curves in Figure S18, the mean harmonic force curve overlaps with the dashed balanced force curves at the beginning and end stages of the engine cycle when the driving velocity is not very high. As the driving velocity increases, the waveform of the mean harmonic force curve changes and its amplitude declines. When v_{dr} is very high, the mean harmonic force stays nearly constant during one cycle, which is consistent with the approximate parallelism between the corresponding mean displacement curve and the driver center line [not plotted, cf. the main text Figure 2(B)] in Figure S18. In this high driving velocity regime, the nearly constant mean harmonic force increases to balance the high damping force, cf. Figure S25.

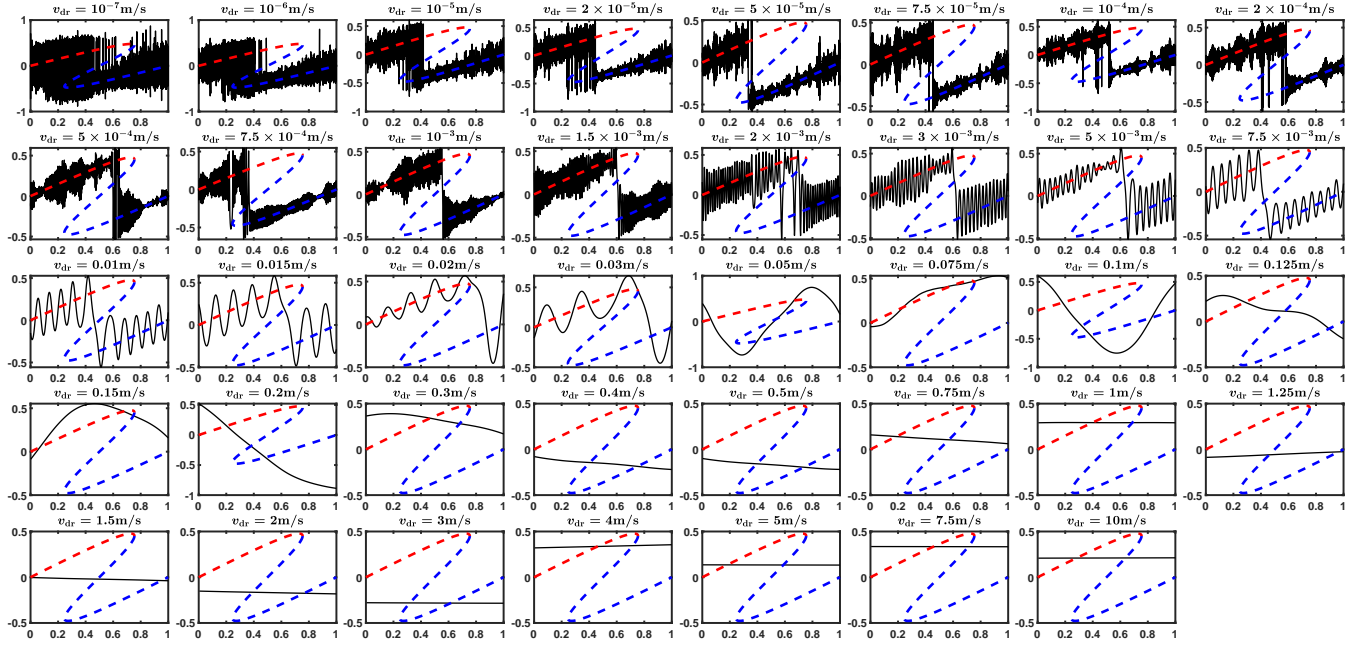


Fig. S21. The harmonic force F_h during one single cycle at different driving velocities of the case of $\eta = 3$, $\mu = 4 \times 10^4 \text{s}^{-1}$ and $\Theta_{h,c} = 0.4, 0.04$. All the x -coordinates are the driver center's nondimensional position $v_{dr}t/a$ relative to the latest cycle starting point, i.e. the same as that in the main text Figure 2(C). All the y -coordinates and the dashed red and blue curves are the same as those in the main text Figure 2(C). Other parameters are given in Sec. 8.H. At each driving velocity, the simulation cycle is computed with the initial values inherited from the end values of the last simulation cycle used to calculate the corresponding point at the same v_{dr} on the purple $\langle W_{cyc} \rangle - v_{dr}$ curve of the $\eta = 3$, $\Theta_{h,c} = 0.4, 0.04$ case in the main text Figure 3(B), so that we can make sure that the steady state has already been achieved. The waveform of the one single cycle harmonic force curve gradually becomes clear and then becomes irregular in the resonance regime and finally becomes flat, consistent with the corresponding one single cycle displacement curve in Figure S19. Its amplitude is also modulated by the stochastic force at low driving velocities. At very high driving velocity, the nearly constant harmonic force in one cycle is random due to the stochastic force and not equal to the corresponding nearly constant mean harmonic force in Figure S20.

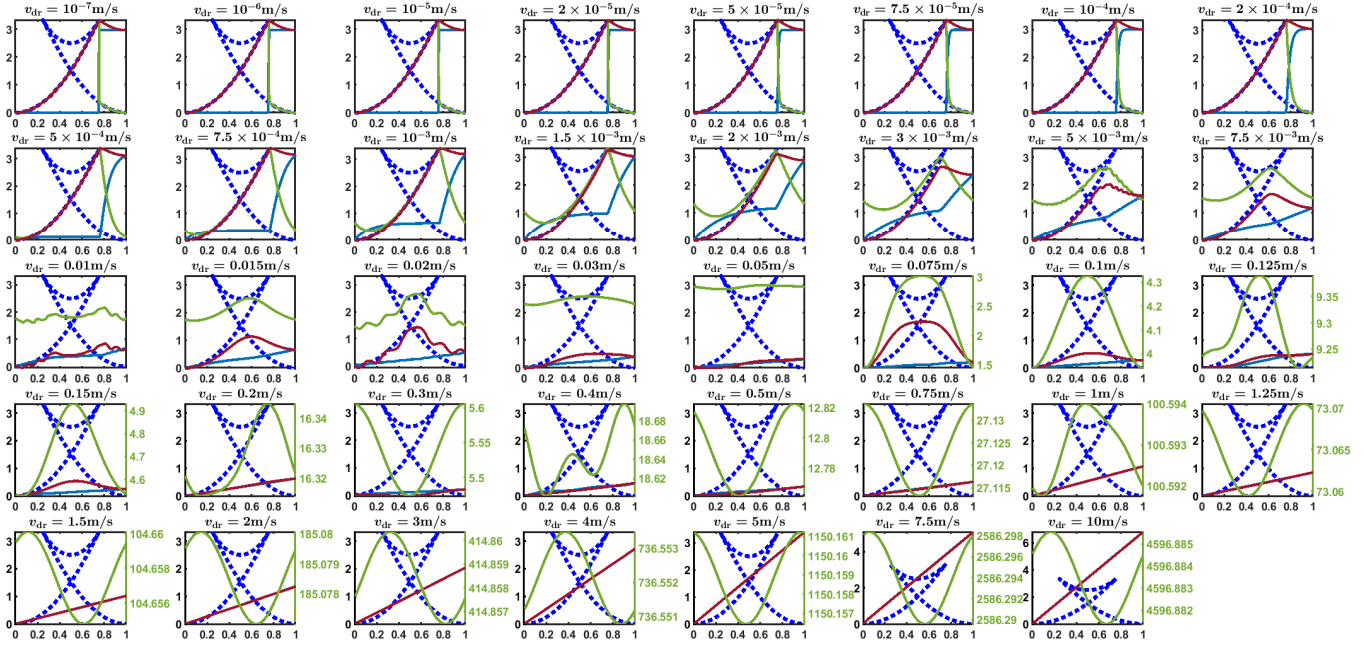


Fig. S22. The mean internal energy $\langle U \rangle$ (dark green), the mean heat to the heat bath $\langle Q \rangle$ (dark blue) and the mean work input to the system $\langle W \rangle$ (dark red) during one cycle at different driving velocities of the case of $\eta = 3$, $\mu = 4 \times 10^{-4} \text{s}^{-1}$ and $\Theta = 0$. All the x -coordinates are the driver center's nondimensional position $v_{dr}t/a$ relative to the latest cycle starting point, i.e. the same as those in Figure S5(B) and (C). All the y -coordinates and the dotted blue curves are the same as those in Figure S5(A). Other parameters are given in Sec. 8.H. The number of simulation cycles at each driving velocity is given in Table S3. At each driving velocity, all of the simulation cycles are computed sequentially with the initial values of the first simulation cycle inherited from the end values of the last simulation cycle used to calculate the corresponding point at the same v_{dr} on the black $\langle W_{cyc} \rangle - v_{dr}$ curve of the $\Theta = 0$ case in the main text Figure 3(C), so that we can make sure that the steady state has already been achieved and we don't need to exclude a certain number of cycles at the beginning transient process as we have done when calculating the mean values and standard deviations of W_{cyc} and obtaining the count distributions of W_{cyc} in Figure S40, cf. Sec. 8.H.

In the first row of the subfigures, i.e. from $v_{dr} = 10^{-7} \text{m/s}$ to $v_{dr} = 2 \times 10^{-4} \text{m/s}$, the mean internal energy curve after the cusp (slip) instant is gradually uplifted from the dashed blue curve because of the oscillating relaxation process relative to the driver center gets longer with the driving velocity increasing, cf. the text at the beginning of this subsection. At and after $v_{dr} = 5 \times 10^{-4} \text{m/s}$ the cycle starting (and also the cycle end, due to the periodicity) point of the mean internal energy curve is also gradually uplifted from the dotted blue curve due to the residual kinetic energy from the last cycle's slip. At and after $v_{dr} = 2 \times 10^{-3}$, the cusp of the mean internal energy curve begins to descend and move to the left, i.e. the residual kinetic energy from slipping in the last cycle arrives. At and after $v_{dr} = 0.1 \text{m/s}$, the mean internal energy curve is higher than the entire dashed blue balanced resultant potential curve and is entirely uplifted gradually, so we put its y -axis to the right separately. When the mean internal energy curve is on the dashed blue balanced resultant potential curve, the mean heat curve keeps constant, while when the mean internal energy curve is uplifted from the dashed curve, the mean heat curve becomes exponential correspondingly, in that the residual kinetic energy from slipping is partly dissipated into heat during the longer relaxation process relative to the driver center. From $v_{dr} = 10^{-7} \text{m/s}$ to $2 \times 10^{-4} \text{m/s}$ (subfigures in the first row), the mean work curve nearly unchanged, consistent with the nearly constant work input in this velocity range on the $\langle W_{cyc} \rangle - v_{dr}$ curve of the $\Theta = 0$ case in the main text Figure 3(C). From $v_{dr} = 5 \times 10^{-4} \text{m/s}$ to 10^{-3}m/s , the descent segment of the mean work curve is shortened in height because the longer oscillating relaxation process after slipping leads to the effective temperature increasing, which is similar to the thermolubricity mechanism. So there is a short elevation before the plateau peak point ($v_{dr} = 10^{-3} \text{m/s}$) on the $\langle W_{cyc} \rangle - v_{dr}$ curve of the $\Theta = 0$ case in the main text Figure 3(C). At and after $v_{dr} = 1.5 \times 10^{-3} \text{m/s}$, the ascent segment of the mean work curve is also shortened in height, resulting in the decreasing of the mean cycle work in the velocity weakening regime, which we have explained in the text at the beginning of this subsection. In the resonance regime, the three curves are all irregular. At very high driving velocities, the mean work and heat curves overlap with each other and the mean internal energy keeps nearly constant during one cycle, cf. Figure S25.

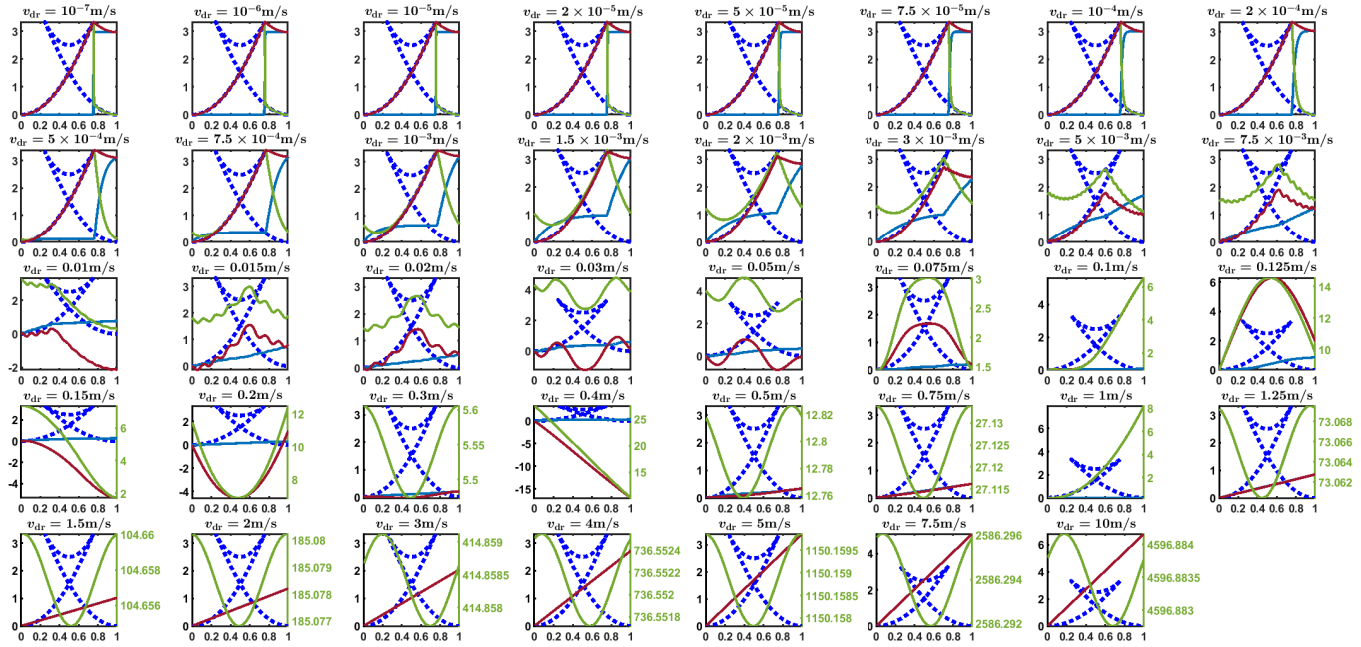


Fig. S23. The internal energy U (dark green the heat to the heat bath Q (dark blue) and the work input to the system W (dark red) during one single cycle at different driving velocities of the case of $\eta = 3$, $\mu = 4 \times 10^4 \text{ s}^{-1}$ and $\Theta = 0$. All the x -coordinates are the driver center's nondimensional position $v_{\text{dr}} t / a$ relative to the latest cycle starting point, i.e. the same as those in Figure S5(B) and (C). All the y -coordinates and the dotted blue curves are the same as those in Figure S5(A). Other parameters are given in Sec. 8.H. At each driving velocity, the simulation cycle is computed with the initial values inherited from the end values of the last simulation cycle used to calculate the corresponding point at the same v_{dr} on the black $\langle W_{\text{cyc}} \rangle - v_{\text{dr}}$ curve of the $\Theta = 0$ case in the main text Figure 3(C), so that we can make sure that the steady state has already been achieved.

The starting and end points of the one single cycle internal energy curve should have the same value if the particle's movement is periodic with as period the time of the driver center going over one cycle. If they are not the same, the particle's movement may not be periodic or have a period of the time of the driver center going over more than one lattice period. The latter is common in the velocity weakening regime and the resonance regime, cf. the main text subsection "Bifurcation of Mean Cycle Work with Driving Velocity as Parameter at Zero Temperature".

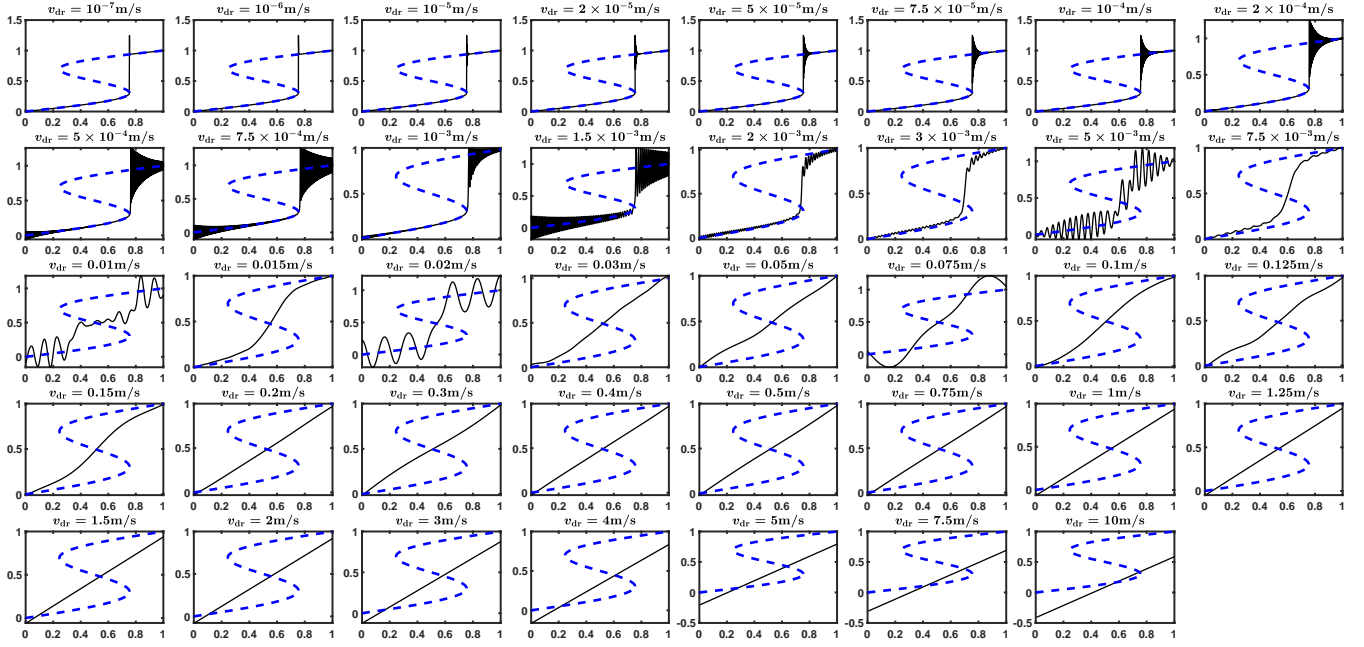


Fig. S24. The mean displacement of the particle $\langle x \rangle$ during one cycle at different driving velocities of the case of $\eta = 3$, $\mu = 4 \times 10^4 \text{s}^{-1}$ and $\Theta = 0$. All the x -coordinates are the driver center's nondimensional position $v_{dr}t/a$ relative to the latest cycle starting point, i.e. the same as that in Figure S5(B). All the y -coordinates and the dashed blue curves are the same as those in Figure S5(B). Other parameters are given in Sec. 8.H. The number of simulation cycles at each driving velocity is given in Table S3. At each driving velocity, all of the simulation cycles are computed sequentially with the initial values of the first simulation cycle inherited from the end values of the last simulation cycle used to calculate the corresponding point at the same v_{dr} on the black $\langle W_{cyc} \rangle - v_{dr}$ curve of the $\Theta = 0$ case in the main text Figure 3(C), so that we can make sure that the steady state has already been achieved and we don't need to exclude a certain number of cycles at the beginning transient process as we have done when calculating the mean values and standard deviations of W_{cyc} and obtaining the count distributions of W_{cyc} in Figure S40, cf. Sec. 8.H. If the mean displacement curve during one cycle is different from the corresponding one single cycle displacement curve in Figure S25 at the same driving velocity, then the particle's movement is not periodic or is periodic with as period the time of the driver center moving over more than one lattice period.

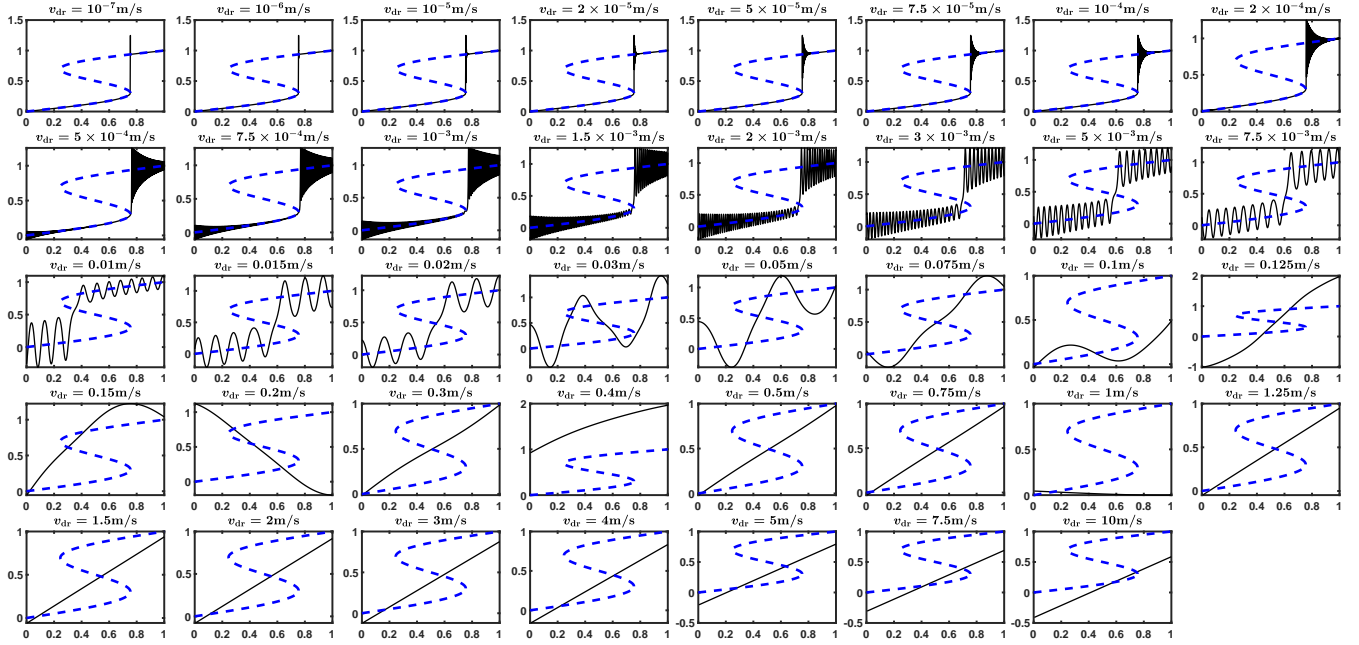


Fig. S25. The displacement x during one single cycle at different driving velocities of the case of $\eta = 3$, $\mu = 4 \times 10^4 \text{s}^{-1}$ and $\Theta = 0$. All the x -coordinates are the driver center's nondimensional position $v_{dr} t / a$ relative to the latest cycle starting point, i.e. the same as that in Figure S5(B). All the y -coordinates and the dashed blue curves are the same as those in Figure S5(B). Other parameters are given in Sec. 8.H. At each driving velocity, the simulation cycle is computed with the initial values inherited from the end values of the last simulation cycle used to calculate the corresponding point at the same v_{dr} on the black $\langle W_{cyc} \rangle - v_{dr}$ curve of the $\Theta = 0$ case in the main text Figure 3(C), so that we can make sure that the steady state has already been achieved.

In the text at the beginning of this subsection, we have analyzed the stick-slip regime and the velocity weakening regime. At $v_{dr} = 10^{-5} \text{m/s}$, stick-slip occurs and we have projected the position of the particle on the resultant potential curves varying with time in the main text Figure 6(A1) which can be compared with the one single cycle displacement curve at the same driving velocity $v_{dr} = 10^{-5} \text{m/s}$ in the subfigure at (row,column)=(1,3). The velocity weakening case at $v_{dr} = 0.003 \text{m/s}$ is plotted in the main text Figure 6(A2), which can also be compared with the corresponding one single cycle displacement curve in the subfigure at (row,column)=(2,6). At $v_{dr} = 0.4 \text{m/s}$ in the resonance regime, three solutions are plotted in the main text Figure 6(A3), (A4) and (A5), with the cycle number period $P_{c.n.} = 6, 6$ and 1 (Eq. 48) respectively. In the corresponding subfigure at the same driving velocity at (row,column)=(4,4), this specific one single cycle displacement curve has a cycle number period $P_{c.n.} > 1$. At $v_{dr} = 10 \text{m/s}$, we can see that the particle's position is far behind the driver center in the main text Figure 6(A6) and in the subfigure (row,column)=(5,7). At such a high driving velocity, the damping force $\mu m \dot{x}$ is so large that the harmonic force has to be large enough to balance it so that the particle's displacement from the driver center $x - v_{dr} t$ should be large. Because the sinusoidal lattice force's amplitude is constant, its effect compared with such a large harmonic force is small. Therefore, the particle's acceleration is small and its velocity is nearly constant so that the displacement curve is approximately linear at the high driving velocity end.

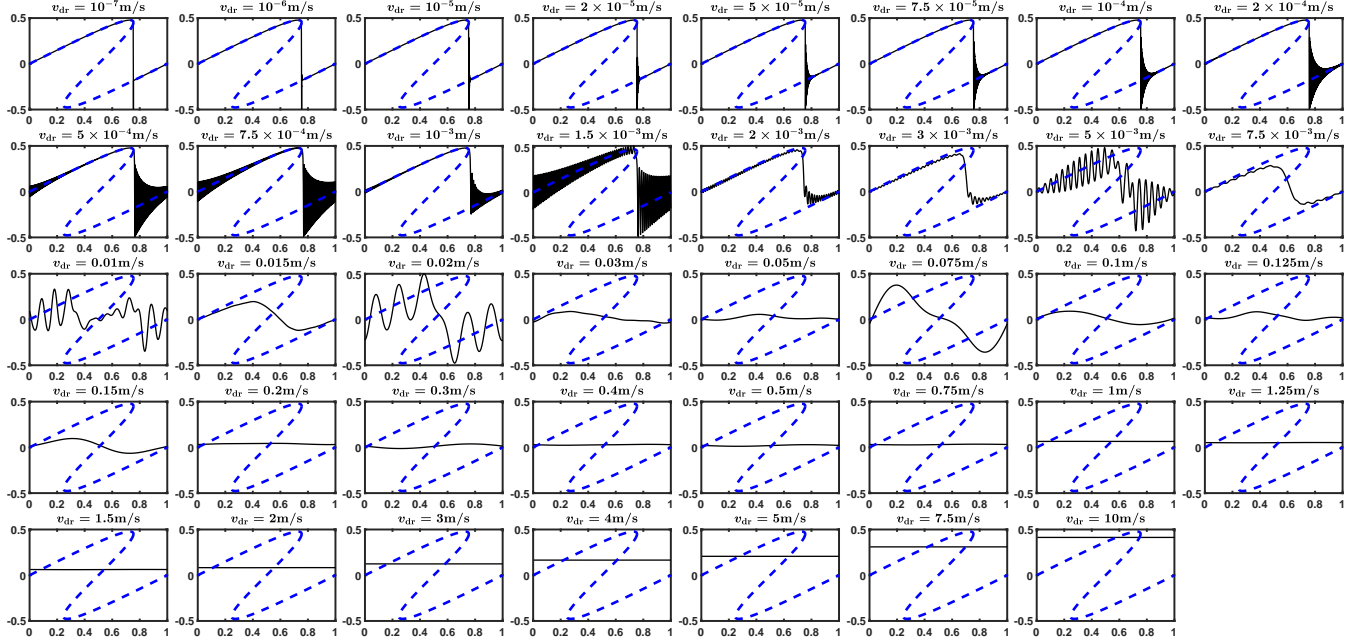


Fig. S26. The mean harmonic force $\langle F_h \rangle$ during one cycle at different driving velocities of the case of $\eta = 3$, $\mu = 4 \times 10^4 \text{s}^{-1}$ and $\Theta = 0$. All the x -coordinates are the driver center's nondimensional position $v_{dr}t/a$ relative to the latest cycle starting point, i.e. the same as that in Figure S5(C). All the y -coordinates and the dashed blue curves are the same as those in Figure S5(C). Other parameters are given in Sec. 8.H. The number of simulation cycles at each driving velocity is given in Table S3. At each driving velocity, all of the simulation cycles are computed sequentially with the initial values of the first simulation cycle inherited from the end values of the last simulation cycle used to calculate the corresponding point at the same v_{dr} on the black $\langle W_{cyc} \rangle - v_{dr}$ curve of the $\Theta = 0$ case in the main text Figure 3(C), so that we can make sure that the steady state has already been achieved and we don't need to exclude a certain number of cycles at the beginning transient process as we have done when calculating the mean values and standard deviations of W_{cyc} and obtaining the count distributions of W_{cyc} in Figure S40, cf. Sec. 8.H.

In homogeneous zero temperature, the mean harmonic force curves during one cycle are not smooth at low driving velocities, in that the oscillating relaxation process is the same in each single cycle and will stay the same after average, rather than being smoothed after average at some of the mediate driving velocities at which the particle's movement has no period or has a period of the time of the driver center moving over more than one lattice period, e.g. at $v_{dr} = 2 \times 10^{-3} \text{m/s}$, $3 \times 10^{-3} \text{m/s}$, $5 \times 10^{-3} \text{m/s}$, $7.5 \times 10^{-3} \text{m/s}$, etc. The mean harmonic force curves are also smoothed after average in the finite temperature cases as can be seen in Figure S20, S32 and S38.

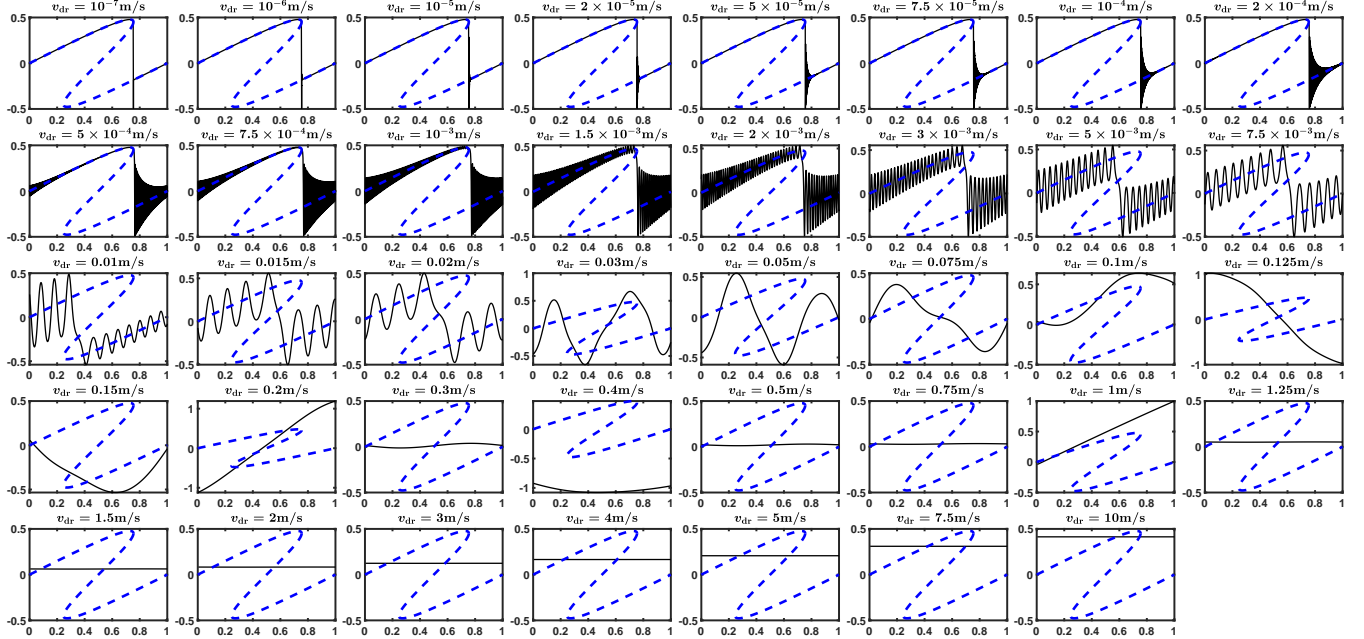


Fig. S27. The harmonic force F_h during one single cycle at different driving velocities of the case of $\eta = 3$, $\mu = 4 \times 10^4 \text{s}^{-1}$ and $\Theta = 0$. All the x -coordinates are the driver center's nondimensional position $v_{dr}t/a$ relative to the latest cycle starting point, i.e. the same as that in Figure S5(C). All the y -coordinates and the dashed blue curves are the same as those in Figure S5(C). Other parameters are given in Sec. 8.H. At each driving velocity, the simulation cycle is computed with the initial values inherited from the end values of the last simulation cycle used to calculate the corresponding point at the same v_{dr} on the black $\langle W_{cyc} \rangle - v_{dr}$ curve of the $\Theta = 0$ case in the main text Figure 3(C), so that we can make sure that the steady state has already been achieved.

We can see that when the driving velocity is so high, the harmonic force is very large and keeps nearly constant, cf. Figure S25.

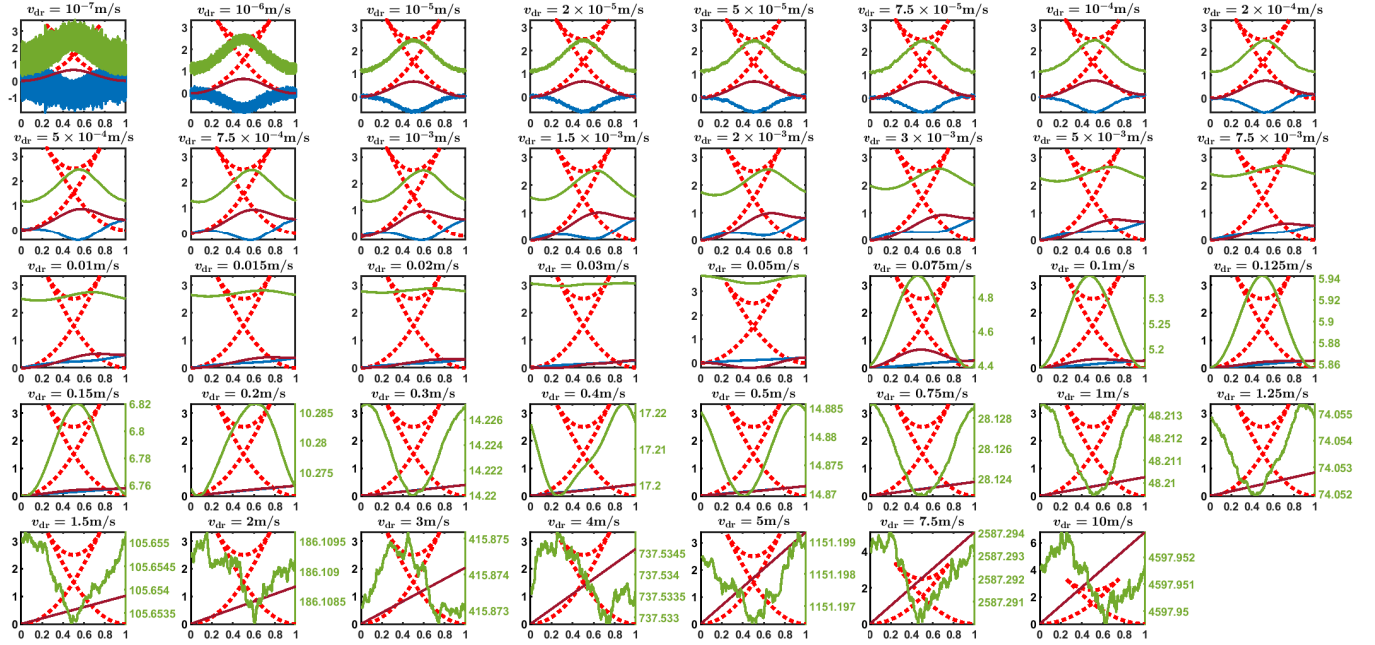


Fig. S28. The mean internal energy $\langle U \rangle$ (dark green), the mean heat to the heat bath $\langle Q \rangle$ (dark blue) and the mean work input to the system $\langle W \rangle$ (dark red) during one cycle at different driving velocities of the case of $\eta = 3$, $\mu = 4 \times 10^4 \text{s}^{-1}$ and $\Theta = 0.4$. All the x -coordinates are the driver center's nondimensional position $v_{dr}t/a$ relative to the latest cycle starting point, i.e. the same as those in Figure S6(B) and (C). All the y -coordinates and the dotted red curves are the same as those in Figure S6(A). Other parameters are given in Sec. 8.H. The number of simulation cycles at each driving velocity is given in Table S3. At each driving velocity, all of the simulation cycles are computed sequentially with the initial values of the first simulation cycle inherited from the end values of the last simulation cycle used to calculate the corresponding point at the same v_{dr} on the pink $\langle W_{cyc} \rangle - v_{dr}$ curve of the $\Theta = 0.4$ case in the main text Figure 3(C), so that we can make sure that the steady state has already been achieved and we don't need to exclude a certain number of cycles at the beginning transient process as we have done when calculating the mean values and standard deviations of W_{cyc} and obtaining the count distributions of W_{cyc} in Figure S40, cf. Sec. 8.H.

At such a high temperature, the particle is easy to achieve equilibrium at each instant at low enough driving velocity. Because the temperature is homogeneous, the mean internal energy, heat and work curves are nearly all symmetric about the middle of one cycle when the driving velocity is low, such as those in the first 4 subfigures. At $v_{dr} = 10^{-7} \text{m/s}$ and 10^{-6}m/s , the curves are noisy because of the small sample number of simulation cycles.

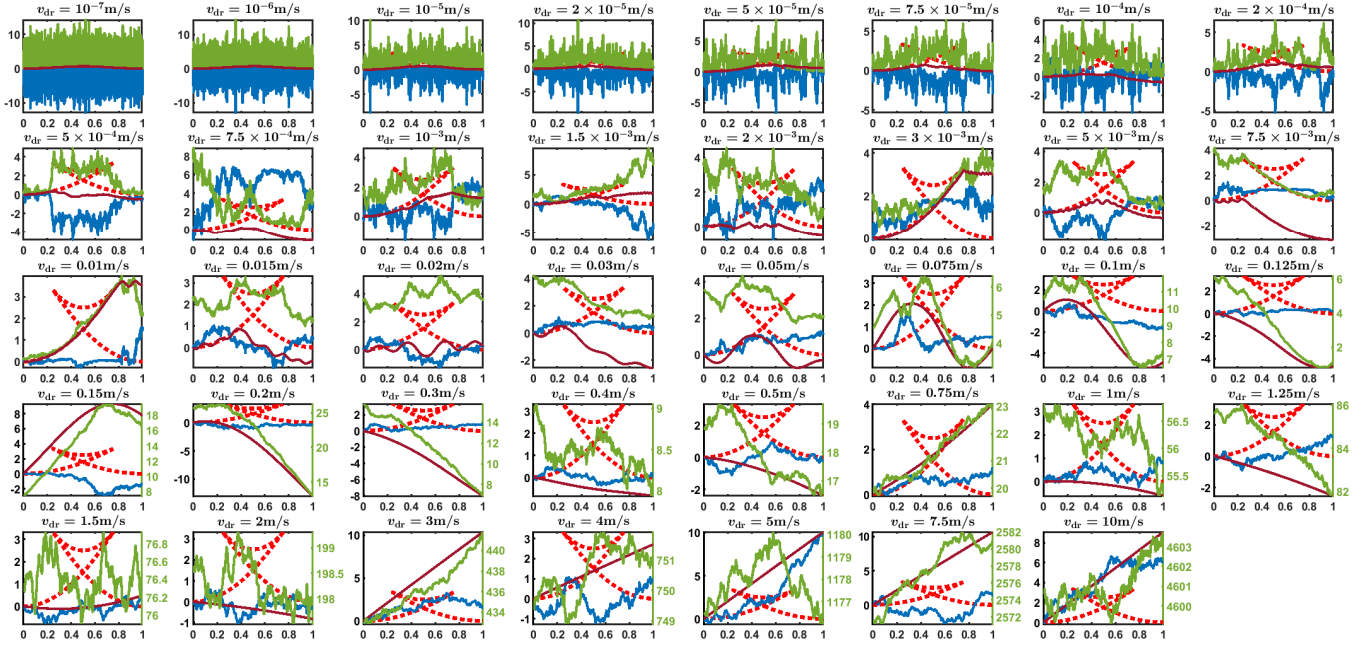


Fig. S29. The internal energy U (dark green), the heat to the heat bath Q (dark blue) and the work input to the system W (dark red) during one single cycle at different driving velocities of the case of $\eta = 3$, $\mu = 4 \times 10^4 \text{s}^{-1}$ and $\Theta = 0.4$. All the x -coordinates are the driver center's nondimensional position $v_{\text{dr}}t/a$ relative to the latest cycle starting point, i.e. the same as those in Figure S6(B) and (C). All the y -coordinates and the dotted red curves are the same as those in Figure S6(A). Other parameters are given in Sec. 8.H. At each driving velocity, the simulation cycle is computed with the initial values inherited from the end values of the last simulation cycle used to calculate the corresponding point at the same v_{dr} on the pink $W_{\text{cyc}} - v_{\text{dr}}$ curve of the $\Theta_{\text{h,c}} = 0.4$ case in the main text Figure 3(C), so that we can make sure that the steady state has already been achieved.

At such a high temperature, the stochastic force is large so that the internal energy, heat and work curves during one single cycle are very different from the mean curves in Figure S28. Although the stochastic force is of high amplitude in such a high temperature, the work curve is still very smooth relative to the internal energy and the heat curves.

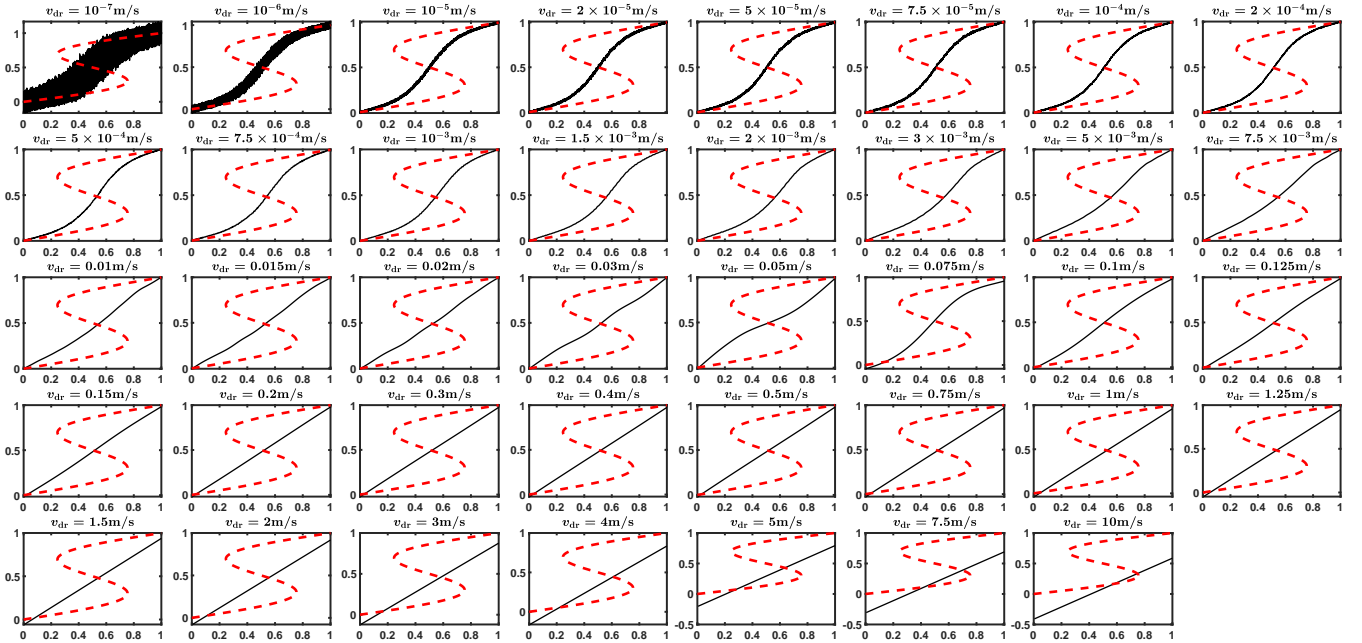


Fig. S30. The mean displacement of the particle $\langle x \rangle$ during one cycle at different driving velocities of the case of $\eta = 3$, $\mu = 4 \times 10^4 \text{s}^{-1}$ and $\Theta = 0.4$. All the x -coordinates are the driver center's nondimensional position $v_{\text{dr}}t/a$ relative to the latest cycle starting point, i.e. the same as that in Figure S6(B). All the y -coordinates and the dashed red curves are the same as those in Figure S6(B). Other parameters are given in Sec. 8.H. The number of simulation cycles at each driving velocity is given in Table S3. At each driving velocity, all of the simulation cycles are computed sequentially with the initial values of the first simulation cycle inherited from the end values of the last simulation cycle used to calculate the corresponding point at the same v_{dr} on the pink $(W_{\text{cyc}}) - v_{\text{dr}}$ curve of the $\Theta = 0.4$ case in the main text Figure 3(C), so that we can make sure that the steady state has already been achieved and we don't need to exclude a certain number of cycles at the beginning transient process as we have done when calculating the mean values and standard deviations of W_{cyc} and obtaining the count distributions of W_{cyc} in Figure S40, cf. Sec. 8.H.

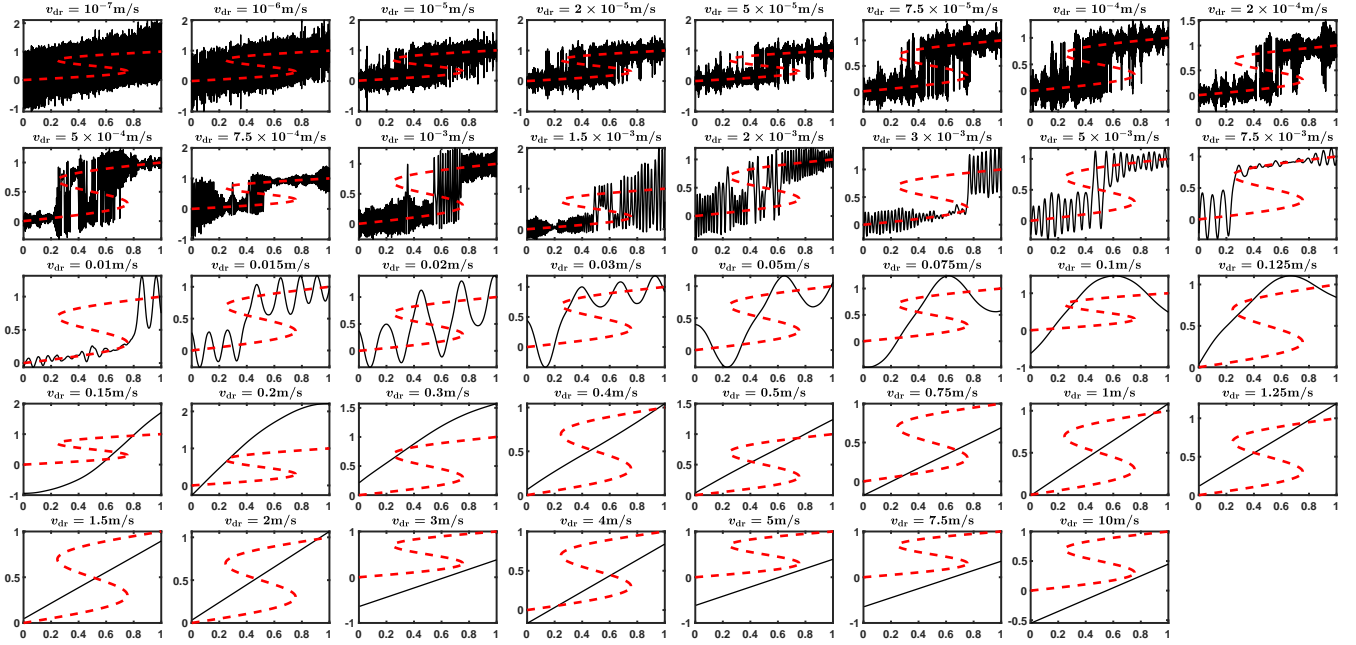


Fig. S31. The displacement x during one single cycle at different driving velocities of the case of $\eta = 3$, $\mu = 4 \times 10^4 \text{s}^{-1}$ and $\Theta = 0.4$. All the x -coordinates are the driver center's nondimensional position $v_{dr}t/a$ relative to the latest cycle starting point, i.e. the same as that in Figure S6(B). All the y -coordinates and the dashed red curves are the same as those in Figure S6(B). Other parameters are given in Sec. 8.H. At each driving velocity, the simulation cycle is computed with the initial values inherited from the end values of the last simulation cycle used to calculate the corresponding point at the same v_{dr} on the pink $\langle W_{cyc} \rangle - v_{dr}$ curve of the $\Theta = 0.4$ case in the main text Figure 3(C), so that we can make sure that the steady state has already been achieved.

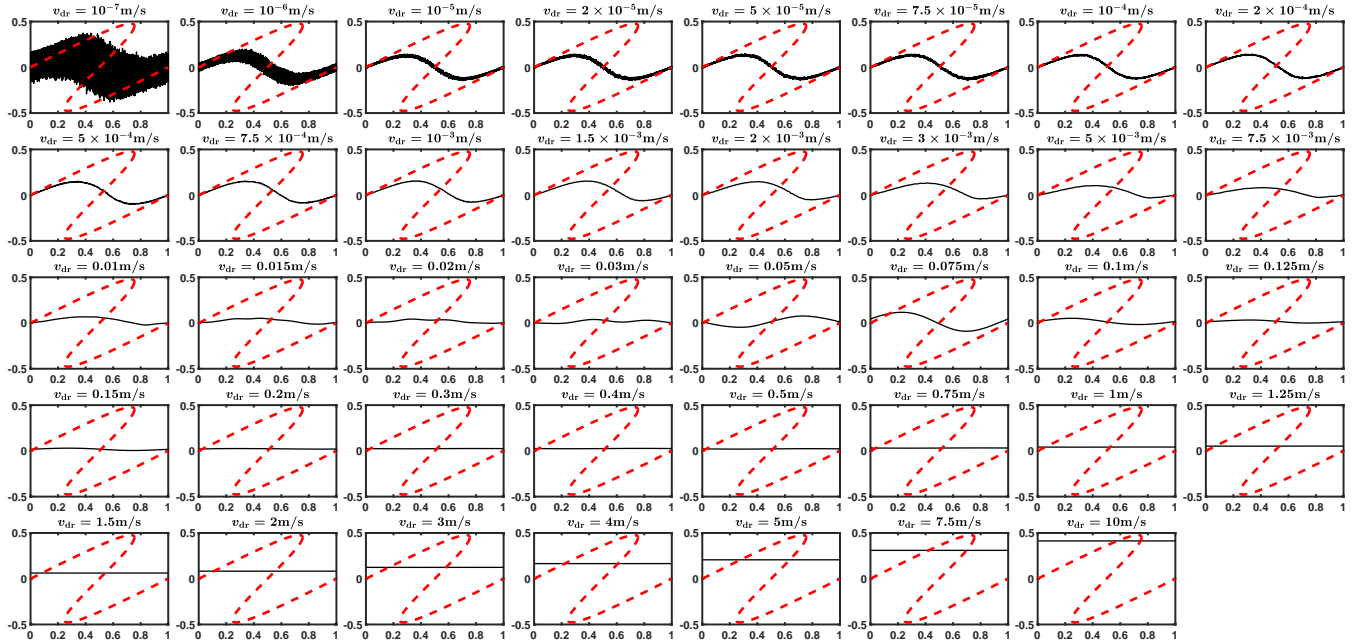


Fig. S32. The mean harmonic force $\langle F_h \rangle$ during one cycle at different driving velocities of the case of $\eta = 3$, $\mu = 4 \times 10^4 \text{s}^{-1}$ and $\Theta = 0.4$. All the x -coordinates are the driver center's nondimensional position $v_{dr}t/a$ relative to the latest cycle starting point, i.e. the same as that in Figure S6(C). All the y -coordinates and the dashed red curves are the same as those in Figure S6(C). Other parameters are given in Sec. 8.H. The number of simulation cycles at each driving velocity is given in Table S3. At each driving velocity, all of the simulation cycles are computed sequentially with the initial values of the first simulation cycle inherited from the end values of the last simulation cycle used to calculate the corresponding point at the same v_{dr} on the pink $\langle W_{cyc} \rangle - v_{dr}$ curve of the $\Theta = 0.4$ case in the main text Figure 3(C), so that we can make sure that the steady state has already been achieved and we don't need to exclude a certain number of cycles at the beginning transient process as we have done when calculating the mean values and standard deviations of W_{cyc} and obtaining the count distributions of W_{cyc} in Figure S40, cf. Sec. 8.H.

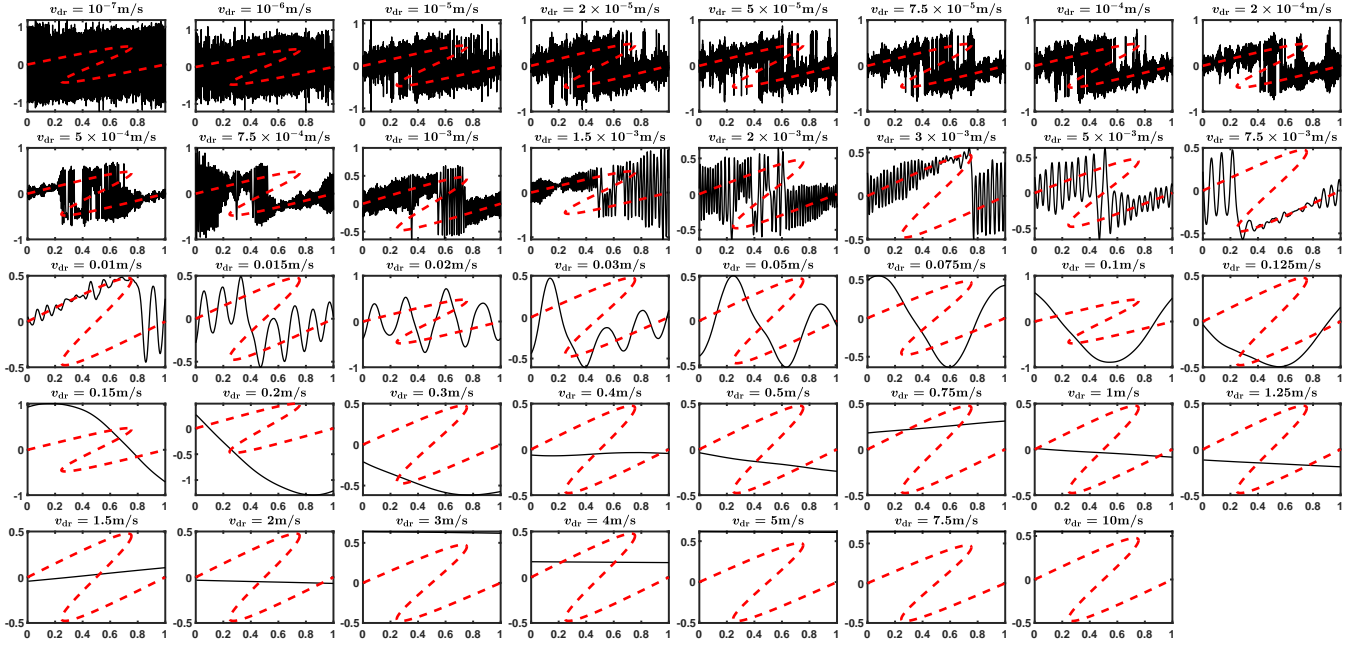


Fig. S33. The harmonic force F_h during one single cycle at different driving velocities of the case of $\eta = 3$, $\mu = 4 \times 10^4 \text{s}^{-1}$ and $\Theta = 0.4$. All the x -coordinates are the driver center's nondimensional position $v_{dr} t/a$ relative to the latest cycle starting point, i.e. the same as that in Figure S6(C). All the y -coordinates and the dashed red curves are the same as those in Figure S6(C). Other parameters are given in Sec. 8.H. At each driving velocity, the simulation cycle is computed with the initial values inherited from the end values of the last simulation cycle used to calculate the corresponding point at the same v_{dr} on the pink $\langle W_{cyc} \rangle - v_{dr}$ curve of the $\Theta = 0.4$ case in the main text Figure 3(C), so that we can make sure that the steady state has already been achieved.

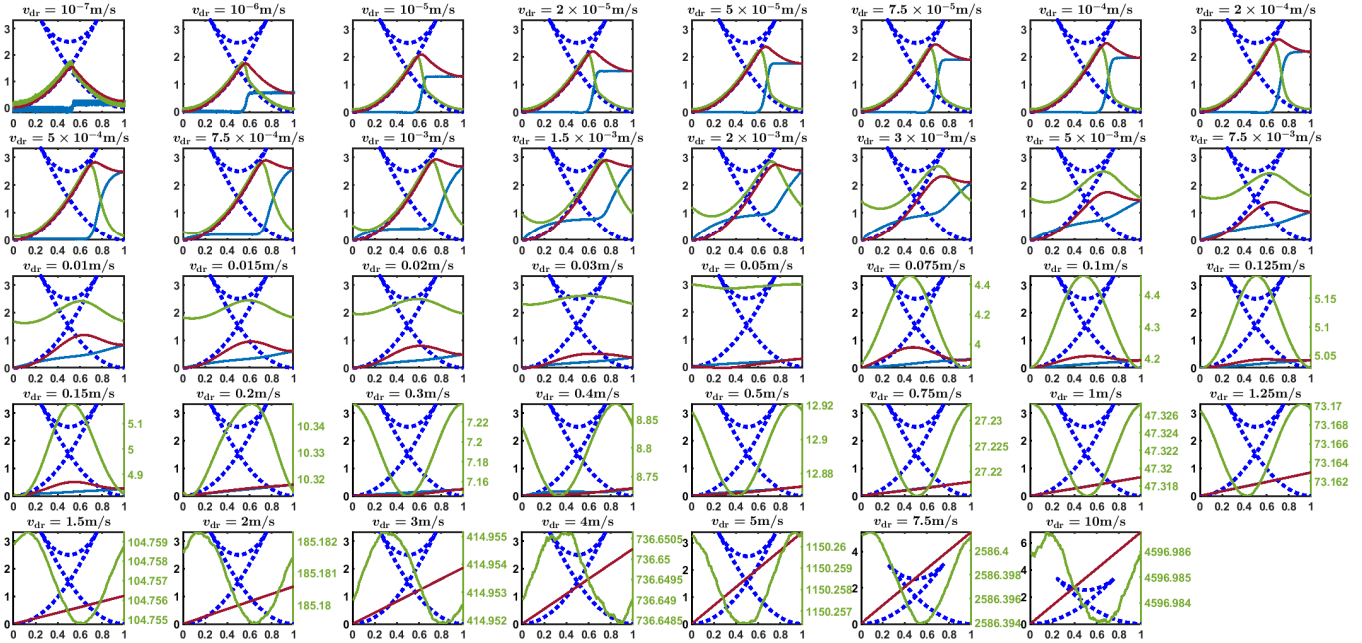


Fig. S34. The mean internal energy $\langle U \rangle$ (dark green), the mean heat to the heat bath $\langle Q \rangle$ (dark blue) and the mean work input to the system $\langle W \rangle$ (dark red) during one cycle at different driving velocities of the case of $\eta = 3$, $\mu = 4 \times 10^4 \text{s}^{-1}$ and $\Theta = 0.4$. All the x -coordinates are the driver center's nondimensional position $v_{dr} t/a$ relative to the latest cycle starting point, i.e. the same as those in Figure S5(B) and (C). All the y -coordinates and the dotted blue curves are the same as those in Figure S5(A). Other parameters are given in Sec. 8.H. The number of simulation cycles at each driving velocity is given in Table S3. At each driving velocity, all of the simulation cycles are computed sequentially with the initial values of the first simulation cycle inherited from the end values of the last simulation cycle used to calculate the corresponding point at the same v_{dr} on the cyan $\langle W_{cyc} \rangle - v_{dr}$ curve of the $\Theta = 0.4$ case in the main text Figure 3(C), so that we can make sure that the steady state has already been achieved and we don't need to exclude a certain number of cycles at the beginning transient process as we have done when calculating the mean values and standard deviations of W_{cyc} and obtaining the count distributions of W_{cyc} in Figure S40, cf. Sec. 8.H.

Because $\Theta = 0.4$ is not a very high temperature, the mean internal energy, heat, and work curves show some similarity to those of the homogeneous zero temperature case in Figure S22. The main difference is that the cusp of the mean internal energy curve moves to the left at low driving velocity because of the finite temperature leading to the particle crossing over the middle energy barrier before the instant of the BCP. Comparing with Figure S35, we can see that the cliffs of the internal energy and heat curves at low driving velocity are no longer that steep after average because of the stochastic instant of the slipping at finite temperature.

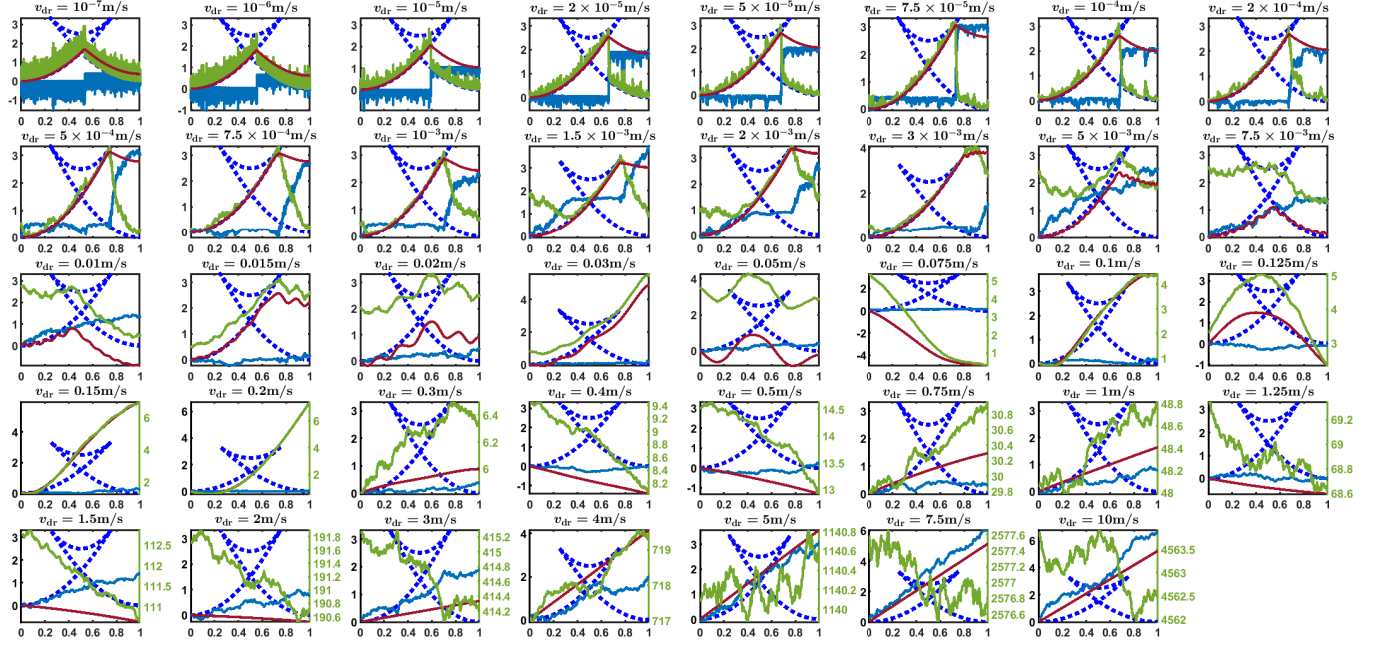


Fig. S35. The internal energy U (dark green), the heat to the heat bath Q (dark blue) and the work input to the system W (dark red) during one single cycle at different driving velocities of the case of $\eta = 3$, $\mu = 4 \times 10^4 \text{s}^{-1}$ and $\Theta = 0.04$. All the x -coordinates are the driver center's nondimensional position $v_{dr}t/a$ relative to the latest cycle starting point, i.e. the same as those in Figure S5(B) and (C). All the y -coordinates and the dotted blue curves are the same as those in Figure S5(A). Other parameters are given in Sec. 8.H. At each driving velocity, the simulation cycle is computed with the initial values inherited from the end values of the last simulation cycle used to calculate the corresponding point at the same v_{dr} on the cyan $\langle W_{cyc} \rangle - v_{dr}$ curve of the $\Theta = 0.04$ case in the main text Figure 3(C), so that we can make sure that the steady state has already been achieved.

Although the temperature is not very high, we can see that the stochastic feature of the one single cycle curves is still very distinct especially when the driving velocity is high so that the particle is at nonequilibrium, compared with the mean curves in Figure S34. Therefore at finite temperature, we'd better analyze the mean results to eliminate stochasticity.

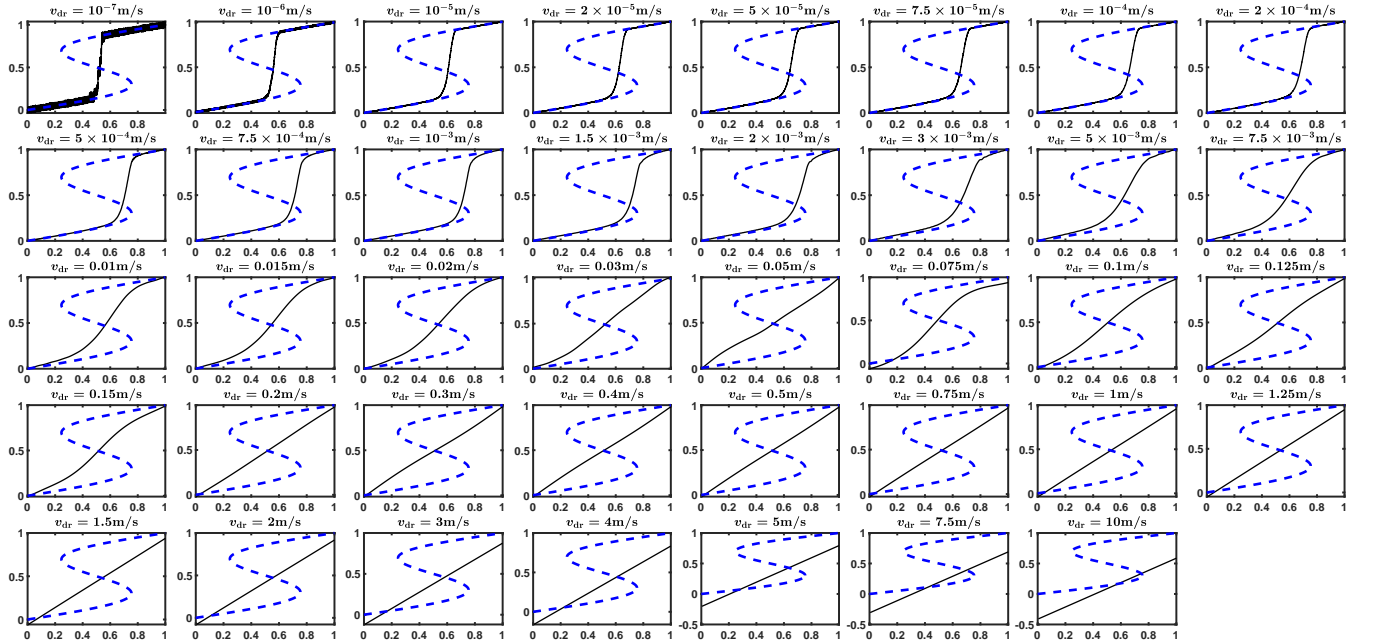


Fig. S36. The mean displacement of the particle $\langle x \rangle$ during one cycle at different driving velocities of the case of $\eta = 3$, $\mu = 4 \times 10^4 \text{s}^{-1}$ and $\Theta = 0.04$. All the x -coordinates are the driver center's nondimensional position $v_{dr}t/a$ relative to the latest cycle starting point, i.e. the same as that in Figure S5(B). All the y -coordinates and the dashed blue curves are the same as those in Figure S5(B). Other parameters are given in Sec. 8.H. The number of simulation cycles at each driving velocity is given in Table S3. At each driving velocity, all of the simulation cycles are computed sequentially with the initial values of the first simulation cycle inherited from the end values of the last simulation cycle used to calculate the corresponding point at the same v_{dr} on the cyan $\langle W_{cyc} \rangle - v_{dr}$ curve of the $\Theta = 0.04$ case in the main text Figure 3(C), so that we can make sure that the steady state has already been achieved and we don't need to exclude a certain number of cycles at the beginning transient process as we have done when calculating the mean values and standard deviations of W_{cyc} and obtaining the count distributions of W_{cyc} in Figure S40, cf. Sec. 8.H.

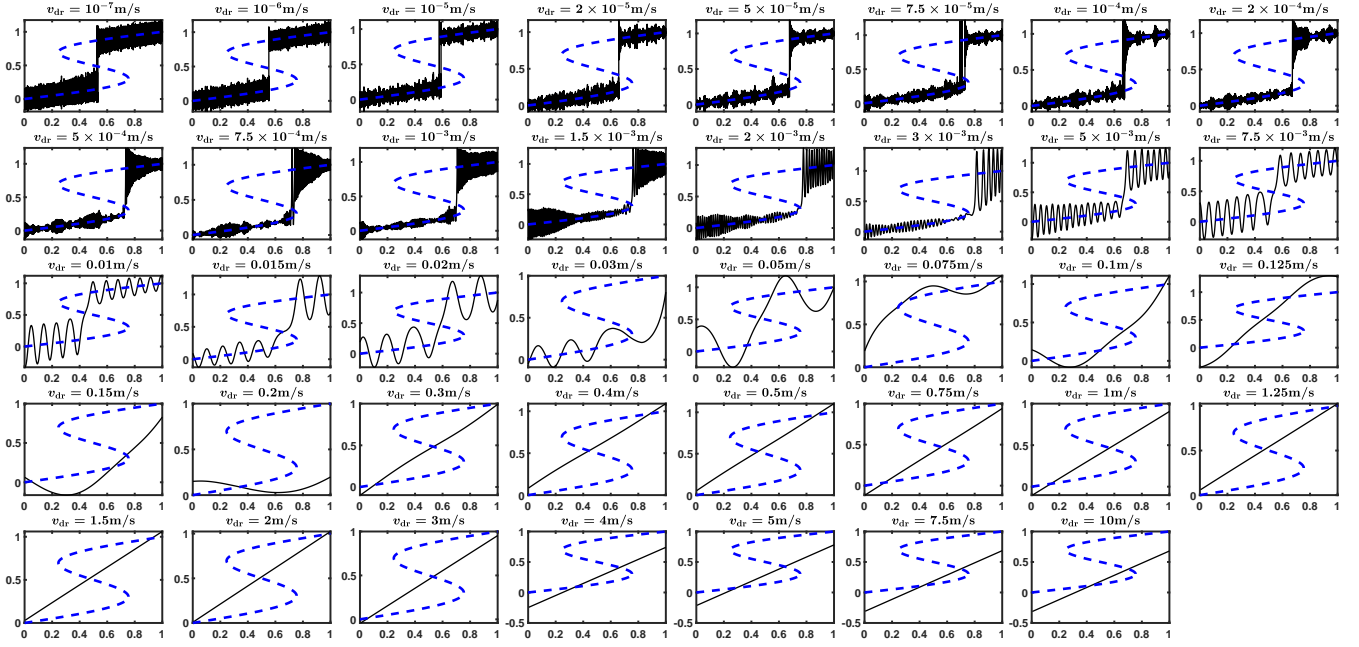


Fig. S37. The displacement x during one single cycle at different driving velocities of the case of $\eta = 3$, $\mu = 4 \times 10^4 \text{s}^{-1}$ and $\Theta = 0.04$. All the x -coordinates are the driver center's nondimensional position $v_{dr}t/a$ relative to the latest cycle starting point, i.e. the same as that in Figure S5(B). All the y -coordinates and the dashed blue curves are the same as those in Figure S5(B). Other parameters are given in Sec. 8.H. At each driving velocity, the simulation cycle is computed with the initial values inherited from the end values of the last simulation cycle used to calculate the corresponding point at the same v_{dr} on the cyan $\langle W_{cyc} \rangle - v_{dr}$ curve of the $\Theta = 0.04$ case in the main text Figure 3(C), so that we can make sure that the steady state has already been achieved.

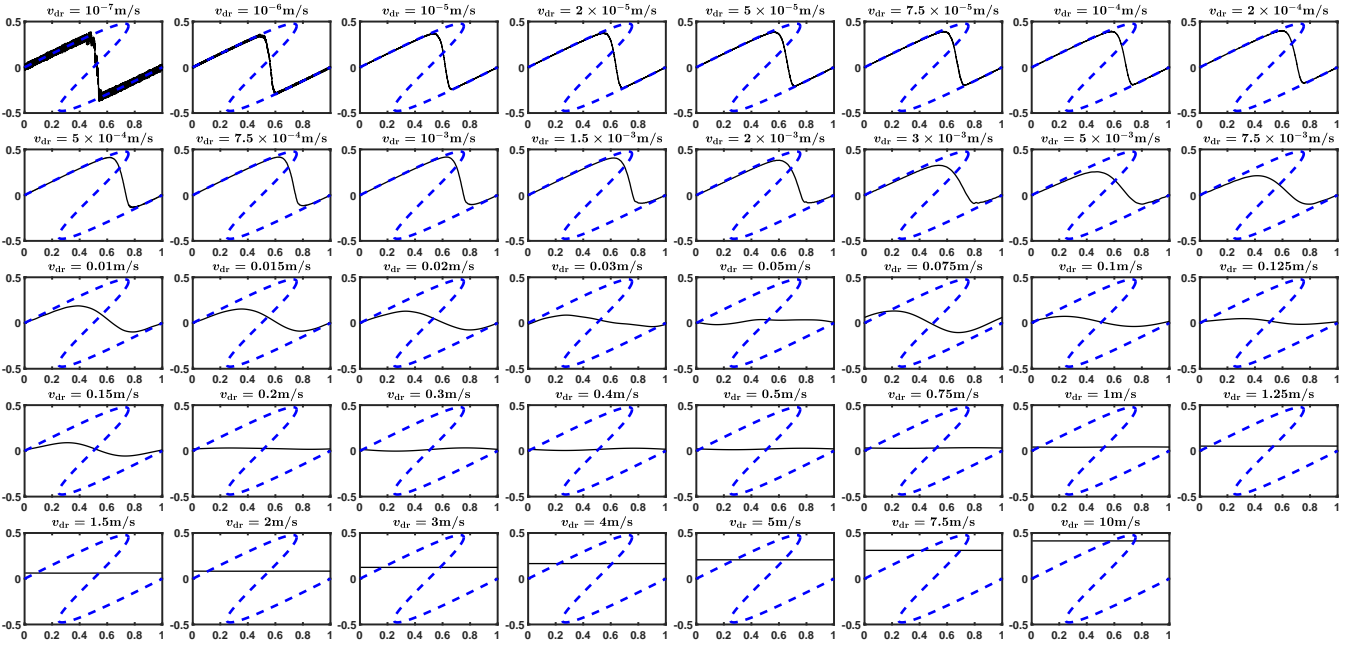


Fig. S38. The mean harmonic force $\langle F_h \rangle$ during one cycle at different driving velocities of the case of $\eta = 3$, $\mu = 4 \times 10^4 \text{s}^{-1}$ and $\Theta = 0.04$. All the x -coordinates are the driver center's nondimensional position $v_{dr}t/a$ relative to the latest cycle starting point, i.e. the same as that in Figure S5(C). All the y -coordinates and the dashed blue curves are the same as those in Figure S5(C). Other parameters are given in Sec. 8.H. The number of simulation cycles at each driving velocity is given in Table S3. At each driving velocity, all of the simulation cycles are computed sequentially with the initial values of the first simulation cycle inherited from the end values of the last simulation cycle used to calculate the corresponding point at the same v_{dr} on the cyan $\langle W_{cyc} \rangle - v_{dr}$ curve of the $\Theta = 0.04$ case in the main text Figure 3(C), so that we can make sure that the steady state has already been achieved and we don't need to exclude a certain number of cycles at the beginning transient process as we have done when calculating the mean values and standard deviations of W_{cyc} and obtaining the count distributions of W_{cyc} in Figure S40, cf. Sec. 8.H.

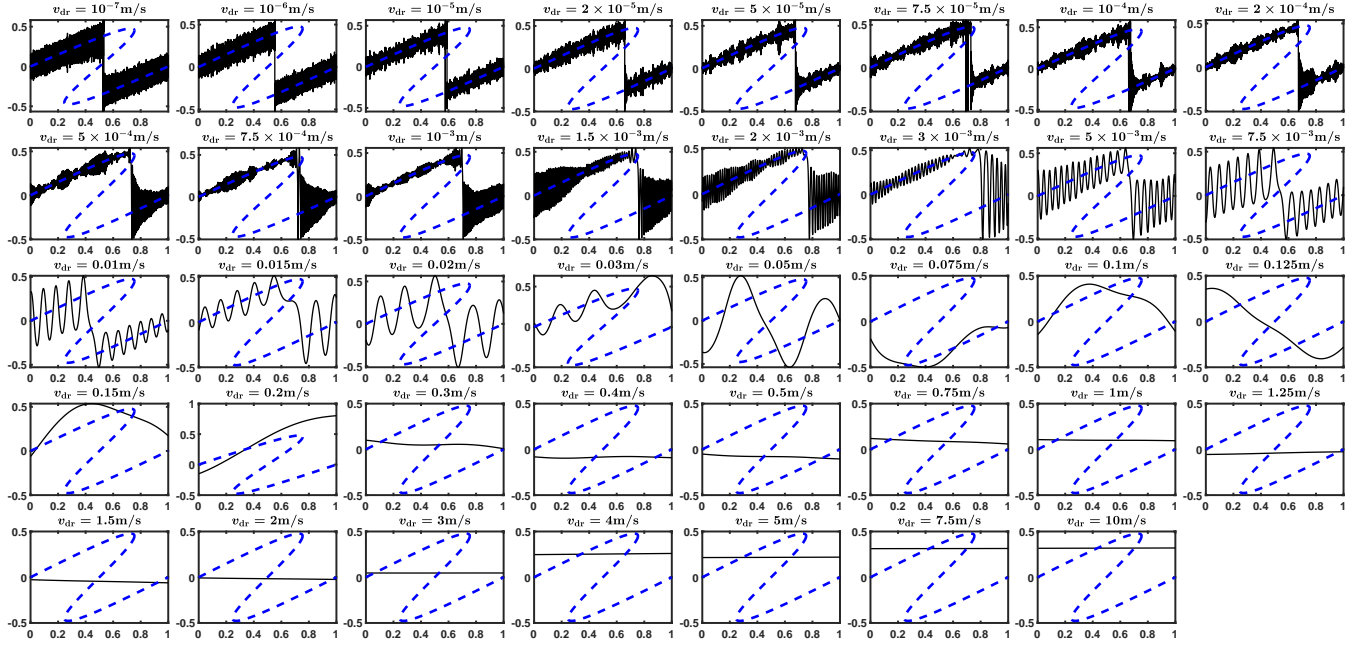


Fig. S39. The harmonic force F_h during one single cycle at different driving velocities of the case of $\eta = 3$, $\mu = 4 \times 10^4 \text{s}^{-1}$ and $\Theta = 0.04$. All the x -coordinates are the driver center's nondimensional position $v_{dr}t/a$ relative to the latest cycle starting point, i.e. the same as that in Figure S5(C). All the y -coordinates and the dashed blue curves are the same as those in Figure S5(C). Other parameters are given in Sec. 8.H. At each driving velocity, the simulation cycle is computed with the initial values inherited from the end values of the last simulation cycle used to calculate the corresponding point at the same v_{dr} on the cyan $\langle W_{cyc} \rangle - v_{dr}$ curve of the $\Theta = 0.04$ case in the main text Figure 3(C), so that we can make sure that the steady state has already been achieved.

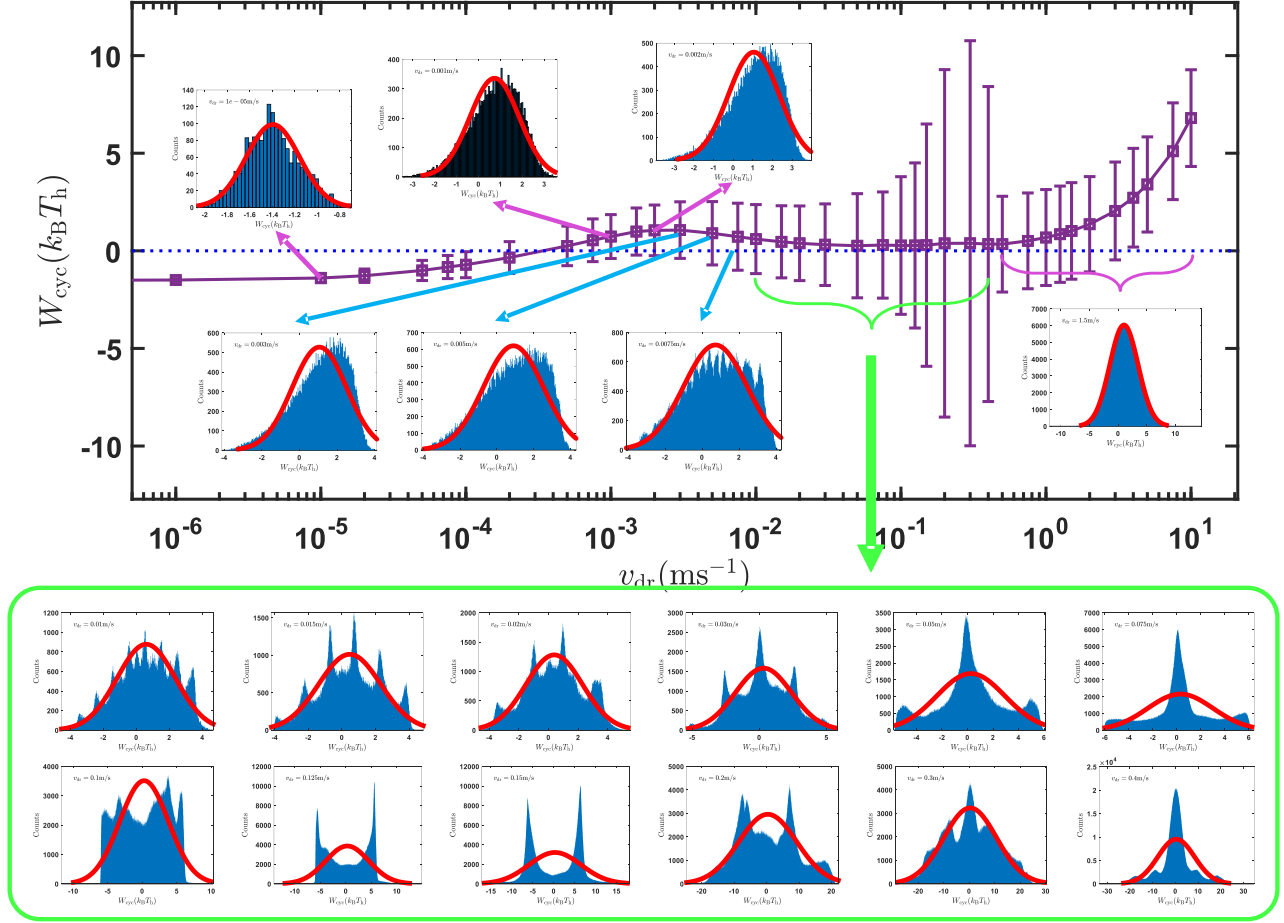


Fig. S40. The count distributions of W_{cyc} at different v_{dr} 's of the case of $\eta = 3$, $\mu = 4 \times 10^4 \text{ s}^{-1}$ and $\Theta_{\text{h,c}} = 0.4, 0.04$ in the main text Figure 3(B). The red curve is a normal distribution fit. From the low driving velocity end to the high driving velocity limit, the distribution of W_{cyc} is first normal and then has several peaks and finally becomes normal again. When $v_{\text{dr}} \in (10^{-2}, 4 \times 10^{-1}) \text{ m/s}$, the distributions of W_{cyc} at different v_{dr} 's are exotic. The sample of simulation engine cycles to obtain the count distribution of W_{cyc} at each driving velocity is the same as the sample to calculate the mean values and standard deviations of W_{cyc} at the same driving velocity, cf. Sec. 8.H. Incidentally, the count distribution of W_{cyc} in the main text Figure 3(C1) and (C2) are inherited from here.

I. The count distribution of W_{cyc} and its standard deviation. In Figure S40, we plot the count distributions of W_{cyc} at different driving velocity v_{dr} 's. In the high and low driving velocity end, the distributions are normal while in the middle driving velocity range the distributions are no longer normal and have several peaks especially in $(10^{-2}, 4 \times 10^{-1}) \text{ m/s}$, indicating the periodicity and multiplicity of W_{cyc} , cf. the main text Figure 3(C2) and (C3) and Sec. 6.J.

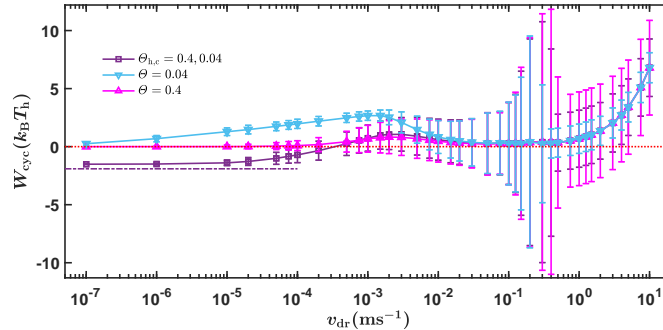


Fig. S41. The standard deviations of W_{cyc} in the homogeneous high ($\Theta = 0.4$) and low ($\Theta = 0.04$) temperature case. The $\Theta_{\text{h,c}} = 0.4, 0.04$ case is plotted for comparison. The parameters are the same as those of the three corresponding cases in the main text Figure 3(C). We can see that in all the three cases, the standard deviation of W_{cyc} has a peak at a certain v_{dr} dependent on the specific temperature field. The nearly constant standard deviation at the high velocity end also depends on the temperature.

In Figure S41, the standard deviations of W_{cyc} in the homogeneous high ($\Theta = 0.4$) and low ($\Theta = 0.04$) temperature cases are plotted with the $\Theta_{h,c} = 0.4, 0.04$ case for comparison. We can see that at very low driving velocity, the standard deviations of the three cases are all very small, indicating the equilibrium at each instant and thus the reversibility of the cycles.

With the driving velocity increasing, the standard deviation gradually goes up to a maximum when stochastic resonance occurs (41). After the maximum, the standard deviation goes down to a constant although the driving velocity is still increasing to the infinity. At the high driving velocity end, the stochastic noise (which is Gaussian white noise) is of larger time scale than the driver center (and the particle) moving over a lattice period, resulting in that the cycle work W_{cyc} has a normal distribution with constant standard deviations at increasing driving velocities. On the other hand, at the low driving velocity end, the stochastic noise is of smaller time scale than the driver center (and the particle) moving over a lattice period, so that at each instant of one cycle the particle relaxes to quasi-equilibrium and the ensemble average of the cycles, i.e. $\langle W_{\text{cyc}} \rangle$, is nearly identical to the time average of one cycle, i.e. W_{cyc} , cf. the main text subsection “The Second Mechanism of Work Output and the Consequence of Its Excess”. As $v_{\text{dr}} \rightarrow 0$, $W_{\text{cyc}} \rightarrow \langle W_{\text{cyc}} \rangle$ and the standard deviation goes to zero, so the distribution of W_{cyc} goes to an one-point distribution. In the mediate driving velocity range, the time scale of the stochastic noise is of the same order as the time scale for the driver center (and the particle) to move over one lattice period so that the particle’s movement synchronizes with the stochastic noise and stochastic resonance occurs at a certain v_{dr} , leading to the standard deviation of W_{cyc} maximizing. The resonant driving velocity is affected by the temperature field and it is a noteworthy problem to seek for an analytical solution for the standard deviation of W_{cyc} varying with v_{dr} .

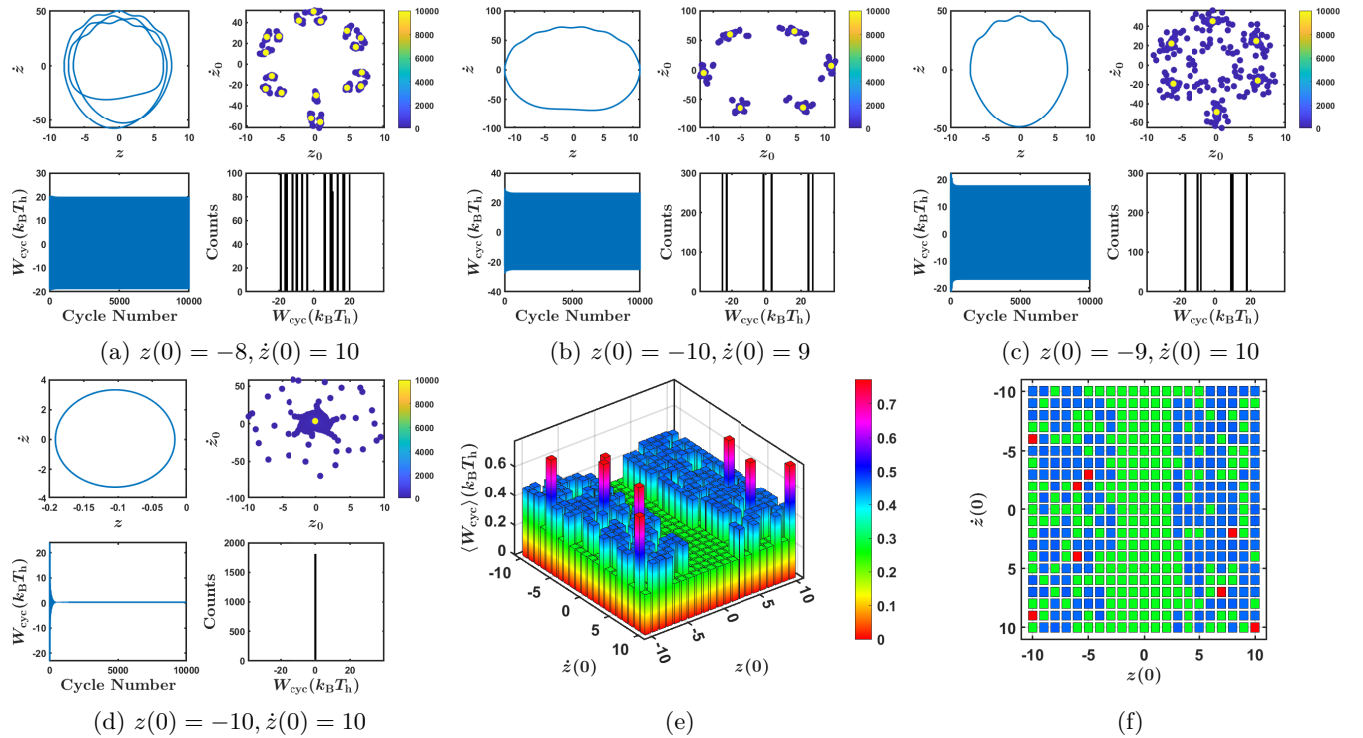


Fig. S42. Different solutions of the zero temperature Langevin equation at $v_{\text{dr}} = 0.4 \text{ m/s}$, $\eta = 3.0$ and $\mu = 4 \times 10^{-4} \text{ s}^{-1}$. (a), (b), (c) and (d) Four different solutions of different initial conditions. In each of the four subfigures, the top left subgraph is the limit cycle on the $z - \dot{z}$ phase plane. The bottom left subgraph is the cycle work from the first to the last simulation cycle during the simulation time range. The bottom right subgraph is the count distribution of W_{cyc} of the last 1800 simulation cycles. The top right subgraph is the Poincaré (or stroboscopic) map (42) sampled at the starting point of each cycle, i.e. the set of the initial point (z_0, \dot{z}_0) of each cycle with the cycle number indicated by the color of the points ranging from blue at the beginning to yellow at the end. (e) The mean cycle work $\langle W_{\text{cyc}} \rangle$ corresponding to different initial conditions $(z(0), \dot{z}(0))$, which is different from the initial point (z_0, \dot{z}_0) of each cycle. (f) The airview of (e). Other parameters are given in Sec. 8.H. The main text Figure 3(C3) is inherited from (a), (b), (c) and (d) in this figure.

J. The multiple solutions of the zero temperature Langevin equation. The nondimensional Langevin equation at zero temperature is an ordinary differential equation

$$\ddot{z} + \beta \eta \dot{z} + 4\pi^2(z - \tilde{v}\tau) - 4\pi^2 \eta \sin z = 0, \quad [42]$$

and is equivalent to the system

$$\begin{cases} \frac{dz}{d\tau} = \dot{z}, \\ \frac{d\dot{z}}{d\tau} = -\beta \eta \dot{z} - 4\pi^2(z - \tilde{v}\tau) + 4\pi^2 \eta \sin z. \end{cases} \quad [43]$$

Substitute $y_1 = z - \tilde{v}\tau$, $y_2 = \dot{z}$ into Eq. 43, we obtain

$$\begin{cases} \frac{dy_1}{d\tau} = y_2, \\ \frac{dy_2}{d\tau} = -\beta\eta y_2 - 4\pi^2 y_1 + 4\pi^2 \eta \sin(y_1 + \tilde{v}\tau). \end{cases} \quad [44]$$

It's clearer now that this equation system has periodic solution from the last term on the right hand side of the second equation. Using the standard integrator ode113 in Matlab, which is of lower cost and higher precision than ode45 based on an explicit Runge-Kutta (4,5) formula (43), we can obtain these periodic solutions.

In Figure S42, four solutions at $v_{dr} = 0.4\text{m/s}$ are plotted and we can see that different initial conditions lead to different limit cycles with different periods and different mean cycle work $\langle W_{cyc} \rangle$. Solutions at other driving velocities are represented by the red circles in Figure S44 and the main text Figure 6. The mean cycle work $\langle W_{cyc} \rangle$ is calculated from the last cycles of a number of multiple $P_{c.n.}$'s (Eq. 48) if the steady state solution is periodic. If the steady state solution is nonperiodic (including the cases in which we haven't achieved the steady state solution after a too long simulation time), the $\langle W_{cyc} \rangle$ is calculated from the last cycles of a presumably adequate number.

In Figure S43, we plot the solutions at $v_{dr} = 0.1\text{m/s}$, $\eta = 3.0$ and $\mu = 4 \times 10^4\text{s}^{-1}$ to give an impression of the peculiarity of the limit cycles and Poincare maps at some driving velocities. More limit cycles can be found in Figure S47, S48 and S49.

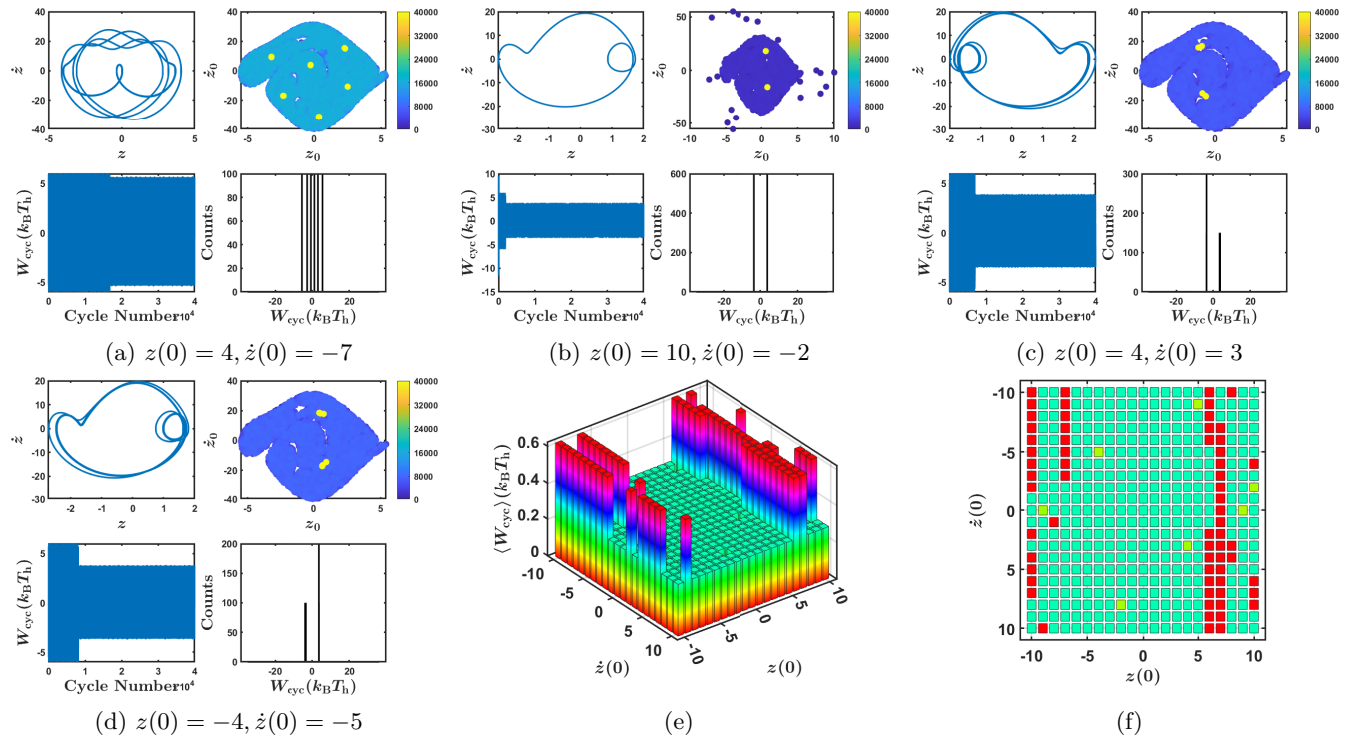


Fig. S43. Different solutions of the zero temperature Langevin equation at $v_{dr} = 0.1\text{m/s}$, $\eta = 3.0$ and $\mu = 4 \times 10^4\text{s}^{-1}$. (a), (b), (c) and (d) Four different solutions of different initial conditions. In each of the four subfigures, the top left subgraph is the limit cycle on the $z - \dot{z}$ phase plane. The bottom left subgraph is the cycle work from the first to the last simulation cycle during the simulation time range. The bottom right subgraph is the count distribution of W_{cyc} of the last 1200 simulation cycles. The top right subgraph is the Poincare (or stroboscopic) map (42) sampled at the starting point of each cycle, i.e. the set of the initial point (z_0, \dot{z}_0) of each cycle with the cycle number indicated by the color of the points ranging from blue at the beginning to yellow at the end. (e) The mean cycle work $\langle W_{cyc} \rangle$ corresponding to different initial conditions $(z(0), \dot{z}(0))$, which is different from the initial point (z_0, \dot{z}_0) of each cycle. (f) The Airview of (e). Other parameters are given in Sec. 8.H.

K. The nonlinear bifurcation of $\langle W_{cyc} \rangle$ with respect to v_{dr} .

K.1. Continuation of the zero temperature $\langle W_{cyc} \rangle - v_{dr}$ curve. We first need to transform the ordinary equation system Eq. 43 into a form which is easy to continue. Substitute $y_1 = z - \tilde{v}\tau$, $y_2 = \dot{z}$, $y_3 = \sin z$ and $y_4 = \cos z$ into Eq. 43 we obtain

$$\begin{cases} \dot{y}_1 = y_2, \\ \dot{y}_2 = -\beta\eta y_2 - 4\pi^2 y_1 + 4\pi^2 \eta y_3, \\ \dot{y}_3 = (y_1 + \tilde{v}) \cos z, \\ \dot{y}_4 = -(y_1 + \tilde{v}) \sin z, \end{cases} \quad [45]$$

which is equivalent to

$$\begin{cases} \dot{y}_1 = y_2, \\ \dot{y}_2 = -\beta\eta y_2 - 4\pi^2 y_1 + 4\pi^2 \eta y_3, \\ \dot{y}_3 = y_3 + (y_2 + \tilde{v})y_4 - y_3(y_3^2 + y_4^2), \\ \dot{y}_4 = y_4 - (y_2 + \tilde{v})y_3 - y_4(y_3^2 + y_4^2). \end{cases} \quad [46]$$

This equation system can be used as a model system for the continuation software MatCont (44).

We first solve the ordinary differential equation with the Matlab integrator ode113 to obtain several periodic solutions, i.e. limit cycles in the phase plane (45). Starting with one of the limit cycles, we can continue the branch containing this limit cycle.

The mean cycle work is calculated by

$$\begin{aligned} \langle W_{\text{cyc}} \rangle &= \frac{1}{T v_{\text{dr}}/a} \int_0^T \kappa(v_{\text{dr}}t - x) v_{\text{dr}} dt = \frac{a}{T v_{\text{dr}}} \int_0^T \kappa(v_{\text{dr}}t - x) d(v_{\text{dr}}t) \\ &= \frac{a}{\tilde{T} \tilde{v} \frac{a}{2\pi}} \int_0^{\tilde{T}} \kappa \frac{a}{2\pi} (\tilde{v}\tau - z) d\left(\frac{a}{2\pi} \tilde{v}\tau\right) = \frac{1}{2\pi \tilde{T}} \int_0^{\tilde{T}} \kappa a^2 (\tilde{v}\tau - z) d\tau, \end{aligned} \quad [47]$$

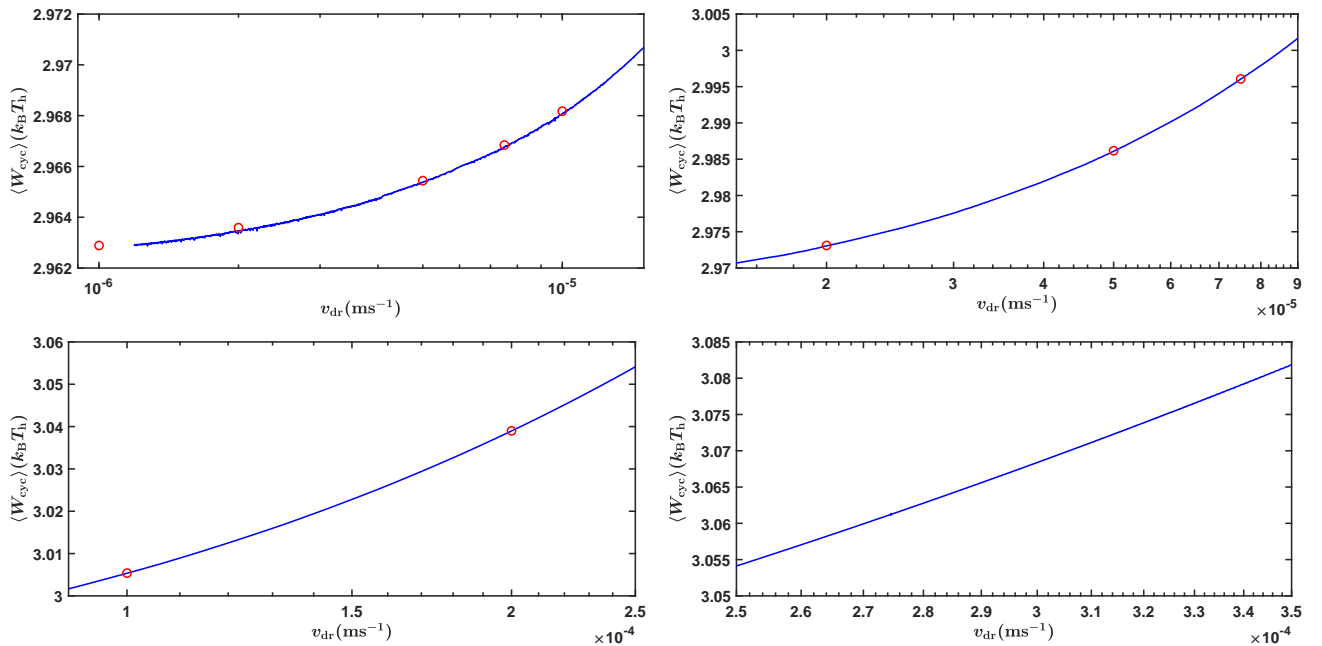
where $\tilde{T} = \frac{\omega_0 T}{2\pi}$ is the nondimensional period of the limit cycle on the branch. The period T of the limit cycle may equal to one or several $\frac{a}{v_{\text{dr}}}$ s.

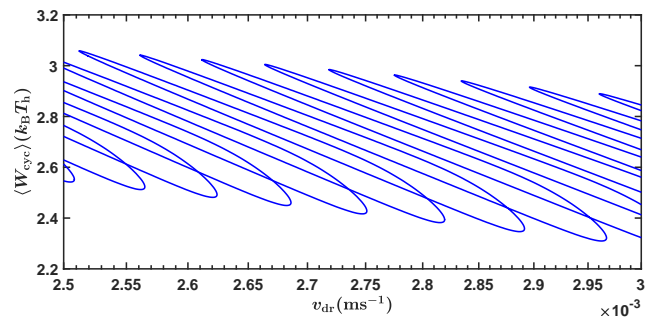
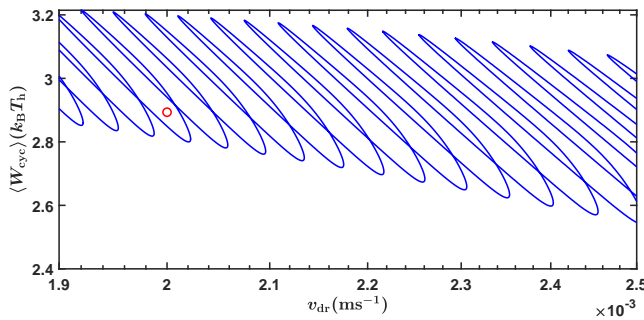
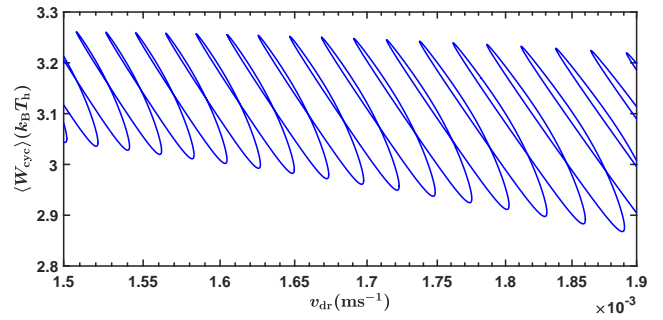
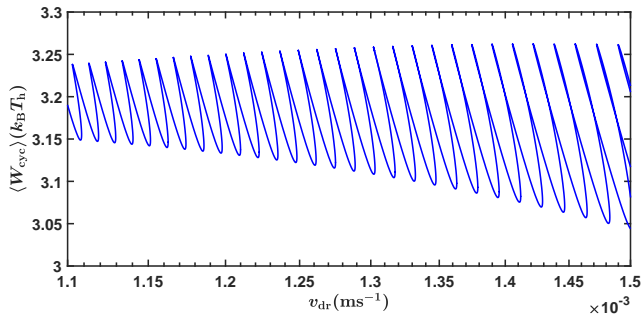
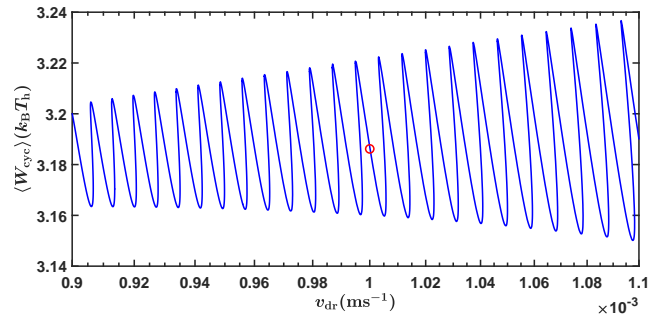
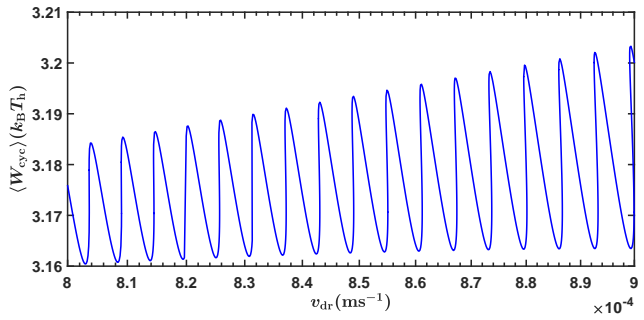
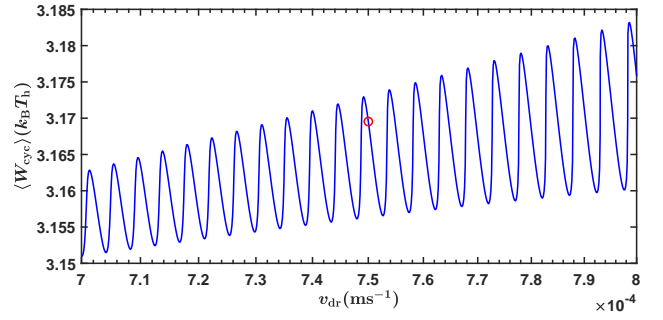
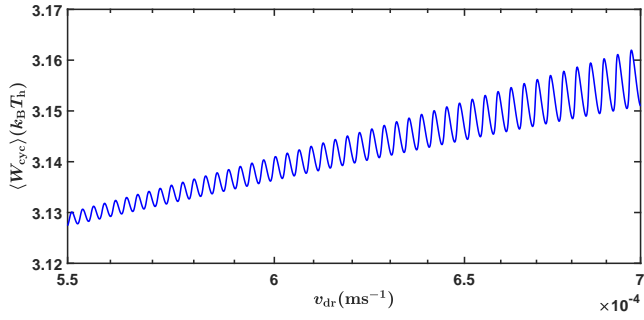
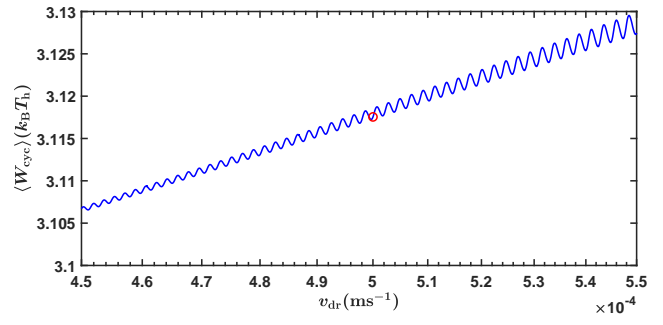
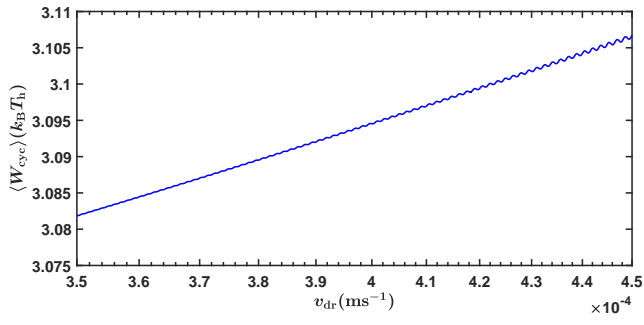
K.2. Details of the $\langle W_{\text{cyc}} \rangle - v_{\text{dr}}$ bifurcation diagram. Some details of the bifurcation diagram of $\langle W_{\text{cyc}} \rangle$ with v_{dr} as the parameter, i.e. Figure 6 in the main text, are plotted in Figure S44.

The cycle number period

$$P_{\text{c.n.}} = \frac{T v_{\text{dr}}}{a}, \quad [48]$$

is an invariant of each curve distinguished by the color. Here T is the actual temporal period of the particle which should be one or more integer multiples of $\frac{a}{v_{\text{dr}}}$. In the main text Figure 6, besides the first and higher order period doubling curves with $P_{\text{c.n.}} = 2^n, n = 1, 2, \dots$ on the blue backbone curve ($P_{\text{c.n.}} = 1$) as shown in detail in the last subfigure in Figure S44, other isolated loops have other values of $P_{\text{c.n.}}$. For instance, on the black loops $P_{\text{c.n.}} = 3$; on the dark green loops $P_{\text{c.n.}} = 6$; on the dark red loops $P_{\text{c.n.}} = 12$; on the orange loop $P_{\text{c.n.}} = 9$; on the purple loop, which is a period doubling branch of the orange loop, $P_{\text{c.n.}} = 18$.





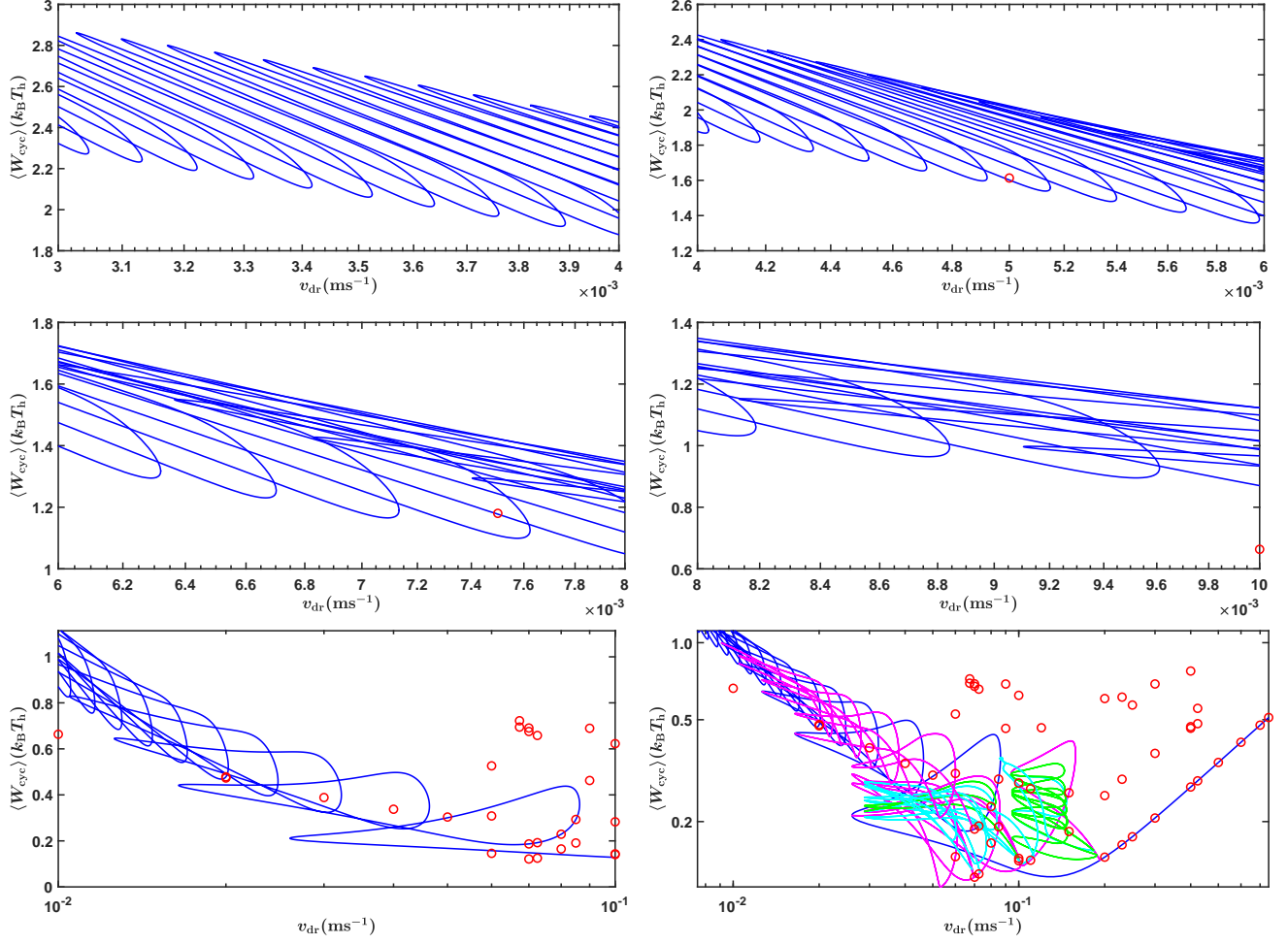


Fig. S44. Details of Figure 6 in the main text with some of its segments zoomed in. The last subfigure gives some of the first and higher order period doubling (42) branches of the blue backbone curve on which the cycle number period $P_{\text{c.n.}} = 1$. The megenta curves have $P_{\text{c.n.}} = 2$; the cyan ones have $P_{\text{c.n.}} = 4$; and the green ones have $P_{\text{c.n.}} = 8$. The cycle number period $P_{\text{c.n.}}$ is an invariant of each curve. Parameters: $\eta = 3.0$, $\mu = 4 \times 10^4 \text{ s}^{-1}$, $\Theta = 0$ and others are given in Sec. 8.H.

K.3. Some of the peculiar nonlinear features of the ordinary differential equation based on the PT model. In this subsection, we discuss some of the peculiar nonlinear features of the ordinary differential equation based on the PT model, including the following three topics: symmetry, limit cycles and tori. We give a preliminary analysis of the three topics in this subsection to attract the readers', especially the nonlinear science community's, attention to the peculiar nonlinearity of the ordinary differential equation based on the PT model and and we hope more scholars can join us to analyze it further.

1. **Symmetry** When projected to the $\langle W_{\text{cyc}} \rangle - v_{\text{dr}}$ space, some unclosed $x(0) - v_{\text{dr}}$ and $v(0) - v_{\text{dr}}$ curves become closed as shown in Figure S45. Here the $x(0)$ and $v(0)$ are the coordinates of the first point of the limit cycle at the specific v_{dr} calculated by continuation (44, 45). In Figure S46, we plot a case of closed $x(0) - v_{\text{dr}}$ and $v(0) - v_{\text{dr}}$ curves remaining closed when projected to the $\langle W_{\text{cyc}} \rangle - v_{\text{dr}}$ space for comparison.

In Figure S46, we also plot the first order and one of the second order period doubling branches. We can see that the closed period doubling loops in the $x(0) - v_{\text{dr}}$ and $v(0) - v_{\text{dr}}$ spaces become two unclosed curves when projected to the $\langle W_{\text{cyc}} \rangle - v_{\text{dr}}$ space, indicating some special symmetry (46).

2. **Limit cycles** In Figure S47, S48, we plot the limit cycles corresponding to some of the red circles in Figure S44. The rest red circles with no period or with a torus as the limit are given in Figure S49. All the limit cycles are calculated with the method described in Sec. 6.J.

In Figure S47, all the limit cycles have the cycle number period $P_{\text{c.n.}} = 1$ and are on the blue backbone curve in the main text Figure 6, comparing with which we can see the corresponding features of the limit cycles at different driving velocity regimes, cf. the caption of Figure S47.

The limit cycles of some of the red circles out of the blue backbone curve are plotted in Figure S48 to give the readers an impression of the exotic shapes of the limit cycles.

3. **Tori** In Figure S49, the six phase curves represent solutions with a torus as the limit or with no period. They are in the velocity weakening regime, or to be exact, in the transition regime between the stick-slip regime and the resonance regime, cf. Figure S25 and Sec. 6.H.

If we set $y_5 = \tilde{v}\tau$ and add $\dot{y}_5 = \tilde{v}$ to Eq. 46, the four dimensional phase space consisting of four variables (y_1, y_2, y_3, y_4) becomes a five dimensional phase space of $(y_1, y_2, y_3, y_4, y_5)$. y_5 is a variable with radian as dimension and can be mapped onto a circle so that we can project the five dimensional phase space of $(y_1, y_2, y_3, y_4, y_5)$ in the three dimension cylindrical coordinate space $(y_5, y_1, y_2) = (\theta, r, h)$. In the top left subgraph of each subfigure in Figure S50, we plot the projection results of the six cases in Figure S49. To avoid the curves intersect themselves, we have add 10 to y_1 in these six subgraphs, i.e. the particle's trajectories are actually embedded in the cylindrical coordinate space $(\theta, r, h) = (\tilde{v}\tau, z - \tilde{v}\tau + 10, \dot{z})$ in the top left subgraph of each subfigure in Figure S50. The Poincare (or stroboscopic) map (42) sampled at the initial instant of each cycle (z_0, \dot{z}_0) are plotted in the top right subgraphs of each subfigure in Figure S50 without shift of y_1 . From the cylindrical coordinate embedded phase trajectories and the Poincare maps of the cases of $v_{dr} = 10^{-3}$ and 5×10^{-3} m/s we can recognize two clear tori, whose intersection with the $\tilde{v}\tau = 0$ plane (the Poincare section) are on two ellipses after the steady state has been achieved. We can see that the two Poincare maps are continuous curves rather than discrete points, so the two trajectories have no period of rational multiples of $\frac{a}{v_{dr}}$, i.e. the two solutions are quasiperiodic. So the angular frequency of the longitudinal motion along the axis of the torus $\omega_1 = 2\pi \frac{v_{dr}}{a}$ and the angular frequency of the latitudinal motion surrounding the cross section of the torus ω_2 are incommensurate, i.e. the ratio $\frac{\omega_1}{\omega_2}$ is irrational (42). For both of the two torus solutions, we can see that the mean cycle work $\langle W_{cyc} \rangle$ denoted by the two red circles in Figure S44 are on the blue backbone curve at the corresponding v_{dr} 's, indicating that at the two v_{dr} 's the $P_{c.n.} = 1$ limit cycles are unstable and the torus bifurcation branches are stable with the two limit cycles as their axes (42). So after being averaged the torus branch will coincide with its axis limit cycle branch in the $\langle W_{cyc} \rangle - v_{dr}$ bifurcation diagram. This is a speculation and should be verified further.

At $v_{dr} = 2 \times 10^{-3}$ and 7.5×10^{-3} m/s, there seems to be several tori for the particle to shift from one to another. The rest two cases in Figure S49 with no period indicating that there may be no stable solutions at these two driving velocities. We haven't considered the stability of the branches, which should be investigated further.

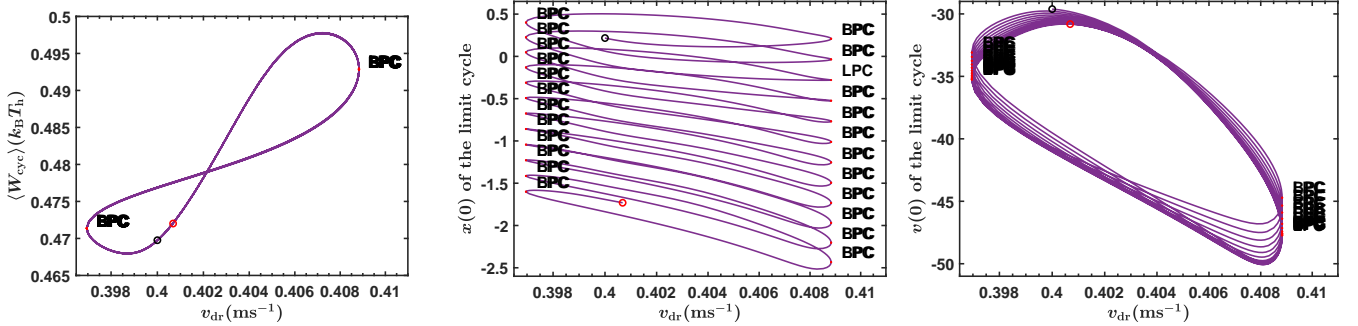


Fig. S45. Closed $\langle W_{cyc} \rangle - v_{dr}$ curve and unclosed $x(0) - v_{dr}$ and $v(0) - v_{dr}$ curves at zero temperature. The red circle at $v_{dr} = 0.4$ m/s is the starting point of this batch of continuation and the black circle is the end point. For the $\langle W_{cyc} \rangle - v_{dr}$ curve, the starting and end points are on the same closed curve, while for the $x(0) - v_{dr}$ and $v(0) - v_{dr}$ curves, the starting and end points are at the two ends of an unclosed curve. Here BPC represents "Branch Point of Cycles" and LPC represent "Limit Point bifurcation of Cycles" (44). Parameters: $\eta = 3.0$, $\mu = 4 \times 10^4 \text{ s}^{-1}$, $\Theta = 0$ and others are given in Sec. 8.H.

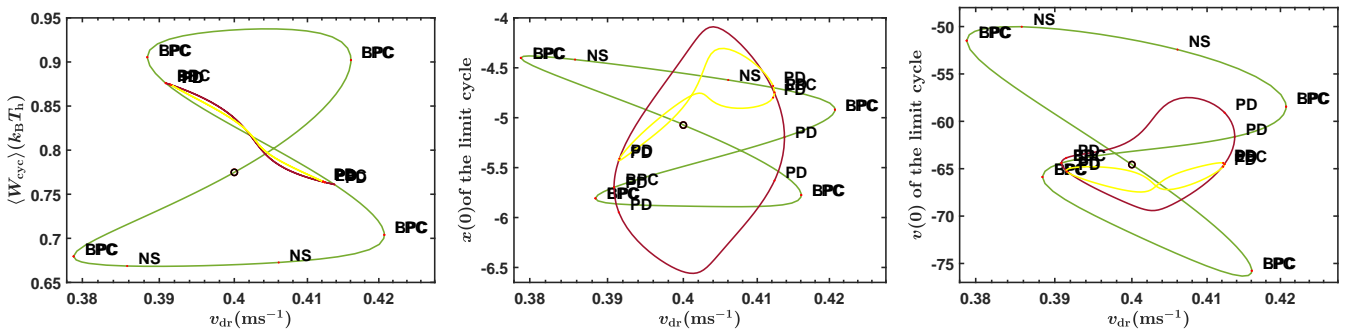
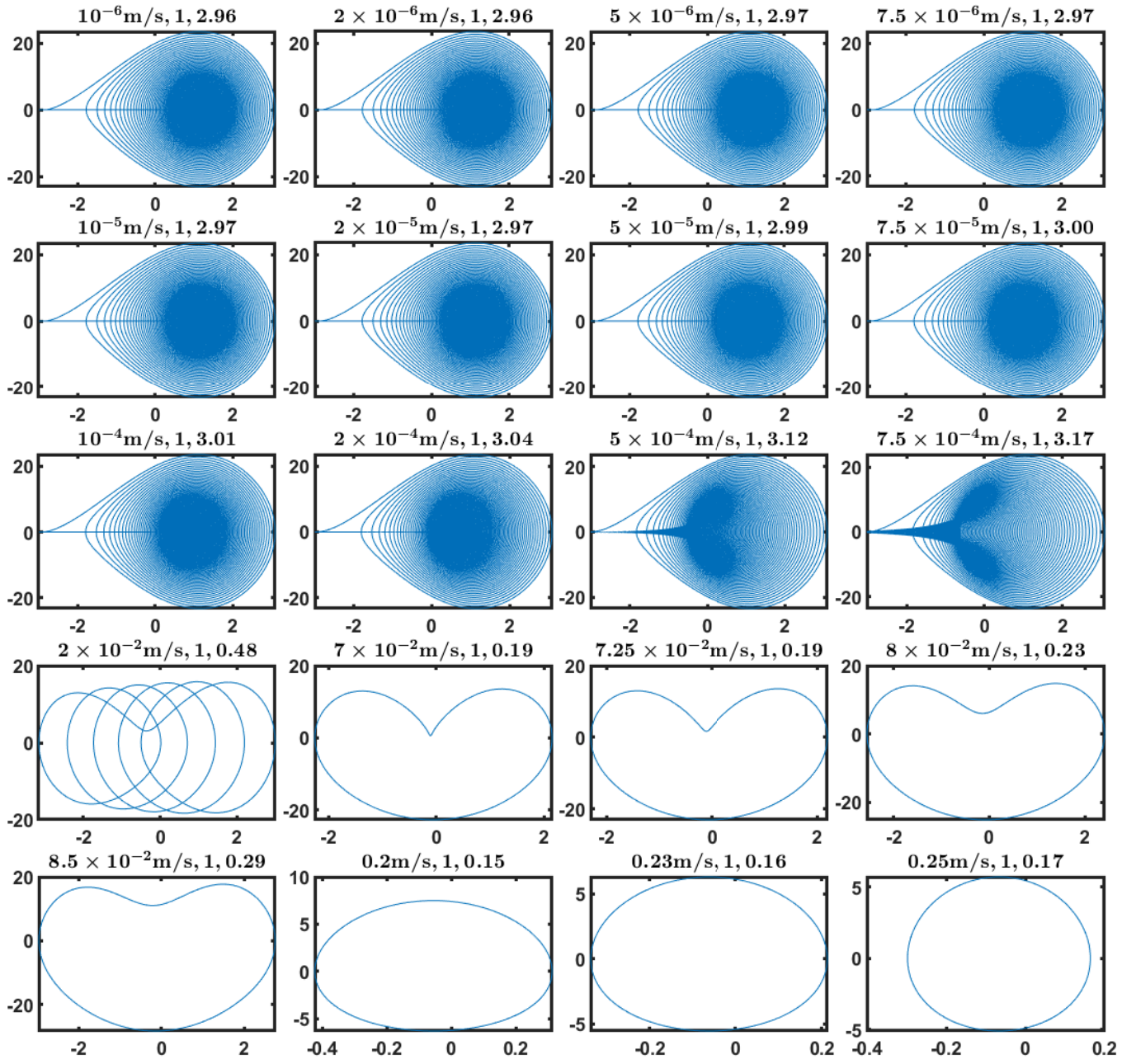


Fig. S46. Closed $\langle W_{cyc} \rangle - v_{dr}$, $x(0) - v_{dr}$ and $v(0) - v_{dr}$ curves at zero temperature. The red circle at $v_{dr} = 0.4$ m/s is the starting point of this batch of continuation and the black circle is the end point. Because the two circles coincide, we can only see the black one. The dark green loop has a cycle number period $P_{c.n.} = 6$ (Eq. 48). The dark red curve is a period doubling branch of the dark green one while the yellow curve is a period doubling branch of the dark red one. Here BPC represents "Branch Point of Cycles"; LPC represents "Limit Point bifurcation of Cycles" and PD represents "Period Doubling points" (44). Parameters: $\eta = 3.0$, $\mu = 4 \times 10^4 \text{ s}^{-1}$, $\Theta = 0$ and others are given in Sec. 8.H.



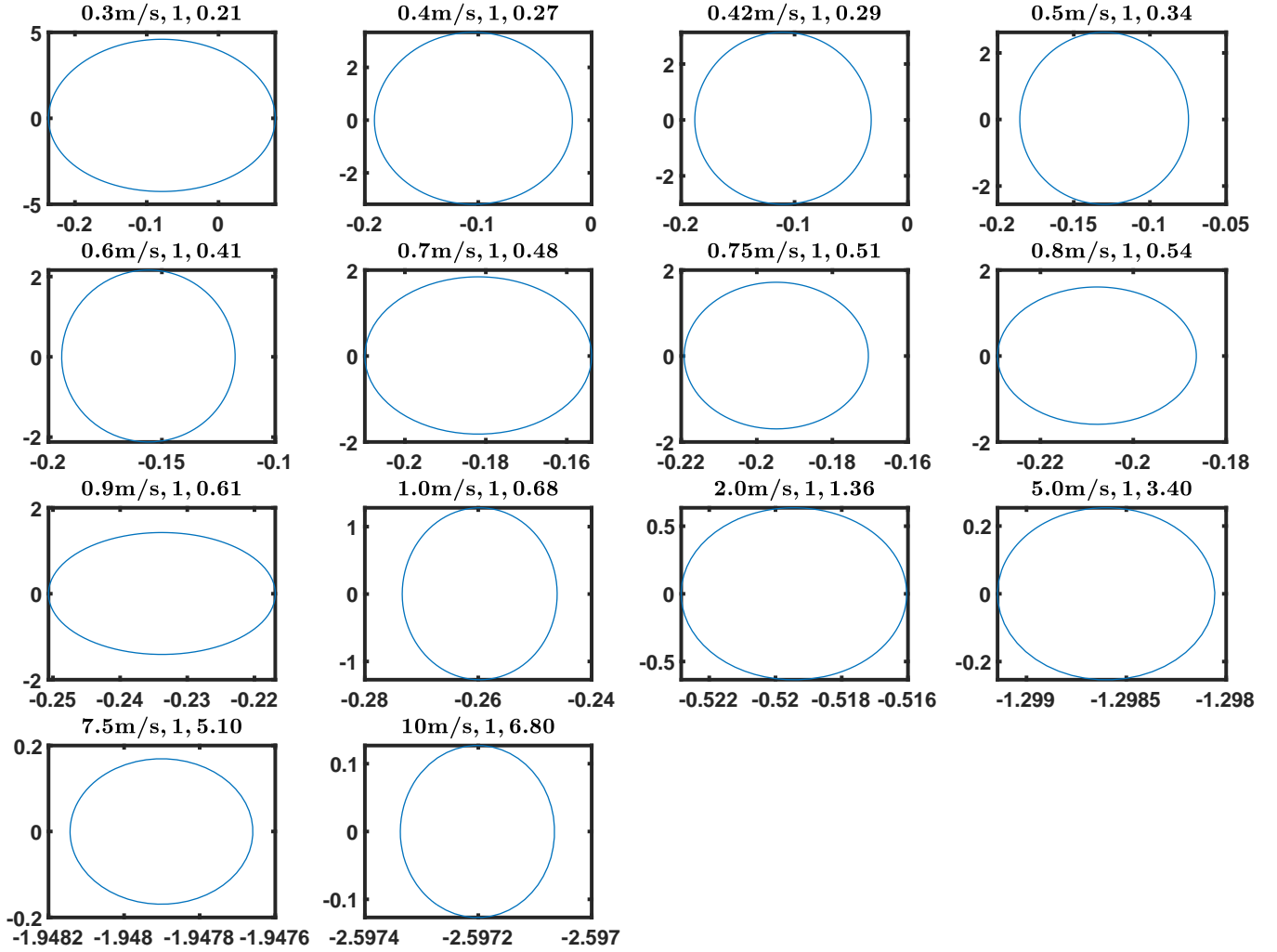
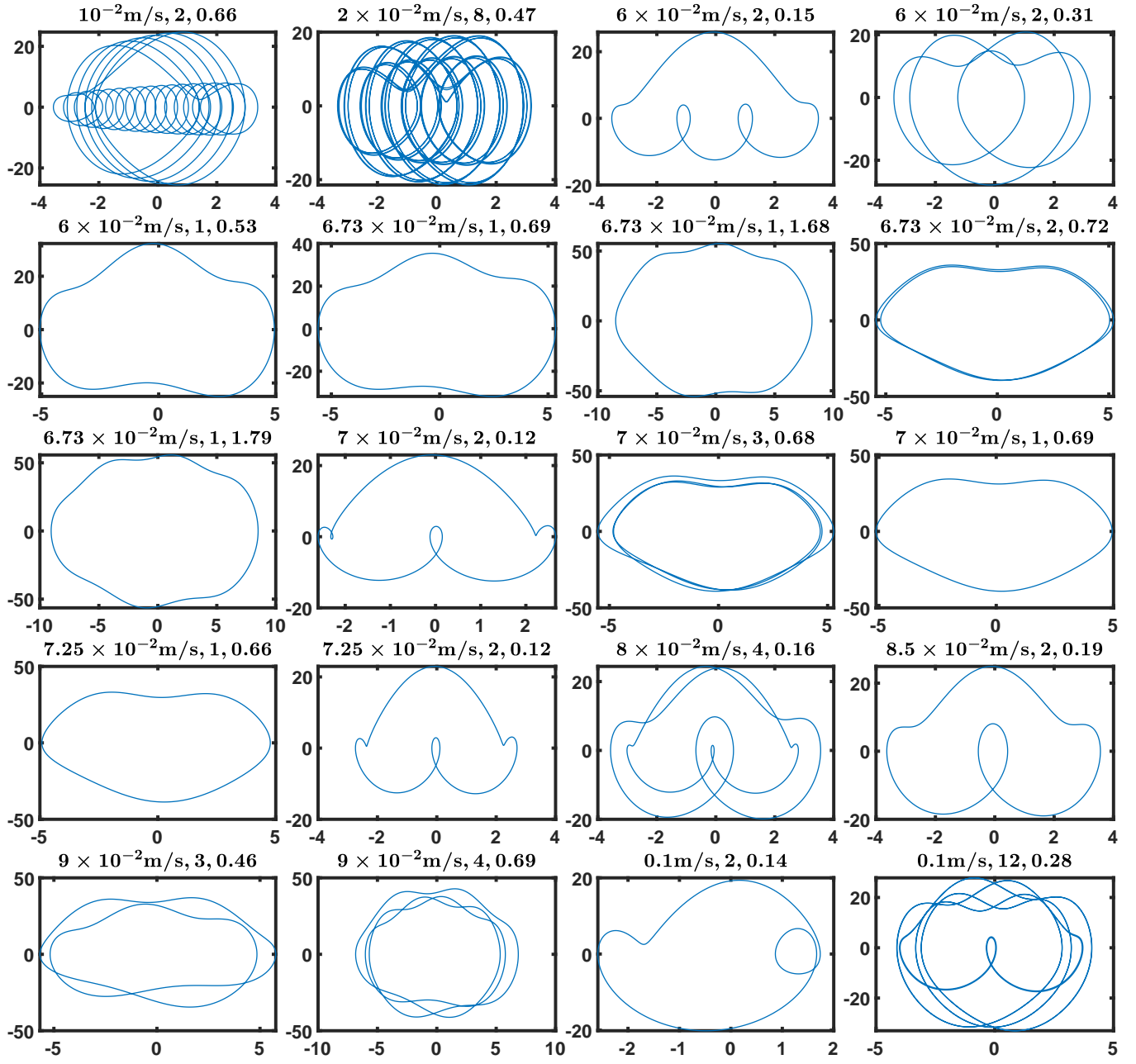


Fig. S47. Limit cycles with the cycle number period $P_{c.n.} = 1$ at different driving velocity v_{dr} corresponding to some red circles on the blue backbone curve in Figure S44 (or the main text Figure 6). The title of each limit cycle has three numbers: the driving velocity v_{dr} , the cycle number period $P_{c.n.}$ and the mean cycle work $\langle W_{cyc} \rangle = W_{cyc}(k_B T_h)$. Here $k_B T_h$ is the same as that in Figure 6 in the main text. All the x -coordinates are the particle's nondimensional position z and the y -coordinates are the particle's nondimensional velocity \dot{z} . The first 9 limit cycles at $v_{dr} \in [10^{-6}, 7.5 \times 10^{-4}]$ m/s corresponding the stick-slip solutions, cf. Figure S25. At and after $v_{dr} = 10^{-3}$ m/s, the interference from the last cycle occurs and there is a short transient stage of torus and nonperiodic solutions as shown in Figure S49, with the limit cycle at $v_{dr} = 2 \times 10^{-2}$ m/s as an exception, whose $P_{c.n.} = 2$ and whose shape is a little complicated. At $v_{dr} \in [7 \times 10^{-2}, 8.5 \times 10^{-2}]$ m/s, the limit cycle becomes one simple loop with a notch. We note that in this velocity regime the blue backbone curve in Figure S44 has more than one solution at a specific v_{dr} . At $v_{dr} \geq 0.2$ m/s the blue backbone curve has only one solution and the notch disappears and the loop approaches to an ellipse.



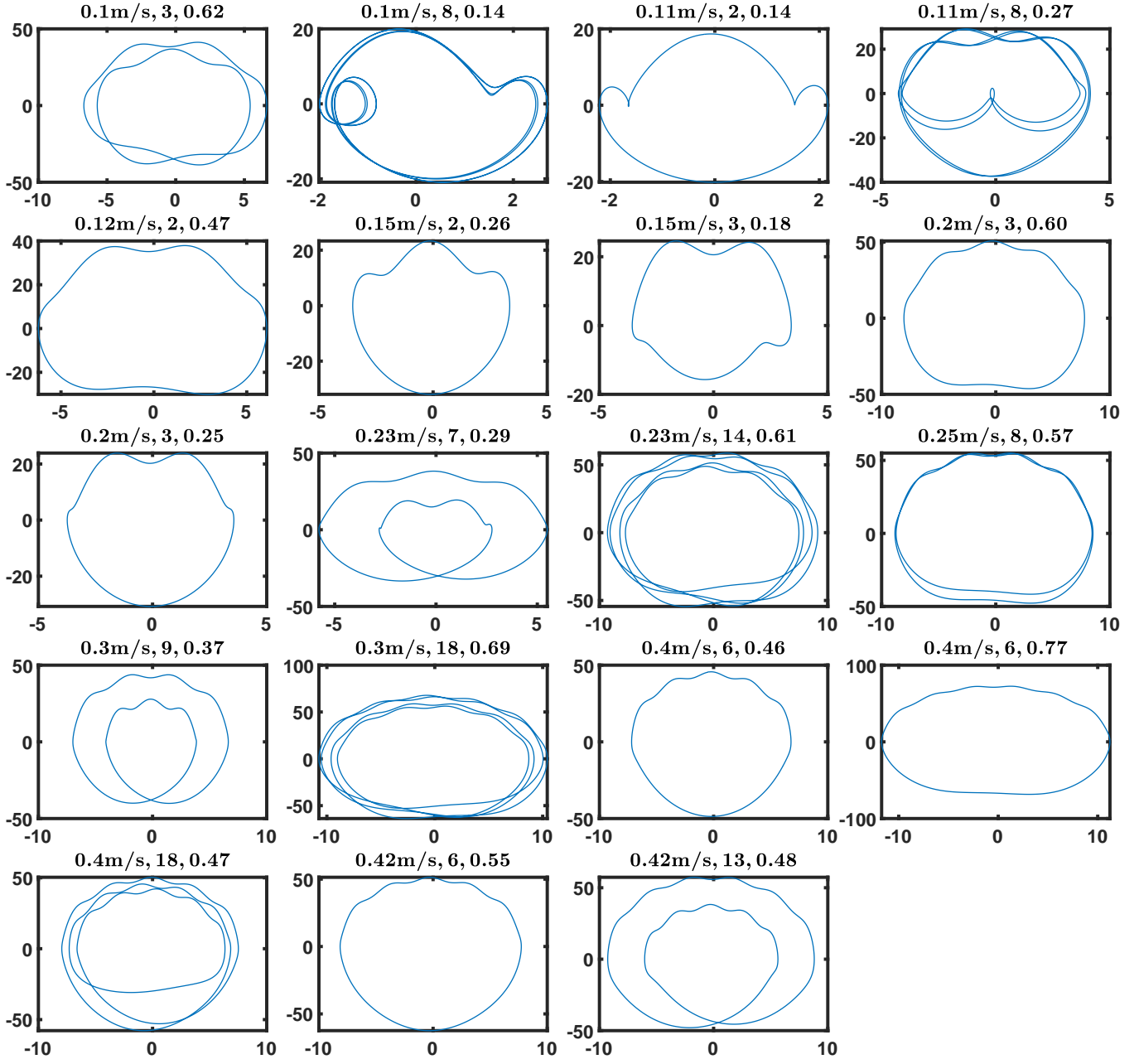


Fig. S48. Limit cycles of some of the red circles out of the blue backbone curve in Figure S44 (or the main text Figure 6). The title of each limit cycle has three numbers: the driving velocity v_{dr} , the cycle number period $P_{c.n.}$, and the mean cycle work $\langle W_{cyc} \rangle / (k_B T_h)$. Here $k_B T_h$ is the same as that in Figure 6 in the main text. All the x -coordinates are the particle's nondimensional position z and the y -coordinates are the particle's nondimensional velocity \dot{z} . These limit cycles are solutions on the isolated loops or the period doubling branches in the main text Figure 6. We can see the shapes of these limit cycles are peculiar.

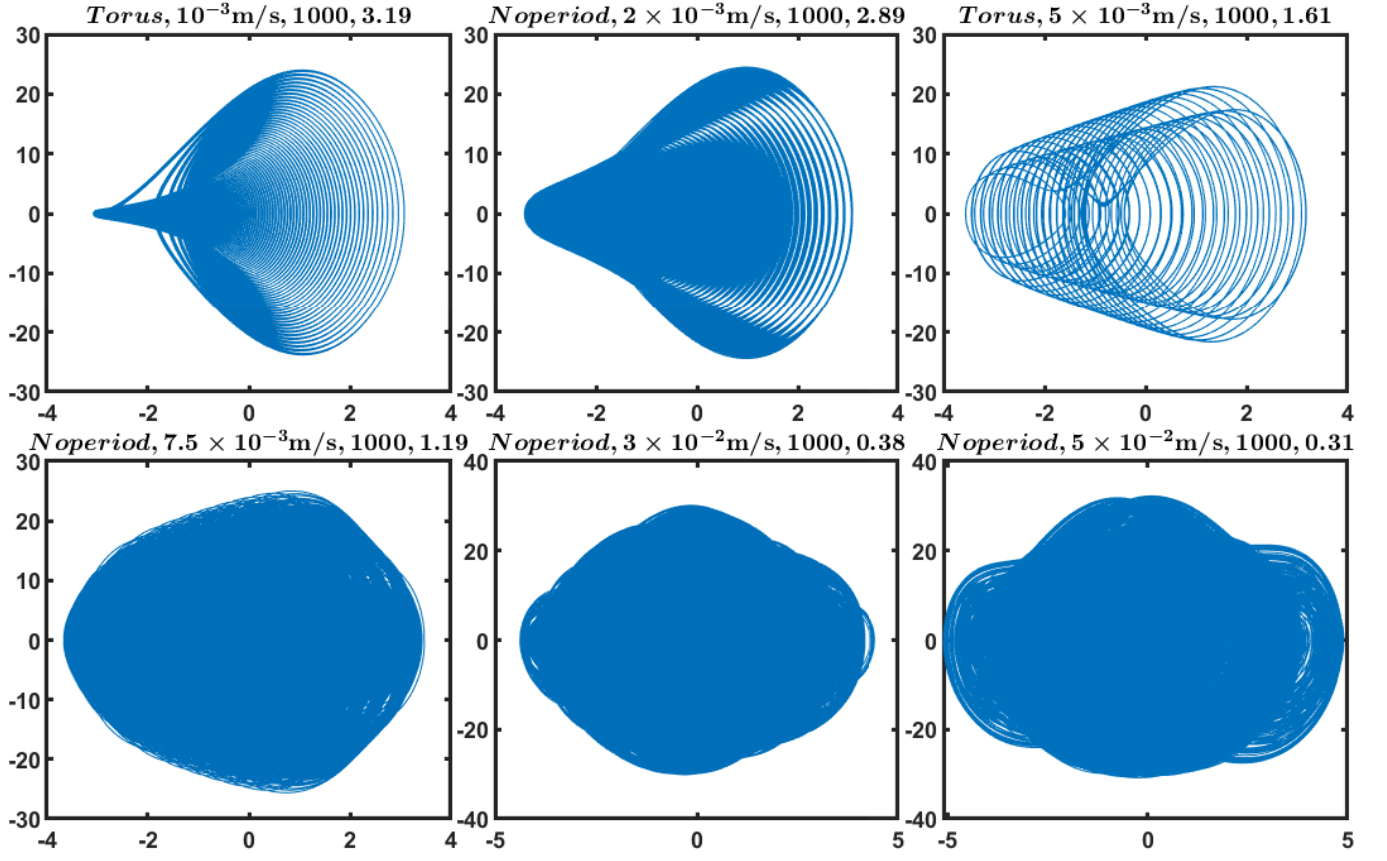


Fig. S49. Phase curves of solutions with a torus as the limit or with no period in Figure S44 (or the main text Figure 6). The title of each subfigure has four fields: Torus or Noperiod, the driving velocity v_{dr} , the number of simulation cycles (different from Figure S47 and S48) and the mean cycle work $\langle W_{cyc} \rangle (k_B T_h)$ averaged over the simulation cycles. Here $k_B T_h$ is the same as that in Figure 6 in the main text. The initial values of the six cases are inherited from the end values of the last simulation cycle used to calculate the corresponding red circles in Figure S44 so that we can make sure that the steady state has already been achieved. All the x -coordinates are the particle's nondimensional position z and the y -coordinates are the particle's nondimensional velocity \dot{z} . These solutions are in the velocity weakening regime after the stick-slip regime and before the resonance regime (Figure S25 and Sec. 6.H). So the torus and nonperiodic solutions are a mark of transition between the stick-slip and the resonance regime. Other aspects of these six solutions are given in Figure S50.

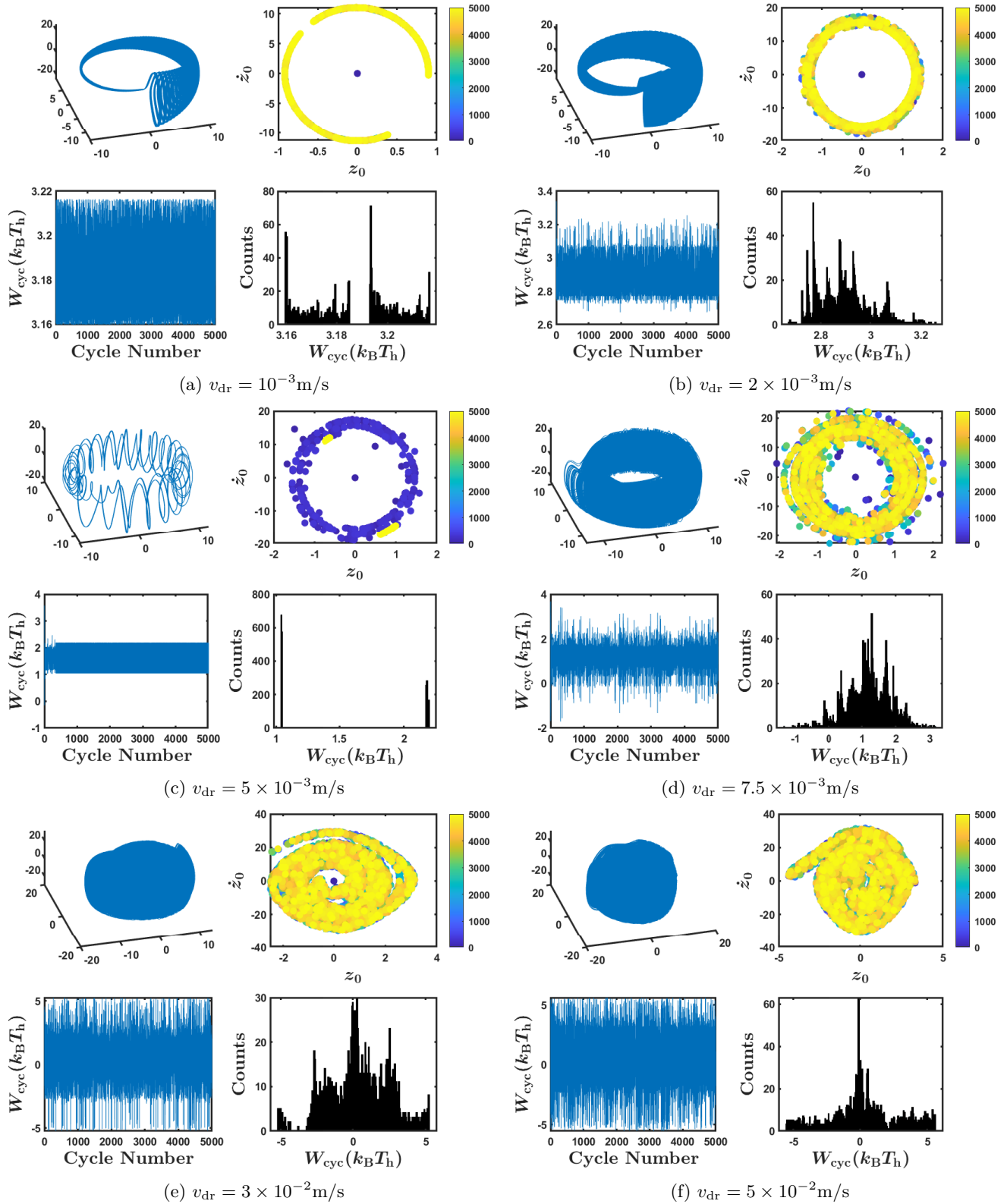


Fig. S50. Other aspects of the six solutions in Figure S49. In each subfigure at different driving velocity v_{dr} , the top left subgraph plots the phase trajectory embedded in the 3-dimensional cylindrical coordinate space $(\theta, r, h) = (\bar{v}\tau, z - \bar{v}\tau + 10, \dot{z})$. The top right subgraph plots the Poincaré (or stroboscopic) map (42) sampled at the starting point of each cycle, i.e. the set of the initial point (z_0, \dot{z}_0) of each cycle with the cycle number indicated by the color of the points ranging from blue at the beginning to yellow at the end. The bottom left subgraph is the cycle work from the first to the last simulation cycle during the simulation time range. The bottom right subgraph is the count distribution of the cycle work W_{cyc} of the total 5000 simulation cycles. In (a) and (c), we can recognize two clear tori. In (b) and (d), there seems to be several tori for the particle to shift from one to another. In (e) and (f), there is no recognizable period.

L. More on the $\eta > 4.6$ cases. In Figure S51 and S52, we plot the energy and displacement curves at $\eta = 8$ and 14 for the subsection “Mean Cycle Work at $\eta > 4.6$ ” in the main text to refer.

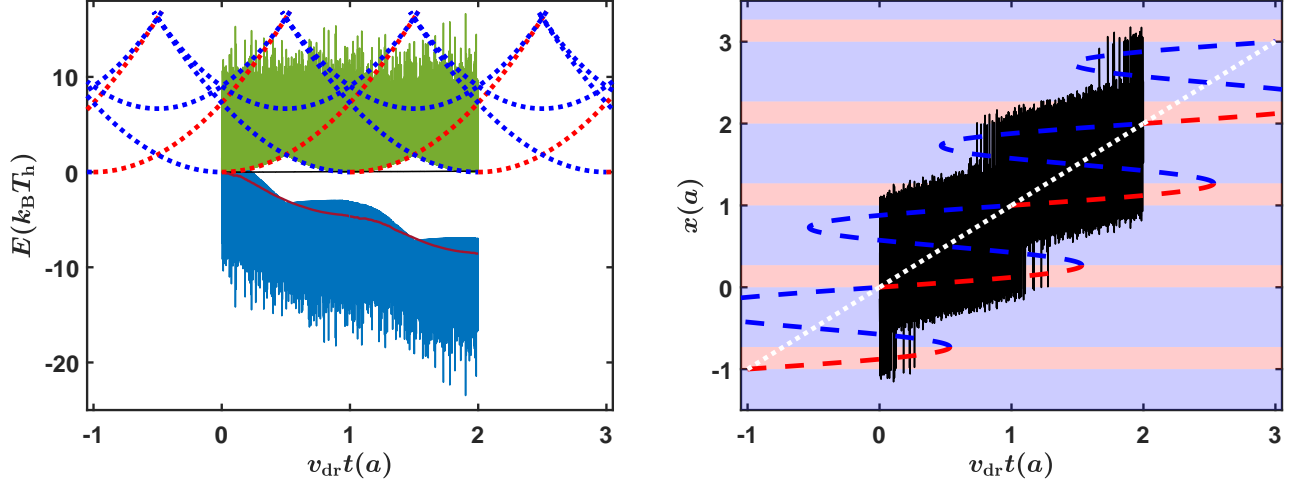


Fig. S51. Energy and displacement curves at $\eta = 8$, $\Theta_{h,c} = 0.4, 0.04$ and $\mu = 4 \times 10^4 \text{s}^{-1}$. Curve colors and types are the same as those in the main text Figure 2(A) and (B) and $k_B T_h$ is of the same value as that in the main text Figure 2(A). The complete picture of the balanced resultant potential curves (the dotted red and blue curves in the left subfigure) and the loci of the balanced point (the dashed red and blue curves in the right subfigure) are given as a complement for the main text Figure 7(B) and (C). Comparing with the $\eta < 4.6$ cases, we can see from the left subfigure that a dotted red local minimum branch goes through two engine cycles, in consistency with that it takes more than one cycle for the middle global minimum in the main text Figure 7(F1) to go leftward and upward through one of the hot zones and out of it at the instant of the BCP (F5) of the next cycle. Symmetrically, a dotted blue energy barrier peak branch even goes through three engine cycles from its appearance at the instant of the FCP of the last cycle to its disappearance at the instant of the BCP of the next cycle. The dashed red and blue curves in the right subfigure are of similar characteristic. So there are two hot and one cold local minima and two energy barriers at the beginning of one cycle while one hot and two cold local minima and two energy barriers at the end, cf. the main text Figure 7(F2) and (F6). In the middle of one cycle there are two hot and two cold local minima and three energy barriers, cf. the main text Figure 7(F4). Please pay attention to the representation of the local minima and the energy barrier peaks by the dotted curves in the left subfigure and the dashed curves in the right subfigure. Simulation results in two consecutive steady state cycles are plotted here. In the middle of either engine cycle, the particle covers two local minima and most of the time stays around the cold local minimum point represented by the bottommost dotted blue branch [marked by the solid purple segment on the bottommost dotted blue curve in Figure S55(a)] in the left subfigure, so the middle stage of the work curve is parallel to the bottommost dotted blue branch in either cycle. However, at the beginning and end of either cycle, the particle covers all the three local minima and tends to neglect the two energy barriers (also see the right subfigure) so that its distribution center approaches the driver center and the work output at the beginning and end stages of the work curve are both reduced, leading to the beginning and end stages of the work curve not parallel to the bottommost dotted blue branch in either cycle in the left subfigure. Although very similar, the work curves during the two cycles are not identical, consistent with the nonzero standard deviation of the $\eta = 8$ circle in the main text Figure 7(A1). Other parameters are given in Sec. 8.H.

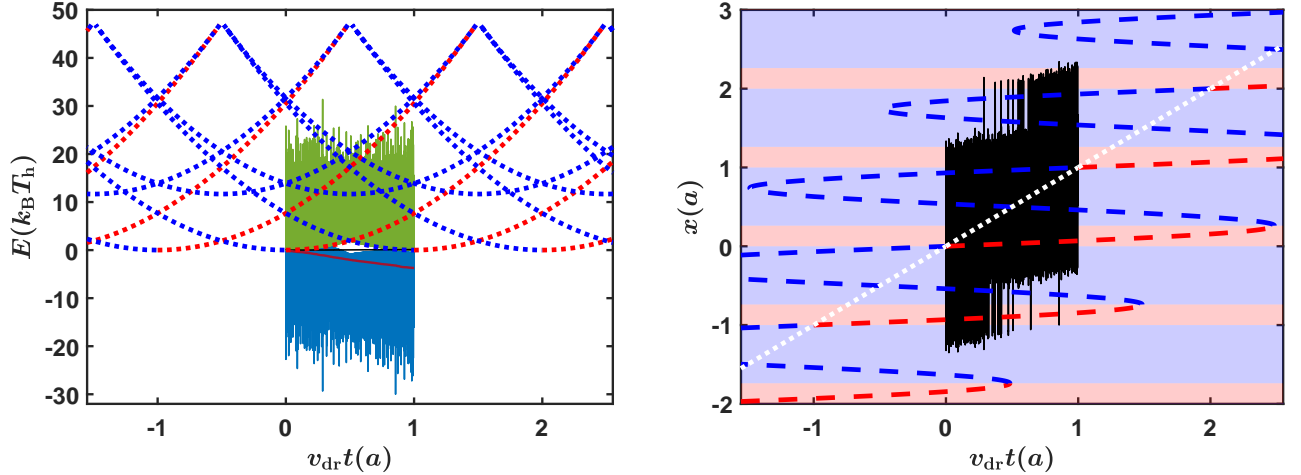


Fig. S52. Energy and displacement curves at $\eta = 14$, $\Theta_{h,c} = 0.4, 0.04$ and $\mu = 4 \times 10^4 \text{s}^{-1}$. Curve colors and types are the same as those in the main text Figure 2(A) and (B) and $k_B T_h$ is of the same value as that in the main text Figure 2(A). The balanced resultant potential curves of the $\eta = 14$ case is more complex than those of the $\eta = 8$ and $\eta \leq 4.6$ cases. We can see that, for instance, in the left subfigure a dotted red local minimum branch goes through 3 engine cycles and at the beginning of one engine cycle there are 3 hot and 2 cold local minima and 4 energy barrier peaks. Other parameters are given in Sec. 8.H.

At the middle instant of one engine cycle, the bottommost energy barrier peak branch has the value of V_0 resulting from the superposition of the global minimum of the harmonic potential, which equals to zero, and a local maximum of the sinusoidal

lattice potential, which equals to V_0 . Due to the same $\Theta_{h,c} = \frac{k_B T_h}{V_0} = 0.4, 0.04$ for both cases in Figure S51 and S52, we can see from the two left subfigures that the dark green internal energy curve exceeds a similar proportion above the bottommost energy barrier peak branch at the middle instant of one engine cycle. However, for the $\eta = 14$ case, the dotted red local minimum branch starting at the beginning of the last (not current) cycle, and the dotted blue local minimum branch ending at the end of the next (not current) cycle, intrude the internal energy curve more deeply than the $\eta = 8$ case, so that the particle remains longer in the neighbor wells both ahead of and behind the global minimum, i.e. the particle covers three wells for a longer period (also cf. the two right subfigures in Figure S51 and S52). Actually, from the right subfigure of Figure S52 we can see that the particle nearly always covers three wells during one cycle and sometimes even covers four wells in the cycle middle, rather than covering three wells only at the beginning and end of one cycle and two wells in the rest of one cycle as in the $\eta = 8$ case. Thus the particle's position distribution center stays close to the driver center rather than nearby one of the local minimum points during the entire cycle, and so the work curve is no longer similar to not only the bottommost dotted blue branch [marked by the solid purple segment on the bottommost dotted blue curve in Figure S55(b)] but also any of the dotted branches in the left subfigure of Figure S52, and it goes down much slower than the bottommost dotted blue local minimum branch. Comparing the two left subfigures of Figure S51 and S52, we can see that the bottommost dotted blue local minimum branches are of similar height in one engine cycle, cf. the end of this subsection. So the work output of the $\eta = 14$ case is declined more and smaller than that of the $\eta = 8$ case [Figure 7(A1) in the main text]. Therefore for the $\eta = 14$ case, the particle's covering more (than two) wells causes the work output reduces a lot from the prediction of the potential mechanism.

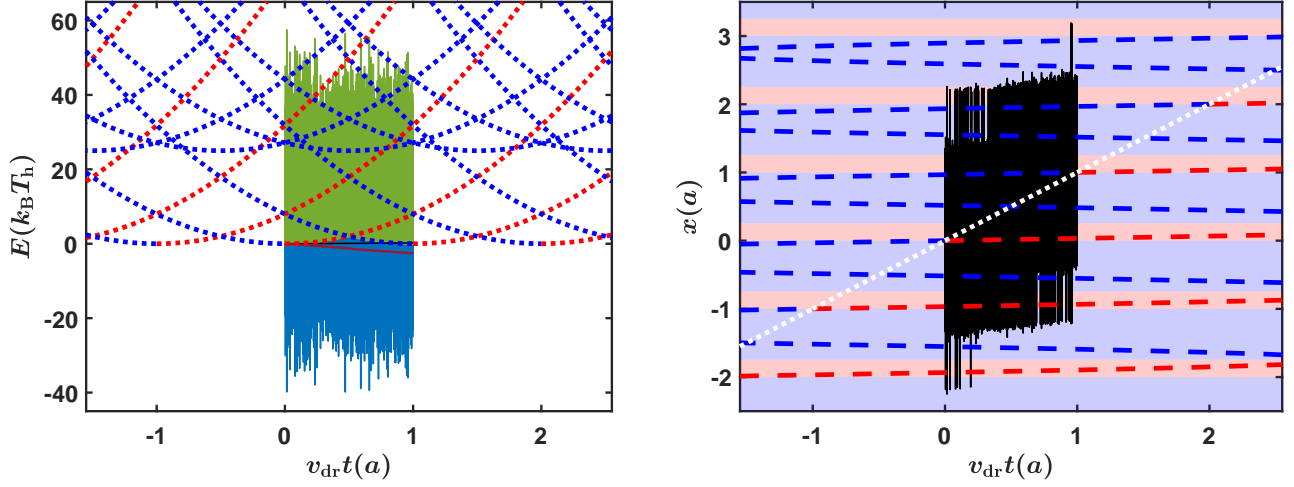


Fig. S53. Energy and displacement curves at $\eta = 30$, $\Theta_{h,c} = 0.4, 0.04$ and $\mu = 4 \times 10^4 \text{s}^{-1}$. Curve colors and types are the same as those in the main text Figure 2(A) and (B) and $k_B T_h$ is of the same value as that in the main text Figure 2(A). The balanced resultant potential curves of the $\eta = 30$ case are even more complex than those of the $\eta = 14$ cases. In the right subfigure we can see that at the beginning of one engine cycle there are 3 hot and 2 cold local minima and 4 energy barrier peaks. In the left subfigure, the dotted red local minimum branches starting at the beginning of the two upstream cycles, and the dotted blue local minimum branches ending at the end of the two downstream cycles, intrude the dark green internal energy curve, so that the particle remains longer in more neighbor wells both ahead of and behind the global minimum. In fact, from the right subfigure we can see that the displacement curve covers two hot local minimum branches and two cold local minimum branches nearly all the way and a third hot branch or a third cold branch part of the way from the beginning to the end of one engine cycle, i.e. the particle always covers four (lowest, of course) wells and sometimes covers five (lowest, of course) wells. Thus the particle's position distribution center stays closer to the driver center and the work curve is very different from and becomes much flatter than the bottommost dotted blue branch in the left subfigure. Other parameters are given in Sec. 8.H.

In Figure S53, we plot the energy and displacement curves of the case of $\eta = 30$, $\Theta_{h,c} = 0.4, 0.04$ and $\mu = 4 \times 10^4 \text{s}^{-1}$. We can see that at the same $\Theta_{h,c}$ as the $\eta = 8$ and 14 cases above, the dark green internal energy curve exceeds a similar proportion above the bottommost dotted blue energy barrier peak branch at the middle point of one engine cycle. With η increasing to 30 there are more dotted red local minimum branches starting at the beginning of upstream cycles, and dotted blue local minimum branches ending at the end of downstream cycles, intrude the internal energy curve. We can see from the right subfigure of Figure S53 that the particle covers two hot and two cold wells all the way and a third hot (at the beginning) or a third cold (at the end) well part of the way from the beginning to the end of one cycle, and in total the particle always covers at least four wells, which is more than the $\eta = 8$ and 14 cases. So the particle's position distribution center is much closer to the driver center [Figure 7(E) in the main text] and the work curve's shape deviates from the bottommost dotted blue local minimum branch much more and is now very close to a horizontal line. At $\eta = 30$ the bottommost dotted blue branch is still of similar height to those of the $\eta = 8$ and 14 cases in one engine cycle, cf. the end of this subsection. So the work output is reduced much more than the $\eta = 14$ and also the $\eta = 8$ case [Figure 7(A1) in the main text].

At $\eta = 30$, the internal energy curve always covers five dotted local minimum branches (three red and two blue or two red and three blue) and sometimes covers six (three red and three blue) in the middle of one cycle. However, this doesn't mean that the particle always covers five wells. In fact, in the right subfigure of Figure S53, we can see that the particle always covers four wells and five only at the beginning and end of one cycle. The reason is that to reach a remote outside well, the particle has to cross over an energy barrier. In the middle of the engine cycle, although the internal energy curve frequently covers the

fifth blue or red local minimum branch, it cannot cover the neighbor energy barrier peak branch above it so that the particle cannot cross over the energy barrier in the way and reach the fifth well. Comparatively, in the $\eta = 8$ case in Figure S51, we can see that the third red or blue branch covered by the internal energy curve is close to the neighbor energy barrier peak branch above it and so the range of the third well covered by the particle is similar to the range of its near center neighbor energy barrier covered. In the $\eta = 14$ case in Figure S52 the range of the third well covered by the particle is also approximate to the range of its near center neighbor energy barrier covered. Generally speaking, at higher η the outward energy barriers outside become higher and harder to be crossed over. So our above conclusion that in the $\eta = 8$ case in Figure S51, the particle always covers two wells and three at the beginning and end of one cycle is correct and the conclusion that in the $\eta = 14$ case in Figure S52, the particle always covers three wells and four in the middle of one cycle is also roughly correct, which can be validated by the displacement curves in the two right subfigures of Figure S51 and S52. To avoid making mistakes, we'd better get the information of the number of wells covered by the particle from the displacement curves.

We want to note that we mean the particle's covering two or more wells by that the particle can stay around one of or hop between or among these wells, which can be represented by the displacement curve (or the internal energy curve, although sometimes not rigorous as we have explained) covering two or more local minimum branches, as in the right subfigures in Figure S51, S52 and S53.

For the $\eta > 4.6$ cases, due to the more local minima of the resultant potential, the approximation of the equilibrium limit of the cycle work is more difficult and the method we utilized in Sec. 6.E no longer works. For instance, in Figure S54, the schematic represents the $\eta = 8$ case corresponding to Figure S7 which we have used to derive $W_{\text{cyc,e.p.}}$ at $\eta \leq 4.6$. We can see that the average jumping point gets out of the current engine cycle to last cycle's cold zone and the particle goes backward along the cold branch and then jumps to the next cold branch back to the current cycle over the energy barrier in-between. This is not physical but it is how we actually calculate the $W_{\text{cyc,e.p.}}$ for the $\eta = 8$ point on the black dot-dashed curve in the main text Figure 7(A1). So at $\eta > 4.6$ the black dot-dashed curve in the main text Figure 7(A1) is incorrect or exactly speaking too loose as we will see next.

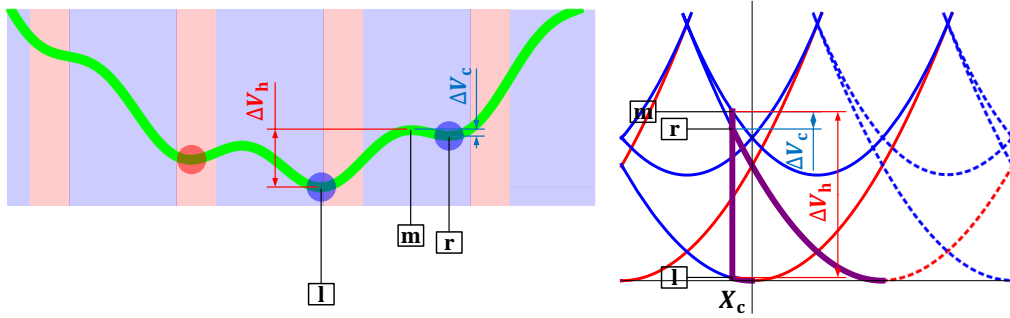


Fig. S54. The schematic of calculating the $W_{\text{cyc,e.p.}}$ value at $\eta = 8$ on the dot-dashed black curve in the main text Figure 7(A1) with the method described in Sec. 6.E. This schematic is the $\eta = 8$ version of Figure S7 with the temperature background of the left subschematic and the balanced resultant potential curves of the right subschematic a little more delicate. On the right we can see that at $\eta = 8 > 4.6$, the balanced resultant potential curve of the current engine cycle extends to the last and next cycles. At the ratio $\Theta_h/\Theta_c = 10$, the jumping point of the particle X_c gets out of the current engine cycle to the last one, so the ascent stage of the resultant potential energy represented by the solid purple curve starting from the cycle starting point goes backward to the last cycle while the descent stage continues more than one cycle, which is not physical. Moreover, from the left subschematic we can see that the particle jumps from a cold well to another cold one which is different from the $\eta \leq 4.6$ cases where the particle usually jumps from a hot well to a cold one. Therefore this method is only suitable for the $\eta \leq 4.6$ cases and does not work for the $\eta > 4.6$ cases, see the caption of Figure S55.

As we have explained above, at $\eta \approx 8$ the work curve is similar to and at $\eta \gtrsim 14$ the work curve gets flatter and flatter than the bottommost dotted blue local minimum branch, so we can approximate the equilibrium cycle work output by the resultant potential energy change of the particle on this branch during one cycle, which is a lower bound and lose espacially at $\eta \gtrsim 14$. In Figure S55(a) and (b), the solid purple vertical line indicates that the particle's resultant potential energy jumps at the beginning of one cycle from the global minimum over the right neighbor energy barrier to the right first local minimum. Then the resultant potential energy decreases to zero along the bottommost dotted blue branch indicated by the solid purple segment. (a) and (b) correspond to the cases of $\eta = 8$ and 14 respectively. The equilibrium work output $W_{\text{cyc,e.p.},\eta > 4.6}$ can be approximated by the height of the solid purple segment on the bottommost dotted blue branch, i.e. the value of the bottommost dotted blue branch at $\frac{v_{\text{dr}} t}{a} = 0$. Note here we indeed approximate the work curve by the bottommost dotted blue branch, i.e. we assume the particle jumps over the right first energy barrier at the beginning of the cycle and then stays on the right first local minimum point driving the driver to transform the resultant potential energy into work output until the end of the cycle, cf. the main text Figure 7(F1)-(F7) where we can see the right first blue ball in (F1) goes backward to the end of the cycle approaching to the driver center, which is equivalent to that the blue ball goes forward to the end of the cycle and the driver center goes after and catches up with it at the end. So this approximation is still based on the potential mechanism, indicated by the subscript 'p'.

Set $\tilde{X}(z(\tau)^*) = 0$ in Eq. 10, we will obtain

$$\begin{cases} 0 = z^* + \eta \sin(z^*), \\ \tilde{V}(z^*) = \frac{1}{2}\eta^2 \sin^2(z^*) + \eta[1 - \cos(z^*)], \end{cases} \quad [49]$$

the first equation of which is equivalent to

$$\frac{\sin(z^*)}{z^*} = -\frac{1}{\eta}, \quad [50]$$

excluding the trivial solution $z^* = 0$.

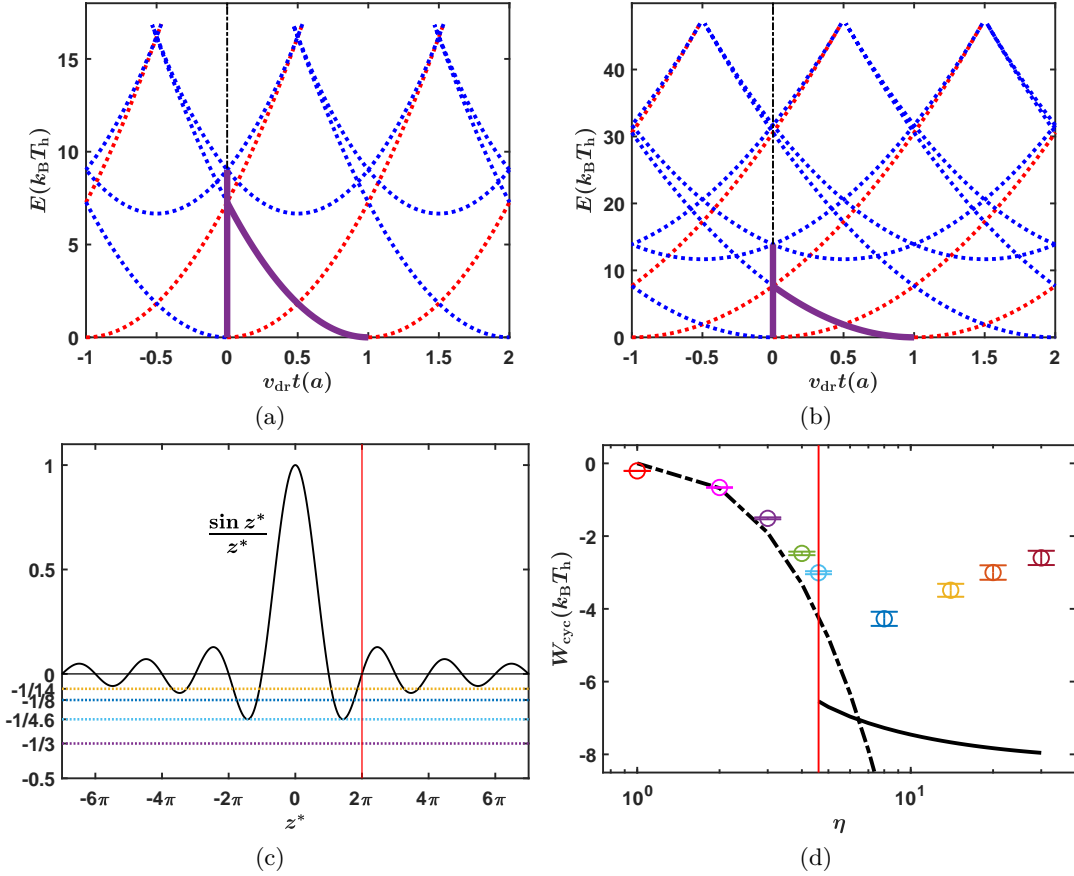


Fig. S55. The approximation of the equilibrium limit cycle work output by the bottommost dotted blue local minimum resultant potential branch at $\eta > 4.6$. In (a) and (b), the solid purple curve represents the particle's resultant potential energy jumps at the beginning of one engine cycle from the global minimum point over the right first energy barrier to the right neighbor local minimum point and then decreases along the bottommost dotted blue local minimum resultant potential branch to zero at $\eta = 8$ and 14 respectively. The dotted red and blue curves in (a) and (b) are inherited from Figure S51 and S52 respectively. In (c), we describe how to locate the nondimensional position z^* of the particle's landing point on the bottommost blue branch, which is represented by the intersection points of the horizontal line $-\frac{1}{\eta}$ with $\frac{\sin(z^*)}{z^*}$ nearby $z^* = 2\pi$ indicated by the vertical solid red line. As $\eta \rightarrow +\infty$, $-\frac{1}{\eta} \rightarrow -0$ and $z^* \rightarrow 2\pi$. In (c), we can see that at $\eta < 4.6$, the horizontal line $-\frac{1}{\eta}$ (e.g. the dotted purple $-\frac{1}{\eta} = -\frac{1}{3}$ line) doesn't intersect $\frac{\sin(z^*)}{z^*}$ and at the first critical value of $\eta \approx 4.6$, the $-\frac{1}{\eta}$ line touches $\frac{\sin(z^*)}{z^*}$ at its two lowest local minima and we can generalize that at the second critical value of η , the $-\frac{1}{\eta}$ line touches $\frac{\sin(z^*)}{z^*}$ at its two second lowest local minima and so on, which gives us another way to calculate the critical values of η (29), cf. Sec. 4. (d) The results of $W_{\text{cyc}, \text{e.p.}, \eta > 4.6}$ at $\Theta_{\text{h}, \text{c}} = 0.4, 0.04$ and $\mu = 10^4 \text{s}^{-1}$ approximated by the height change of the bottommost dotted blue resultant potential curve during one engine cycle, represented by the solid black curve. The results are plotted in the main text Figure 7(A1) for comparison. The dot-dashed black curve representing $W_{\text{cyc}, \text{e.p.}}$ approximated by the method introduced in Sec. 6.E and we have shown in Figure S54 that this approximation is not physical at $\eta \gtrsim 4.6$, which leads to a higher value than the approximation $W_{\text{cyc}, \text{e.p.}, \eta > 4.6} \approx \frac{m\omega_0^2 a^2}{4\pi^2} \tilde{V}(z^*)$ made here. Comparing Figure S54 and (a), we can see that at $\eta \gtrsim 4.6$, the approximation made with the method in Sec. 6.E is a loser lower bound, as can be validated by the lower value of the dot-dashed black curve than the solid black one at high η . Here $\Theta_{\text{h}, \text{c}} = 0.4, 0.04$ and for this ratio $\frac{\Theta_{\text{h}}}{\Theta_{\text{c}}} = 10$, the dot-dashed black curve still has a small physical range from $\eta = 4.6$ to its intersection point with the solid black one, where although the balanced resultant potential curve of the current engine cycle extends out, the jumping point X_{c} is still in the current engine cycle. With η increasing from 4.6 , X_{c} gradually approaches the cycle starting point until the intersection point where X_{c} is just at the cycle starting point, cf. Figure S54.

In Figure S55(c), we plot the function $\frac{\sin(z^*)}{z^*}$. The solution of Eq. 50 can be obtained from the intersection points of $\frac{\sin(z^*)}{z^*}$ with the horizontal line $-\frac{1}{\eta}$. For instance, the dotted dark blue horizontal line representing $-\frac{1}{\eta} = -\frac{1}{8}$ has four intersection points with $\frac{\sin(z^*)}{z^*}$ corresponding to the four nonzero, excluding the trivial zero, intersection points of the vertical dot-dashed line at $\frac{v_{\text{dr}} t}{a} = 0$ with the resultant potential curves in Figure S55(a). The middle two intersection points on the $-\frac{1}{\eta} = -\frac{1}{8}$ line in Figure S55(c) corresponds to the upper two intersection points on the two dotted blue energy barrier peak branches of the current and last cycles in Figure S55(a). The intersection point z^* nearby $z^* = 2\pi$ in Figure S55(c) corresponds to the intersection point of the vertical dot-dashed line with the bottommost blue branch in Figure S55(a), which is what we want. Solve the z^* out with a nonlinear solver and substitute it into the second equation of Eq. 49, we will get the height of the solid purple segment on the bottommost blue branch, $\tilde{V}(z^*)$, which is used to approximate $W_{\text{cyc}, \text{e.p.}, \eta > 4.6} \approx \frac{m\omega_0^2 a^2}{4\pi^2} \tilde{V}(z^*)$

after dimensionalizing back, the result of which is plotted in Figure S55(d) compared with the main text Figure 7(A1). In Figure S55(c), we can see that the dotted dark yellow horizontal line representing $-\frac{1}{\eta} = -\frac{1}{14}$ intersects $\frac{\sin(z^*)}{z^*}$ at 8 points corresponding to the 8 nonzero intersection points of the vertical dot-dashed line with the dotted resultant potential curves in Figure S55(b). And again the intersection point nearby $z^* = 2\pi$ corresponds to the solid purple segment on the bottommost dotted blue branch at $\eta = 14$.

From Figure S55(d), we can see that the above approximation $W_{\text{cyc,e.p.}\eta>4.6} \approx \frac{m\omega_0^2 a^2}{4\pi^2} \tilde{V}(z^*)$ is a lower bound and is loose especially at $\eta \gtrsim 14$ when the particle always covers more than two wells and the work output is declined from $W_{\text{cyc,e.p.}\eta>4.6}$ more. We must note that this curve is obtained at $\Theta_{\text{h,c}} = 0.4, 0.04$, which is high at $\eta > 4.6$ as can be seen in Figure S51, S52 and S53 where the upper bound of the internal energy curve exceeds the bottommost dotted energy barrier peak branch by a large amount from the beginning to the end of one engine cycle, compared with the $\eta < 4.6$ cases in the main text Figure 4. At other values of $\Theta_{\text{h,c}}$, the results may be different especially when $\Theta_{\text{h,c}}$ are low, as we will explain next.

We have seen that keeping $\Theta_{\text{h,c}}$ constant makes the internal energy curve exceeds the bottommost energy barrier peak branch a similar proportion at the middle instant of one engine cycle and makes it possible for us to distinguish the effect of the more teeth of the resultant potential curve at $\eta > 4.6$. Meanwhile, as we have chosen two relatively high values of $\Theta_{\text{h,c}} = 0.4, 0.04$, we can achieve quasi-equilibrium at a not very low driving velocity $v_{\text{dr}} = 10^{-7}$ m/s. At lower v_{dr} , more time steps are needed to simulate one engine cycle, causing high computational cost and long computing time, especially at high η which leads to small time step (Eq. 97). We have mentioned in the main text that at higher η the absolute temperatures $T_{\text{h,c}}$ are higher so that the high absolute temperatures, or rather thermolubricity, play an important role in the reduction of the equilibrium cycle work output at high η , and to have a complete understanding about the effect of the increasing number of teeth of the resultant potential with increasing η on the equilibrium limit of $\langle W_{\text{cyc}} \rangle$, we can keep the absolute temperatures $T_{\text{h,c}}$ constant to see how $\langle W_{\text{cyc}} \rangle$ varies with η or keep η constant at a high value to see how $\langle W_{\text{cyc}} \rangle$ varies with $\Theta_{\text{h,c}}$, at low driving velocity. Here we give a qualitative analysis.

At $8 \lesssim \eta \lesssim 14$ if we reduce $T_{\text{h,c}}$, the period for the particle to cover more than two wells is shortened and the work curve may be more parallel to the bottommost curve so that the work output will increase, cf. Figure S51. Nonetheless, the high temperature T_{h} cannot be too low for the particle to jump over the right first energy barrier early at the beginning of the cycle. At $\eta \gtrsim 14$, even if we decrease $T_{\text{h,c}}$, the work curve is not easy to parallel the bottommost blue branch. The reason is that T_{h} cannot be so low for the internal energy curve to get below the bottommost energy barrier peak branch, otherwise the work input in one cycle may get higher than the work output due to the jumping point moving to the second half of the cycle. Or the work output may be declined due to the jumping point moving to the next cycle or the cycle after the next and so on, which means that the particle starting at the cycle starting point of the current cycle won't slip until the next cycle or the cycle after the next and so on. In this case the engine cycle covers more than one lattice period and multislip may occur and the particle would cover more wells so that the work output would be declined, cf. Figure S52 and S53. We speculate that although T_{h} is low, as long as $T_{\text{h}} > T_{\text{c}}$ there will still be work output even if declined, which is not easy to be validated by the Langevin dynamics simulation due to the low temperatures leading to the particle's difficulty to arrive at equilibrium.

Whereas, if T_{c} is still high and makes the internal energy curve exceed the bottommost energy barrier peak branch from the beginning to the end of one engine cycle, the particle will nearly always cover more than two wells so that the work curve cannot parallel the bottommost dotted blue branch, like the current cases of $\Theta_{\text{h,c}} = 0.4, 0.04$ (at $\eta \gtrsim 14$) we are considering.

If T_{h} is high, T_{c} is low and the ratio $T_{\text{h}}/T_{\text{c}}$ is not too large, the particle could jump from the bottommost dotted red branch over the barrier in-between to the bottommost dotted blue branch in the first half of one engine cycle. For the $\eta = 30$ case in Figure S53, we can see that this situation occurs when $T_{\text{h}}/T_{\text{c}}$ is not greater than 2. In this situation the work curve will similar to those in the main text Figure 4 with two segments and only the descent segment parallels the bottommost dotted blue branch. The high temperature T_{h} should not be too high or too low and the particle should just jump from the bottommost red branch to the bottommost blue branch over the energy barrier in-between and not jump too high to cross over the next energy barrier to the second bottommost red branch, which means the particle jumps to the backward well. Then multislip may occur and the particle may covers more wells and the work curve would deviate from the bottommost dotted blue branch and the cycle work output would be declined. With an appropriate T_{h} , T_{c} could be chosen as low as possible for the particle to jump over the right first energy barrier at the beginning of the cycle and then to be immediately cooled down in the right first cold well, which will make the work curve parallel to the bottommost dotted blue branch and the cycle work output close to $W_{\text{cyc,e.p.}\eta>4.6}$. However, the practical realization of T_{c} which is low enough is difficult and the validation by Langevin dynamics simulation of this situation is also of high computational cost and long computing time.

So we can see at $\eta > 4.6$ the PTSHE is more complicated and the above analysis is preliminary. If the above explanation makes the readers feel confused, they don't need to worry. It's partly due to the authors' weak expression skill. But it does output work and we can turn to the Fokker-Planck or Kramers equation methods (37) to get further understanding.

We have presumed above that covering more wells makes the particle's position distribution center closer to the driver center and so the work output is much smaller, cf. the main text Figure 7(E). This presumption could be further validated by the Fokker-Planck or Kramers equation methods (37).

We have mentioned above that at $\eta > 4.6$ the bottommost dotted blue branches are of similar height in one engine cycle, which can be validated by the solid black curve in Figure S55(d), which changes mildly with η and goes to a limit as $\eta \rightarrow +\infty$. The limit can be calculated. Substitute the first equation of Eq. 49 into the second equation and eliminate η we will obtain

$$\tilde{V}(z^*) = \frac{1}{2}(z^*)^2 + \frac{z^*[\cos(z^*) - 1]}{\sin(z^*)}, \quad [51]$$

in which we have replaced z^* by the specific \hat{z}^* nearby $z^* = 2\pi$. We can see from Figure S55 that as $\eta \rightarrow +\infty$, $-\frac{1}{\eta} \rightarrow -0$ and $\hat{z}^* \rightarrow 2\pi - 0$, so that both the numerator and denominator of the second term on the RHS goes to zero. Using L'Hôpital's rule, the limit

$$\lim_{\hat{z}^* \rightarrow 2\pi - 0} \frac{\hat{z}^* [\cos(\hat{z}^*) - 1]}{\sin(\hat{z}^*)} = \lim_{\hat{z}^* \rightarrow 2\pi - 0} \frac{[\cos(\hat{z}^*) - 1] - \hat{z}^* \sin(\hat{z}^*)}{\cos(\hat{z}^*)} = 0. \quad [52]$$

Therefore, as $\eta \rightarrow +\infty$,

$$\tilde{V}(\hat{z}^*) = \frac{1}{2}(\hat{z}^*)^2 + \frac{\hat{z}^* [\cos(\hat{z}^*) - 1]}{\sin(\hat{z}^*)} \rightarrow \frac{1}{2}(2\pi)^2 = 2\pi^2, \quad [53]$$

and after dimensionalizing back,

$$V(\hat{z}^*) = \frac{m\omega_0^2 a^2}{4\pi^2} \tilde{V}(\hat{z}^*) \rightarrow 2\pi^2 \frac{m\omega_0^2 a^2}{4\pi^2} = \frac{1}{2} m\omega_0^2 a^2 = \frac{1}{2} \frac{m\omega_0^2 a^2}{0.4 \frac{3m\omega_0^2 a^2}{2\pi^2}} k_B T_h = \frac{\pi^2}{1.2} k_B T_h \approx 8.22 k_B T_h, \quad [54]$$

where $k_B T_h = 0.4 \frac{3m\omega_0^2 a^2}{2\pi^2}$ is the same as that of the main text Figure 7(A1).

M. More remarks on the temperature. Comparing the cases of $1 \leq \eta \leq 4.6$ in the same absolute temperatures in Figure 3(B) and in the same nondimensional temperatures in Figure 7(A), we can see that at the same η , in high absolute temperatures the probabilities of jumping over the barrier, $\exp(-\frac{\Delta V_{h,c}}{k_B T_{h,c}})$, are higher so that the equilibrium state is easier to be achieved than the cases in lower absolute temperatures. In other words, in lower temperature equilibrium has to be achieved at lower driving velocity. For instance, the mean cycle work at the low driving velocity end of the $\eta = 4.6$, $\Theta_{h,c} = 0.4, 0.04$ case in Figure 7(A) has almost touches ground while that of the $\eta = 4.6$, $\Theta_{h,c} = 0.26, 0.026$ case in Figure 3(B) still has a trend to decrease if v_{dr} decreases further. For another instance, in Figure 3(B) we can see that in the same absolute temperatures, the velocity range of the work output shrinks to the left as η increases. However, with the absolute temperatures increasing in Figure 7(A) the shrinked velocity ranges extend to the right again.

At nonequilibrium (or rather quasiequilibrium) such as when $v_{dr} = 10^{-5}$ m/s, the high and low temperature zone can be separately considered due to the rare occurrence of the particle's crossing over the middle energy barrier. Then we can deduce that the hot temperature should make the particle easily cross over the barrier from the hot zone and the residual kinetic energy should not be too high for the particle to be cooled down on the right easily. In the cold zone, $k_B T_c$ should be adequately lower than the backward energy barrier ΔV_c so that the particle can be cooled down and stay in the forward well and ahead of the driver center. On the other hand, at equilibrium, the particle crosses over the energy barrier frequently and the hot and cold zone on both sides of the energy barrier should be treated as a whole with the distribution of the particle at each instant calculated by considering the current shape of the resultant potential curve immersed in the alternative high and low temperature field.

In the main case of $\eta = 3$, $\mu = 4 \times 10^4 \text{ s}^{-1}$, $\Theta_{h,c} = 0.4, 0.04$, we can calculate that $\Delta V_h \approx 2.12 k_B T_h$ and $\Delta V_c \approx 2.12 k_B T_c$. At $v_{dr} = 10^{-5}$ m/s (nonequilibrium) the two temperatures $\Theta_{h,c} = 0.4, 0.04$ are a little higher and the driver center should go forward a little to make the forward barrier lower and the backward one higher for the particle to jump backward more rarely so that the mean cycle work output at $v_{dr} = 10^{-5}$ m/s is smaller than $W_{cyc,e.p.}$.

N. Topics about the practical implementation of the PTSHE.

N.1. Parameter choice constrained by the obtainable values of and the mutual relations between temperature and other quantities. In practice, to determine the nondimensional low temperature $\Theta_c = \frac{k_B T_c}{V_0}$ we should first consider the obtainable range of T_c and V_0 and then choose an appropriate Θ_c which is moderately low. The nondimensional high temperature $\Theta_h = \frac{k_B T_h}{V_0}$ can then be chosen appropriately considering the obtainable T_h .

Because the stiffness of the parabola harmonic potential κ is restricted by $\eta = \frac{2\pi^2 V_0}{\kappa a^2}$, the practically attainable range of κ should also be taken into consideration to obtain an appropriate η . As $\kappa = m\omega_0^2$, the mass of the particle m , the intrinsic frequency of the parabola harmonic potential ω_0 can be adjusted to achieve a suitable κ . The lattice period a can also be chosen accordingly on condition that it is large enough relative to the particle's diameter. After choosing the parameters, we'd better do Langevin dynamics simulation to have a big picture of the performance of the PTSHE at these parameters, as different combination of parameters may lead to different behaviors of the PTSHE as we have seen in the main text Figure 3. In a word, the parameters are mutually constrained by each other and to achieve a good performance, we can solve a constraint optimization problem to get the optimum parameters of the PTSHE, in which the Fokker-Planck or Kramers equation method (37) might need to be turned to.

N.2. Implementation of the spatially alternative high and low temperature field. It's not easy to implement a discontinuous temperature curve practically. In Figure S56 we simulate two $\langle W_{cyc} \rangle - v_{dr}$ curves with the change from the high temperature to the low temperature more gently and there is still work output at low driving velocity. Moreover, we can see that a sinusoidal temperature field with the same wavelength and the same highest and lowest temperature values as the discontinuous one can lead to considerable work output at low driving velocity too. So the temperature field is not that demanding. And a sinusoidal temperature field like that in the laser-induced transient thermal grating (47–49) may serve as a possible solution. To obtain a rectangular waveform temperature field, it's promising to superpose several sinusoidal waves with different amplitude, phase

and wavelength. The optically levitated dielectric nanosphere system in cavity with two standing-wave optical modes, one for trapping and the other weaker one for cooling (50, 51), superposed with a uniformly moving Paul trap, may also work. And we can also speculate that the trapped ion system with two lasers, one for trapping and the other for cooling, superposed with a uniformly moving Paul trap, may work too.

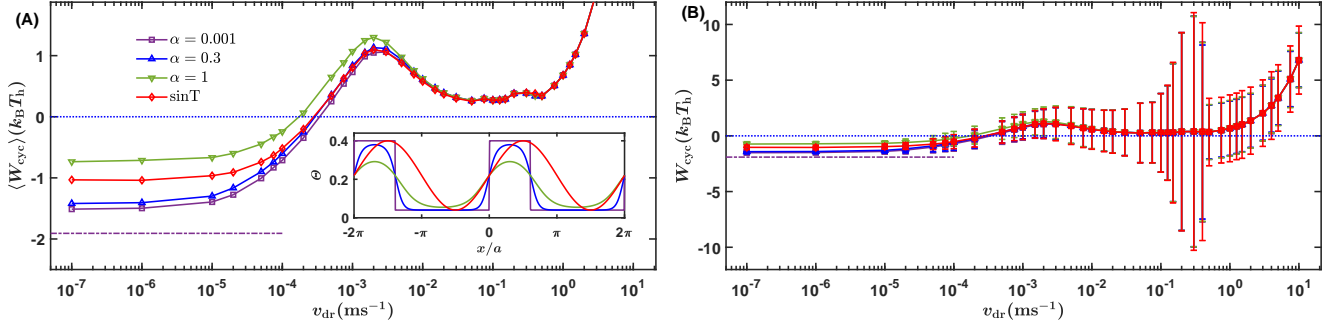


Fig. S56. Simulation results of mildly changing temperature fields compared with the sharply changing one. (A) The $\langle W_{\text{cyc}} \rangle - v_{\text{dr}}$ curves of different temperature field. The red curve with diamond denoted by sinT represents the case of a sinusoidal temperature field with the same wavelength and the same highest and lowest temperature values as the discontinuous one that we have adopted in the PTSHE. For the rest three curves, the temperature field $\Theta(z)$ is calculated by Eq. 87 with the same $\Theta_{h,c} = 0.4, 0.04$ and different α . The temperature profiles of the four curves are plotted in the inset with the purple one representing the $\alpha = 0.001$ case as a reference, which we have utilized to approximate the discontinuous alternative high and low temperature field, cf. Sec. 8.D. The purple dot-dashed line on the bottom left is the equilibrium cycle work output approximated by the potential mechanism, $W_{\text{cyc,e.p.}}$, cf. Eq. 39. We can see that there is still work output at low driving velocity for the case of α as large as 1.0 as well as the case of the sinusoidal temperature profile, in both of which the temperature field changes very gently. So the demand for the temperature field is not very high and the experimental implementation is not unreachable. (B) The standard deviations of W_{cyc} with respect to v_{dr} . Here $\eta = 3.0$, $\mu = 4 \times 10^4 \text{s}^{-1}$ and other parameters are given in Sec. 8.H.

N.3. On the damping coefficient. In the main text Figure 3(A), we can see that for the cases considered there the low driving velocity limit of the mean cycle work is nearly independent on μ , i.e. the overdamped and underdamped cases have similar work output. Therefore we can implement the PTSHE both with microscale colloidal particle in liquid medium at the overdamped regime (33, 34) and with optically levitated nanoparticle (52) or trapped ion (53) at the underdamped regime.

To evaluate the temperature dependence of the damping coefficient, we simulate a case in which the damping coefficient field $\mu(z)$ is proportional to the temperature field $\Theta(z)$ (Eq. 87):

$$\mu(z) = \frac{1}{2} \left\{ \mu_h + \mu_c + (\mu_h - \mu_c) \tanh\left(\frac{1}{\alpha} \left[\sin(z + \arctan \sqrt{\frac{\eta-1}{\eta+1}}) - \sqrt{\frac{\eta-1}{2\eta}} \right] \right) \right\}, \quad [55]$$

where we choose $\mu_h \approx 6.32 \times 10^3 \text{s}^{-1}$ and $\mu_c = 4 \times 10^4 \text{s}^{-1}$. The value of μ_h is calculated from $\mu_c = 4 \times 10^4 \text{s}^{-1}$ and the assumption that $\Theta \propto \frac{1}{\mu^2}$, based on which we will actually obtain $\mu_h = \frac{50 \times 2}{50 \times \sqrt{10 \times 10^{-6}}} \text{s}^{-1} \approx 1.26 \times 10^4 \text{s}^{-1}$. To make the damping coefficient change more noteworthy, we halved this value to $\mu_h = \frac{1}{2} \frac{50 \times 2}{50 \times \sqrt{10 \times 10^{-6}}} \text{s}^{-1} \approx 6.32 \times 10^3 \text{s}^{-1}$. Indeed, Eq. 55 would be very close to $\mu(z) = \mu_c \sqrt{\frac{\Theta_c}{\Theta(z)}}$ if we chose $\mu_h \approx 1.26 \times 10^4 \text{s}^{-1}$, because $\Theta(z)$ is very close to a piecewise function composed of two constant functions. The simulation results are plotted in Figure S57. We can see that there is still distinct work output at low driving velocity.

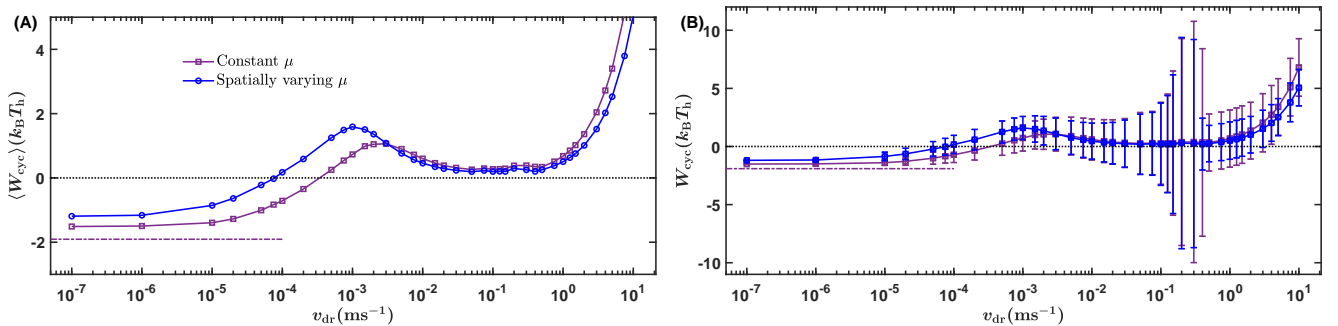


Fig. S57. The simulation results at spatially varying damping coefficient compared with the constant damping coefficient case. The $\langle W_{\text{cyc}} \rangle - v_{\text{dr}}$ curves are plotted in (A) and the standard deviations of W_{cyc} are given in (B). Here $\eta = 3.0$, $\Theta_{h,c} = 0.4, 0.04$ and other parameters except $\mu(z)$ are given in Sec. 8.H.

In the main text, we have mentioned that it seems that the low velocity limit of the mean cycle work is nearly independent on the damping coefficient for the parameter ranges we considered there. However, from Figure S57, we can see the damping coefficient actually affects the equilibrium cycle work. If we observe carefully the low driving velocity end of the main text

Figure 3(A), we can see that the equilibrium cycle work output seems to first increase and then decrease with the damping coefficient increasing. It's valuable to investigate that how the equilibrium crossover probability is dependent on the damping coefficient and what's the effect the damping coefficient has on the equilibrium cycle work output, for which we may need to turn to the Fokker-Planck or Kramers equation method (37) for help.

Qualitatively speaking, the damping coefficient affects the relaxation time from out of equilibrium to equilibrium as well as the damping force $m\mu\dot{x}$ which is proportional to the velocity \dot{x} of the particle. In the underdamped regime, the particle will relax to equilibrium more quickly when the damping coefficient increases, i.e. equilibrium is arrived at more quickly relative to the driving velocity. So the driving velocity range of work output extends to the right [Figure 3(A) in the main text], until the damping coefficient is so large that the damping force becomes very high at low driving velocity, which leads to the driving velocity range of work output shrinks to the left again. Therefore, to avoid too small driving velocity a moderate μ should be chosen.

7. Fluctuation-dissipation theorem

In Langevin Eq. 4 in the main text, we assume that the intensity Γ of the stochastic force $\xi(t) = \Gamma\zeta(t)$ satisfies the fluctuation-dissipation theorem. Here we give a brief derivation. The Langevin equation can be linearized into a nonhomogeneous ordinary differential equation describing a Brownian motion of a harmonic oscillator (54)

$$\ddot{x}(t) + \mu\dot{x}(t) + \omega_0^2(1 + \eta)x(t) = \frac{\Gamma}{m}\zeta(t), \quad [56]$$

which is equivalent to a first order differential equation system

$$\frac{d}{dt} \begin{pmatrix} x \\ \dot{x} \end{pmatrix} = \begin{bmatrix} 0 & 1 \\ -\omega_0^2(1 + \eta) & -\mu \end{bmatrix} \begin{pmatrix} x \\ \dot{x} \end{pmatrix} + \begin{pmatrix} 0 \\ \frac{\Gamma}{m}\zeta(t) \end{pmatrix}. \quad [57]$$

It can be represented compactly as

$$\dot{\mathbf{x}} = \mathbf{A}\mathbf{x} + \mathbf{b}. \quad [58]$$

We first consider the case in which $\mu \neq 2\omega_0\sqrt{1 + \eta}$ and \mathbf{A} has two eigenvalues

$$\begin{aligned} \lambda_1 &= \frac{-\mu - \sqrt{\mu^2 - 4\omega_0^2(1 + \eta)^2}}{2}, \\ \lambda_2 &= \frac{-\mu + \sqrt{\mu^2 - 4\omega_0^2(1 + \eta)^2}}{2}, \end{aligned} \quad [59]$$

with two eigenvectors

$$\mathbf{v}_1 = \begin{pmatrix} \frac{\lambda_2}{\omega_0^2(1 + \eta)^2} \\ 1 \end{pmatrix}, \mathbf{v}_2 = \begin{pmatrix} \frac{\lambda_1}{\omega_0^2(1 + \eta)^2} \\ 1 \end{pmatrix}, \quad [60]$$

respectively. The corresponding homogeneous equation $\dot{\mathbf{x}} = \mathbf{A}\mathbf{x}$ has general solutions of the form $\mathbf{x} = (e^{\lambda_1 t} \mathbf{v}_1 \quad e^{\lambda_2 t} \mathbf{v}_2) \begin{pmatrix} c_1 \\ c_2 \end{pmatrix}$ with two constants c_1 and c_2 . By the method of variation of constant, the solution of Eq. 58 can be obtained as

$$\begin{aligned} \mathbf{x} = \begin{pmatrix} x \\ \dot{x} \end{pmatrix} &= c_1(0)e^{\lambda_1 t} \mathbf{v}_1 + c_2(0)e^{\lambda_2 t} \mathbf{v}_2 \\ &+ \frac{\Gamma}{m} \frac{1}{\sqrt{\mu^2 - 4\omega_0^2(1 + \eta)^2}} \left[\begin{pmatrix} 1 \\ \lambda_1 \end{pmatrix} e^{\lambda_1 t} \int_0^t -e^{-\lambda_1 t'} \zeta(t') dt' + \begin{pmatrix} 1 \\ \lambda_2 \end{pmatrix} e^{\lambda_2 t} \int_0^t e^{-\lambda_2 t'} \zeta(t') dt' \right] \\ &= c_1(0)e^{\lambda_1 t} \mathbf{v}_1 + c_2(0)e^{\lambda_2 t} \mathbf{v}_2 \\ &+ \frac{\Gamma}{m} \frac{1}{\sqrt{\mu^2 - 4\omega_0^2(1 + \eta)^2}} \int_0^t \left[-\begin{pmatrix} 1 \\ \lambda_1 \end{pmatrix} e^{\lambda_1(t-t')} + \begin{pmatrix} 1 \\ \lambda_2 \end{pmatrix} e^{\lambda_2(t-t')} \right] \zeta(t') dt', \end{aligned} \quad [61]$$

with two constants $c_{1,2}(0)$ determined by the initial conditions. The mean squared value is calculated by

$$\begin{aligned} \langle \mathbf{x}^T \mathbf{x} \rangle &= \langle x^2 \rangle + \langle \dot{x}^2 \rangle = [c_1(0)e^{\lambda_1 t} \mathbf{v}_1 + c_2(0)e^{\lambda_2 t} \mathbf{v}_2]^2 \\ &+ 2[c_1(0)e^{\lambda_1 t} \mathbf{v}_1 + c_2(0)e^{\lambda_2 t} \mathbf{v}_2]^T \frac{\Gamma}{m} \frac{1}{\sqrt{\mu^2 - 4\omega_0^2(1 + \eta)^2}} \int_0^t \left[-\begin{pmatrix} 1 \\ \lambda_1 \end{pmatrix} e^{\lambda_1(t-t')} + \begin{pmatrix} 1 \\ \lambda_2 \end{pmatrix} e^{\lambda_2(t-t')} \right] \langle \zeta(t') \rangle dt' \\ &+ \frac{\Gamma^2}{m^2} \frac{1}{\mu^2 - 4\omega_0^2(1 + \eta)^2} \left\langle \int_0^t \left[-\begin{pmatrix} 1 \\ \lambda_1 \end{pmatrix} e^{\lambda_1(t-t')} + \begin{pmatrix} 1 \\ \lambda_2 \end{pmatrix} e^{\lambda_2(t-t')} \right] \zeta(t') dt' \right\rangle^2. \end{aligned} \quad [62]$$

As $t \rightarrow \infty$, when the particle arrives at equilibrium, the first term on the RHS goes to zero due to the real parts of λ_1 and λ_2 are negative, cf. Eq. 59. The second one is also zero in that $\langle \zeta(t) \rangle = 0$. Because $\langle \zeta(t)\zeta(t') \rangle = \delta(t - t')$, in the third term we have

$$\begin{aligned}
& \left\langle \int_0^t \left[-\left(\frac{1}{\lambda_1}\right) e^{\lambda_1(t-t')} + \left(\frac{1}{\lambda_2}\right) e^{\lambda_2(t-t')} \right] \zeta(t') dt' \right\rangle^2 \\
&= \int_0^t \int_0^t \left[-\left(\frac{1}{\lambda_1}\right) e^{\lambda_1(t-t')} + \left(\frac{1}{\lambda_2}\right) e^{\lambda_2(t-t')} \right]^T \left[-\left(\frac{1}{\lambda_1}\right) e^{\lambda_1(t-t'')} + \left(\frac{1}{\lambda_2}\right) e^{\lambda_2(t-t'')} \right] \langle \zeta(t') \zeta(t'') \rangle dt' dt'' \\
&= \int_0^t \int_0^t \left[-\left(\frac{1}{\lambda_1}\right) e^{\lambda_1(t-t')} + \left(\frac{1}{\lambda_2}\right) e^{\lambda_2(t-t')} \right]^T \left[-\left(\frac{1}{\lambda_1}\right) e^{\lambda_1(t-t'')} + \left(\frac{1}{\lambda_2}\right) e^{\lambda_2(t-t'')} \right] \delta(t' - t'') dt' dt'' \\
&= \int_0^t \left[-\left(\frac{1}{\lambda_1}\right) e^{\lambda_1(t-t')} + \left(\frac{1}{\lambda_2}\right) e^{\lambda_2(t-t')} \right]^T \left[-\left(\frac{1}{\lambda_1}\right) e^{\lambda_1(t-t')} + \left(\frac{1}{\lambda_2}\right) e^{\lambda_2(t-t')} \right] dt' \\
&= \int_0^t \left[-e^{\lambda_1(t-t')} + e^{\lambda_2(t-t')} \right]^2 dt' + \int_0^t \left[-\lambda_1 e^{\lambda_1(t-t')} + \lambda_2 e^{\lambda_2(t-t')} \right]^2 dt' \\
&= \left[\left(-\frac{1}{2\lambda_1}\right)(1 - e^{2\lambda_1 t}) - 2\left(-\frac{1}{\lambda_1 + \lambda_2}\right)(1 - e^{(\lambda_1 + \lambda_2)t}) + \left(-\frac{1}{2\lambda_2}\right)(1 - e^{2\lambda_2 t}) \right] \\
&\quad + \left[\lambda_1^2 \left(-\frac{1}{2\lambda_1}\right)(1 - e^{2\lambda_1 t}) - 2\lambda_1 \lambda_2 \left(-\frac{1}{\lambda_1 + \lambda_2}\right)(1 - e^{(\lambda_1 + \lambda_2)t}) + \lambda_2^2 \left(-\frac{1}{2\lambda_2}\right)(1 - e^{2\lambda_2 t}) \right] \\
&\xrightarrow{t \rightarrow \infty} \left[\left(-\frac{1}{2\lambda_1}\right) - 2\left(-\frac{1}{\lambda_1 + \lambda_2}\right) + \left(-\frac{1}{2\lambda_2}\right) \right] + \left[\lambda_1^2 \left(-\frac{1}{2\lambda_1}\right) - 2\lambda_1 \lambda_2 \left(-\frac{1}{\lambda_1 + \lambda_2}\right) + \lambda_2^2 \left(-\frac{1}{2\lambda_2}\right) \right] \\
&= \frac{1}{\lambda_1 \lambda_2} \left(-\frac{\lambda_1 + \lambda_2}{2} + \frac{2\lambda_1 \lambda_2}{\lambda_1 + \lambda_2} \right) + \left(-\frac{\lambda_1 + \lambda_2}{2} + \frac{2\lambda_1 \lambda_2}{\lambda_1 + \lambda_2} \right) \\
&= \frac{1}{\omega_0^2(1 + \eta)^2} \frac{\mu^2 - 4\omega_0^2(1 + \eta)^2}{2\mu} + \frac{\mu^2 - 4\omega_0^2(1 + \eta)^2}{2\mu}.
\end{aligned} \tag{63}$$

The limit step above roots in that the real parts of $2\lambda_1, (\lambda_1 + \lambda_2), 2\lambda_2$ are all negative, whether $\mu > 2\omega_0\sqrt{1 + \eta}$ or $\mu < 2\omega_0\sqrt{1 + \eta}$, cf. Eq. 59.

Therefore, at the equilibrium state,

$$\begin{aligned}
\langle x(t)^2 \rangle &= \frac{\Gamma^2}{m^2} \frac{1}{\mu^2 - 4\omega_0^2(1 + \eta)^2} \frac{1}{\omega_0^2(1 + \eta)^2} \frac{\mu^2 - 4\omega_0^2(1 + \eta)^2}{2\mu} = \frac{\Gamma^2}{2\mu m^2 \omega_0^2(1 + \eta)^2}, \\
\langle v(t)^2 \rangle &= \frac{\Gamma^2}{m^2} \frac{1}{\mu^2 - 4\omega_0^2(1 + \eta)^2} \frac{\mu^2 - 4\omega_0^2(1 + \eta)^2}{2\mu} = \frac{\Gamma^2}{2\mu m^2}.
\end{aligned} \tag{64}$$

Substitute the equipartition theorem

$$\begin{aligned}
\frac{1}{2} m \omega_0^2 (1 + \eta) \langle x(t)^2 \rangle &= \frac{1}{2} k_B T, \\
\frac{1}{2} m \langle v(t)^2 \rangle &= \frac{1}{2} k_B T.
\end{aligned} \tag{65}$$

into Eq. 64 we will obtain

$$\Gamma = \sqrt{2m\mu k_B T} \tag{66}$$

from both equations. This is a form of fluctuation-dissipation theorem for the Brownian motion of a linear harmonic oscillator (54).

For the case in which $\mu = 2\omega_0\sqrt{1 + \eta}$, \mathbf{A} has two degenerate eigenvalues

$$\lambda_1 = \lambda_2 = \frac{-\mu}{2} = -\omega_0\sqrt{1 + \eta} = \lambda, \tag{67}$$

with one eigenvector

$$\mathbf{v} = \begin{pmatrix} \frac{-\mu}{2\omega_0^2(1 + \eta)^2} \\ 1 \end{pmatrix} = \begin{pmatrix} -\frac{1}{\omega_0(1 + \eta)} \\ 1 \end{pmatrix}. \tag{68}$$

The corresponding homogeneous equation $\dot{\mathbf{x}} = \mathbf{A}\mathbf{x}$ has general solutions of the form $\mathbf{x} = e^{\lambda t} (\mathbf{v} \quad \mathbf{v}_0 + \mathbf{v}t) \begin{pmatrix} c_1 \\ c_2 \end{pmatrix}$, with \mathbf{v}_0

satisfying $\begin{cases} (\mathbf{A} - \lambda \mathbf{I})^2 \mathbf{v}_0 = \mathbf{0}, \\ (\mathbf{A} - \lambda \mathbf{I}) \mathbf{v}_0 = \mathbf{0}, \end{cases}$ and two constants c_1 and c_2 . Again by the method of variation of constant, the solution of Eq.

58 can be obtained. We will achieve the same fluctuation-dissipation theorem as Eq. 66 with a similar procedure as above.

For our nonlinear Langevin equation, we assume the noise intensity Γ is related to the friction coefficient μ by the same fluctuation-dissipation theorem as the linear case, which is customary (55).

We can see that for a harmonic oscillator, the fluctuation-dissipation theorem Eq. 66 is equivalent to the equipartition theorem Eq. 65. In the next section the Langevin dynamics simulation method will be evaluated basing on this point to guarantee that it satisfies the fluctuation-dissipation theorem and that the time stepsize we choose is reasonable.

8. Langevin dynamics simulation

A. Nondimensionalization of the Langevin equation. The Langevin Eq. 4 in the main text is numerically solved by the 4th order Stochastic Runge-Kutta (SRK4) method (26, 56). We first nondimensionalize it to reduce the floating point computation error (57):

$$\frac{d^2 z}{d\tau^2} + \beta \eta \frac{dz}{d\tau} + 4\pi^2(z - \tilde{v}\tau) + 4\pi^2 \eta \sin z = 4\pi^2 \eta \Xi(\tau), \quad [69]$$

with $z = \frac{2\pi}{a}x$, $\tau = \frac{\omega_0}{2\pi}t$, $\beta = \frac{m\mu\omega_0 a^2}{\pi V_0}$, and $\eta = \frac{2\pi^2 V_0}{m\omega_0^2 a^2}$ being the nondimensional corrugation number, $\tilde{v} = \frac{4\pi^2}{a\omega_0}v_{\text{dr}}$ and

$$\begin{aligned} \Xi(\tau)d\tau &= \frac{a}{\pi V_0} \xi\left(\frac{2\pi}{\omega_0}\tau\right)d\tau = \frac{a}{\pi V_0} \Gamma\left(\frac{a}{2\pi}z\right)\zeta\left(\frac{2\pi}{\omega_0}\tau\right)d\tau = \frac{a\omega_0}{2\pi^2 V_0} \Gamma\left(\frac{a}{2\pi}z\right)\zeta\left(\frac{2\pi}{\omega_0}\tau\right)d\left(\frac{2\pi}{\omega_0}\tau\right) \\ &= \frac{a\omega_0}{2\pi^2 V_0} \Gamma\left(\frac{a}{2\pi}z\right)\zeta(t)dt = \frac{a\omega_0}{2\pi^2 V_0} \Gamma\left(\frac{a}{2\pi}z\right)d\mathcal{W}_t = \frac{a\omega_0}{2\pi^2 V_0} \Gamma\left(\frac{a}{2\pi}z\right)\sqrt{\frac{2\pi}{\omega_0}}d\mathcal{W}_\tau \\ &= \frac{a\omega_0}{2\pi^2 V_0} \sqrt{2m\mu k_B T\left(\frac{a}{2\pi}z\right)}\sqrt{\frac{2\pi}{\omega_0}}d\mathcal{W}_\tau = \sqrt{\frac{1}{\pi^2} \frac{m\mu\omega_0 a^2}{\pi V_0} \frac{k_B T\left(\frac{a}{2\pi}z\right)}{V_0}}d\mathcal{W}_\tau \\ &= \sqrt{\frac{\beta}{\pi^2} \frac{k_B T\left(\frac{a}{2\pi}z\right)}{V_0}}d\mathcal{W}_\tau \\ &= \sqrt{\frac{\beta}{\pi^2}} \Theta(z)d\mathcal{W}_\tau. \end{aligned} \quad [70]$$

Here, $\Theta(z) = \frac{k_B T\left(\frac{a}{2\pi}z\right)}{V_0}$ is the nondimensional temperature. $\mathcal{W}_t = \mathcal{W}(t)$ is a Weiner process with independent increment $d\mathcal{W}_t = \zeta(t)dt$ satisfying

$$\begin{aligned} \langle d\mathcal{W}_t \rangle &= 0, \\ \langle d\mathcal{W}_t^2 \rangle &= dt, \end{aligned} \quad [71]$$

i.e. $d\mathcal{W}_t \sim N(0, dt)$ (58). After nondimensionalizing $d\mathcal{W}_t$ to $d\mathcal{W}_\tau$, $d\mathcal{W}_\tau$ should satisfy $d\mathcal{W}_\tau \sim N(0, d\tau)$ and

$$\frac{d\mathcal{W}_\tau - 0}{\sqrt{d\tau}} = \frac{d\mathcal{W}_t - 0}{\sqrt{dt}} \sim N(0, 1), \quad [72]$$

i.e.

$$d\mathcal{W}_t = \sqrt{\frac{dt}{d\tau}}d\mathcal{W}_\tau = \sqrt{\frac{2\pi}{\omega_0}}d\mathcal{W}_\tau, \quad [73]$$

which leads to the last equality in the second line of Eq. 70.

B. Equivalent form of the Stratonovich and the Ito stochastic differential equation. Eq. 69 can be transformed to the first-order stochastic differential equation system

$$\begin{cases} dz = \dot{z}d\tau, \\ d\dot{z} = d\frac{dz}{d\tau} = [-\beta\eta\dot{z} - 4\pi^2(z - \tilde{v}\tau) - 4\pi^2\eta\sin z]d\tau + 4\pi^2\eta\sqrt{\frac{\beta}{\pi^2}}\Theta(z)d\mathcal{W}_\tau = a(z, \dot{z}, \tau)d\tau + b(z)d\mathcal{W}_\tau. \end{cases} \quad [74]$$

Here the symbol $d\mathcal{W}_\tau$ should be interpreted as obeying the Stratonovich's mid-point rule when integrated, i.e. this is a Stratonovich stochastic differential equation (58, 59). It's easier to implement numerical discretization on the Ito stochastic differential equation, which is explicit (58). And the stochastic Runge-Kutta method used in this paper is based on the discretization of the Ito stochastic differential equation (56). So we'd better transform the Stratonovich stochastic Eq. 74 into Ito's form. Fortunately, because the temperature in this paper is constant or varies with the nondimensional spatial coordinate z , not with the nondimensional velocity \dot{z} , the Stratonovich and the Ito form are the same (58). Here we give a brief and not rigorous derivation.

Consider discretization of the Stratonovich stochastic integral

$$\int_{\tau_0}^{\tau} b(z) \circ d\mathcal{W}_\tau = \sum_{i=1}^n b\left(\frac{z_{i-1} + z_i}{2}\right)\Delta\mathcal{W}_i, \quad [75]$$

in which $\Delta\mathcal{W}_i = \mathcal{W}_i - \mathcal{W}_{i-1}$, and the \circ represents the Stratonovich's mid-point rule (see the next subsection) for the moment. The mid-point value of $b(z)$ can be Taylor expanded to

$$\begin{aligned} b\left(\frac{z_{i-1} + z_i}{2}\right) &= b\left(z_{i-1} + \frac{z_i - z_{i-1}}{2}\right) \\ &= b(z_{i-1}) + \frac{d}{dz}b(z_{i-1})\frac{z_i - z_{i-1}}{2} + \frac{1}{2}\frac{d^2}{dz^2}b(z_{i-1})\left(\frac{z_i - z_{i-1}}{2}\right)^2 + \dots \\ &= b(z_{i-1}) + \frac{d}{dz}b(z_{i-1})\frac{\dot{z}_{i-1}\Delta\tau_i}{2} + \frac{1}{2}\frac{d^2}{dz^2}b(z_{i-1})\left(\frac{\dot{z}_{i-1}\Delta\tau_i}{2}\right)^2 + \dots, \end{aligned} \quad [76]$$

in which $\Delta\tau_i = \tau_i - \tau_{i-1}$ and $z_i - z_{i-1} = \dot{z}_{i-1}\Delta\tau_i$ because of the discretization of the first equation of Eq. 74 (we only need to keep the first order term here because the higher-order terms will vanish, cf. Eq. 102). Substitute Eq. 76 into Eq. 75 and take the mean square limit (58), which can be regarded as omitting the terms of order higher than 1 ($\Delta\mathcal{W}_i$ can be regarded as of order 0.5), we obtain

$$\int_{\tau_0}^{\tau} b(z) \circ d\mathcal{W}_\tau = \sum_{i=1}^n \left[b(z_{i-1}) + \frac{d}{dz} b(z_{i-1}) \frac{\dot{z}_{i-1}\Delta\tau_i}{2} + \frac{1}{2} \frac{d^2}{dz^2} b(z_{i-1}) \left(\frac{\dot{z}_{i-1}\Delta\tau_i}{2} \right)^2 + \dots \right] \Delta\mathcal{W}_i = \int_{\tau_0}^{\tau} b(z) d\mathcal{W}_\tau, \quad [77]$$

where the last integral is Ito stochastic integral. Hence the two forms of stochastic integrals (and also the stochastic differential equations) are the same and we can omit the \circ in Eq. 74.

Therefore we can apply the numerical methods below directly to Eq. 74.

C. The mid-point rule of discretizing the Stratonovich stochastic integral. Here we give a brief and not rigorous derivation of the mid-point rule, i.e. the Stratonovich rule. The necessity of the mid-point rule results from the form invariance of the first order differential of the Stratonovich interpretation of the stochastic Eq. 74, i.e. for a smooth enough function $f(z(\tau), \dot{z}(\tau), \tau)$

$$df(z(\tau), \dot{z}(\tau), \tau) = \frac{\partial f}{\partial z} \circ dz + \frac{\partial f}{\partial \dot{z}} \circ d\dot{z} + \frac{\partial f}{\partial \tau} d\tau, \quad [78]$$

which is also known as the chain rule. To obtain this form, we first Taylor expand $f(z(\tau), \dot{z}(\tau), \tau)$ into

$$\begin{aligned} df(z(\tau), \dot{z}(\tau), \tau) &= f(z(\tau) + dz(\tau), \dot{z}(\tau) + d\dot{z}(\tau), \tau + d\tau) - f(z(\tau), \dot{z}(\tau), \tau) \\ &= \left[\frac{\partial}{\partial z} dz(\tau) + \frac{\partial}{\partial \dot{z}} d\dot{z}(\tau) + \frac{\partial}{\partial \tau} d\tau \right] f + \frac{1}{2} \left[\frac{\partial}{\partial z} dz(\tau) + \frac{\partial}{\partial \dot{z}} d\dot{z}(\tau) + \frac{\partial}{\partial \tau} d\tau \right]^2 f + \dots \\ &= \left[\frac{\partial}{\partial z} dz(\tau) + \frac{\partial}{\partial \dot{z}} d\dot{z}(\tau) + \frac{\partial}{\partial \tau} d\tau \right] f + \frac{1}{2} \frac{\partial^2 f}{\partial z^2} b(z)^2 d\tau + o(d\tau), \end{aligned} \quad [79]$$

in which the third equality results from substituting Eq. 74 into the second term on the RHS of the second equality, expanding this term, replacing $d\mathcal{W}_\tau^2$ with $d\tau$ [here we have used Eq. 71 and omitted the process of taking mean square limit (58)] and absorbing the terms of higher than first order into $o(d\tau)$. Omitting $o(d\tau)$, the last equality is a form of Ito's formula (58), in which an extra term $\frac{1}{2} \frac{\partial^2 f}{\partial z^2} b(z)^2 d\tau$ is added to Eq. 78 if we neglect the \circ .

Next we will show that utilizing the mid-point rule, we can transform Eq. 78 into Ito's formula. In the integral form, Eq. 78 can be represented by

$$f(z(\tau), \dot{z}(\tau), \tau) = f(z(\tau_0), \dot{z}(\tau_0), \tau_0) + \int_{\tau_0}^{\tau} \frac{\partial f(z(s), \dot{z}(s), s)}{\partial z} \circ dz(s) + \int_{\tau_0}^{\tau} \frac{\partial f(z(s), \dot{z}(s), s)}{\partial \dot{z}} \circ d\dot{z}(s) + \int_{\tau_0}^{\tau} \frac{\partial f(z(s), \dot{z}(s), s)}{\partial \tau} ds. \quad [80]$$

Substitute Eq. 74 into Eq. 80, we will obtain

$$\begin{aligned} f(z(\tau), \dot{z}(\tau), \tau) &= f(z(\tau_0), \dot{z}(\tau_0), \tau_0) + \int_{\tau_0}^{\tau} \frac{\partial f(z(s), \dot{z}(s), s)}{\partial z} \dot{z}(s) ds \\ &\quad + \int_{\tau_0}^{\tau} \frac{\partial f(z(s), \dot{z}(s), s)}{\partial \dot{z}} [a(z(s), \dot{z}(s), s) ds + b(z(s)) \circ d\mathcal{W}_s] + \int_{\tau_0}^{\tau} \frac{\partial f(z(s), \dot{z}(s), s)}{\partial \tau} ds. \end{aligned} \quad [81]$$

The stochastic integral on the RHS can be discretized using mid-point rule:

$$\begin{aligned} \int_{\tau_0}^{\tau} \frac{\partial f(z(s), \dot{z}(s), s)}{\partial \dot{z}} b(z(s)) \circ d\mathcal{W}_s &= \sum_{i=1}^n \frac{\partial f(\frac{z(\tau_i) + z(\tau_{i-1})}{2}, \frac{\dot{z}(\tau_i) + \dot{z}(\tau_{i-1})}{2}, \tau_{i-1})}{\partial \dot{z}} b(\frac{z(\tau_i) + z(\tau_{i-1})}{2}) (\mathcal{W}_{\tau_i} - \mathcal{W}_{\tau_{i-1}}) \\ &= \sum_{i=1}^n g(\frac{z(\tau_i) + z(\tau_{i-1})}{2}, \frac{\dot{z}(\tau_i) + \dot{z}(\tau_{i-1})}{2}, \tau_{i-1}) (\mathcal{W}_{\tau_i} - \mathcal{W}_{\tau_{i-1}}), \end{aligned} \quad [82]$$

where we have replaced $\frac{\partial f(z(\tau), \dot{z}(\tau), \tau)}{\partial \dot{z}} b(z(\tau))$ by $g(z(\tau), \dot{z}(\tau), \tau)$ for compactness. As in Eq. 76 we can expand the mid-point value of $g(z(\tau), \dot{z}(\tau), \tau)$ into

$$\begin{aligned} &g(\frac{z(\tau_i) + z(\tau_{i-1})}{2}, \frac{\dot{z}(\tau_i) + \dot{z}(\tau_{i-1})}{2}, \tau_{i-1}) \\ &= g(z_{i-1} + \frac{z_i - z_{i-1}}{2}, \dot{z}_{i-1} + \frac{\dot{z}_i - \dot{z}_{i-1}}{2}, \tau_{i-1}) \\ &= g(z_{i-1}, \dot{z}_{i-1}, \tau_{i-1}) + \frac{\partial g(z_{i-1}, \dot{z}_{i-1}, \tau_{i-1})}{\partial z} \frac{z_i - z_{i-1}}{2} + \frac{\partial g(z_{i-1}, \dot{z}_{i-1}, \tau_{i-1})}{\partial \dot{z}} \frac{\dot{z}_i - \dot{z}_{i-1}}{2} + \dots \\ &= g(z_{i-1}, \dot{z}_{i-1}, \tau_{i-1}) + \frac{\partial g(z_{i-1}, \dot{z}_{i-1}, \tau_{i-1})}{\partial z} \frac{\dot{z}_{i-1}(\tau_i - \tau_{i-1})}{2} \\ &\quad + \frac{\partial g(z_{i-1}, \dot{z}_{i-1}, \tau_{i-1})}{\partial \dot{z}} \frac{a(z_{i-1}, \dot{z}_{i-1}, \tau_{i-1})(\tau_i - \tau_{i-1}) + b(z_{i-1})(\mathcal{W}_{\tau_i} - \mathcal{W}_{\tau_{i-1}})}{2} + \dots, \end{aligned} \quad [83]$$

substitute which into Eq. 82 and discard the terms of higher than first order of $\tau_i - \tau_{i-1}$, we will get

$$\begin{aligned}
\int_{\tau_0}^{\tau} \frac{\partial f(z(s), \dot{z}(s), s)}{\partial \dot{z}} b(z(s)) \circ d\mathcal{W}_s &= \sum_{i=1}^n \left[g(z_{i-1}, \dot{z}_{i-1}, \tau_{i-1})(\mathcal{W}_{\tau_i} - \mathcal{W}_{\tau_{i-1}}) + \frac{1}{2} \frac{\partial g(z_{i-1}, \dot{z}_{i-1}, \tau_{i-1})}{\partial \dot{z}} b(z(\tau_{i-1}))(\mathcal{W}_{\tau_i} - \mathcal{W}_{\tau_{i-1}})^2 \right] \\
&= \sum_{i=1}^n \left[g(z_{i-1}, \dot{z}_{i-1}, \tau_{i-1})(\mathcal{W}_{\tau_i} - \mathcal{W}_{\tau_{i-1}}) + \frac{1}{2} \frac{\partial g(z_{i-1}, \dot{z}_{i-1}, \tau_{i-1})}{\partial \dot{z}} b(z(\tau_{i-1}))(\tau_i - \tau_{i-1}) \right] \\
&= \int_{\tau_0}^{\tau} \frac{\partial f(z(s), \dot{z}(s), s)}{\partial \dot{z}} b(z(s)) d\mathcal{W}_s + \frac{1}{2} \int_{\tau_0}^{\tau} \frac{\partial g(z(s), \dot{z}(s), s)}{\partial \dot{z}} b(z(s)) ds \\
&= \int_{\tau_0}^{\tau} \frac{\partial f(z(s), \dot{z}(s), s)}{\partial \dot{z}} b(z(s)) d\mathcal{W}_s + \frac{1}{2} \int_{\tau_0}^{\tau} \frac{\partial^2 f(z(s), \dot{z}(s), s)}{\partial \dot{z}^2} b(z(s))^2 ds,
\end{aligned} \tag{84}$$

where on the RHS of the second equality we replace $(\mathcal{W}_{\tau_i} - \mathcal{W}_{\tau_{i-1}})^2$ by $(\tau_i - \tau_{i-1})$ [here we have used $\langle (\mathcal{W}_{\tau_i} - \mathcal{W}_{\tau_{i-1}})^2 \rangle = \tau_i - \tau_{i-1}$ and omitted the process of taking mean square limit (58)] and the two stochastic integrals on the RHS of the last two equalities are of Ito's form.

In the last equality of Eq. 83, we have substituted $\dot{z}_i - \dot{z}_{i-1}$ with $a(z_{i-1}, \dot{z}_{i-1}, \tau_{i-1})(\tau_i - \tau_{i-1}) + b(z_{i-1})(\mathcal{W}_{\tau_i} - \mathcal{W}_{\tau_{i-1}})$ utilizing the left-point rule for compactness. We can also substitute $\dot{z}_i - \dot{z}_{i-1}$ with $a(z_{i-1}, \dot{z}_{i-1}, \tau_{i-1})(\tau_i - \tau_{i-1}) + b(\frac{z_{i-1} + z_i}{2})(\mathcal{W}_{\tau_i} - \mathcal{W}_{\tau_{i-1}})$ and then Taylor expand $b(\frac{z_{i-1} + z_i}{2})$ as in Eq. 76. After substituting what we get of Eq. 83 in this way into Eq. 82 and discard the terms of higher than first order of $\tau_i - \tau_{i-1}$, we will obtain Eq. 84 again.

Substitute Eq. 84 into Eq. 81 and convert it back into differential form we will obtain Ito's formula Eq. 79. From the derivation process in Eq. 79, we can see that the extra term $\frac{1}{2} \frac{\partial^2 f}{\partial \dot{z}^2} b(z)^2 d\tau$ of Ito's formula is resulted from the left-point rule, which makes Eq. 78 no longer valid. To apply the form variance of the first order differential, i.e. Eq. 78, as in the ordinary calculus, the mid-point rule is necessary. (Actually here we can only prove that the mid-point rule is sufficient, there may be another rule which can also lead to Eq. 78, so our derivation is not rigorous.)

In Eq. 77, $\frac{\partial f(z(\tau), \dot{z}(\tau), \tau)}{\partial \dot{z}} = 1$ and the second term on the RHS of Eq. 84 vanishes, so that the Stratonovich and the Ito stochastic integral as well as the Stratonovich and the Ito stochastic differential equation are the same and we can integrate the Stratonovich stochastic differential Eq. 74 using methods applicable to the Ito stochastic differential equation. However for other stochastic integrals, the function $f(z(\tau), \dot{z}(\tau), \tau)$ may not be that trivial. So we think that it's necessary to use the mid-point rule when integrate stochastic integrals with stochastic quantities like $z(\tau)$ and $\dot{z}(\tau)$ as integral variables, e.g. the one in Eq. 20. Although in the stochastic integral in Eq. 20, the integral variable is $x(t)$ and we can change $dx(t)$ into $\dot{x}(\tau)d\tau$ to avoid the mid-point rule, we find that it's not as precise as we use $dx(t)$ directly with the mid-point rule and the absolute value of the energy difference $\Delta = \Delta U + Q - W$, which should be as close to zero as possible to obey the first law of thermodynamics (cf. Sec. 8.1), is about one order of magnitude higher than using the mid-point rule. Maybe we should change $dx(t)$ into a higher order approximation as in Eq. 102. In our opinion, because $d\dot{z}(\tau)$ includes $d\mathcal{W}_\tau$, the Stratonovich stochastic integral with respect to $\dot{z}(\tau)$ should be discretized using the mid-point rule. And because $dz(\tau)$ can be represented by $\dot{z}(\tau)$ and $d\mathcal{W}_\tau$ (cf. Eq. 74), the Stratonovich stochastic integral in Eq. 20 should be discretized by the mid-point rule too. Therefore we should add a \circ in front of $dx(t)$ of this stochastic integral. We omit it to avoid some unnecessary confusion.

There is another form of mid-point rule like that in (34):

$$\begin{aligned}
\int_{\tau_0}^{\tau} \frac{\partial f(z(s), \dot{z}(s), s)}{\partial \dot{z}} b(z(s)) \circ d\mathcal{W}_s &= \sum_{i=1}^n \frac{1}{2} \left[\frac{\partial f(z(\tau_i), \dot{z}(\tau_i), \tau_i)}{\partial \dot{z}} b(z(\tau_i)) + \frac{\partial f(z(\tau_{i-1}), \dot{z}(\tau_{i-1}), \tau_{i-1})}{\partial \dot{z}} b(z(\tau_{i-1})) \right] (\mathcal{W}_{\tau_i} - \mathcal{W}_{\tau_{i-1}}) \\
&= \sum_{i=1}^n \frac{1}{2} [g(z(\tau_i), \dot{z}(\tau_i), \tau_i) + g(z(\tau_{i-1}), \dot{z}(\tau_{i-1}), \tau_{i-1})] (\mathcal{W}_{\tau_i} - \mathcal{W}_{\tau_{i-1}}),
\end{aligned} \tag{85}$$

which we actually use in our simulation. Because

$$\begin{aligned}
&\frac{1}{2} [g(z(\tau_i), \dot{z}(\tau_i), \tau_i) + g(z(\tau_{i-1}), \dot{z}(\tau_{i-1}), \tau_{i-1})] \\
&= g(z(\tau_{i-1}), \dot{z}(\tau_{i-1}), \tau_{i-1}) + \frac{1}{2} [g(z(\tau_i), \dot{z}(\tau_i), \tau_i) - g(z(\tau_{i-1}), \dot{z}(\tau_{i-1}), \tau_{i-1})] \\
&= g(z(\tau_{i-1}), \dot{z}(\tau_{i-1}), \tau_{i-1}) + \frac{1}{2} \left[\frac{\partial}{\partial z} (z(\tau_i) - z(\tau_{i-1})) + \frac{\partial}{\partial \dot{z}} (\dot{z}(\tau_i) - \dot{z}(\tau_{i-1})) + \frac{\partial}{\partial \tau} (\tau_i - \tau_{i-1}) \right] g(z(\tau_{i-1}), \dot{z}(\tau_{i-1}), \tau_{i-1}) + \dots \\
&= g(z(\tau_{i-1}), \dot{z}(\tau_{i-1}), \tau_{i-1}) \\
&\quad + \frac{1}{2} \left\{ \frac{\partial}{\partial z} \dot{z}(\tau_{i-1})(\tau_i - \tau_{i-1}) + \frac{\partial}{\partial \dot{z}} [a(z(\tau_i), \dot{z}(\tau_{i-1}), \tau_{i-1})(\tau_i - \tau_{i-1}) + b(z(\tau_{i-1}))(\mathcal{W}_i - \mathcal{W}_{i-1})] + \frac{\partial}{\partial \tau} (\tau_i - \tau_{i-1}) \right\} \\
&\quad \times g(z(\tau_{i-1}), \dot{z}(\tau_{i-1}), \tau_{i-1}) + \dots,
\end{aligned} \tag{86}$$

substitute which into Eq. 85 and discard the terms of higher than first order of $\tau_i - \tau_{i-1}$, we will get Eq. 84 again.

Therefore the two forms of mid-point rule are equivalent. And we find that using the two methods to calculate $\Delta = \Delta U + Q - W$ leads to similar results and they work equally well.

D. The continuous temperature function. In the derivation of Eq. 77 and the mid-point rule, the function $b(z)$ should be continuous. To avoid the not well-defined derivation resulting from the discontinuity of the temperature field in our PTSHE, we construct a continuous function to approximate the nondimensional temperature (60)

$$\Theta(z) = \frac{1}{2} \left\{ \Theta_h + \Theta_c + (\Theta_h - \Theta_c) \tanh\left(\frac{1}{\alpha} \left[\sin\left(z + \arctan \sqrt{\frac{\eta-1}{\eta+1}}\right) - \sqrt{\frac{\eta-1}{2\eta}} \right] \right) \right\}, \quad [87]$$

where $\Theta_{h,c}$ represents the temperature of the hot and the cold zones in our PTSHE. In Figure S58, we compare $\Theta(z)$ with its discontinuous version

$$\Theta^*(z) = \begin{cases} \Theta_h, & 2n\pi \leq z < 2n\pi + \arccos(-\frac{1}{\eta}), \\ \Theta_c, & 2n\pi + \arccos(-\frac{1}{\eta}) \leq z < 2(n+1)\pi, \end{cases} \quad n \in \mathbb{Z}, \quad [88]$$

at different α with $\eta = 4.60, 3.00, 1.00$. When α is small enough, i.e. $\alpha \leq 0.01$, $\Theta(z)$ is nearly the same as the discontinuous one. We choose $\alpha = 0.001$ in all our simulations unless otherwise noted.

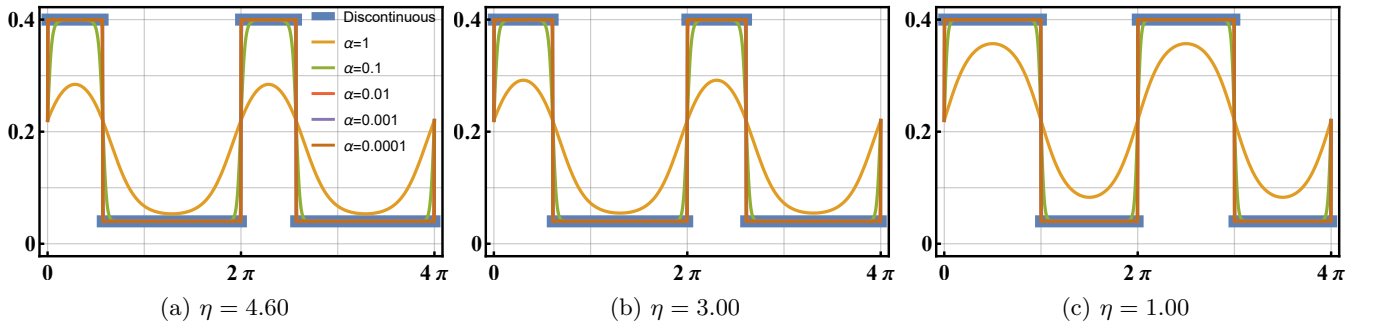


Fig. S58. The function $\Theta(z)$ at different α with $\eta = 4.60, 3.00, 1.00$ from left to right respectively. The corresponding discontinuous temperature function $\Theta^*(z)$ is plotted for comparison. Here $\Theta_h = 0.4$, $\Theta_c = 0.04$. The three curves of $\alpha \leq 0.01$ almost overlap so we can only see the curve of $\alpha = 0.0001$.

E. Stochastic Runge-Kutta method to integrate the Langevin equation. We use the 4-step Stochastic Runge-Kutta (SRK4) method in (26, 56) to numerically discretize the stochastic Eq. 74 into

$$\begin{aligned} z_1 &= \dot{z}_k \Delta\tau, \\ \dot{z}_1 &= a(z_k, \dot{z}_k, \tau_k) \Delta\tau \\ &\quad + b(z_k) \sqrt{q_1 \Delta\tau} w_{k,1}; \\ z_2 &= (\dot{z}_k + a_{21} \dot{z}_1) \Delta\tau, \\ \dot{z}_2 &= a(z_k + a_{21} z_1, \dot{z}_k + a_{21} \dot{z}_1, \tau_k + a_{21} \tau_1) \Delta\tau \\ &\quad + b(z_k + a_{21} z_1) \sqrt{q_2 \Delta\tau} w_{k,2}; \\ z_3 &= (\dot{z}_k + a_{31} \dot{z}_1 + a_{32} \dot{z}_2) \Delta\tau, \\ \dot{z}_3 &= a(z_k + a_{31} z_1 + a_{32} z_2, \dot{z}_k + a_{31} \dot{z}_1 + a_{32} \dot{z}_2, \tau_k + a_{31} \tau_1 + a_{32} \tau_2) \\ &\quad + b(z_k + a_{31} z_1 + a_{32} z_2) \sqrt{q_3 \Delta\tau} w_{k,3}; \\ z_4 &= (\dot{z}_k + a_{41} \dot{z}_1 + a_{42} \dot{z}_2 + a_{43} \dot{z}_3) \Delta\tau, \\ \dot{z}_4 &= a(z_k + a_{41} z_1 + a_{42} z_2 + a_{43} z_3, \dot{z}_k + a_{41} \dot{z}_1 + a_{42} \dot{z}_2 + a_{43} \dot{z}_3, \tau_k + a_{41} \tau_1 + a_{42} \tau_2 + a_{43} \tau_3) \\ &\quad + b(z_k + a_{41} z_1 + a_{42} z_2 + a_{43} z_3) \sqrt{q_4 \Delta\tau} w_{k,4}; \\ z_{k+1} &= z_k + \alpha_1 z_1 + \alpha_2 z_2 + \alpha_3 z_3 + \alpha_4 z_4, \\ \dot{z}_{k+1} &= \dot{z}_k + \alpha_1 \dot{z}_1 + \alpha_2 \dot{z}_2 + \alpha_3 \dot{z}_3 + \alpha_4 \dot{z}_4. \end{aligned} \quad [89]$$

The random numbers are independent and obey identical standard normal distribution with zero-mean and one-variance: $w_{k,i} \sim N(0, 1)$, $i = 1, 2, 3, 4$. The parameters are

a_{21}				q_1
a_{31}	a_{32}			q_2
a_{41}	a_{42}	a_{43}		q_3
α_1	α_2	α_3	α_4	q_4

$$=$$

0.66667754298442				3.99956364361748
0.63493935027993	0.00342761715422			1.64524970733585
-2.32428921184321	2.69723745129487	0.29093673271592		1.59330355118722
0.25001351164789	0.67428574806272	-0.00831795169360	0.08401868181222	0.26330006501868

F. Choice of the time stepsize. In order to avoid loss of precision or waste of time, the time stepsize $\Delta\tau$ cannot be too large or too small. It is not only constrained by the original differential equation for the specific practical problem, but also determined by the precision of the numerical method we used. We calculate the time stepsize from approximation of the Langevin equation first. The discussion of the feasibility of the time stepsize we will choose is given in the next subsection.

The second derivative of the resultant potential energy Eq. 1 with respect to x is

$$\begin{aligned}\frac{\partial^2 V}{\partial x^2} &= \kappa + \kappa\eta \cos\left(\frac{2\pi}{a}x(t)\right) \leq \kappa(1 + \eta) \\ &= m\omega_0^2(1 + \eta).\end{aligned}\quad [90]$$

We can approximate the resultant potential energy as $V \approx \frac{1}{2}m\omega_0^2(1 + \eta)x(t)^2$ at the points where its stiffness as well as intrinsic oscillating frequency are both maximum: $\omega_0\sqrt{1 + \eta}$. At these points neglecting the stochastic force $\xi(t)$, the Langevin Eq. 4 in the main text can be approximated by

$$m\ddot{x}(t) + m\mu\dot{x}(t) + m\omega_0^2(1 + \eta)x(t) = 0. \quad [91]$$

Let's change the sign before the third term on the LHS,

$$m\ddot{x}(t) + m\mu\dot{x}(t) - m\omega_0^2(1 + \eta)x(t) = 0, \quad [92]$$

so that the characteristic equation

$$r^2 + \mu r - \omega_0^2(1 + \eta) = 0 \quad [93]$$

with two characteristic roots $r_{1,2} = \frac{-\mu \pm \sqrt{\mu^2 + 4\omega_0^2(1 + \eta)}}{2}$, achieves a larger “characteristic frequency”:

$$\frac{1}{t^*} = \frac{\mu + \sqrt{\mu^2 + 4\omega_0^2(1 + \eta)}}{2}, \quad [94]$$

which is an upper bound of the frequency scale of both the oscillation and the damping relaxation of the particle.

Another frequency scale affecting the discrete time step is that of the driver center, and also the particle, passing over the periodic lattice:

$$\frac{1}{t^{**}} = \frac{v_{dr}}{a}. \quad [95]$$

When v_{dr} is small, the particle oscillates many cycles during it passing over one lattice period, so the former frequency scale contributes mainly. On the other hand, when v_{dr} is large, the mass point can pass over many lattice period during one oscillating cycle, and the latter frequency scale contributes more. Therefore, the discrete time stepsize can be computed from

$$\Delta t = \frac{1}{100} \frac{1}{\frac{1}{t^*} + \frac{1}{t^{**}}} = \frac{1}{100} \frac{1}{\frac{\mu + \sqrt{\mu^2 + 4\omega_0^2(1 + \eta)}}{2} + \frac{v_{dr}}{a}}, \quad [96]$$

which is a lower bound. The choice of the factor $\frac{1}{100}$ is described in the next subsection.

After being nondimensionalized, the simulation discrete time stepsize can be chosen as

$$\Delta\tau = \frac{\omega_0}{2\pi} \Delta t = \frac{1}{100} \frac{1}{\frac{\beta\eta + \sqrt{(\beta\eta)^2 + 16\pi^2(1 + \eta)}}{2} + \frac{\bar{v}}{2\pi}}. \quad [97]$$

G. Evaluation of the SRK4 method. We now evaluate the SRK4 method introduced above. Kasdin, J (56) made all the four substeps stochastic with four independent random numbers respectively, which results in more degrees of freedom so that the coefficients of his SRK4 method can be derived by matching the covariance of the Taylor expansion of the discrete solution with the Taylor expansion of the covariance of the continuous solution to a specific order. Because it's difficult to obtain the covariance of the solution of a nonlinear stochastic differential equation, his derivation is based on linear stochastic differential equation with zero mean. He applied this method to a nonlinear stochastic differential equation and proposed that the same set of coefficients derived for the time-varying linear case are appropriate for the nonlinear case.

In Sec. 7, we derived the fluctuation-dissipation theorem of the linearized Langevin Eq. 56, the solution of which, Eq. 61, is zero-mean with the covariances satisfying the equipartition theorem Eq. 65, as $t \rightarrow \infty$. Thus, at equilibrium the simulation results of the linear Eq. 56 with this SRK4 method, Eq. 89, should satisfy equipartition theorem in high precision.

Eq. 56 can be transformed into a nondimensional stochastic differential equation system

$$\begin{cases} dz = \dot{z}d\tau, \\ d\dot{z} = [-\beta\eta\dot{z} - 4\pi^2(1+\eta)z]d\tau + 4\pi^2\eta\sqrt{\frac{\beta}{\pi^2}}\Theta d\mathcal{W}_\tau = \bar{a}(z, \dot{z})d\tau + \bar{b}d\mathcal{W}_\tau. \end{cases} \quad [98]$$

We integrate it using the SRK4 method described in Eq. 89. The results are given in Figure S59 represented by the red circles. We can see that for all the time stepsizes considered, the simulation results of Eq. 98 at equilibrium with the SRK4 method obey equipartition theorem (represented by the black dotted lines) in high precision.

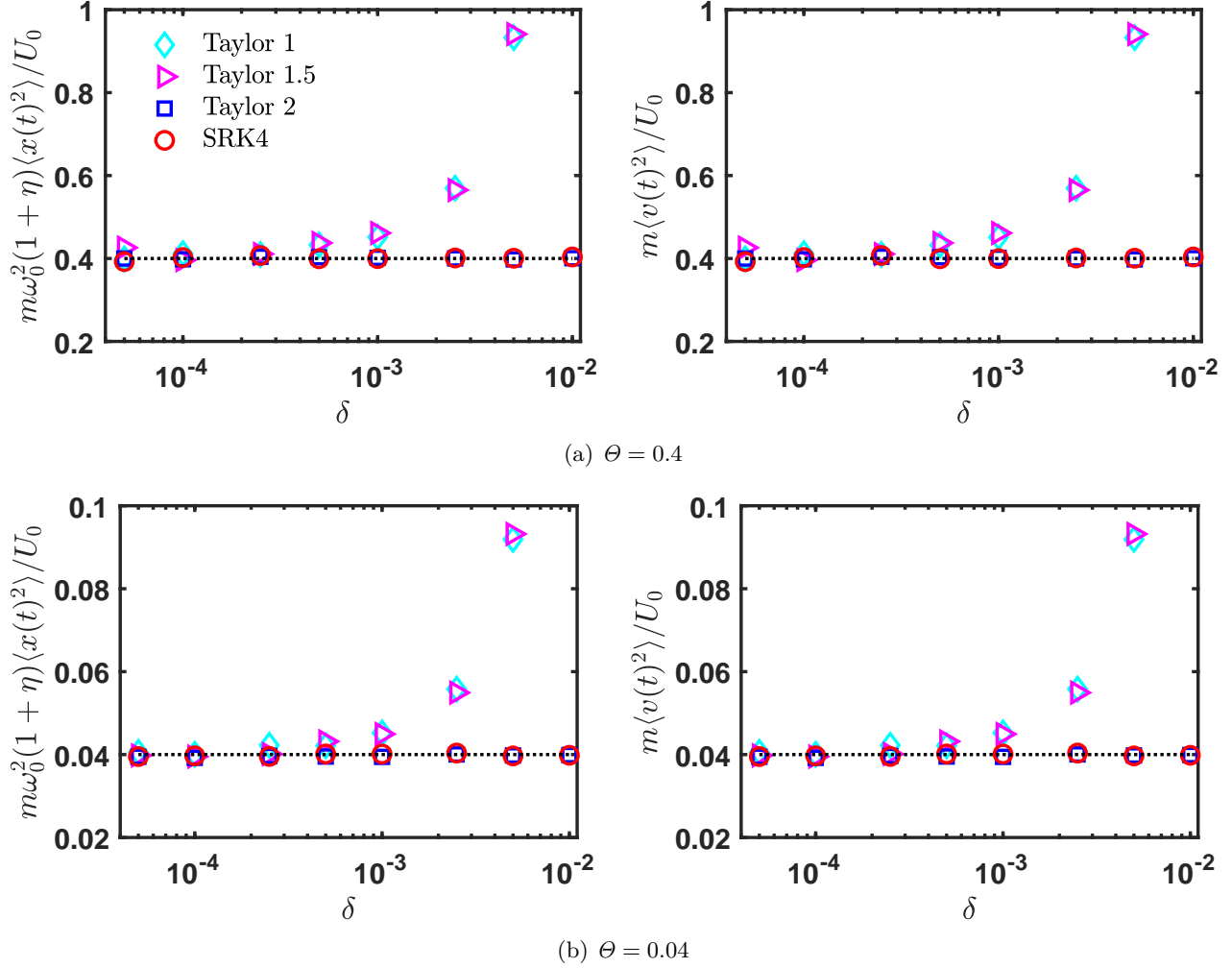


Fig. S59. Comparison between different simulation methods. The dotted black lines represent the values of $m\omega_0^2(1+\eta)\langle x(t)^2 \rangle/V_0$ and $m\langle v(t)^2 \rangle/V_0$ at equilibrium approximated by the equipartition theorem, which should be equal to the corresponding nondimensional temperature Θ . The x -coordinates of all the four subfigures are the time stepsize coefficient δ , see the text below. The SRK4 method performs well for all the δ values considered. The order 2 strong Taylor scheme works equally well. Whereas, the performance of the order 1 and 1.5 strong Taylor schemes depend much on the time stepsize. Note that when $\delta = 0.01$, the time step is too large for the order 1 and 1.5 strong Taylor schemes to converge.

Here the time stepsizes are calculated by Eq. 97 with $\frac{1}{100}$ replaced by a coefficient δ and $\bar{v} = 0$. We start the particle at $(x = 0, v = 0)$ and iterate an enough number of time steps to ensure equilibrium has been arrived at so that we can utilize the time average to approximate the ensemble average. The δ 's and the corresponding number N 's of time steps which we finally chose in simulation of Eq. 98 after some trial and error are listed in Table S1. Each ensemble average is calculated by the time average from the $(N/2 + 1)$ st time step, at which we presume that the equilibrium has been arrived at, to the end.

Table S1. The δ 's and the corresponding N 's in simulation of Eq. 98 with different methods

δ	5×10^{-5}	1×10^{-4}	2.5×10^{-4}	5×10^{-4}	1×10^{-3}	2.5×10^{-3}	5×10^{-3}	1×10^{-2}
$N(2 \times 10^8)$	200	100	40	20	10	10	10	10

We compare this SRK4 method to the stochastic Taylor approximations of strong convergence order 1.0, 1.5 and 2.0 (61), which are explicit iterative method utilizing the stochastic Taylor expansion (62) to different orders. We give a brief derivation of the stochastic Taylor expansion at the end of this subsection. The order 1, 1.5 and 2.0 Taylor schemes to integrate the Langevin Eq. 98 are listed here.

Order 1 strong Taylor scheme (61) (Taylor 1):

$$\begin{aligned} z_{k+1} &= z_k + \dot{z}_k \Delta\tau, \\ \dot{z}_{k+1} &= \dot{z}_k + \bar{b} \sqrt{\Delta\tau} w_k + \bar{a}(z_k, \dot{z}_k) \Delta\tau, \end{aligned} \quad [99]$$

with w_k independently normally distributed with zero-mean and one-variance: $w_k \sim N(0, 1)$. This scheme is also called Milstein scheme (61) and is derived from truncating Eq. 113 and Eq. 114 to the first order. We can obtain the same scheme using (3.2) in (61) with b^1 and b^2 substituted by 0 and \bar{b} respectively and because the function \bar{b} is independent of \dot{z} , the third term on the RHS of (3.2) in (61) vanishes. Therefore for Eq. 98 this scheme is the same as the Euler scheme, i.e. (2.4) in (61), which is of strong order 0.5.

Order 1.5 strong Taylor scheme (61) (Taylor 1.5):

$$\begin{aligned} z_{k+1} &= z_k + \dot{z}_k \Delta\tau + \bar{b} \Delta Z_k, \\ \dot{z}_{k+1} &= \dot{z}_k + \bar{b} \Delta W_k + \bar{a}(z_k, \dot{z}_k) \Delta\tau - \beta \eta \bar{b} \Delta Z_k, \end{aligned} \quad [100]$$

where $\Delta W_k = w_{k,1} \sqrt{\Delta\tau}$, $\Delta Z_k = \frac{1}{2} \Delta\tau^{\frac{3}{2}} (w_{k,1} + \frac{1}{\sqrt{3}} w_{k,2})$ with $w_{k,i}$, $i = 1, 2$ independently normally distributed with zero-mean and one-variance: $w_{k,i} \sim N(0, 1)$, $i = 1, 2$. This scheme is derived from truncating Eq. 113 and Eq. 114 to order 1.5. And we can also obtain the same scheme using (4.5) in (61) with b^1 and b^2 substituted by 0 and \bar{b} respectively. Here we haven't included the second order term on the RHS of (4.5) in (61), whose order is higher than 1.5.

Order 2 strong Taylor scheme (61) (Taylor 2):

$$\begin{aligned} z_{k+1} &= z_k + \dot{z}_k \Delta\tau + \bar{b} \Delta Z_k + \frac{1}{2} \bar{a}(z_k, \dot{z}_k) \Delta\tau^2, \\ \dot{z}_{k+1} &= \dot{z}_k + \bar{a}(z_k, \dot{z}_k) \Delta\tau + \bar{b} \Delta W_k - \beta \eta \bar{b} \Delta Z_k + \frac{1}{2} [-4\pi^2 (1 + \eta) \dot{z}_k - \beta \eta \bar{a}(z_k, \dot{z}_k)] \Delta\tau^2, \end{aligned} \quad [101]$$

where $\Delta W_k = w_{k,1} \sqrt{\Delta\tau}$, $\Delta Z_k = \frac{1}{2} \Delta\tau^{\frac{3}{2}} (w_{k,1} + \frac{1}{\sqrt{3}} w_{k,2})$ with $w_{k,i}$, $i = 1, 2$ independently normally distributed with zero-mean and one-variance: $w_{k,i} \sim N(0, 1)$, $i = 1, 2$. The scheme is derived from truncating Eq. 113 and Eq. 114 to order 2.

The simulation results are given in Figure S59. We can see that the order 1 and 1.5 strong Taylor schemes are not precise when the stepsize is large. The computation even diverges at $\delta = 0.01$. The Taylor 1.5 scheme (Eq. 100) appends the 1.5 order term containing ΔZ_k to the Taylor 1 scheme (Eq. 99), which improves little and the two schemes performs almost equally.

In constast, appended by the second order term, the Taylor 2 scheme improves a lot and performs equally to the SRK4 method. It's appeal to use Taylor 2 scheme instead of SRK4, because the Taylor 2 scheme needs less random numbers generated and less function evaluations, so it runs fast. However, our nonlinear Langevin Eq. 74 is not so trivial as the linear one.

The order 2 strong Taylor scheme for nonlinear Langevin Eq. 74 is

$$\begin{aligned} z_{k+1} &= z_k + b(z_k) \Delta Z_k + \dot{z}_k \Delta\tau + \frac{1}{2} a(\tau_k, z_k, \dot{z}_k) \Delta\tau^2, \\ \dot{z}_{k+1} &= \dot{z}_k + a(\tau_k, z_k, \dot{z}_k) \Delta\tau + b(z_k) \Delta W_k \\ &\quad + L_b a(\tau_k, z_k, \dot{z}_k) \Delta Z_k + L_a b(z_k) (\Delta\tau \Delta W_k - \Delta Z_k) + \frac{1}{2} L_a a(\tau_k, z_k, \dot{z}_k) \Delta\tau^2 + L_b L_a b(z_k) I_{(1,0,1)}, \end{aligned} \quad [102]$$

which is derived from Eq. 115 and Eq. 116. We can see that for the discretization of the nonlinear Langevin equation to the second order, we need to evaluate more functions. What's more, the multiple stochastic integral $I_{(1,0,1)}$ in the last term needs to be simulate, which is complicated. To estimate this term we plot the function $L_b L_a b(z)$ in Figure S60. We can see that it's almost zero everywhere except at the boundaries of the hot and the cold heat baths. In view of this we as a compromise neglect the term $L_b L_a b(z_k) I_{(1,0,1)}$, which is of second order. We can regard it as an earlier truncation of the stochastic Taylor expansion to less than 2nd order. And we will call this scheme Taylor 2-.

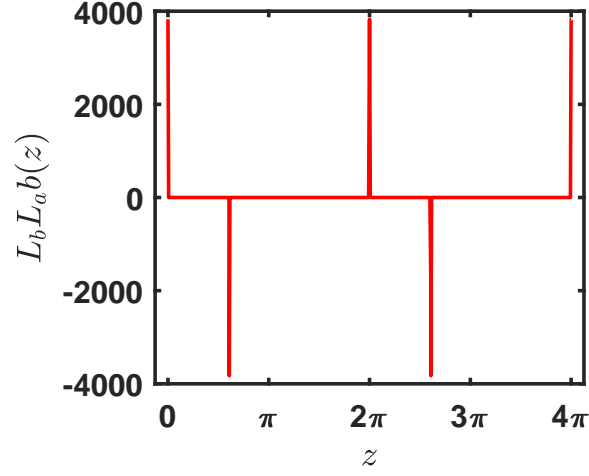


Fig. S60. The function $L_b L_a b(z)$ is nearly a train of periodic pulses.

We have seen that the appending the terms of order 1.5, which is stochastic, to the Taylor 1 scheme doesn't improve the performance at least in the sense of mean square values. Therefore we can presume that neglecting the stochastic term $L_b L_a b(z_k) I_{(1,0,1)}$ won't affect the performance of the Taylor 2 scheme much either. If the temperature of the heat bath is constant, i.e. $b(z_k) = \text{constant}$, this term will vanish, and the Taylor 2- method can achieve higher precision than 2nd order. Moreover, by choosing small enough time step size, the Taylor 2- scheme can achieve the accuracy we need.

In Figure S61, we compare the Taylor 2- scheme with SRK4 in calculating the cycle work W_{cyc} . We can see that both the mean value and the standard deviation values are nearly the same using the two methods at each driving velocity v_{dr} . Therefore we can conclude that the SRK4 and the Taylor 2- method are both appropriate for the simulation of our nonlinear Langevin equation, although the SRK4 scheme is derived from the linear stochastic differential equation (56). And we can also conclude that the time stepsize Eq. 97 we have chosen is also appropriate.

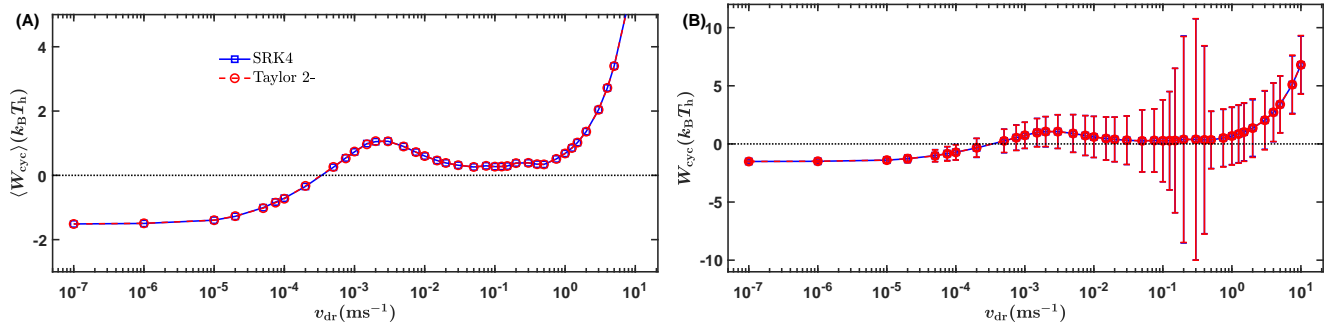


Fig. S61. The cycle work W_{cyc} with respect to the driving velocity v_{dr} simulated by Taylor 2- and SRK4. The left plot gives the mean values and the right one is added by the standard deviations to the left one. Both the mean values and the standard deviations simulated by the two methods coincide. The time stepsize is calculated by Eq. 97. The parameters are $\eta = 3.0$, $\mu = 4 \times 10^4 \text{ s}^{-1}$, $\Theta_h = 0.4$, $\Theta_c = 0.04$, and other parameters are given in Table S2.

The Taylor 2- scheme runs a little faster than the SRK4, and is more comprehensible. In spite of this, we still choose the SRK4 method in all our simulations of the nonlinear Langevin equation in the main text. It is easy to implement and there is ready-made codes (26).

Another advantage of the SRK4 is that it does not need the evaluations of the partial derivatives as in the case of Taylor 2-. At our first simulations of the PTSHE, we treat the temperature field with the discontinuous function Eq. 88, which is not differentiable at the boundaries of the hot and the cold heat baths. With the SRK4, we can still process our simulations without dealing with the derivatives, although it's not very rigorous. We have compared the results of the discontinuous temperature with that of the continuous one, and we didn't find any significant differences. So it is possible that the equivalence of the Stratonovich and the Ito form of the Langevin Eq. 74 is still correct with discontinuous spatio temperature function. Maybe there are relevant theorems which have been proved. We hope we can find or prove this in the future.

The stochastic Taylor expansion. Here we give a brief derivation of the Ito stochastic Taylor expansion (62) based on the form

$$\begin{cases} dz = \dot{z}(\tau) d\tau, \\ dz = a(z(\tau), \dot{z}(\tau), \tau) d\tau + b(z(\tau)) dW_\tau, \end{cases} \quad [103]$$

by which both the nonlinear and the linear Langevin Eq. 74 and Eq. 98 can be represented. Integrate Eq. 103 from τ_0 to τ we obtain

$$\begin{cases} \Delta z = \int_{\tau_0}^{\tau} \dot{z}(s) ds, \\ \Delta \dot{z} = \int_{\tau_0}^{\tau} a(z(s), \dot{z}(s), s) ds + \int_{\tau_0}^{\tau} b(z(s)) d\mathcal{W}_s, \end{cases} \quad [104]$$

in which $\Delta z = z(\tau) - z(\tau_0)$. The Ito formula Eq. 79 will be used iteratively next, so we write it down here again in the integral form

$$\begin{aligned} f(z(\tau), \dot{z}(\tau), \tau) &= f(z(\tau_0), \dot{z}(\tau_0), \tau_0) + \int_{\tau_0}^{\tau} \left[\frac{\partial f}{\partial z} dz(s) + \frac{\partial f}{\partial \dot{z}} d\dot{z}(s) + \frac{\partial f}{\partial \tau} ds \right] + \int_{\tau_0}^{\tau} \frac{1}{2} \frac{\partial^2 f}{\partial \dot{z}^2} b(z(s))^2 ds \\ &= f(z_0, \dot{z}_0, \tau_0) + \int_{\tau_0}^{\tau} \left\{ \frac{\partial f}{\partial z} \dot{z} ds + \frac{\partial f}{\partial \dot{z}} [a(z, \dot{z}, s) ds + b(z) d\mathcal{W}_s] + \frac{\partial f}{\partial \tau} ds \right\} + \int_{\tau_0}^{\tau} \frac{1}{2} \frac{\partial^2 f}{\partial \dot{z}^2} b(z)^2 ds \\ &= f(z_0, \dot{z}_0, \tau_0) + \int_{\tau_0}^{\tau} \left[\frac{\partial f}{\partial \tau} + \dot{z} \frac{\partial f}{\partial z} + a(z, \dot{z}, s) \frac{\partial f}{\partial \dot{z}} + \frac{1}{2} \frac{\partial^2 f}{\partial \dot{z}^2} b(z)^2 \right] ds + \int_{\tau_0}^{\tau} b(z) \frac{\partial f}{\partial \dot{z}} d\mathcal{W}_s \\ &= f(z_0, \dot{z}_0, \tau_0) + \int_{\tau_0}^{\tau} L_a f(z(s), \dot{z}(s), s) ds + \int_{\tau_0}^{\tau} L_b f(z(s), \dot{z}(s), s) d\mathcal{W}_s, \end{aligned} \quad [105]$$

in which the second equality results from substituting Eq. 103 and we use the operators

$$\begin{aligned} L_a &= \frac{\partial}{\partial \tau} + \dot{z} \frac{\partial}{\partial z} + a(z(\tau), \dot{z}(\tau), \tau) \frac{\partial}{\partial \dot{z}} + \frac{1}{2} b(z(\tau))^2 \frac{\partial^2}{\partial \dot{z}^2}, \\ L_b &= b(z(\tau)) \frac{\partial}{\partial \dot{z}}, \end{aligned} \quad [106]$$

and $z_0 = z(\tau_0)$, $\dot{z}_0 = \dot{z}(\tau_0)$ for compactness.

We first expand Δz . Apply Ito formula Eq. 105 to $\dot{z}(s)$ and substitute it into the first equation of Eq. 104 we will obtain

$$\begin{aligned} \Delta z &= \int_{\tau_0}^{\tau} \left[\dot{z}_0 + \int_{\tau_0}^s a(z(u), \dot{z}(u), u) du + \int_{\tau_0}^s b(z(u)) d\mathcal{W}_u \right] ds \\ &= \dot{z}_0 \Delta \tau + \int_{\tau_0}^{\tau} \int_{\tau_0}^s a(z(u), \dot{z}(u), u) du ds + \int_{\tau_0}^{\tau} \int_{\tau_0}^s b(z(u)) d\mathcal{W}_u ds, \end{aligned} \quad [107]$$

in which $\Delta \tau = \int_{\tau_0}^{\tau} ds$. Apply Ito formula again to $a(z(u), \dot{z}(u), u)$ and $b(z(u))$ and substitute them to this equation, we will obtain

$$\begin{aligned} \Delta z &= \dot{z}_0 \Delta \tau + \int_{\tau_0}^{\tau} \int_{\tau_0}^s \left[a(z_0, \dot{z}_0, \tau_0) + \int_{\tau_0}^u L_a a(z(v), \dot{z}(v), v) dv + \int_{\tau_0}^u L_b b(z(v), \dot{z}(v), v) d\mathcal{W}_v \right] du ds \\ &\quad + \int_{\tau_0}^{\tau} \int_{\tau_0}^s \left[b(z_0) + \int_{\tau_0}^u L_a b(z(v)) dv + \int_{\tau_0}^u L_b b(z(v)) d\mathcal{W}_v \right] d\mathcal{W}_u ds \\ &= \dot{z}_0 \Delta \tau + a(z_0, \dot{z}_0, \tau_0) \frac{1}{2} \Delta \tau^2 + \int_{\tau_0}^{\tau} \int_{\tau_0}^s \int_{\tau_0}^u L_a a(z(v), \dot{z}(v), v) dv du ds + \int_{\tau_0}^{\tau} \int_{\tau_0}^s \int_{\tau_0}^u L_b b(z(v), \dot{z}(v), v) d\mathcal{W}_v du ds \\ &\quad + b(z_0) I_{(1,0)} + \int_{\tau_0}^{\tau} \int_{\tau_0}^s \int_{\tau_0}^u L_a b(z(v)) dv d\mathcal{W}_u ds + \int_{\tau_0}^{\tau} \int_{\tau_0}^s \int_{\tau_0}^u L_b b(z(v)) d\mathcal{W}_v d\mathcal{W}_u ds \\ &= \dot{z}_0 \Delta \tau + a(z_0, \dot{z}_0, \tau_0) \frac{1}{2} \Delta \tau^2 + b(z_0) I_{(1,0)} + \int_{\tau_0}^{\tau} \int_{\tau_0}^s \int_{\tau_0}^u L_b b(z(v)) d\mathcal{W}_v d\mathcal{W}_u ds + o(\Delta \tau^2), \end{aligned} \quad [108]$$

in which $I_{(1,0)} = \int_{\tau_0}^{\tau} \int_{\tau_0}^s d\mathcal{W}_u ds$, which is of order 1.5 because $d\mathcal{W}_u$ is of order 0.5. In this equation, all the multiple stochastic integrals of order higher than 2 are absorbed in $o(\Delta \tau^2)$, except the remaining one $\int_{\tau_0}^{\tau} \int_{\tau_0}^s \int_{\tau_0}^u L_b b(z(v)) d\mathcal{W}_v d\mathcal{W}_u ds$, which is order 2.

Apply the Ito formula to $L_b b(z(v))$, substitute it into Eq. 108 and absorb the stochastic multiple integrals of order higher than 2 into $o(\Delta \tau^2)$, we will obtain

$$\Delta z = \dot{z}_0 \Delta \tau + b(z_0) I_{(1,0)} + a(z_0, \dot{z}_0, \tau_0) \frac{1}{2} \Delta \tau^2 + L_b b(z_0) I_{(1,1,0)} + o(\Delta \tau^2), \quad [109]$$

where $I_{(1,1,0)} = \int_{\tau_0}^{\tau} \int_{\tau_0}^s \int_{\tau_0}^u d\mathcal{W}_v d\mathcal{W}_u ds$ is of order 2.

Then we expand $\Delta\dot{z}$. Apply Ito formula to $a(z(s), \dot{z}(s), s)$ and $b(z(s))$, and substitute them into the second equation of Eq. 104, we will obtain

$$\begin{aligned}\Delta\dot{z} &= \int_{\tau_0}^{\tau} \left[a(z_0, \dot{z}_0, \tau_0) + \int_{\tau_0}^s L_a a(z(u), \dot{z}(u), u) du + \int_{\tau_0}^s L_b a(z(u), \dot{z}(u), u) d\mathcal{W}_u \right] ds \\ &\quad + \int_{\tau_0}^{\tau} \left[b(z_0) + \int_{\tau_0}^s L_a b(z(u)) du + \int_{\tau_0}^s L_b b(z(u)) d\mathcal{W}_u \right] d\mathcal{W}_s \\ &= a(z_0, \dot{z}_0, \tau_0) \Delta\tau + \int_{\tau_0}^{\tau} \int_{\tau_0}^s L_a a(z(u), \dot{z}(u), u) dud s + \int_{\tau_0}^{\tau} \int_{\tau_0}^s L_b a(z(u), \dot{z}(u), u) d\mathcal{W}_u ds \\ &\quad + b(z_0) \Delta\mathcal{W}_\tau + \int_{\tau_0}^{\tau} \int_{\tau_0}^s L_a b(z(u)) dud \mathcal{W}_s + \int_{\tau_0}^{\tau} \int_{\tau_0}^s L_b b(z(u)) d\mathcal{W}_u d\mathcal{W}_s,\end{aligned}\tag{110}$$

where $\Delta\mathcal{W}_\tau = \int_{\tau_0}^{\tau} d\mathcal{W}_s$.

Apply the Ito formula to $L_a a(z(u), \dot{z}(u), u)$, $L_b a(z(u), \dot{z}(u), u)$, $L_a b(z(u))$ and $L_b b(z(u))$ again and substitute them into the above equation, we will obtain

$$\begin{aligned}\Delta\dot{z} &= a(z_0, \dot{z}_0, \tau_0) \Delta\tau + \int_{\tau_0}^{\tau} \int_{\tau_0}^s \left[L_a a(z_0, \dot{z}_0, \tau_0) + \int_{\tau_0}^u L_a L_a a(z(v), \dot{z}(v), v) dv + \int_{\tau_0}^u L_b L_a a(z(v), \dot{z}(v), v) d\mathcal{W}_v \right] dud s \\ &\quad + \int_{\tau_0}^{\tau} \int_{\tau_0}^s \left[L_b a(z_0, \dot{z}_0, \tau_0) + \int_{\tau_0}^u L_a L_b a(z(v), \dot{z}(v), v) dv + \int_{\tau_0}^u L_b L_b a(z(v), \dot{z}(v), v) d\mathcal{W}_v \right] d\mathcal{W}_u ds \\ &\quad + b(z_0) \Delta\mathcal{W}_\tau + \int_{\tau_0}^{\tau} \int_{\tau_0}^s \left[L_a b(z_0) + \int_{\tau_0}^u L_a L_a b(z(v)) dv + \int_{\tau_0}^u L_b L_a b(z(v)) d\mathcal{W}_v \right] dud \mathcal{W}_s \\ &\quad + \int_{\tau_0}^{\tau} \int_{\tau_0}^s \left[L_b b(z_0) + \int_{\tau_0}^u L_a L_b b(z(v)) dv + \int_{\tau_0}^u L_b L_b b(z(v)) d\mathcal{W}_v \right] d\mathcal{W}_u d\mathcal{W}_s \\ &= a(z_0, \dot{z}_0, \tau_0) \Delta\tau + L_a a(z_0, \dot{z}_0, \tau_0) \frac{1}{2} \Delta\tau^2 + L_b a(z_0, \dot{z}_0, \tau_0) I_{(1,0)} + \int_{\tau_0}^{\tau} \int_{\tau_0}^s \int_{\tau_0}^u L_b L_b a(z(v), \dot{z}(v), v) d\mathcal{W}_v d\mathcal{W}_u ds \\ &\quad + b(z_0) \Delta\mathcal{W}_\tau + L_a b(z_0) I_{(0,1)} + \int_{\tau_0}^{\tau} \int_{\tau_0}^s \int_{\tau_0}^u L_b L_a b(z(v)) d\mathcal{W}_v dud \mathcal{W}_s \\ &\quad + L_b b(z_0) I_{(1,1)} + \int_{\tau_0}^{\tau} \int_{\tau_0}^s \int_{\tau_0}^u L_a L_b b(z(v)) dv d\mathcal{W}_u d\mathcal{W}_s + \int_{\tau_0}^{\tau} \int_{\tau_0}^s \int_{\tau_0}^u L_b L_b b(z(v)) d\mathcal{W}_v d\mathcal{W}_u d\mathcal{W}_s + o(\Delta\tau^2),\end{aligned}\tag{111}$$

where $I_{(0,1)} = \int_{\tau_0}^{\tau} \int_{\tau_0}^s dud \mathcal{W}_s$ and $I_{(1,1)} = \int_{\tau_0}^{\tau} \int_{\tau_0}^s d\mathcal{W}_u d\mathcal{W}_s$ and the stochastic mutiple integrals of order higher than 2 are absorbed into $o(\Delta\tau^2)$.

Apply the Ito formula iteratively, absorb the stochastic mutiple integrals of order higher than 2, we can obtain the stochastic Taylor expansion of $\Delta\dot{z}$ up to the second order

$$\begin{aligned}\Delta\dot{z} &= a(z_0, \dot{z}_0, \tau_0) \Delta\tau + L_a a(z_0, \dot{z}_0, \tau_0) \frac{1}{2} \Delta\tau^2 + L_b a(z_0, \dot{z}_0, \tau_0) I_{(1,0)} + L_b L_b a(z_0, \dot{z}_0, \tau_0) I_{(1,1,0)} \\ &\quad + b(z_0) \Delta\mathcal{W}_\tau + L_a b(z_0) I_{(0,1)} + L_b L_a b(z_0) I_{(1,0,1)} \\ &\quad + L_b b(z_0) I_{(1,1)} + L_a L_b b(z_0) I_{(0,1,1)} + L_b L_b b(z_0) I_{(1,1,1)} + L_b L_b L_b b(z_0) I_{(1,1,1,1)} + o(\Delta\tau^2) \\ &= b(z_0) \Delta\mathcal{W}_\tau \\ &\quad + a(z_0, \dot{z}_0, \tau_0) \Delta\tau + L_b b(z_0) I_{(1,1)} \\ &\quad + L_b a(z_0, \dot{z}_0, \tau_0) I_{(1,0)} + L_a b(z_0) I_{(0,1)} + L_b L_b b(z_0) I_{(1,1,1)} \\ &\quad + L_a a(z_0, \dot{z}_0, \tau_0) \frac{1}{2} \Delta\tau^2 + L_b L_b a(z_0, \dot{z}_0, \tau_0) I_{(1,1,0)} + L_b L_a b(z_0) I_{(1,0,1)} + L_a L_b b(z_0) I_{(0,1,1)} \\ &\quad + L_b L_b L_b b(z_0) I_{(1,1,1,1)} + o(\Delta\tau^2),\end{aligned}\tag{112}$$

in which $I_{(1,1,0)} = \int_{\tau_0}^{\tau} \int_{\tau_0}^s \int_{\tau_0}^u d\mathcal{W}_v d\mathcal{W}_u ds$, $I_{(1,0,1)} = \int_{\tau_0}^{\tau} \int_{\tau_0}^s \int_{\tau_0}^u d\mathcal{W}_v dud \mathcal{W}_s$, $I_{(0,1,1)} = \int_{\tau_0}^{\tau} \int_{\tau_0}^s \int_{\tau_0}^u dv d\mathcal{W}_u d\mathcal{W}_s$, $I_{(1,1,1)} = \int_{\tau_0}^{\tau} \int_{\tau_0}^s \int_{\tau_0}^u d\mathcal{W}_v d\mathcal{W}_u d\mathcal{W}_s$ and $I_{(1,1,1,1)} = \int_{\tau_0}^{\tau} \int_{\tau_0}^s \int_{\tau_0}^u \int_{\tau_0}^v d\mathcal{W}_p d\mathcal{W}_v d\mathcal{W}_u d\mathcal{W}_s$.

The stochastic Taylor expansions of Δz (Eq. 109) and $\Delta\dot{z}$ (Eq. 112) are a little complicated in the general form. However, we can simplify them utilizing the relatively simple form of our linear and nonlinear Langevin equations.

In the linear case, $\bar{a}(z(\tau), \dot{z}(\tau)) = -\beta\eta\dot{z} - 4\pi^2(1+\eta)z$ and \bar{b} is constant, then

$$\Delta z = \dot{z}_0 \Delta\tau + \bar{b} I_{(1,0)} + \frac{1}{2} \bar{a}(z_0, \dot{z}_0) \Delta\tau^2 + o(\Delta\tau^2)\tag{113}$$

and

$$\Delta \dot{z} = \bar{b} \Delta \mathcal{W}_\tau + \bar{a}(z_0, \dot{z}_0) \Delta \tau - \beta \eta \bar{b} I_{(1,0)} + \frac{1}{2} \left\{ [-4\pi^2(1+\eta)] \dot{z}_0 + (-\beta \eta) \bar{a}(z_0, \dot{z}_0) \right\} \Delta \tau^2 + o(\Delta \tau^2). \quad [114]$$

In the nonlinear case, $a(z(\tau), \dot{z}(\tau), \tau) = -\beta \eta \dot{z} - 4\pi^2(z - \bar{v}\tau) - 4\pi^2 \eta \sin z$ and $b(z(\tau)) = 4\pi^2 \eta \sqrt{\frac{\beta}{\pi^2} \Theta(z(\tau))}$, which is only dependent on $z(\tau)$, then

$$\Delta z = \dot{z}_0 \Delta \tau + b(z_0) I_{(1,0)} + \frac{1}{2} a(z_0, \dot{z}_0, \tau_0) \Delta \tau^2 + o(\Delta \tau^2), \quad [115]$$

and

$$\Delta \dot{z} = b(z_0) \Delta \mathcal{W}_\tau + a(z_0, \dot{z}_0, \tau_0) \Delta \tau + L_b a(z_0, \dot{z}_0, \tau_0) I_{(1,0)} + L_a b(z_0) I_{(0,1)} + \frac{1}{2} L_a a(z_0, \dot{z}_0, \tau_0) \Delta \tau^2 + L_b L_a b(z_0) I_{(1,0,1)} + o(\Delta \tau^2), \quad [116]$$

in which

$$\begin{aligned} L_b a(z(\tau), \dot{z}(\tau), \tau) &= b(z(\tau)) \frac{\partial}{\partial \dot{z}} a(z(\tau), \dot{z}(\tau), \tau) = b(z(\tau))(-\beta \eta), \\ L_a b(z(\tau)) &= \left[\frac{\partial}{\partial \tau} + \dot{z}(\tau) \frac{\partial}{\partial z} + a(z(\tau), \dot{z}(\tau), \tau) \frac{\partial}{\partial \dot{z}} + \frac{1}{2} b(z(\tau))^2 \frac{\partial^2}{\partial \dot{z}^2} \right] b(z(\tau)) \\ &= \dot{z}(\tau) \pi^2 \eta \sqrt{\frac{\beta}{\pi^2}} (\Theta_h - \Theta_c) \frac{1}{\sqrt{\Theta(z(\tau))}} \frac{1}{\cosh^2(\frac{1}{\alpha} [\sin(z(\tau)) + \arctan \sqrt{\frac{\eta-1}{\eta+1}} - \sqrt{\frac{\eta-1}{2\eta}}])} \\ &\quad \times \frac{1}{\alpha} \cos(z(\tau) + \arctan \sqrt{\frac{\eta-1}{\eta+1}}), \\ L_a a(z(\tau), \dot{z}(\tau), \tau) &= \left[\frac{\partial}{\partial \tau} + \dot{z}(\tau) \frac{\partial}{\partial z} + a(z(\tau), \dot{z}(\tau), \tau) \frac{\partial}{\partial \dot{z}} + \frac{1}{2} b(z(\tau))^2 \frac{\partial^2}{\partial \dot{z}^2} \right] a(z(\tau), \dot{z}(\tau), \tau) \\ &= 4\pi^2 \bar{v} + \dot{z}(\tau) (-4\pi^2 - 4\pi^2 \eta \cos z) + a(z(\tau), \dot{z}(\tau), \tau) (-\beta \eta), \\ L_b L_a b(z(\tau)) &= b(z(\tau)) \frac{\partial}{\partial \dot{z}} L_a b(z(\tau)) \\ &= b(z(\tau)) \pi^2 \eta \sqrt{\frac{\beta}{\pi^2}} (\Theta_h - \Theta_c) \frac{1}{\sqrt{\Theta(z(\tau))}} \frac{1}{\cosh^2(\frac{1}{\alpha} [\sin(z(\tau)) + \arctan \sqrt{\frac{\eta-1}{\eta+1}} - \sqrt{\frac{\eta-1}{2\eta}}])} \\ &\quad \times \frac{1}{\alpha} \cos(z(\tau) + \arctan \sqrt{\frac{\eta-1}{\eta+1}}). \end{aligned}$$

We now calculate the mean values and variances of $I_{(1,0)}$ and $I_{(0,1)}$, both of which are normal.

$$\langle I_{(0,1)} \rangle = \langle \int_{\tau_0}^\tau \int_{\tau_0}^s du d\mathcal{W}_s \rangle = \int_{\tau_0}^\tau (s - \tau_0) \langle d\mathcal{W}_s \rangle = 0. \quad [117]$$

$$\begin{aligned} \langle I_{(0,1)}^2 \rangle &= \langle \int_{\tau_0}^\tau \int_{\tau_0}^s du d\mathcal{W}_s \int_{\tau_0}^\tau \int_{\tau_0}^{s'} du' d\mathcal{W}_{s'} \rangle = \langle \int_{\tau_0}^\tau (s - \tau_0) d\mathcal{W}_s \int_{\tau_0}^\tau (s' - \tau_0) d\mathcal{W}_{s'} \rangle \\ &= \langle \int_{\tau_0}^\tau \int_{\tau_0}^\tau (s - \tau_0)(s' - \tau_0) d\mathcal{W}_s d\mathcal{W}_{s'} \rangle = \int_{\tau_0}^\tau \int_{\tau_0}^\tau (s - \tau_0)(s' - \tau_0) \langle d\mathcal{W}_s d\mathcal{W}_{s'} \rangle \\ &= \int_{\tau_0}^\tau \int_{\tau_0}^\tau (s - \tau_0)(s' - \tau_0) \delta(s - s') ds ds' \\ &= \int_{\tau_0}^\tau (s - \tau_0)^2 ds = \frac{1}{3} \Delta \tau^3, \end{aligned} \quad [118]$$

where we have used the independence of the increments at different instants of the Gaussian process, i.e. $\langle d\mathcal{W}_s d\mathcal{W}_{s'} \rangle = \delta(s - s') ds ds'$.

Because $I_{(0)} = \int_{\tau_0}^\tau ds$, $I_{(1)} = \int_{\tau_0}^\tau d\mathcal{W}_s = \Delta \mathcal{W}_\tau$, we can constitute a stochastic differential equation system

$$\begin{cases} dI_{(0)} = d\tau, \\ dI_{(1)} = d\mathcal{W}_\tau, \end{cases} \quad [119]$$

which is of the same form as Eq. 103. Utilizing the Ito formula Eq. 105 leads to

$$\begin{aligned}
I_{(0)}I_{(1)} &= \int_{\tau_0}^{\tau} \left[\frac{\partial I_{(0)}I_{(1)}}{\partial I_{(0)}} dI_{(0)} + \frac{\partial I_{(0)}I_{(1)}}{\partial I_{(1)}} dI_{(1)} + \frac{\partial I_{(0)}I_{(1)}}{\partial \tau} ds \right] + \int_{\tau_0}^{\tau} \frac{1}{2} \frac{\partial^2 I_{(0)}I_{(1)}}{\partial I_{(1)}^2} \times 1^2 ds \\
&= \int_{\tau_0}^{\tau} \left[\frac{\partial I_{(0)}I_{(1)}}{\partial I_{(0)}} ds + \frac{\partial I_{(0)}I_{(1)}}{\partial I_{(1)}} d\mathcal{W}_s + \frac{\partial I_{(0)}I_{(1)}}{\partial \tau} ds \right] + \int_{\tau_0}^{\tau} \frac{1}{2} \frac{\partial^2 I_{(0)}I_{(1)}}{\partial I_{(1)}^2} \times 1^2 ds \\
&= \int_{\tau_0}^{\tau} I_{(1),s} ds + \int_{\tau_0}^{\tau} I_{(0),s} d\mathcal{W}_s = \int_{\tau_0}^{\tau} \int_{\tau_0}^s d\mathcal{W}_u ds + \int_{\tau_0}^{\tau} \int_{\tau_0}^s du d\mathcal{W}_s \\
&= I_{(1,0)} + I_{(0,1)}.
\end{aligned} \tag{120}$$

Then $I_{(1,0)} = I_{(1)}I_{(0)} - I_{(0,1)}$. Therefore we can treat $I_{(1)}$ and $I_{(0,1)}$ as two normal random variables: $I_{(1)} = \Delta\mathcal{W}_{\tau} \sim N(0, \Delta\tau)$ and $I_{(0,1)} \sim N(0, \frac{1}{3}\Delta\tau^3)$, and then $I_{(1,0)}$ can be obtained. The covariance of $I_{(1)}$ and $I_{(0,1)}$ is

$$\langle I_{(1)}I_{(0,1)} \rangle = \langle \int_{\tau_0}^{\tau} d\mathcal{W}_s \int_{\tau_0}^{\tau} \int_{\tau_0}^{s'} du d\mathcal{W}_{s'} \rangle = \int_{\tau_0}^{\tau} \int_{\tau_0}^{\tau} (s' - \tau_0) \langle d\mathcal{W}_s d\mathcal{W}_{s'} \rangle = \int_{\tau_0}^{\tau} (s - \tau_0) ds = \frac{1}{2} \Delta\tau^2. \tag{121}$$

To simulate $I_{(1)}$ and $I_{(0,1)}$ with two independent standard normal random variables $w_{1,2} \sim N(0, 1)$, we can institute

$$I_{(1)} = Aw_1 + Bw_2, \quad I_{(0,1)} = Cw_1 + Dw_2, \tag{122}$$

into $\langle \Delta\mathcal{W}_{\tau}^2 \rangle = \Delta\tau$, Eq. 117, Eq. 118 and Eq. 121. Solve the equation system with respect to A, B, C and D , we will achieve

$$I_{(1)} = \sqrt{\Delta\tau} w_1, \quad I_{(0,1)} = \frac{1}{2} \Delta\tau^{\frac{3}{2}} w_1 + \frac{1}{2\sqrt{3}} \Delta\tau^{\frac{3}{2}} w_2. \tag{123}$$

There is another way around, which is used in (61) and which we actually adopt in this paper. We can represent $I_{(0,1)}$ with $I_{(1)}$ and $I_{(1,0)}$: $I_{(0,1)} = I_{(1)}I_{(0)} - I_{(1,0)}$, and the mean and variance of $I_{(1,0)}$ can be calculated by

$$\langle I_{(1,0)} \rangle = \langle \int_{\tau_0}^{\tau} \int_{\tau_0}^s d\mathcal{W}_u ds \rangle = \int_{\tau_0}^{\tau} \int_{\tau_0}^s \langle d\mathcal{W}_u \rangle ds = 0, \tag{124}$$

$$\begin{aligned}
\langle I_{(1,0)}^2 \rangle &= \langle [I_{(0)}I_{(1)} - I_{(0,1)}]^2 \rangle = \langle I_{(0)}^2 I_{(1)}^2 - 2I_{(0)}I_{(1)}I_{(0,1)} + I_{(0,1)}^2 \rangle = \Delta\tau^2 \langle \Delta\mathcal{W}_{\tau}^2 \rangle - 2\Delta\tau \langle I_{(1)}I_{(0,1)} \rangle + \langle I_{(0,1)}^2 \rangle \\
&= \Delta\tau^2 \Delta\tau - 2\Delta\tau \frac{1}{2} \Delta\tau^2 + \frac{1}{3} \Delta\tau^3 = \frac{1}{3} \Delta\tau^3,
\end{aligned} \tag{125}$$

and we can also calculate the covariance of $I_{(1)}$ and $I_{(1,0)}$:

$$\begin{aligned}
\langle I_{(1)}I_{(1,0)} \rangle &= \langle \int_{\tau_0}^{\tau} d\mathcal{W}_s \int_{\tau_0}^{\tau} \int_{\tau_0}^{s'} d\mathcal{W}_u ds' \rangle = \langle \int_{\tau_0}^{\tau} \left[\int_{\tau_0}^{\tau} d\mathcal{W}_s \int_{\tau_0}^{s'} d\mathcal{W}_u \right] ds' \rangle = \int_{\tau_0}^{\tau} \left[\int_{\tau_0}^{s'} \int_{\tau_0}^{\tau} \langle d\mathcal{W}_s d\mathcal{W}_u \rangle \right] ds' \\
&= \int_{\tau_0}^{\tau} \left[\int_{\tau_0}^{s'} \int_{\tau_0}^{\tau} \delta(s - u) ds du \right] ds' = \int_{\tau_0}^{\tau} \left[\int_{\tau_0}^{s'} du \right] ds' = \frac{1}{2} \Delta\tau^2.
\end{aligned} \tag{126}$$

Because $\langle I_{(1,0)} \rangle$, $\langle I_{(1,0)}^2 \rangle$ and $\langle I_{(1)}I_{(1,0)} \rangle$ are equal to $\langle I_{(0,1)} \rangle$, $\langle I_{(0,1)}^2 \rangle$ and $\langle I_{(1)}I_{(0,1)} \rangle$ respectively, we can simulate $I_{(1)}$ and $I_{(1,0)}$ with two independent standard normal random variables: $w_{1,2} \sim N(0, 1)$ in the same way as $I_{(1)}$ and $I_{(0,1)}$:

$$I_{(1)} = \sqrt{\Delta\tau} w_1, \quad I_{(1,0)} = \frac{1}{2} \Delta\tau^{\frac{3}{2}} w_1 + \frac{1}{2\sqrt{3}} \Delta\tau^{\frac{3}{2}} w_2. \tag{127}$$

H. Parameters used in the simulation. Although we have nondimensionalized the Langevin equation, we will use the parameters in the trapped ion friction emulating experiment implemented by Gangloff et al. (40, 53, 63) so that our results will be more realistic and we can validate our numerical model through comparing with the experimental results. We must emphasize that because our simulation results are nondimensional, our simulation results may not only apply to the trapped ion system but may also apply to other systems such as a levitated nanosphere in optomechanical cavity (52, 64) and a microparticle suspended in liquid (33). The implementation of the PTSHE should depend on the practical obtainable ranges of all the parameters, which are mutually constrained as discussed in Sec. 6.N.1.

In (40, 53, 63), Yb^+ ion is chosen as the trapped ion whose mass $m = 2.8887 \times 10^{-25} \text{kg}$ and diameter $a = 185 \times 10^{-9} \text{m}$. The corrugation number η is determined by the amplitude of the lattice potential $V_0/2$ and the Paul trap longitudinal vibrational frequency $\omega_0/(2\pi) = 364 \text{kHz}$, both of which can be tuned to obtain a specific value of η . If we fix ω_0 and choose a specific η , then V_0 will be determined by $\eta = \frac{2\pi^2 V_0}{m\omega_0^2 a^2}$. The range of temperature is constrained by the experimental condition which is several to dozens of μK . Temperature T and V_0 determine the nondimensional temperature $\Theta = \frac{k_B T}{V_0}$. We choose $\Theta = 0.4$ and 0.04 as the high and the low temperature respectively in the main simulation case in the main text and the corresponding absolute temperatures are $22.77 \mu\text{K}$ and $2.277 \mu\text{K}$. In the parameter analysis, we have to change η , Θ and μ . Attention has to

be payed to the mutual constraints between these parameters. Ranges of all the parameters used in this paper are listed in Table S2 unless otherwise specified.

Table S2. Parameters used in the simulation

Parameters	$m(10^{-25}\text{kg})$	$a(10^{-9}\text{m})$	$\omega_0/(2\pi)(\text{kHz})$	η	$\mu(\text{s}^{-1})$	Θ	V_0	β
Values	2.8887	185	364	[1, 30]	$[0, 4 \times 10^7]$	$[0, 400]$	$\eta \frac{m\omega_0^2 a^2}{2\pi^2}$	$\frac{m\mu\omega_0 a^2}{\pi V_0}$

The numbers of simulation cycles should be large enough for the particle to arrive at steady state. However, we cannot simulate too many cycles at low driving velocity due to the small time stepsize and the large number of time steps in one cycle leading to the long simulation time. We chose the number of simulation cycles at each driving velocity after some trial and error and they are listed in Table S3.

At $v_{\text{dr}} = 0.4\text{m/s}$ and 0.5m/s , the numbers of simulation cycles are larger than their neighbors, because we find that for the main simulation case with parameters $\eta = 3.0$, $\mu = 4 \times 10^4\text{s}^{-1}$ and $\Theta_{\text{h,c}} = 0.4, 0.04$, at these driving velocities the stable mean values and standard deviations of W_{cyc} cannot be achieved until the number of cycles are large enough. The two numbers are chosen after some trial and error when the mean values and standard deviations of W_{cyc} no longer change obviously with the number of simulation cycles increasing.

For the main simulation case of $\eta = 3.0$, $\mu = 4 \times 10^4\text{s}^{-1}$ and $\Theta_{\text{h,c}} = 0.4, 0.04$ computed in a Dell Inc. PowerEdge T630 Server with two Intel(R) Xeon(R) CPU's (E5-2680 v4 @ 2.40GHz) and 192GB RAM with Matlab R2021a on Windows Server 2019 Standard Evaluation, the time to simulate all the cycles at all the driving velocities using SRK4 is about 20 hours.

Table S3. The number of simulation cycles at different driving velocities

$v_{\text{dr}}(\text{m/s})$	10^{-7}	10^{-6}	10^{-5}	2×10^{-5}	5×10^{-5}	7.5×10^{-5}	10^{-4}	2×10^{-4}	5×10^{-4}	7.5×10^{-4}
Number of cycles	20	200	2000	2000	2000	2000	5000	5000	8000	8000
$v_{\text{dr}}(\text{m/s})$	10^{-3}	1.5×10^{-3}	2×10^{-3}	3×10^{-3}	5×10^{-3}	7.5×10^{-3}	10^{-2}	1.5×10^{-2}	2×10^{-2}	3×10^{-2}
Number of cycles	20000	30000	40000	60000	100000	150000	200000	300000	400000	600000
$v_{\text{dr}}(\text{m/s})$	5×10^{-2}	7.5×10^{-2}	0.1	0.125	0.15	0.2	0.3	0.4	0.5	0.75
Number of cycles	1000000	1500000	3000000	3000000	3000000	3000000	3000000	22000000	12000000	3000000
$v_{\text{dr}}(\text{m/s})$	1	1.25	1.5	2	3	4	5	7.5	10	
Number of cycles	3000000	3000000	3000000	3000000	3000000	3000000	3000000	3000000	3000000	

For the case of $\mu = 4 \times 10^{-1}\text{s}^{-1}$ in the main text Figure 3(A), six more driving velocities are simulated at the low driving velocity end to make the curve smoother. The simulation cycles at these driving velocities are: 40 at $2 \times 10^{-7}\text{m/s}$, 100 at $5 \times 10^{-7}\text{m/s}$, 150 at $7.5 \times 10^{-7}\text{m/s}$, 200 at $2 \times 10^{-6}\text{m/s}$, 200 at $5 \times 10^{-6}\text{m/s}$ and 200 at $7.5 \times 10^{-6}\text{m/s}$.

At each driving velocity v_{dr} , the initial conditions are $(z(0), \dot{z}(0)) = (0, 0)$. Incidentally, we now realize that if we chose $(z(0), \dot{z}(0)) = (0, \bar{v})$, the transient stage before steady state being arrived at might be shortened at the beginning of the simulation time range, especially at the high driving velocity regime where \bar{v} is large.

The mean values and standard deviations of the cycle work W_{cyc} are averaged from the last 2000000 simulation cycles when the cycle number is 3000000, from the last 8000000 simulation cycles at $v_{\text{dr}} = 0.4\text{m/s}$, from the last 5000000 simulation cycles at $v_{\text{dr}} = 0.5\text{m/s}$, and from the last 90% of the simulation cycles at the rest driving velocities. These sample numbers are chosen after some trial and error to eliminate the influence from the beginning transient stage and to make sure that the sample numbers are large enough to reflect the true first and second order moments of the stochastic variable W_{cyc} .

We can give a check for the choice of the sample numbers. In Figure S62, we calculate the moving mean of the cycle work W_{cyc} with a sliding window of different number of simulation cycles. We can see that when the sample number is large enough the mean cycle work $\langle W_{\text{cyc}} \rangle$ is nearly constant with influence from the starting transient stage nearly unobservable. The purple curves represent our final choice of the sample numbers to calculate $\langle W_{\text{cyc}} \rangle$, which remains nearly unchanged when we increase the sample number further. Actually, we can see that at $v_{\text{dr}} = 0.5\text{m/s}$, the simulation cycle number we chose is excessive and a simulation cycle number of 3000000 and a sample number of 2000000 should be enough. Thus our choice of the sample numbers as well as the simulation cycle numbers is still rough. Even so, considering that our choice of the simulation cycle numbers is not very small and that the change of the mean values and the standard deviations calculated from different numbers of simulation cycles is not very large and doesn't affect our main conclusions, we didn't choose the number of simulation cycles for each simulation case specifically and used this set of cycle numbers for all of our simulation cases.

The count distribution of the cycle work at each driving velocity in Figure S40 is obtained from the same sample of simulation cycles as those used to calculate the mean values and the standard deviations at the same driving velocities.

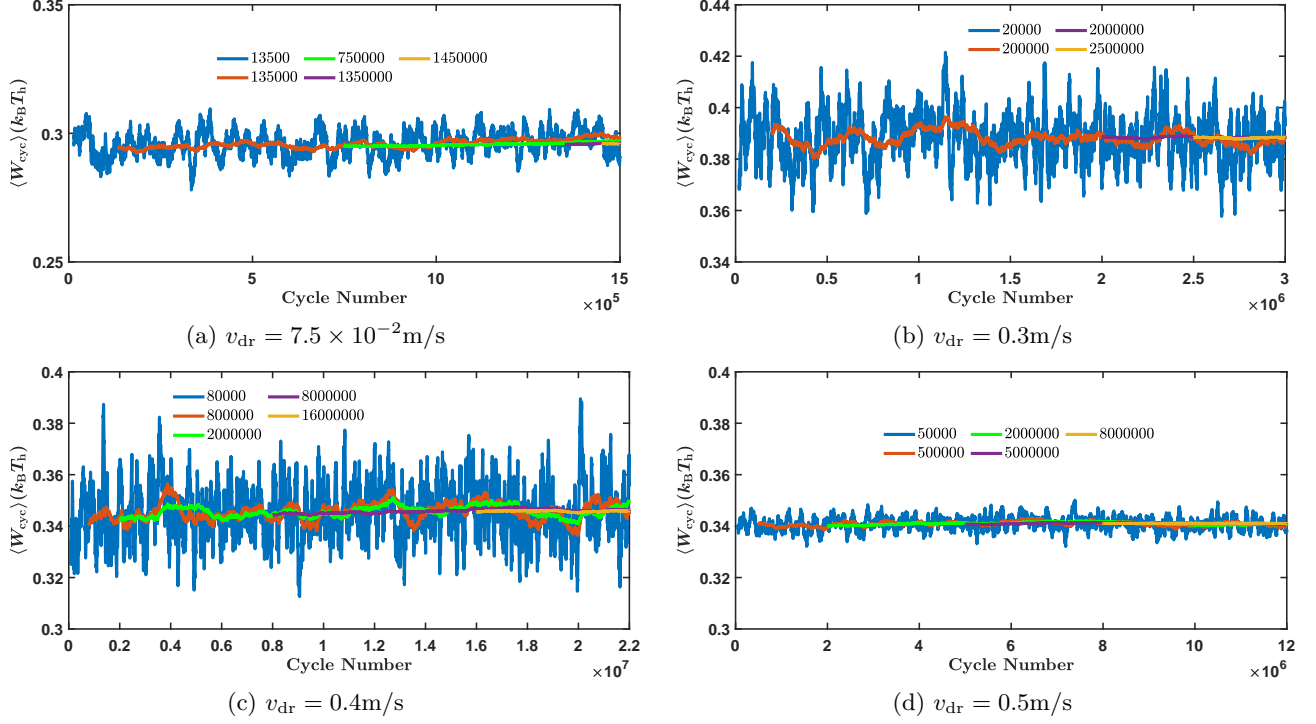


Fig. S62. The mean cycle work calculated from different sample number of simulation cycles at four typical driving velocities. The y -coordinate is the moving mean cycle work $\langle W_{\text{cyc}} \rangle$ averaged over a sliding window of different sample number of simulation cycles. The x -coordinate is the simulation cycle number from the beginning to the end of the simulation time range. Different color indicates different sample number to calculate the mean value $\langle W_{\text{cyc}} \rangle$. We take the case of $\eta = 3.0$, $\mu = 4 \times 10^4 \text{ s}^{-1}$ and $\Theta_{h,c} = 0.4, 0.04$ as an example. Each curve begins after the cycle number is greater than the corresponding sample number. We can see that at all the four driving velocities, our choice of the sample numbers (represented by the purple curves) are suitable in that the mean value $\langle W_{\text{cyc}} \rangle$ remains nearly unchanged with the sample number increased further. The range of the y -axis is $1 k_B T_h$ for all the four subfigures for comparison. In (c), we can see that at $v_{\text{dr}} = 0.4 \text{ m/s}$, the amplitude of $\langle W_{\text{cyc}} \rangle$ averaged from 80000 cycles is large and similar to that averaged from 20000 cycles at $v_{\text{dr}} = 0.3 \text{ m/s}$ in (b). At $v_{\text{dr}} = 0.4 \text{ m/s}$, the moving mean $\langle W_{\text{cyc}} \rangle$ averaged from 2000000 cycles still varies a little violently compared with the purple curve in (b) at $v_{\text{dr}} = 0.3 \text{ m/s}$, indicating that at $v_{\text{dr}} = 0.4 \text{ m/s}$, 2000000 cycles are not enough for the particle to traverse all the possible states sufficiently and the frequency obtained deviates from the steady-state probability to a certain extent, while at $v_{\text{dr}} = 0.3 \text{ m/s}$, the sample number of 2000000 is enough for the particle to traverse all the possible states with the frequency obtained close to the steady-state probability. The starting transient stage is observable when the sample number is small [≤ 80000 in (c) and ≤ 200000 in (b)] and becomes less observable when the sample number increases. At $v_{\text{dr}} = 0.5 \text{ m/s}$ in (d), we can see that the simulation number of 12000000 and the sample number of 5000000 are chosen excessively and 3000000 and 2000000 for the simulation and the sample number respectively should be enough. In (a) at $v_{\text{dr}} = 7.5 \times 10^{-2} \text{ m/s}$, we choose the last 90% simulation cycles as the sample, i.e. a sample number of 1350000. We presume that 10% simulation cycles at the beginning are enough for the particle to achieve steady state and it seems reasonable. There should be a critical sample number of simulation cycles at steady state for the particle's frequency distribution to reflect the steady-state probability distribution. This number should depend on the driving velocity, which is different from the dependence of the standard deviation of W_{cyc} on the driving velocity in that the standard deviation of W_{cyc} at $v_{\text{dr}} = 0.3 \text{ m/s}$ is greater than that at $v_{\text{dr}} = 0.4 \text{ m/s}$. This number should reflect the complexity of the steady-state probability distribution of W_{cyc} and may be related to the entropy of the particle. We will consider the entropy of the particle in the PTSHE in the future.

I. Further check of the simulation method: the first law of thermodynamics. In the above, we have evaluated the SRK4 method by using it to validate the equipartition theorem for the linear Langevin equation and comparing its performance with a nonlinear scheme from the simulation of our nonlinear Langevin equation. Through both of the two aspects we are able to choose an appropriate time stepsize and confirm that the SRK4 is suitable for solving our nonlinear Langevin equation. In this and next subsections, we will further check the SRK4 method, in the sense of low cumulative errors and the parameters chosen leading to results consistent with experiments.

We have derived the first law of thermodynamics from the Langevin equation in Sec. 5. The error

$$\delta_{\text{err}} = dU + dQ - dW, \quad [128]$$

should keep small throughout the time range of each simulation case (65). To measure this, we consider its integral over one cycle in which the driver goes through one lattice period

$$\Delta_{\text{err,cyc}} = \Delta U_{\text{cyc}} + Q_{\text{cyc}} - W_{\text{cyc}}. \quad [129]$$

In Figure S63, the cycle work W_{cyc} is compared with $\Delta_{\text{err,cyc}}$. We can see that for both the low driving velocity $v_{\text{dr}} = 10^{-5} \text{ m/s}$ and the high driving velocity $v_{\text{dr}} = 10 \text{ m/s}$, the cycle error $\Delta_{\text{err,cyc}}$ keeps small and is about four orders of magnitude lower than W_{cyc} from the beginning to the end of the time range of each simulation case, which is true even in the violent transient process at the beginning of the $v_{\text{dr}} = 10 \text{ m/s}$ case.

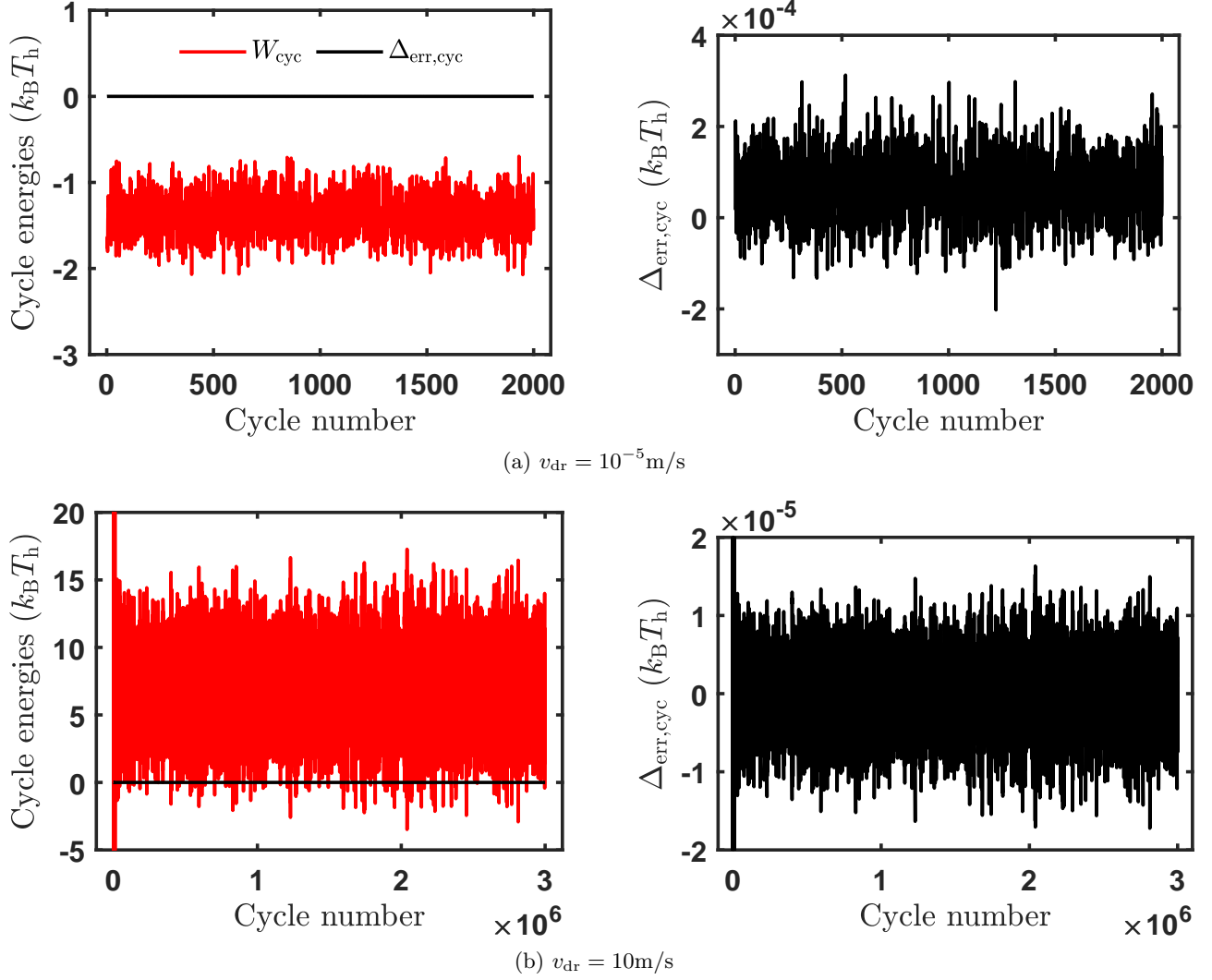


Fig. S63. The cycle error $\Delta_{\text{err,cyc}}$ compared with the cycle work W_{cyc} . The upper two figures are simulation results at $v_{\text{dr}} = 10^{-5} \text{ m/s}$, in the case of which we simulate 2000 cycles. The lower two figures correspond to $v_{\text{dr}} = 10 \text{ m/s}$, in the case of which we simulate 3×10^6 cycles. When compared with the cycle work, the cycle errors keep small throughout the simulating time range, as shown in the left two figures. The right two figures are the zoom-in of the cycle errors on the left, indicating that the cycle errors are about four orders of magnitude lower than the cycle work values.

J. Further check of the simulation method: comparison with the experimental results. To confirm that our mathematical model is predictable for practical problems, we do more numerical experiments to simulate the trapped ion friction simulator in (40, 53) and compare our results with the experiments.

In (40, 53), the fluorescence of the ion, which is proportional to the lattice potential energy $\tilde{V}_1 = \eta(1 - \cos z)$, is detected to measure the friction force. The green dashed curves in Figure S65, S66 and S67 represent the lattice potential energy \tilde{V}_1 at the resultant potential energy extrema z^* with respect to $\tilde{X}(t) = \frac{v_{\text{dr}} t}{a}$, which can be represented by Eq. 10 and has been obtained in Figure S3. As we have shown in Figure S3, at zero temperature and infinite damping coefficient, i.e. quasis-tatic state, the particle slips at the instant of the BCP [i.e. $\tilde{X}(z_1^{**})$, cf. Sec. 2 and Sec. 3] of one cycle if the driver moves forward. If the driver moves backward, the particle will slip at the instant of the FCP [i.e. $\tilde{X}(z_2^{**})$, cf. Sec. 2 and Sec. 3]. So the forward and backward sweeping of the driver causes hysteresis, and half of the separation between the two critical points is proportional to the maximum friction force defined in (40, 53):

$$\begin{aligned}
 F_\eta &= \frac{1}{2} m \omega_0^2 a [\tilde{X}(z_1^{**}) - \tilde{X}(z_2^{**})] \\
 &= \frac{1}{2} m \omega_0^2 a \{z_1^{**} + \eta \sin(z_1^{**}) - [z_2^{**} + \eta \sin(z_2^{**})]\} \\
 &= \frac{1}{2} m \omega_0^2 a \left\{ \arccos\left(-\frac{1}{\eta}\right) + \eta \sin\left(\arccos\left(-\frac{1}{\eta}\right)\right) - \left[2\pi - \arccos\left(-\frac{1}{\eta}\right) + \eta \sin\left(2\pi - \arccos\left(-\frac{1}{\eta}\right)\right)\right] \right\} \\
 &= m \omega_0^2 a \left[-\pi + \arccos\left(-\frac{1}{\eta}\right) + \eta \sin\left(\arccos\left(-\frac{1}{\eta}\right)\right) \right],
 \end{aligned} \tag{130}$$

which is only determined by η . When the temperature is finite, the particle tends to slips early and both of the two slipping points approach to the middle and the friction force F will be smaller than the maximum friction force. In the experiment the driver moves forward for several lattice periods and then moves backward and this loop is repeated many times. The fluorescence counts are detected at different time bins and then averaged over the all the repeated loops. To simulate the experiment as closely as possible, we integrate the Langevin equation forward three (or six at some very high velocities, cf. Figure S65, S66 and S67) lattice periods and then backward three (or six at some very high velocities, cf. Figure S65, S66 and S67) lattice periods, and this loop is repeated for a large number of times which we presume are enough to reflect the true statistics. The number of simulation loops are given in Table S4, S5 and S6 before Figure S65, S66 and S67 respectively. During each loop, the forward and backward three (six) lattice periods passed by the driver center are both divided into 50 (100) bins. In each bin, the value of $\cos^2(z/2)$ at each discrete time step is summed and averaged to achieve the $\overline{\cos^2(z/2)}$ at the middle of each bin. Then we average $\overline{\cos^2(z/2)}$ at each specific bin through all the repeated simulation loops and obtain $\langle \cos^2(z/2) \rangle$ at the middle of each bin, which is proportional to the fluorescence counts of the ion in the experiments. The results are given in Figure S65, S66 and S67.

All the x-coordinates in the three figures are applied force $F/(m\omega_0^2 a)$ (53) which is equal to the nondimensional driver center position $\tilde{X}(\tau) = X(t)/a$ relative to the starting point 0. The error bars represent the standard deviations calculated from the ensemble of the repeated simulation loops of each simulation case at each specific bin. In each of the three cases, the separations of the peaks (at which slips occur) of the hysteresis loops first increase (and then decrease in two of the three cases), i.e. twofold of the so-defined friction forces (40, 53) first increase (and then decrease in two of the three cases). The peaks of the hysteresis loops are each fitted to the quadratic polynomial $a(x - b)^2 + c$ from 7 points (3 points on either side of the local maximum point) by quadratic nonlinear least square method. Half of the separation of two b 's in one hysteresis loop is equal to the friction force $F/(m\omega_0^2 a)$. The error of F is calculated from the 67% confidence intervals of the two b 's. At each driving velocity v_{dr} , we can get two or five friction forces and their errors. We then average these values to obtain the final friction forces and errors.

In Figure S64, we plot the simulation friction force with respect to the driving velocity compared with the experimental results for the three cases in Figure 2 of (40). We can see that for the first and the third case in (A) and (C) respectively, the simulation results and the experimental results are close. For the second case, the simulation results are a little larger than the experimental results at low driving velocities. From Figure S66 we can see that at low driving velocities the measuring of the friction force is conservative, while in spite of this the simulation results are still larger. We note that in (40) the authors correct the temperature in their simulation and analytical models [see the supplementary information of (40)], while we introduce no correction. Therefore our simulation results agree quantitatively or at least semi-quantitatively with the experimental results and we can conclude that our numerical method is predictable for practical problems.

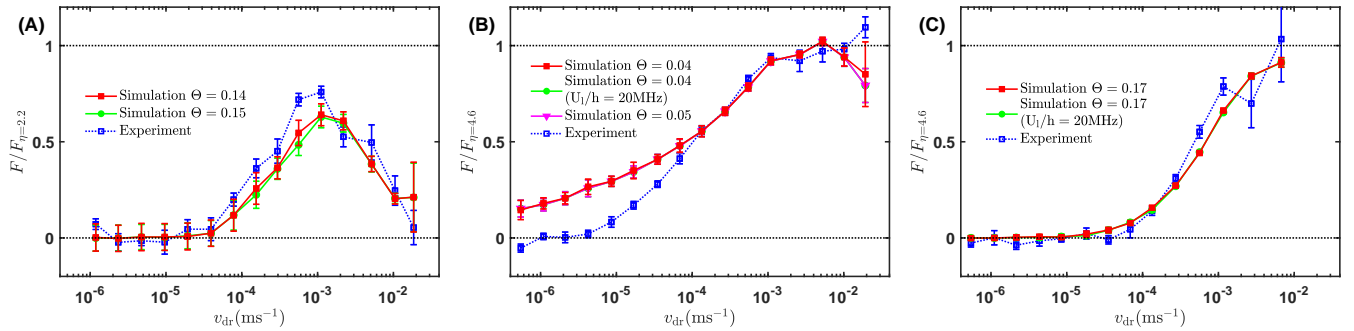


Fig. S64. The friction force with respect to the driving velocity: comparison between the simulation and the experiment. (A) The results of the case of $\eta = 2.2$, $\mu = 2 \times 10^4 \text{ s}^{-1}$, $V_0 = 2\pi\hbar \times 9.5 \text{ MHz}$ and $\Theta = 0.14(0.15)$. (B) The results of the case of $\eta = 4.6$, $\mu = 4 \times 10^4 \text{ s}^{-1}$, $V_0 = 2\pi\hbar \times 18(20) \text{ MHz}$ and $\Theta = 0.04(0.05)$. (C) The results of the case of $\eta = 4.6$, $\mu = 4 \times 10^4 \text{ s}^{-1}$, $V_0 = 2\pi\hbar \times 18(20) \text{ MHz}$ and $\Theta = 0.17$. The experimental data are from Figure 2 of (40) courtesy of the authors. In each subfigure, we plot two or three sets of simulation results at parameters a little different from each other [corresponding to the tiny difference between the parameters in Figure 2 of the authors' paper (40) and those in Figure 15-5 of one of the authors' theses (66) respectively] and we can see that there is no significant deviation.

Table S4. Number of simulation loops for Figure S65

$v_{dr}(\text{m/s})$	Number of loops	$v_{dr}(\text{m/s})$	Number of loops	$v_{dr}(\text{m/s})$	Number of loops
1.18549201434396e-06	30	2.34735773684298e-06	30	4.75054129690064e-06	48
9.61785513478092e-06	100	1.92947430887720e-05	200	3.92472869445721e-05	400
7.81396573846716e-05	790	0.000154898829332650	1200	0.000295777367511797	3000
0.000562210180376583	5700	0.00111396132026529	12000	0.00218933180613166	22000
0.00515587947242487	57000	0.0105075865958613	110000	0.0185006051024171	190000

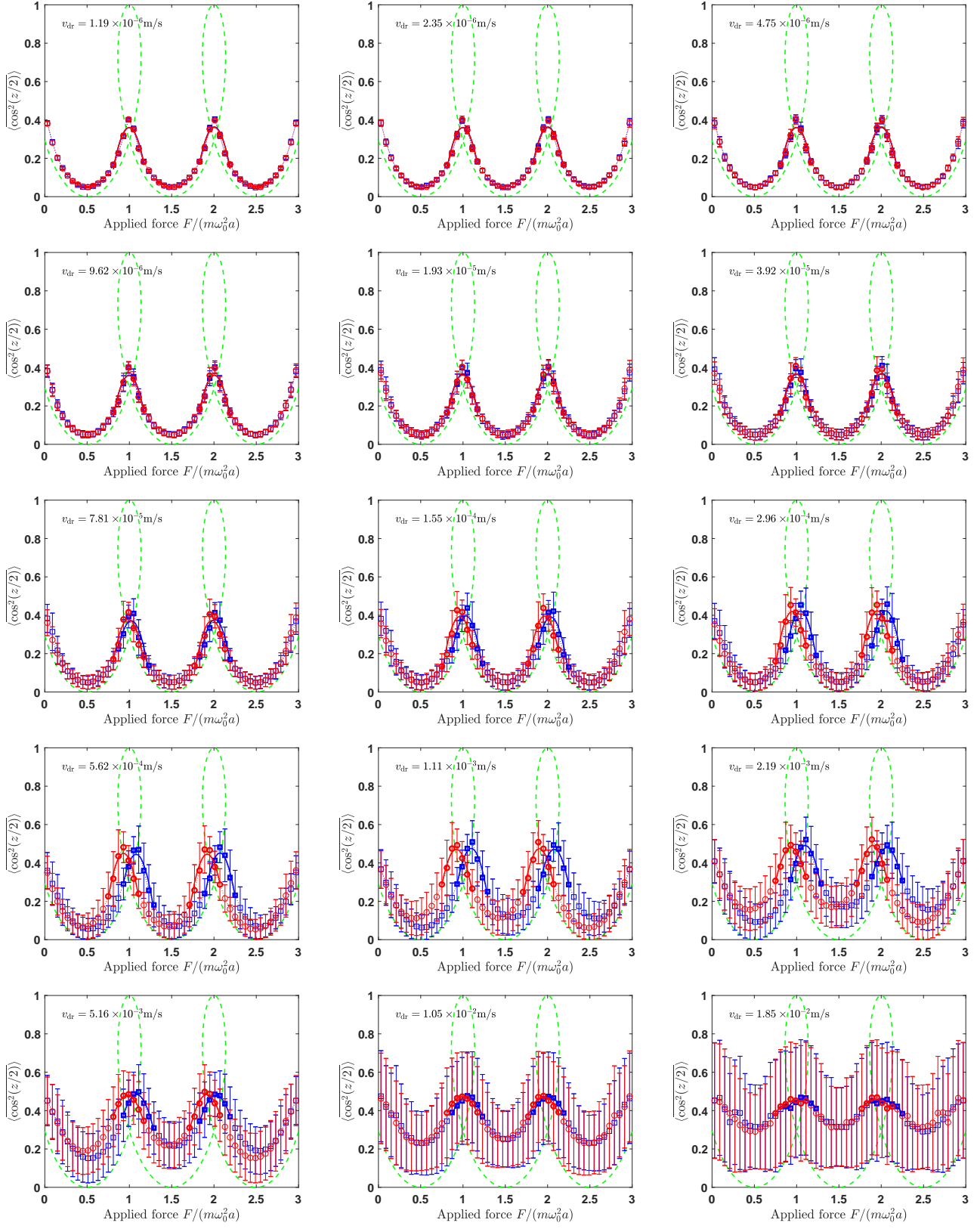
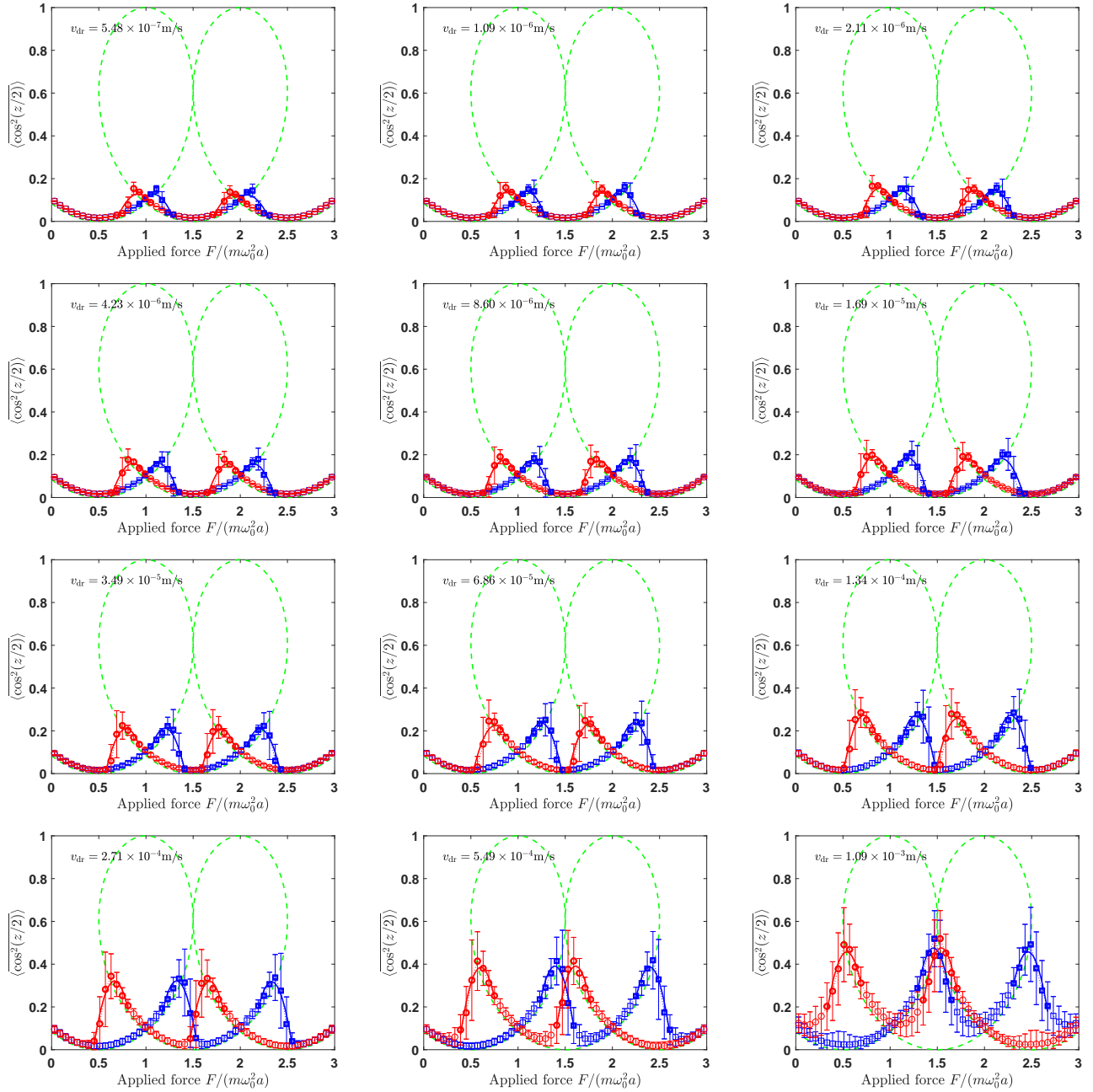


Fig. S65. The simulation fluorescence counts at different driving velocity v_{dr} in the case of $\eta = 2.2$, $\mu = 2 \times 10^4 \text{ s}^{-1}$, $V_0 = 2\pi\hbar \times 9.5 \text{ MHz}$ and $\Theta = 0.14$. The parameters are inherited from Figure 15-5 in (66). ω_0 is determined by η and V_0 with $\eta = \frac{2\pi^2 V_0}{m\omega_0^2 a^2}$ in which m and a are given in Table S2. The green dashed curves are $\cos^2(z^*/2)$ at the balanced points z^* of the resultant potential energy with respect to the driver center's position $\tilde{X}(z^*)$, which is equal to the applied force $F/(m\omega_0^2 a)$, cf. Figure S3. The friction forces measured from different hysteresis loops in each subfigure are averaged to obtain the final friction force at each driving velocity.

Table S5. Number of simulation loops for Figure S66

$v_{dr}(\text{m/s})$	Number of loops	$v_{dr}(\text{m/s})$	Number of loops	$v_{dr}(\text{m/s})$	Number of loops
5.48330003252868e-07	15	1.09148805346082e-06	30	2.10838483259046e-06	30
4.23341275737471e-06	43	8.60114892152780e-06	87	1.68661013327135e-05	170
3.49433799327154e-05	350	6.86477082436799e-05	690	0.000134028433498140	1400
0.000271253909318031	2800	0.000548809185400129	5500	0.00109233256749753	11000
0.00262136175653125	27000	0.00524259937197039	53000	0.0101243891976080	110000
0.0192306183601816	200000				



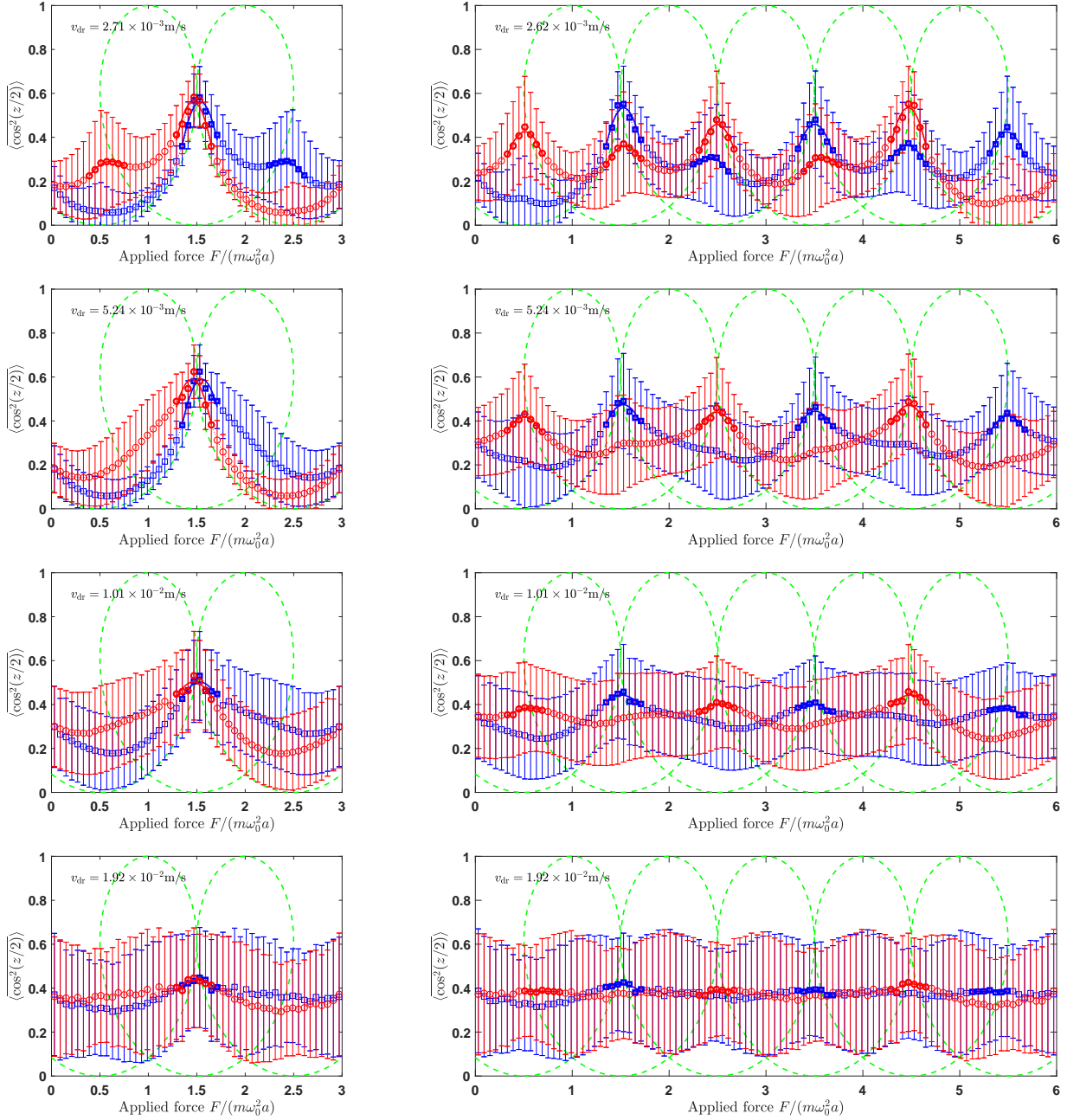
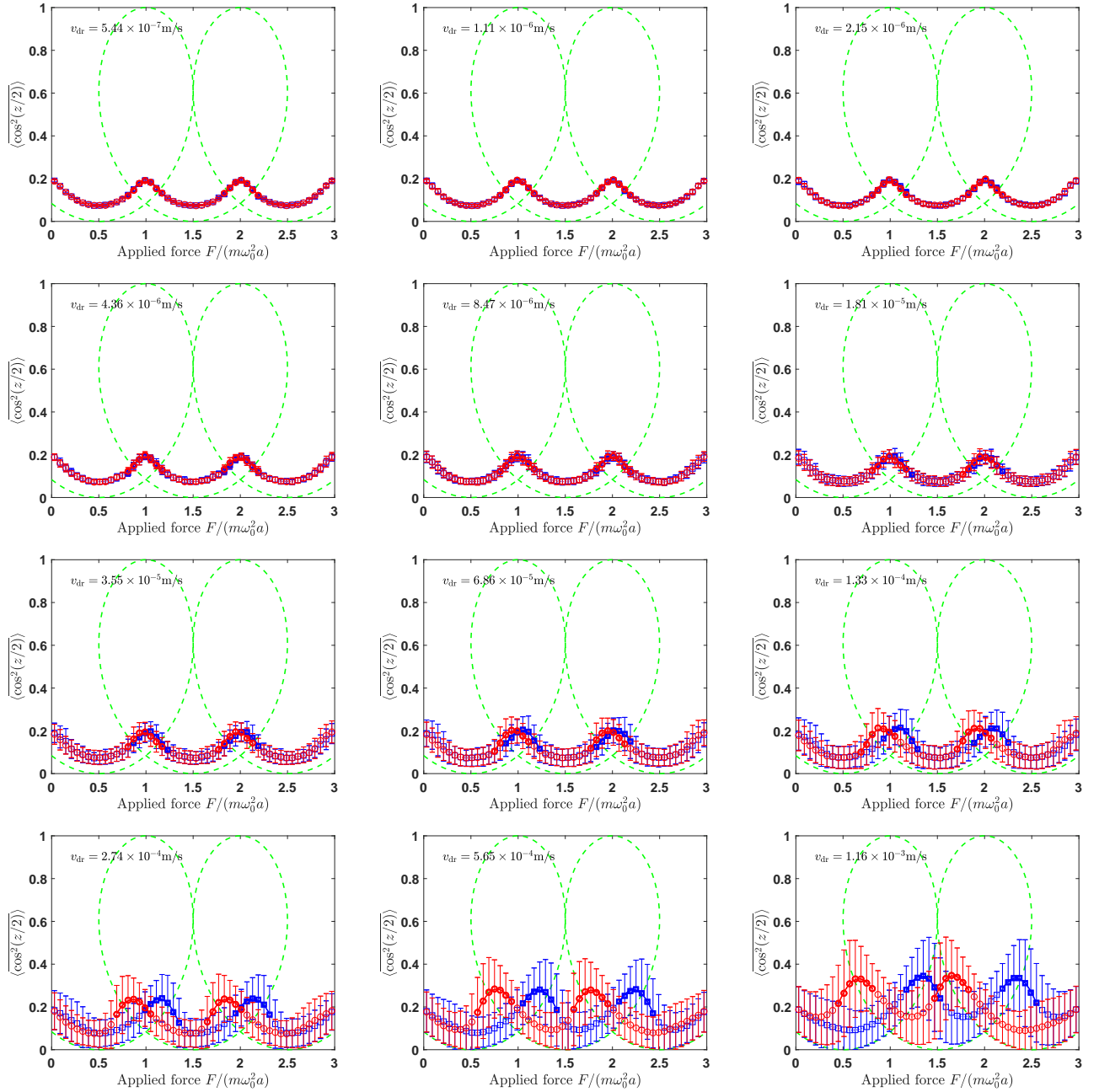


Fig. S66. The simulation fluorescence counts at different driving velocity v_{dr} in the case of $\eta = 4.6$, $\mu = 4 \times 10^4 \text{ s}^{-1}$, $V_0 = 2\pi\hbar \times 18\text{MHz}$ and $\Theta = 0.04$. The parameters are inherited from Figure 15-5 in (66). ω_0 is determined by η and V_0 with $\eta = \frac{2\pi^2 V_0}{m\omega_0^2 a^2}$ in which m and a are given in Table S2. The green dashed curves are $\cos^2(z^*/2)$ at the balanced points z^* of the resultant potential energy with respect to the driver center's position $\tilde{X}(z^*)$, which is equal to the applied force $F/(m\omega_0^2 a)$, cf. Figure S3. At the last four driving velocities, the adjacent hysteresis loops interfere with each other and 3 periods are not adequate for recognizable hysteresis loops, so we simulate 6 periods in either direction and the 3-period results are given on the left of them for comparison. At the last three driving velocities, there are three recognizable hysteresis loops in the 6-period subfigures; at the fourth from the last one, there are five and at the others, there are two. The friction forces measured from different hysteresis loops in each subfigure are averaged to obtain the final friction force at each driving velocity. Incidentally, at the fourth from the last driving velocity, there are still two recognizable hysteresis loops in the 3-period subfigure and the friction force averaged from measuring the two hysteresis loops is close to the result obtained from the 6-period subfigure. Nevertheless, we get the friction force from the 6-period subfigure if there is one.

Table S6. Number of simulation loops for Figure S67

$v_{dr}(\text{m/s})$	Number of loops	$v_{dr}(\text{m/s})$	Number of loops	$v_{dr}(\text{m/s})$	Number of loops
5.44388025066915e-07	15	1.10564067717483e-06	30	2.15141515728251e-06	30
4.35733373350793e-06	44	8.46740770553410e-06	85	1.81424066649033e-05	190
3.54768157470305e-05	360	6.86415767660501e-05	690	0.000133298297451480	1400
0.000273712287989294	2800	0.000564691945089056	5700	0.00116318457296758	12000
0.00271481432041413	28000	0.00674279208568709	68000		



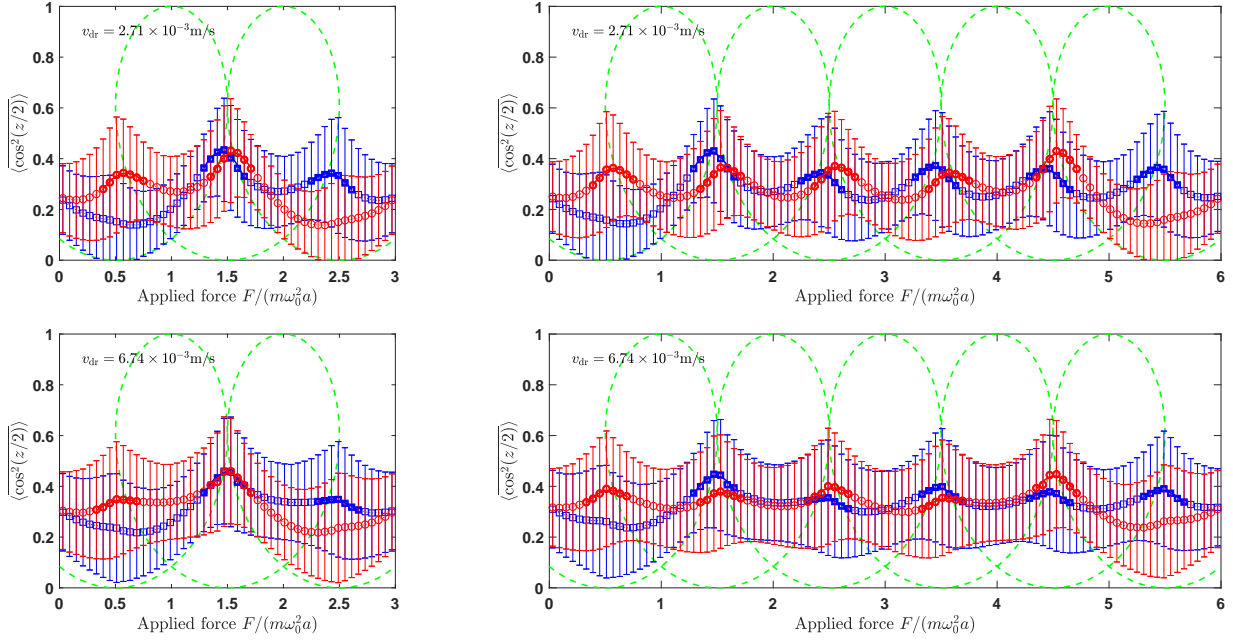


Fig. S67. The simulation fluorescence counts at different driving velocities in the case of $\eta = 4.6$, $\mu = 4 \times 10^4 \text{ s}^{-1}$, $V_0 = 2\pi\hbar \times 18 \text{ MHz}$ and $\Theta = 0.17$. These parameters are inherited from Figure 15-5 in (66). ω_0 is determined by η and V_0 with $\eta = \frac{2\pi^2 V_0}{m\omega_0^2 a^2}$ in which m and a are given in Table S2. The green dashed curves are $\cos^2(z^*/2)$ at the balanced points z^* of the resultant potential energy with respect to the driver center's position $\tilde{X}(z^*)$, which is equal to the applied force $F/(m\omega_0^2 a)$, cf. Figure S3. At the last two driving velocities, the adjacent hysteresis loops tend to interfere with each other and 3 periods seem not adequate for recognizable hysteresis loops, so we simulate 6 periods in either direction with the 3-period results given on the left of them for comparison. At the last two driving velocities, there are five recognizable hysteresis loops in the 6-period subfigures and at the others, there are two. The friction forces measured from different hysteresis loops in each subfigure are averaged to obtain the final friction force at each driving velocity. Actually, at the last two driving velocities, there are still two recognizable hysteresis loops in the two 3-period subfigures and the friction forces averaged from measuring the two hysteresis loops in both of them are close to the results obtained from the corresponding 6-period subfigures. Nevertheless, we get the friction forces from the two 6-period subfigures at the last two driving velocities.

References

1. PA Johnson, H Savage, M Knuth, J Gomberg, C Marone, Effects of acoustic waves on stick-slip in granular media and implications for earthquakes. *Nature* **451**, 57–60 (2008).
2. DA Wiens, S Anandakrishnan, JP Winberry, MA King, Simultaneous teleseismic and geodetic observations of the stick-slip motion of an Antarctic ice stream. *Nature* **453**, 770–774 (2008).
3. JE Kendrick, et al., Volcanic drumbeat seismicity caused by stick-slip motion and magmatic frictional melting. *Nat. Geosci.* **7**, 438–442 (2014).
4. SP Satyabala, Z Yang, R Bilham, Stick-slip advance of the Kohat Plateau in Pakistan. *Nat. Geosci.* **5**, 147–150 (2012).
5. WF Brace, JD Byerlee, Stick-Slip as a Mechanism for Earthquakes. *Science* **153**, 990–992 (1966).
6. RA Bindshadler, MA King, RB Alley, S Anandakrishnan, L Padman, Tidally Controlled Stick-Slip Discharge of a West Antarctic Ice. *Science* **301**, 1087–1089 (2003).
7. FX Passelègue, A Schubnel, S Nielsen, HS Bhat, R Madariaga, From Sub-Rayleigh to Supershear Ruptures During Stick-Slip Experiments on Crustal Rocks. *Science* **340**, 1208–1211 (2013).
8. X Gao, K Wang, Strength of stick-slip and creeping subduction megathrusts from heat flow observations. *Science* **345**, 1038–1041 (2014).
9. BM Kaproth, C Marone, Slow Earthquakes, Preseismic Velocity Changes, and the Origin of Slow Frictional Stick-Slip. *Science* **341**, 1229–1232 (2013).
10. T Johnson, FT Wu, CH Scholz, Source Parameters for Stick-Slip and for Earthquakes. *Science* **179**, 278–280 (1973).
11. SN Patek, Spiny lobsters stick and slip to make sound. *Nature* **411**, 153–154 (2001).
12. NH Fletcher, TD Rossing, *The physics of musical instruments*. (Springer Science & Business Media), (2012).
13. K Hennig, et al., Stick-slip dynamics of cell adhesion triggers spontaneous symmetry breaking and directional migration of mesenchymal cells on one-dimensional lines. *Sci. Adv.* **6**, eaau5670 (2020).
14. P Sens, Stick-slip model for actin-driven cell protrusions, cell polarization, and crawling. *Proc. Natl. Acad. Sci.* **117**, 24670–24678 (2020).
15. UM Mirsaidov, H Zheng, D Bhattacharya, Y Casana, P Matsudaira, Direct observation of stick-slip movements of water nanodroplets induced by an electron beam. *Proc. Natl. Acad. Sci.* **109**, 7187–7190 (2012).
16. DA Weitz, Foams flow by stick and slip. *Nature* **381**, 475–476 (1996).
17. R Budakian, K Weninger, RA Hiller, SJ Putterman, Picosecond discharges and stick-slip friction at a moving meniscus of mercury on glass. *Nature* **391**, 266–268 (1998).
18. CG Camara, JV Escobar, JR Hird, SJ Putterman, Correlation between nanosecond X-ray flashes and stick-slip friction in peeling tape. *Nature* **455**, 1089–1092 (2008).
19. T Palberg, K Streicher, Resonant stick-slip motion in a colloidal crystal. *Nature* **367**, 51–54 (1994).
20. PA Thompson, MO Robbins, Origin of Stick-Slip Motion in Boundary Lubrication. *Science* **250**, 792–794 (1990).
21. O Ben-David, SM Rubinstein, J Fineberg, Slip-stick and the evolution of frictional strength. *Nature* **463**, 76–79 (2010).
22. RG Xu, Y Leng, Squeezing and stick-slip friction behaviors of lubricants in boundary lubrication. *Proc. Natl. Acad. Sci.* **115**, 6560–6565 (2018).
23. DW Lee, X Banquy, JN Israelachvili, Stick-slip friction and wear of articular joints. *Proc. Natl. Acad. Sci.* **110**, E567–E574 (2013).
24. SY Krylov, JWM Frenken, The physics of atomic-scale friction: Basic considerations and open questions. *physica status solidi (b)* **251**, 711–736 (2014).
25. A Vanossi, N Manini, M Urbakh, S Zapperi, E Tosatti, Colloquium: Modeling friction: From nanoscale to mesoscale. *Rev. Mod. Phys.* **85**, 529–552 (2013).
26. Y Dong, A Vadakkepatt, A Martini, Analytical Models for Atomic Friction. *Tribol. Lett.* **44**, 367–386 (2011).
27. MH Müser, Velocity dependence of kinetic friction in the Prandtl-Tomlinson model. *Phys. Rev. B* **84** (2011).
28. ZJ Wang, TB Ma, YZ Hu, L Xu, H Wang, Energy dissipation of atomic-scale friction based on one-dimensional Prandtl-Tomlinson model. *Friction* **3**, 170–182 (2015).
29. SN Medyanik, WK Liu, IH Sung, RW Carpick, Predictions and observations of multiple slip modes in atomic-scale friction. *Phys Rev Lett* **97**, 136106 (2006).
30. U Seifert, Stochastic thermodynamics, fluctuation theorems and molecular machines. *Rep Prog Phys* **75**, 126001 (2012).
31. K Sekimoto, Kinetic Characterization of Heat Bath and the Energetics of Thermal Ratchet Models. *J. Phys. Soc. Jpn.* **66**, 1234–1237 (1997).
32. K Sekimoto, Langevin Equation and Thermodynamics. *Prog. Theor. Phys. Suppl.* **130**, 17–27 (1998).
33. V Blickle, C Bechinger, Realization of a micrometre-sized stochastic heat engine. *Nat. Phys.* **8**, 143–146 (2011).
34. IA Martinez, et al., Brownian Carnot engine. *Nat Phys* **12**, 67–70 (2016).
35. KB Jinesh, SY Krylov, H Valk, M Dienwiebel, JWM Frenken, Thermolubricity in atomic-scale friction. *Phys. Rev. B* **78**, 155440 (2008).
36. A Bylinskii, “15.1 Thermal hopping and dissipation” in *Friction under microscope with trapped ions in optical lattices*, Ph.D. thesis. (Massachusetts Institute of Technology), pp. 145–146 (2016).
37. H Risken, Solutions of the Kramers Equation in *The Fokker-Planck Equation: Methods of Solution and Applications*. (Springer Berlin Heidelberg, Berlin, Heidelberg), pp. 229–275 (1996).
38. KL Johnson, J Woodhouse, Stick-slip motion in the atomic force microscope. *Tribol. Lett.* **5**, 155–160 (1998).

39. EA Jagla, Velocity weakening and possibility of aftershocks in nanoscale friction experiments. *Phys. Rev. B* **86** (2012).
40. D Gangloff, A Bylinskii, I Counts, W Jhe, V Vuletić, Velocity tuning of friction with two trapped atoms. *Nat. Phys.* **11**, 915–919 (2015).
41. L Gammaitoni, P Hänggi, P Jung, F Marchesoni, Stochastic resonance. *Rev. Mod. Phys.* **70**, 223–287 (1998).
42. R Seydel, 7 Stability of Periodic Solutions in *Practical Bifurcation and Stability Analysis*. (Springer New York, New York, NY), pp. 303–356 (2010).
43. LF Shampine, MW Reichelt, The MATLAB ODE Suite. *SIAM J. on Sci. Comput.* **18**, 1–22 (1997).
44. A Dhooge, W Govaerts, YA Kuznetsov, HGE Meijer, B Sautois, New features of the software MatCont for bifurcation analysis of dynamical systems. *Math. Comput. Model. Dyn. Syst.* **14**, 147–175 (2008).
45. R Seydel, 4 Principles of Continuation in *Practical Bifurcation and Stability Analysis*. (Springer New York, New York, NY), pp. 169–198 (2010).
46. R Seydel, 2 Basic Nonlinear Phenomena in *Practical Bifurcation and Stability Analysis*. (Springer New York, New York, NY), p. 70 (2010).
47. JA Johnson, et al., Direct Measurement of Room-Temperature Nondiffusive Thermal Transport Over Micron Distances in a Silicon Membrane. *Phys. Rev. Lett.* **110**, 5 (2013).
48. HJ Eichler, P Günter, DW Pohl, *Laser-induced dynamic gratings*, Springer Series in Optical Sciences. (Springer) Vol. 50, (2013).
49. JA Rogers, AAM and, MJ Banet, KA Nelson, Optical Generation and Characterization of Acoustic Waves in Thin Films: Fundamentals and Applications. *Annu. Rev. Mater. Sci.* **30**, 117–157 (2000).
50. DE Chang, et al., Cavity opto-mechanics using an optically levitated nanosphere. *Proc. Natl. Acad. Sci.* **107**, 1005–1010 (2010).
51. GAT Pender, PF Barker, F Marquardt, J Millen, TS Monteiro, Optomechanical cooling of levitated spheres with doubly resonant fields. *Phys. Rev. A* **85**, 021802 (2012).
52. A Dechant, N Kiesel, E Lutz, All-optical nanomechanical heat engine. *Phys Rev Lett* **114**, 183602 (2015).
53. A Bylinskii, D Gangloff, V Vuletić, Tuning friction atom-by-atom in an ion-crystal simulator. *Science* **348**, 1115–1118 (2015).
54. RK Pathria, PD Beale, “15 - Fluctuations and Nonequilibrium Statistical Mechanics” in *Statistical Mechanics (Third Edition)*, eds. RK Pathria, PD Beale. (Academic Press, Boston), pp. 601–603 (2011).
55. R Zwanzig, 1. Brownian Motion and Langevin Equations in *Nonequilibrium statistical mechanics*. (Oxford University Press), p. 18 (2001).
56. NJ Kasdin, Runge-Kutta Algorithm for the Numerical Integration of Stochastic Differential Equations. *J. Guid. Control. Dyn.* **18**, 114–120 (1995).
57. D Gangloff, “Chapter 10 Full-dynamics simulation of stick-slip friction” in *Nanocontacts controlled atom-by-atom in an ion-crystal friction emulator*, Ph.D. thesis. (Massachusetts Institute of Technology), pp. 161–169 (2016).
58. CW Gardiner, “4 The Ito Calculus and Stochastic Differential Equations” in *Handbook of Stochastic Methods for Physics, Chemistry and the Natural Sciences*, Springer Series in Synergetics. (Springer.), 3rd edition, pp. 80–116 (2009).
59. RL Stratonovich, A New Representation for Stochastic Integrals and Equations. *SIAM J. on Control.* **4**, 362–371 (1966).
60. R Perez-Carrasco, JM Sancho, Stochastic algorithms for discontinuous multiplicative white noise. *Phys. Rev. E* **81**, 032104 (2010).
61. PE Kloeden, E Platen, Strong Taylor Approximations in *Numerical Solution of Stochastic Differential Equations*. (Springer Berlin Heidelberg, Berlin, Heidelberg), pp. 339–371 (1992).
62. PE Kloeden, E Platen, Stochastic Taylor Expansions in *Numerical Solution of Stochastic Differential Equations*. (Springer Berlin Heidelberg, Berlin, Heidelberg), pp. 161–226 (1992).
63. I Counts, et al., Multislip Friction with a Single Ion. *Phys Rev Lett* **119**, 043601 (2017).
64. J Millen, PZG Fonseca, T Mavrogordatos, TS Monteiro, PF Barker, Cavity Cooling a Single Charged Levitated Nanosphere. *Phys. Rev. Lett.* **114**, 123602 (2015).
65. V Blickle, T Speck, L Helden, U Seifert, C Bechinger, Thermodynamics of a colloidal particle in a time-dependent nonharmonic potential. *Phys Rev Lett* **96**, 070603 (2006).
66. A Bylinskii, *Friction under microscope with trapped ions in optical lattices*, Ph.D. thesis. (Massachusetts Institute of Technology), (2016).